THE HYDRODYNAMICS OF THE WATER HAMMER ENERGY SYSTEM

Adam David Roberts

A thesis submitted in partial fulfilment of the requirements for the degree of Doctor of Philosophy

Department of Design and Engineering

Bournemouth University

January 2017

Abstract

The generation of electricity from fossil fuels is a major contributor to climate change and cannot be sustained indefinitely. Renewables can provide electricity in a more sustainable manner, however supplies from sources such as wind and solar can be variable and unpredictable. Hydropower and tidal energy offer more predictable generation capacity, making them appealing for a resilient transmission system. This is particularly true in the context of decentralised power grids, which harness smaller amounts of energy from a wide range of sources to improve transmission efficiency and reliability. Yet for tidal power in particular, little work has been done thus far on developing small scale technology capable of working efficiently in low flow speed (< 2 m/s) conditions. This research was conducted to identify, design and develop a device capable of generating pico scale power (< 1 kW) in shallow water, low input tidal and river conditions. The result is the Water Hammer Energy System (WHES), a novel design that makes use of water hammer pressure surges to generate vertical oscillations from a horizontal flow of water.

The hydrodynamics of the system are investigated through a combination of experimental and theoretical work, with studies conducted into the effect of input head, flow rate, and device size on performance. A 16 mm diameter experimental device was found to provide a piston with a mean power of 8 mW. Data from this study was used to validate a mathematical model, which predicted a maximum hydrodynamic efficiency of 23.1 % for a 1 m^2 device operating at a 0.50 Hz valve closure frequency in 0.4 m/s flow. Assuming a 30 % generator efficiency, such a device operating in the mouth of Poole Harbour (where the peak flow speeds reach 1.69 m/s) could supply an average of 1.14 kW of power. Over the course of a year, this would provide enough electrical energy to supply 2 typical UK houses and offset 5.55 tonnes of CO_2. 5.85 kW would be generated in a constant flow of 1.69 m/s, sufficient to supply the annual electricity requirements of 11 typical UK households and offset nearly 30 tonnes of CO_2. With further development, the system may therefore be a viable method of generating pico scale hydropower from shallow water, low input sites.

Contents

List of Figures

List of Tables

List of publications

Journal articles

- Roberts, A., Thomas, B., Sewell, P., Khan, Z., Balmain, S. and Gillman, J., 2016. Current tidal power technologise and their suitability for small-scale applications in shallow near-shore areas. *Journal of Ocean Engineering and Marine Energy*, 2 (2), 227–245.

- Roberts, A., Thomas, B., Sewell, P., Hoare, E., Balmain, S. and Balmain, I. Generating renewable power with water hammer pressure surges. *To be submitted to Renewable Energy.*

International conferences

- Roberts, A., Thomas, B., Sewell, P. Aslani, N. Balmain, S., Balmain, I. and Gillman, J., 2016. The Potential of the Water Hammer in Pico-Scale Tidal Power Systems: an Experimental Investigation, *Fourth International Symposium on Environment Friendly Energies and Applications*, Belgrade, Serbia.

Internal conferences

- Roberts, A., Thomas, B., Sewell, P., Balmain, S., 2016. The potential of using the water hammer effect in small-scale tidal power applications. *Second Annual Science and Technology Conference*, Bournemouth, UK. Awarded prize for best presentation.

- Roberts, A., Thomas, B., Khan, Z., Balmain, S., 2014. An optimised tidal energy design for Poole Harbour. *Seventh Annual PGR Poster Conference*, Bournemouth, UK. Awarded prize for best poster.

Acknowledgements

I would firstly like to thank my two academic supervisors at Bournemouth University, Dr Ben Thomas and Dr Philip Sewell, for their support, guidance and patience over the course of this project. I would also like to thank Professor Zulfiqar Khan, who was part of the supervisory team during my first year of study.

Secondly, I would like to extend my thanks and gratitude to Stewart and Iain Balmain, for their assistance and support in designing, developing and testing the Water Hammer Energy System. Further gratitude goes to the Balmain Environment Conservation Trust for match-funding this project alongside Bournemouth University. I must also acknowledge and thank the late John Gillman, who introduced me to hydraulic ram pumps and the water hammer effect. Without his suggestions during our first meeting at Bournemouth University, I would have never conceived the ideas within this thesis.

Furthermore, I would like to thank Robert Gardiner, Will Lambert and the rest of the staff in the Tolpuddle workshop for accommodating me and my work during, particularly during busy periods. I am immensely grateful to my fellow PhD students Navid Aslani and Philip Davenport, for showing an interest in my project and their support in overcoming difficulties. Thanks also go to Poole Harbour Commissioners and HR Wallingford for supplying the flow data used in Chapter 6.

Finally, I would like to thank my family and friends for having the patience to listen about this project for 3 years.

Nomenclature

Symbols

α	Angular acceleration	rad/s^2
β	Arbitrary constant	Variable
Δh	Head difference across turbines	m
Λ	Darcy-Weisbach friction factor	–
μ	Dynamic viscosity	$Pa\ s$
ω	Angular velocity	rad/s
Φ_B	Magnetic flux	Wb
ρ	Density	kg/m^2
σ	Rotor solidity	–
τ	Torque	Nm
θ	Crank angle	rad
ε	Efficiency	–
ξ	Electromotive force	V
A	Area	m^2
a	Amplitude	m
b	Blockage ratio	–
C	Hydrofoil chord length	–
c	Sound speed	m/s
C_p	Power coefficient	–

D	Diameter	m
E	Energy	m^2
e	Pipe wall thickness	m
F	Force	N
f	Frequency	m
Fr	Froude number	$-$
g	Acceleration due to gravity	9.81 m/s^2
H	Hydraulic head	m
h	Water depth	m
I	Moment of inertia	kgm^2
K	Bulk modulus	Pa
k	Head loss coefficient	$-$
k	Loss coefficient	$-$
l	Length	N
m	Mass	kg
N	Number of turns of wire	$-$
P	Power	W
p	Pressure	Pa
P_D	Power density	W
Q	Volumetric flow rate	m^3/s
R	Electrical resistance	Ω
r	Radius	m
R^2	Coefficient of determination	$-$
Re	Reynolds number	$-$
S	Piston stroke length	m

t	Time	s
V	Voltage	V
V	Volume	m^3
v	Flow speed	m/s
Y	Young's modulus	Pa
y	Vertical position	m

Notation

$\dot{x}$	First time derivate of x
$\ddot{x}$	Second time derivate of x
$\bar{x}$	Mean of x
$\boldsymbol{x}$	Vector quantity
$\mathbb{Z}$	Integer valve

Abbreviations

ADC	Analogue to Digital Converter
EU	European Union
GHG	Greenhouse Gas
NIMBY	Not In My Backyard
OWC	Oscillating Water Column
PTO	Power take-off
RPM	Revolutions per Minute
UK	United Kingdom
WEC	Wave Energy Convertor
WHES	Water Hammer Energy System

Chapter 1

Introduction

This chapter discusses the background, scope and objectives of the research presented in this thesis. Climate change and the need for renewable energy are first discussed, before the subjects of micro generation and pico scale hydro and tidal power are introduced. This allows the research question to be defined and the objectives and scope of the thesis to be outlined.

1.1 Electricity generation and climate change

Electricity is an essential resource for modern life, with individuals and organisations across the world depending on a reliable supply to go about their daily business. The people of the United Kingdom (UK) consumed 310.47 TWh of electricity in 2014 (Department of Energy and Climate Change, 2015), an amount that is equivalent to the energy within 183 million barrels of oil. As illustrated in Figure 1.1, over 60 % of this electricity was supplied via the combustion of fossil fuels: oil, coal and natural gas. The remainder was provided by a mixture of nuclear fission (19 %) and renewables (19 %).

Fossil fuels are popular for electricity generation because they offer a relatively cheap and reliable form of energy that is storable, transportable and readily accessible. Yet the use of oil, coal and natural gas for electricity generation also comes with several significant drawbacks. These include supplies that can be subject to geopolitical instability (Asif and Muneer, 2007) and negatively impacting human health as a result of air pollution (Kampa and Castanas, 2008).

The largest drawback, however, is the emission of greenhouse gasses (GHGs) like carbon dioxide (CO_2) during fossil fuel combustion. GHGs absorb thermal radiation in the same wavelength range as that emitted by the Earth, acting like a blanket in the atmosphere that traps heat and increases the average temperature of the planet (IPCC, 2013). Since the industrial revolution began

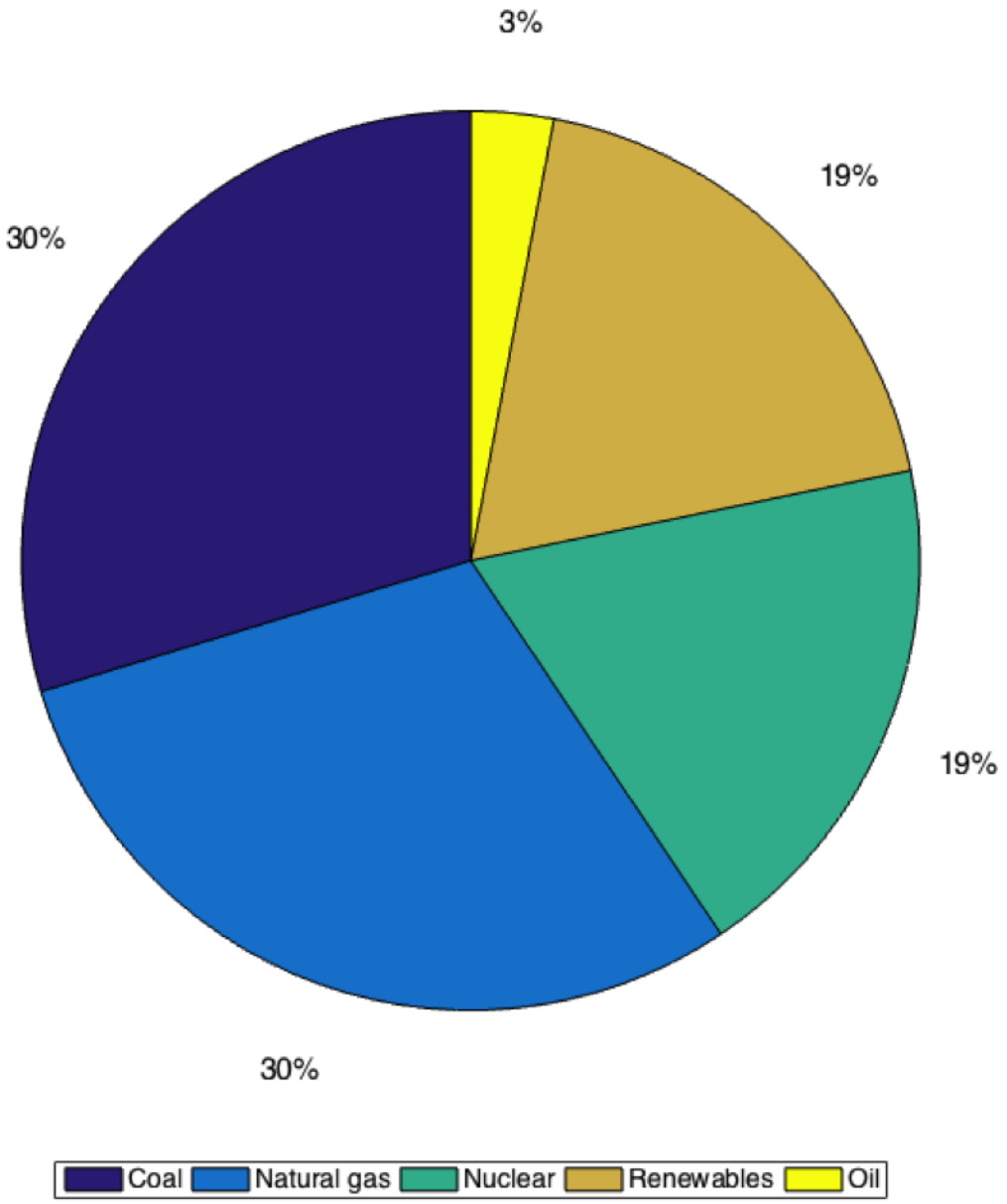

Figure 1.1: 2014 UK electricity supply by source (Department of Energy and Climate Change, 2015). Values add up to 101 % due to rounding in source data.

in the mid-18th century, the atmospheric concentration of CO_2 has risen from 280 ppm in 1750 to over 400 ppm in 2016 (Dlugokencky and Tans, 2016). This increase is mainly due to human activities such as electricity generation, with electricity and heat production accounting for 25 % of anthropogenic GHG emissions in 2010 (Victor et al., 2014). In the UK, it is estimated that power stations emitted 123.7 $MtC0_2e$ (mega tonnes of carbon dioxide equivalent) in 2014; 24 % of the estimated total emissions of 514.4 $MtC0_2e$ (Department of Energy and Climate Change, 2016). If the concentration of atmospheric GHGs, emissions and global temperature levels continue to rise, the resulting climate change could have a severe impact on sea levels, food security and natural ecosystems, among others (IPCC, 2014).

An alternative method for generating electrical power is nuclear fission, which accounted for 19 % of the UK's 2014 electricity supply. Nuclear power has an obvious advantage over fossil fuels as no GHGs are produced during electricity generation. Despite this, events such as the 2011 Fukushima disaster have negatively affected public attitudes towards nuclear power (Kim et al., 2013). In the weeks following the Fukushima meltdown, for example, the German government announced plans to close every nuclear power station in Germany by 2022 due to safety concerns (Jorant, 2011).

As a result of these issues, nations from across the globe are turning towards renewables – low carbon energy sources that replenish on human timescales – to meet their electricity needs. The 2009 Renewables Directive of the European Union (EU) set binding targets for all EU member states, so that 20 % of EU energy will come from renewables by 2020 (European Parliament and Council of the European Union, 2009). In the UK, the government has committed to legally binding targets to reduce carbon emissions from the 1990 baseline by 34 % by 2020 and 80 % by 2050 through the 2008 Climate Change Act (HM Government, 2008). To achieve these targets, it is predicted that 30 % of UK electricity will need to be provided by renewables by 2020, with almost no carbon being emitted during the generation process by 2050 (HM Government, 2011).

1.2 Sustainable generation

1.2.1 Renewable energy

There are many different renewable technologies that can be used to generate electricity in a sustainable manner, such as solar power, wind and wave energy, geothermal power, hydropower and biomass. While all of these technologies

can be used to generate low carbon electricity, each variety also comes with inherent advantages and disadvantages.

One concern that is particularly prevalent among residential users is that of financial costs (Sardianou and Genoudi, 2013), with consumers more willing to accept renewables when incentivised through tax breaks or subsidies. Table 1.1 provides estimates of the levelised costs of electricity generation in the UK from a variety of energy sources, for projects commissioned in 2020, 2025 and 2030. While electricity from combined cycle natural gas plants will have the lowest and most predictable price until at least 2030, all of the renewable technologies are predicted to become more cost effective with time. Depending on the validity of the assumptions used, renewables such as geothermal, onshore wind and solar power could become competitive with nuclear power and gas generation during the 2020s, while offshore wind, biomass, conventional hydropower and tidal stream could become competitive with coal by 2030.

The price of electricity is not the only factor affecting generation with renewables. A different issue can be found in onshore wind power, which often suffers from negative public perceptions due to the visual impact that large turbines may have around homes and beauty spots (Premalatha et al., 2014). Wind turbines must also be cited carefully to minimise adverse effects on local bird populations, with mitigation measures taken during construction (such as avoiding bird breeding seasons) to reduce any impacts (Pearce-Higgins et al., 2012).

Other renewables suffer different drawbacks. Biomass, for example, has the potential to offset a substantial amount of fossil fuel usage, and can provide a dependable and flexible source of electricity. But there are concerns that food security may be affected if the use of biomass becomes too prevalent, since food and fuel crops will compete for finite areas of farm land (Field et al., 2008). Conventional hydropower can also provide electricity on demand, as the flow of water through a dam can be quickly adjusted according to grid requirements. Yet the damming of rivers for large scale projects can have severe impacts on local ecosystems (Ligon et al., 1995), and the flooding of land to create reservoirs may forcibly displace large human populations (Heming et al., 2001).

Many renewables, particularly wind, wave and solar power, also suffer from producing unpredictable and variable supplies. For example, a study of a Dutch wind farm with a nameplate capacity of 7.8 GW found that the power supplied varied by as much ± 14 % every 15 minutes. Uncertainty in weather forecasting meant the generated power also varied from theoretical predictions by as much as 56 % (Gibescu et al., 2009). If renewables are to become widespread and provide a dependable supply of electricity, these twin issues of

Table 1.1: Estimates of the levelised cost of electricity generation for projects commissioned in 2020, 2025 and 2030. Adapted from Department of Energy and Climate Change (2013).

Technology		Estimated costs (£/MWh)		
		2020	2025	2030
Biomass	5 – 50 MW	101 – 137	101 – 136	101 – 135
	>50 MW	116 – 153	116 – 152	116 – 151
Coal with carbon capture and storage	Advanced super critical	N/A	89 – 133	88 – 132
	Integrated gasification combined cycle	N/A	106 – 173	104 – 172
Geothermal		58 – 124	58 – 122	57 – 120
Conventional hydropower	<15 kW	185 – 860	181 – 902	177 – 947
	100 kW – 1000 kW	105 – 419	103 – 439	101 – 459
Natural gas	Combined cycle	80 – 83	84 – 88	86 – 90
	Open cycle	172 – 200	178 – 208	180 – 212
Nuclear		83 – 108	78 – 106	70 – 94
Solar	Photovoltaic	115 – 132	98 – 112	84 – 96
Tidal	Shallow stream (<40 m)	N/A	155 – 207	140 – 185
	Deep stream (>40 m)	N/A	131 – 165	115 – 144
	Range	N/A	173 – 283	173 – 283
Wave		N/A	215 – 259	167 – 201
Wind	Onshore	84 – 123	84 – 121	84 – 118
	Offshore	100 – 142	96 – 136	92 – 129

variability and unpredictability are arguably the most important to overcome.

1.2.2 Distributed grid systems

One method of mitigating variability and unpredictability is through the use of decentralised transmission networks. Traditionally, electrical power is generated at large, centralised units and transmitted to points of demand via a wide network of cables (commonly referred to as the power grid). Since the 1980s, a trend has emerged in power distribution networks whereby centralised grids have been broken up into smaller, regional systems (Wolsink, 2012). In these decentralised networks, which are commonly known as distributed grid systems, power is generated closer to where it is consumed, with large power stations replaced by a greater number of smaller units (Alanne and Saari, 2006).

Decentralisation of an electricity grid comes with several advantages in terms of efficiency, sustainability and reliability. For example, reducing the transmission distance between the power source and the point of use reduces the amount of power lost during transmission to electrical resistance (Allan et al., 2015). A multitude of smaller grids also makes the overall transmission network much more flexible and more resilient in the event of a power failure, while also reducing costs. Distributed systems are therefore particularly beneficial for large, sparsely settled countries such as Canada and Russia (Alanne and Saari, 2006). They also have benefits for smaller, more densely populated nations such as the UK, where the implementation of distributed transmission networks is recognised as a viable method for renewing ageing infrastructure and overcoming concerns with grid capacity (Allan et al., 2015).

Distributed grids become even more useful if large amounts of electricity are to be provided by renewable energy sources, since renewables tend to be geographically dispersed and generate smaller levels of power than conventional plants (Wolsink, 2012). A distributed grid with a variety of generation units is more capable of handling the issues that arise due to intermittent and variable supplies, such as the need to commit alternative generators and the requirement to match electrical demand with supply (Aghaei and Alizadeh, 2013).

Due to technical limitations on the amount of power a given network can handle, distributed grids may be categorised according to the amount of power they are capable of transmitting (Ackermann et al., 2001). Large distributed grids can be capable of handling between 50 to 300 MW, while micro grids, which typically transmit less than 5 kW of power, are at the opposite end

of the scale. Traditionally, micro grids have been used to provide back-up electrical power to crucial infrastructure such as hospitals in the event of a fault with the wider transmission network. But micro grids can also be used to access local renewable energy resources that would otherwise be considered too small or unreliable for a conventional, centralised grid. Such small scale power production, commonly referred to as micro generation, gives small communities the potential to become more energy independent and environmentally friendly (Allen et al., 2008). If micro generation, combined with demand reduction and energy efficiency measures, were to be implemented in homes and communities across the UK, it would be capable of supplying a significant proportion of the UK's energy needs while simultaneously reducing GHG emissions (Allen et al., 2008).

Despite these potential benefits, there are barriers to the widespread implementation of distributed grids and micro generation (Yaqoot et al., 2016). These include economic issues, such as upfront capital costs and the structure of the energy market, as well as institutional and societal obstacles such as government policy. There are also major environmental and technical barriers, including site specific resources, poor current levels of cost-effectiveness, and the need for further research and development work to improve technological performance and develop reliable, long-lasting devices that are relatively easy to maintain.

1.2.3 Pico hydro and tidal power

Micro hydropower is one of the few forms of micro generation that is currently deemed cost effective, alongside biomass and ground source heat pumps (Allen et al., 2008). Somewhat confusingly (since it contrasts with the classification of a micro grid) micro hydropower plants are typically classified as producing 5 to 100 kW of power. Schemes that generate less than 5 kW are generally referred to as pico hydropower.

There are many hydropower generation systems that can be used for either large or small scale generation in rivers (Elbatran et al., 2015), such as axial flow turbines (aka propeller or Kaplan turbines), Pelton wheels and Archimedean screws. As shown in Figure 1.2, these devices require specific ranges of hydraulic head and flow rate, with few designs actually capable of operating effectively in the pico-range (Williamson et al., 2011). The purpose of this research is to develop a device capable of generating power in areas with a combination of low head and low flow rate, where the devices shown in Figure 1.2 cannot operate effectively. The green region below 1 m head

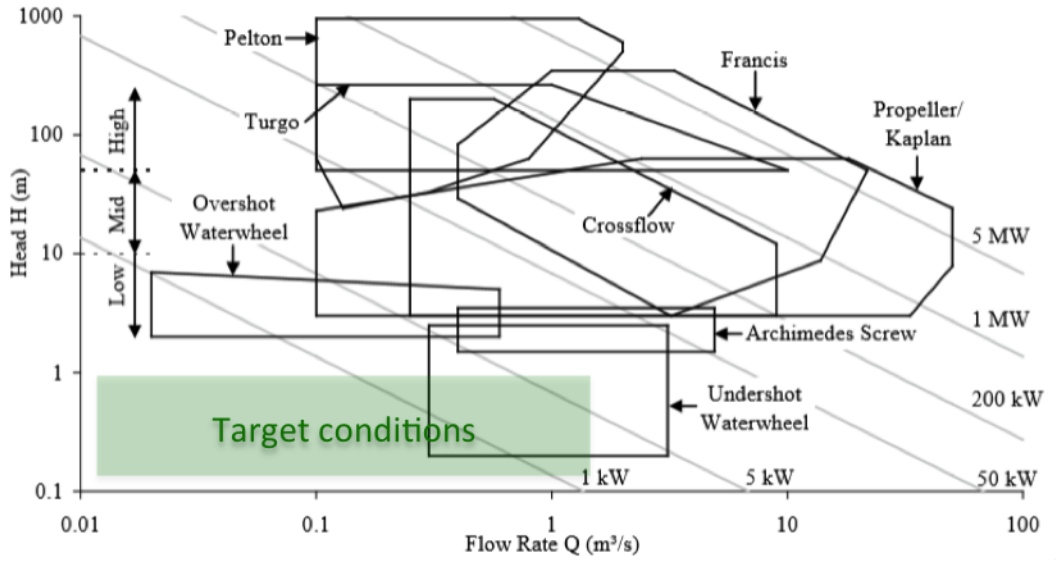

Figure 1.2: Application ranges of various hydropower devices. Adapted from Williamson et al. (2011).

and 2 m^3/s indicates the specific operating conditions targeted by this thesis. These were chosen due to the wide variety of sites they may account for, and the benefits a system capable of operating within them may bring in terms of micro generation and off-grid power supply.

Many of the lower power devices shown in Figure 1.2 (for example, Archimedes screws and waterwheels) have been developed with river deployment in mind. Reviewing the literature suggests that, thus far, relatively little consideration has been given to pico scale generation using the energy of the oceans. Marine renewable energy encompasses a range of technologies including ocean thermal energy conversion, offshore wind power, wave power and tidal power (Pelc and Fujita, 2002). Since these technologies are deployed offshore, they can be located in under-utilised locations (Fraenkel, 2006), overcoming issues with visual impact that can affect other forms of micro generation (Yaqoot et al., 2016).

Of the many varieties of ocean energy, tidal power comes with the advantages of a resource that is both predictable over long timescales (Denny, 2009) and reasonably accessible (unlike ocean thermal energy, which requires tropical seas with a water depth of at least 1 km (Pelc and Fujita, 2002)). There are two predominant methods of generating electricity from the tides:

- tidal range, which utilises the difference in water level between high and low tide.
- tidal stream, which harnesses the energy of the tidal currents accompanying the rise and fall of the water level.

Tidal range is perhaps the most well-known form of tidal energy. This is mainly due to the 220 MW Rance River barrage in Brittany, France, which opened in 1966 and has been operating at full capacity since 1968 (Lebarbier, 1975). Tidal stream is a more recent development that is frequently considered to be analogous to wind power, since it involves extracting energy from a moving fluid. But while the wind industry has focussed on three bladed axial-flow (aka horizontal axis) turbines in recent years, there are currently many different technologies in development in the tidal stream sector. These include a multitude of different axial flow and cross flow (aka vertical or transverse horizontal axis) turbines, as well as more novel concepts such as tidal kites and oscillating hydrofoils. All of these tidal stream devices are discussed in more detail in Chapter 2, with illustrations provided in Figure 2.1.

Although tidal energy is an active area of investigation, the majority of the research and development work done to date has been focussed on developing large schemes to maximise power generation in resource rich locations. As discussed in greater detail in Chapter 2, proposed tidal range projects typically require basins that are at least several km^2 in size, with tidal ranges of at least 4 m. Meanwhile, commercial tidal stream devices tend to target flow speeds in excess of 2 m/s. Many developers have been attracted to the Pentland Firth strait, between mainland Scotland and the Orkney Islands, where flow speeds can be upwards of 5 m/s in some areas – among the highest in the world (Draper et al., 2014). Commercial devices are also typically as large as possible to maximise their power output. The MCT SeaGen device, one of the most well-developed commercial tidal stream turbines, is an example of this; it is considered viable in water depths of 20 – 40 m where the peak spring tidal current speeds that are greater than 2.25 m/s (Denny, 2009).

Many of the locations that meet these size and speed requirements – Pentland Firth being a prime example – are located in sparsely populated areas that are long distances from areas of high electricity demand. The development of smaller devices, capable of operating in shallower, less resource rich waters, would allow the predictable tidal resource to be harnessed in a greater variety of locations. Smaller devices will be cheaper to build, install and maintain than their larger counterparts (Bryden et al., 1998), which, combined with their predictable supply, may make pico scale tidal devices appealing options for coastal homes and communities as useful components of a distributed grid. A small scale tidal energy device would also be capable of operating in the more constant conditions of a river, allowing pico hydropower to be generated from a wide range of locations. Whether or not such generation is desirable, however, will ultimately depend upon the levelised cost of the energy that is

provided, and how it compares to that of other technologies.

1.3 Research objectives

The aim of this thesis is to develop a device that is capable of generating pico scale electricity from shallow water, low input tidal and river sites. The green area in Figure 1.2 illustrates the targeted operating conditions: flow rates of less than 2 m^3/s (equivalent to 2 m/s for a 1 m^2 device) and input heads of less than 1 m. These conditions were chosen due to the potential renewable energy available from them, the wide range of tidal and river sites that would provide these conditions, and the lack of hydropower technology capable of operating effectively within them. To meet this aim, the Balmain Environment Conservation Trust, a charitable organisation that seeks to promote sustainable development, match-funded this research project alongside Bournemouth University.

A research question was agreed to assess whether or not the aim was achieved: "*what is the maximum hydrodynamic efficiency of a purpose-designed pico scale hydropower system and how much energy can one supply from both tidal and conventional hydropower sites over the course of a year?*".

The following four objectives were set so that this question could be answered:

1. Review the state of the art of tidal power to identify the factors that will govern pico scale generation and to assess the suitability of current tidal technologies for this application.

2. Use this information to design a device that is capable of generating electrical power from a range of sites.

3. Study the hydrodynamics of this device to identify criteria that govern its efficiency through mathematical modelling and scale model testing.

4. Propose an effective design from the results of this study and evaluate its annual energy output in a range of input conditions.

1.4 Research scope

To ensure the above objectives were met, the scope of the research in this thesis was initially limited to device hydrodynamics. Given the novel nature of the system that was ultimately investigated, however, providing proof that the

concept can generate useful electrical power was subsequently included. To achieve the former, experimental and mathematical studies were conducted to identify and quantify factors affecting the hydrodynamic behaviour of the system and its theoretical output in a variety of conditions. The latter was achieved by designing, manufacturing and testing two different power take-off systems, although no work was conducted on optimising these systems.

With the research objectives and scope in mind, the rest of the thesis is structured as follows:

- Chapter 2: reviews that state of the art of tidal power and introduces the Water Hammer Energy System (WHES), before discussing the suitability of these technologies for pico scale power generation.
- Chapter 3: presents an experimental investigation into the performance of a small scale WHES to identify its potential power output and the factors governing its performance.
- Chapter 4: investigates the hydrodynamics of the WHES, presenting a more detailed description of its governing physics via mathematical modelling.
- Chapter 5: uses the results of Chapters 4 and 5 to design and test a mechanical power take-off (PTO) system for the WHES, providing proof that the concept is capable of generating electricity.
- Chapter 6: proposes an optimised WHES design and provides a theoretical evaluation of its performance in a variety of tidal and conventional input conditions.
- Chapter 7: draws conclusions on the performance and viability of the WHES and the feasibility of using it in pico scale hydropower applications.

Chapter 2

Literature review

The previous chapter introduced the objectives and scope of this thesis. The purpose of this chapter is to meet the first research objective by reviewing the state of the art of tidal energy and identifying the most appropriate technologies for low input generation. The review includes a discussion of tidal range and stream resources and the various technologies in development to harness them. Tidal power was chosen ahead of conventional hydropower as a device capable of operating in the low head and variable input of the tides should prove equally capable in the more consistent input of a river or stream.

Images of the various technologies that are discussed in this chapter are provided in Figure 2.1. Figure 2.1a shows the La Rance Tidal Barrage (wikimedia.org, 2007), an example of tidal range technology. The other images are of tidal stream devices, like the MCT SeaGen (Marine Current Turbines, 2016a) in Figure 2.1b, which is an example of an axial flow turbine. Figure 2.1c shows a computer generated image of the ORPC RiverGen (Alaska Energy, 2013), a transverse horizontal axis cross flow turbine. The OpenHydro ducted turbine (Marine Technology Ltd, 2015) is shown in Figure 2.1d, Figure 2.1e shows a computer generated image of the Stingray oscillating hydrofoil (underthecblog.org, 2014), and Figure 2.1f shows a computer generated illustration of the Minesto Deep Green tidal kite (Maritime Journal, 2009).

The advantages, drawbacks and necessities of generating power with these various technologies is discussed and compared to identify those that are most suited to operating in low input conditions and at small scales. Following this discussion, hydraulic ram pumps, the water hammer effect, and the Water Hammer Energy System (WHES) are introduced. This WHES was first envisaged during the review of tidal technologies; its mode of operation is outlined and its potential advantages for operating in low input conditions are discussed, providing the reasons for selecting it for the research presented in the rest of the thesis.

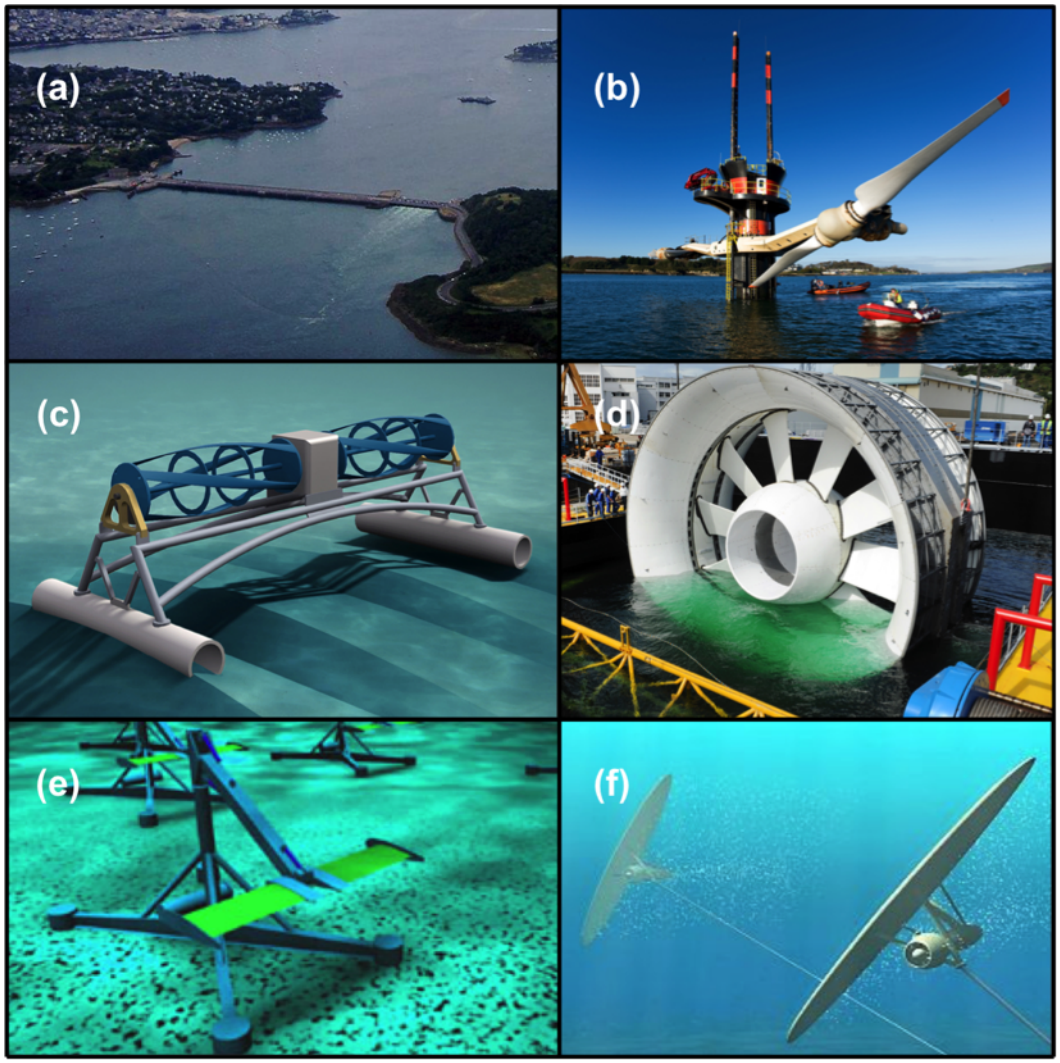

Figure 2.1: Example images of the various tidal power technologies discussed in this chapter. The images are sourced from the references mentioned on Page 12.

2.1 The tides

Due to its rotation and the gravitational forces of the moon, sun and planets, the sea levels of the Earth rise and fall in a periodic fashion known as the tides. People have sought to harness the energy of the tides throughout history, from the ancient Greeks and Romans (Charlier and Menanteau, 1997) to present day scientists and engineers attempting to develop clean, renewable supplies of energy.

The magnitude of the tides varies with time and location, due to a complex combination of factors including the position of the Earth relative to other astronomical bodies, the Coriolis Effect, the size of the sea, the shape of the coastline and the topography of the seabed (commonly referred to as bathymetry). These factors combine to create three dimensional standing waves of water with points of zero amplitude (nodes) and maximum amplitude (anti-nodes). The amplitudes of these waves can be predicted well into the future through the use of tidal constituents (Doodson, 1921), which can be determined by performing Fourier analysis on an observed tidal curve. Combining the results of this analysis with the predicted motion of the sun, moon and planets provides harmonic constituents with frequencies that are constant across the globe. The amplitudes of these constituents are location dependent, allowing a predicted tidal curve to be computed for a given site via the summation of the components for that area. An example prediction curve is provided in Figure 2.2 for Poole Harbour, Dorset, illustrating how the tides vary from day to day at a specific location.

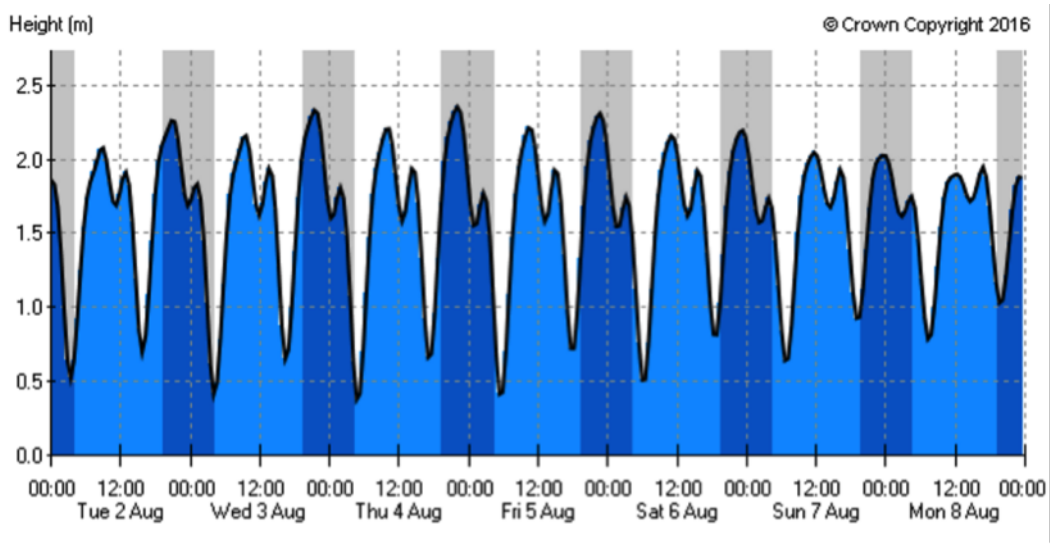

Figure 2.2: An example predicted tidal curve for Poole Harbour, Dorset, showing a 7 day period from the 2nd to the 8th of August, 2016. Sourced from The United Kingdom Hydrographic Office (2016).

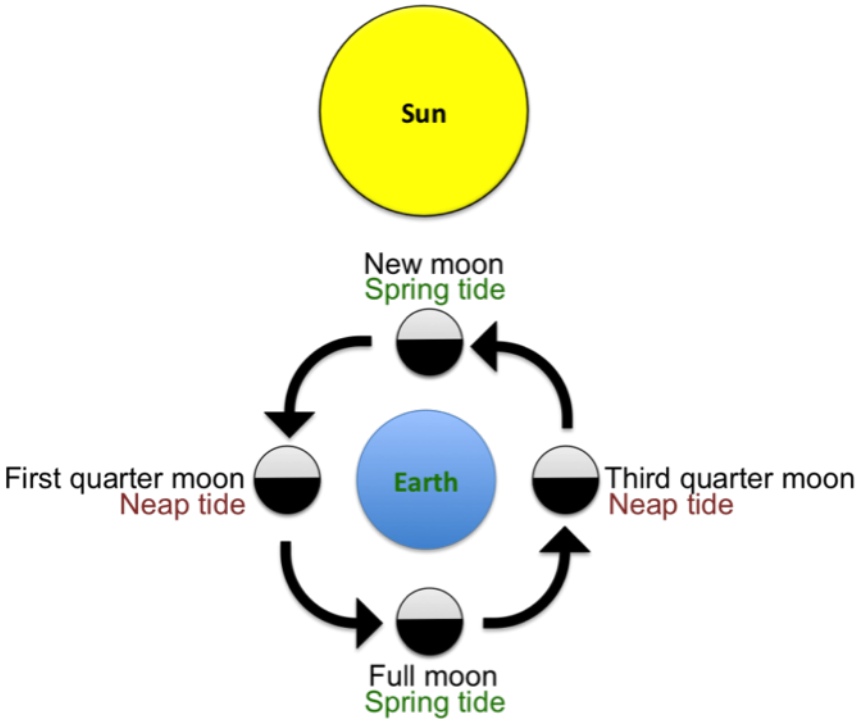

Figure 2.3: How the strength of the tides is governed by the alignment of the Sun, Earth and Moon.

Over the period of a full lunar cycle, these variations become even more pronounced. Spring tides are the strongest and largest tides (with the greatest difference between high and low water), and generally occur during full and new moons, when the Sun, Earth and Moon are aligned. Conversely, neap tides (with the smallest difference between high and low water) occur during first and third quarter moons, when the Sun, Earth and Moon form a right angle, as illustrated in Figure 2.3.

Consequently, the amount of tidal energy that can be extracted from a particular site (commonly known as the tidal energy resource) also changes with time and location. This makes the accurate assessment of the resource a critical factor in the deployment of any tidal energy scheme, and means tidal devices need to be capable of generating power in a range of input conditions.

2.2 Tidal range power

Tidal range devices make use of the difference in water level between high and low tide. As illustrated in Figure 2.4, this is achieved by allowing water to flow into a basin before impounding it through the use of sluice gates. A difference in head subsequently forms across the device as the water level outside of the enclosure changes with the tide. The sluice gates are reopened when this

head difference is suitably large, allowing water to be forced across turbines for electricity generation.

The power available from a tidal range device can be determined from the potential energy (E_p) of the water trapped within the impoundment basin (Lamb, 1994). Assuming the cross-sectional area (A_b) of the basin remains constant and the only force acting on the water in the vertical direction is weight (mg), this can be calculated according to the head difference ($\Delta h = h_2 - h_1$) across the turbines:

$$E_p = -\int_0^r F \, \mathrm{d}y \tag{2.1}$$

$$E_p = \rho g A_b \int_{h_1}^{h_2} y \, \mathrm{d}y \tag{2.2}$$

$$E_p = \frac{1}{2}\rho g A_b \Delta h^2 \tag{2.3}$$

Equation 2.3 shows that the energy available to a tidal range scheme is dependent upon the area of the impoundment basin and the difference in head across the turbines. This indicates that tidal range schemes require large basins and large tidal ranges to provide significant amounts of energy. The factor of 1/2 is indicative of the reduction in the hydraulic head as water flows across the turbines.

The mean power available from a tidal range device can be calculated according to E_p, the tidal period (t, which is the amount of time between high and low tide) and the mean efficiency ($\overline{\varepsilon}$) of the turbines. For a location with semidiurnal tides (two high and two low waters per day), the mean daily power is given by:

$$P = \frac{2E_p\overline{\varepsilon}}{86400} = \frac{\rho g A_p \Delta h^2 \overline{\varepsilon}}{86400} \tag{2.4}$$

Where 86400 is the number of seconds in a day.

When generating power, tidal range projects can make use of three different schemes (Xia et al., 2010a). This provides some flexibility in how the power is generated and helps accommodate grid requirements and variations in the strength of the tides (Frau, 1993). The first of these is ebb generation, in which water is trapped within the impoundment basin at high tide and power generated during the outgoing tide, with flow travelling out of the basin towards the sea.

The second scheme, flood generation, is essentially the mirror image of the first: the sluice gates are closed at low tide, and power generated as the water level outside the basin increases with the incoming tide. This is less efficient

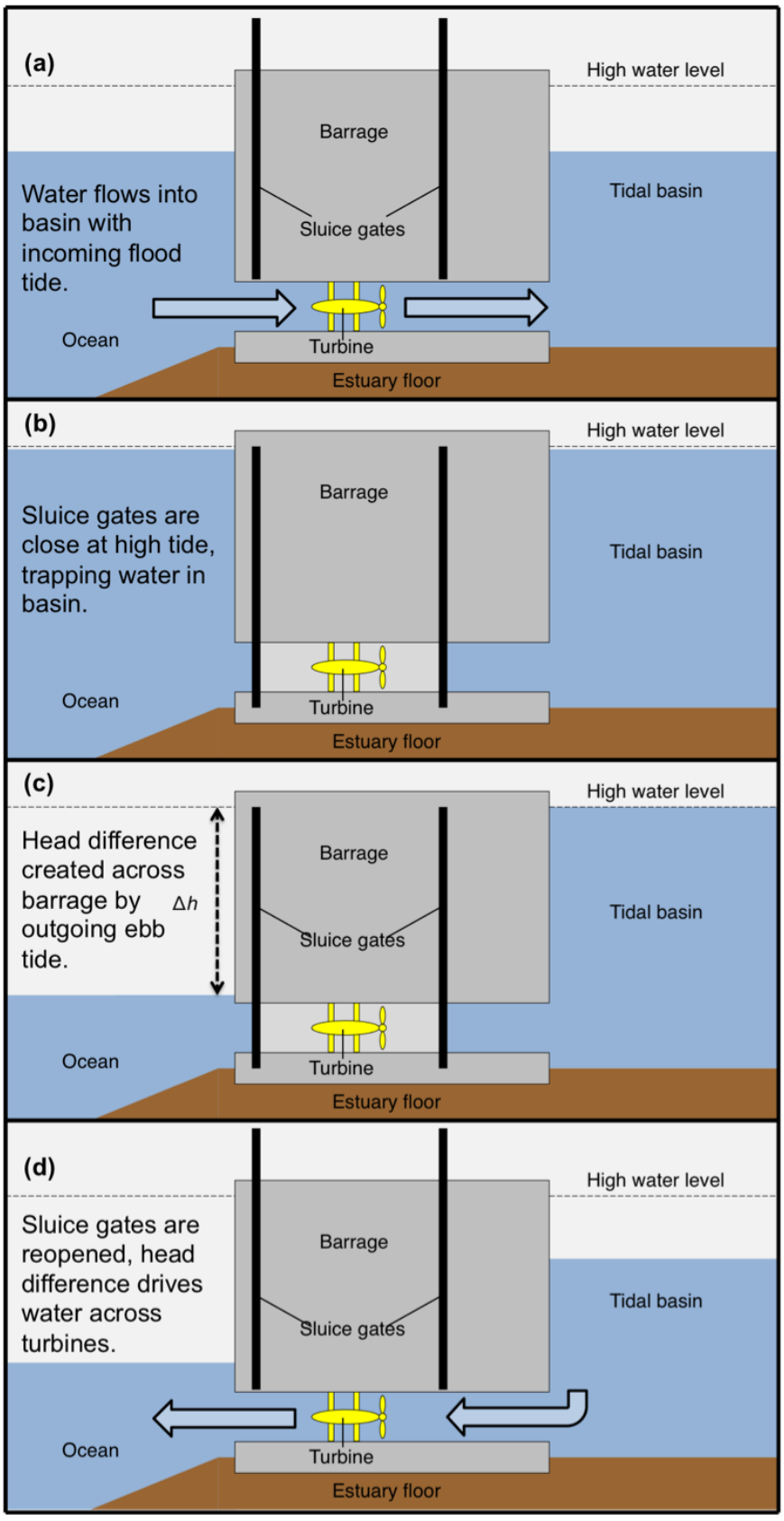

Figure 2.4: Overview of ebb-operation tidal barrage. Adapted from Wyre Tidal Energy (2014).

than ebb generation (Xia et al., 2010a), since the volume of water in the upper half of the impoundment basin (utilised by ebb generation) will typically be greater than the volume in the lower half (filled first during flood generation) due to the shape of the seabed. As a result, the head difference across a range device reduces more quickly in flood generation.

The third scheme is two-way generation, which is an amalgamation of both ebb and flood schemes. This enables the tidal range within the basin to more closely match its natural state, which is hypothesised to reduce environmental impacts. Despite this, two-way generation has still been found to reduce water levels upstream of a range device and significantly impact the environmental characteristics of a basin (Xia et al., 2010a).

To account for the effect of the size of a range device on the power it produces, Equation 2.4 can be divided by A_b to provide an estimate of the power density (i.e. power per unit of basin area) as a function of the available tidal range:

$$P_D = \frac{\rho g \Delta h^2 \overline{\varepsilon}}{86400} \tag{2.5}$$

Figure 2.5 shows the maximum power density of four theoretical range schemes of differencing efficiency calculated using Equation 2.5 for tidal ranges of 0 — 20 m. From this simple analysis, it can be seen that tidal range devices produce a relatively meagre amount of power for their basin area. For example, in the maximum shown range of 20 m, the power density of a theoretical 100 % efficient barrage would be approximately 45 W/m^2. A theoretical 100 % efficient device located in Canada's Bay of Fundy, which has the highest tidal range in the world at 16 m (Archer and Hubbard, 2003), would have a lower power density of 30 W/m^2. There are very few locations in the world that have tidal ranges even approaching this value, however, meaning range devices would be unlikely to come close to this figure in all but a handful of places.

Tidal range schemes are additionally characterised by low levels of average efficiency (Xia et al., 2012), partly due to the varying head difference across the turbines. Values typically range from 20 – 40 %, and an average of 33 % is often used in theoretical power estimations. At these efficiencies, range schemes are clearly going to have to be larger to achieve a given power output. This is illustrated in Figure 2.6, which shows the minimum required basin area of a range scheme aiming to generate 2 kW. Although this is again a simple estimate provided by rearranging Equation 2.4, it suggests that the basin area of even a 40 % efficient range scheme will need to be at least 30 x 30 m if it is to provide 2 kW of power in 6 m high tides. This large size requirement, coupled with the relative scarcity of high tidal ranges, suggests

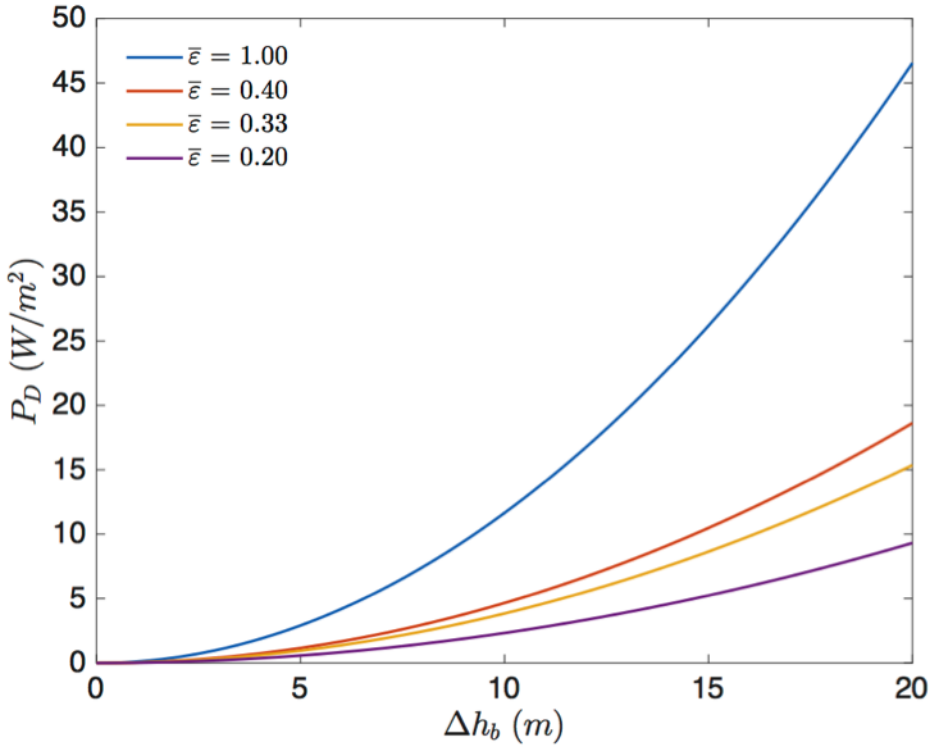

Figure 2.5: Theoretical power density available from tidal range devices in tides of 0 - 20 m.

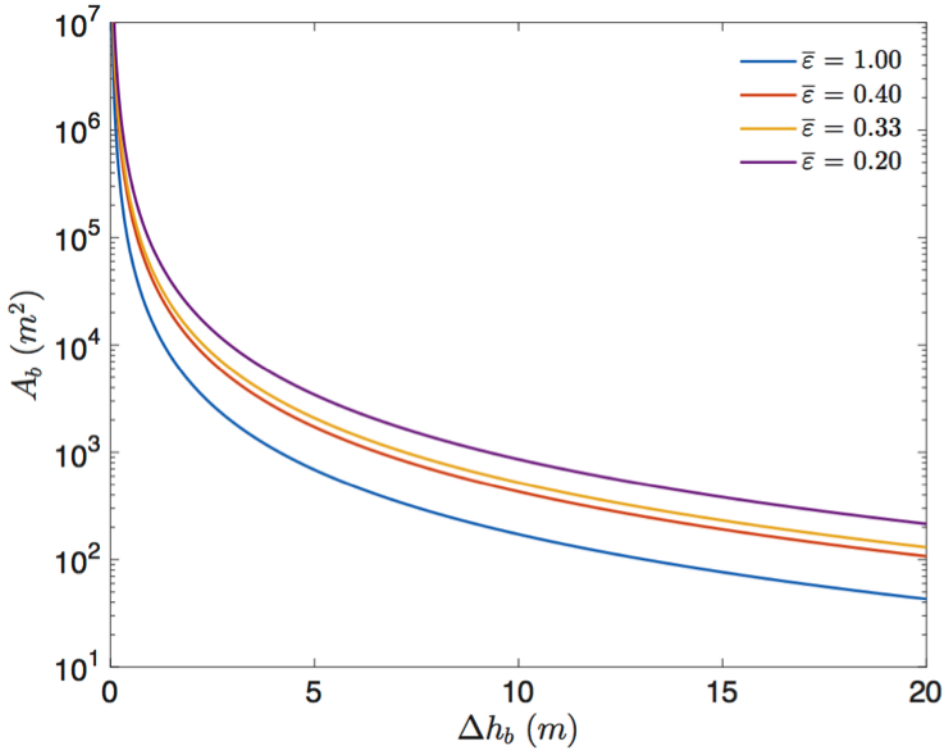

Figure 2.6: Minimum basin area necessary to generate 2 kW in tides of 0 – 20 m.

that tidal range technology will be ill-suited to pico scale tidal power systems in most locations. By extension, conventional hydropower systems are also likely to be an unrealistic option for low input heads.

2.2.1 Tidal range resources

There have been many investigations into the tidal range resources around the UK. Some studies focus on specific sites (e.g. Falconer et al. (2009); Xia et al. (2010c, 2012); Petley and Aggidis (2016)), while others attempt to characterise the total resource around the UK (e.g. ABP Marine Environmental Research Ltd (2008); The Crown Estate (2012)). While Equations 2.3 – 2.5 provide a very basic method of assessing the tidal range resource, factors they do not consider may also affect the energy available from a tidal range scheme. For example, variations in the topography of the seabed enclosed by the basin, the impacts that the scheme may have on the hydrodynamics of the surrounding region, and the characteristics of the turbines used for power generation may all affect the energy available to a tidal range scheme (Xia et al., 2012) .

Numerical modelling, whereby equations governing the evolution of a set of variables are solved iteratively, is a method that can account for these factors, having been found to provide more accurate energy estimates when compared with predictions from Equation 2.3 (Xia et al., 2012). Due to this greater accuracy, many of the tidal range resource estimates in the literature rely on this method for their predictions (e.g. ABP Marine Environmental Research Ltd (2008); Falconer et al. (2009); The Crown Estate (2012). Such models also permit evaluation of the potential environmental impacts of a particular scheme (e.g. Ahmadian et al. (2010a); Xia et al. (2010a)). Yet numerical modelling is not without its drawbacks. For example, it requires much more detailed information about a particular scheme than is necessary for basic predictions using Equation 2.3 (Xia et al., 2012). Additionally, simulating the hydrodynamics of vast areas of ocean in 3 dimensions is extremely computationally demanding (ABP Marine Environmental Research Ltd, 2008).

To make the solution of a numerical model computationally practical, problems are typically split into a grid of cells, within which the governing equations are solved. Using a greater number of small cells consequently enables a more accurate solution to be found, at the cost of being more computationally demanding. There is consequently a trade-off between the accuracy and scale of a numerical resource assessment. Local studies can provide more accurate evaluations on the power available from a specific site, while national assessments provide less detailed information that is still useful for government policy

Table 2.1: Summary of the estimated resources available to several potential UK barrage schemes. Sourced from The Crown Estate (2013).

Location	Mean tidal range (m)	Basin area (km^2)	Peak power output (MW)	Annual energy output (GWh)
Severn Outer	7.2	1000	12000	19700
Severn Cardiff-Weston	7.8	450	7200	12900
Solway Firth	5.6	860	5580	10050
Morecambe Bay	6.3	350	3040	5400
Humber	4.1	270	1200	2010
Thames	4.2	190	1120	1370
Mersey	6.5	70	620	1320
Strangford Lough	3.1	144	210	528
Padstow	4.8	6	20	55
Dovey	2.9	13	20	45

(Blunden and Bahaj, 2007).

As an example, The Crown Estate (2012) used the numerical data of ABP Marine Environmental Research Ltd (2008) to estimate that there is 96 TWh/year of energy available to tidal barrages around the UK, or alternatively 25 TWh/year available to tidal lagoons. These figures are equivalent to 31.7 and 8.25 % of the 303 TWh of electricity consumed by the UK in 2015, respectively Department of Energy and Climate Change (2015). They are subject to a large uncertainty of $\pm$ 25 % due to the course resolution of the model, which employed grid cells of 1.8 km^2. In contrast, the Bristol Channel and Severn Estuary model of (Xia et al., 2010a) had grid cells of 1.0 km^2 at its coarsest and 0.0004 km^2 at its finest, suggesting it was capable of achieving more realistic results, although the uncertainty was not quantified.

Table 2.1 summarises the theoretical energy and power that would be available to ebb-only barrages operating in a range of locations around the UK. These estimates serve to illustrate the potential resources of many areas around the UK coastline and how the available energy is dependent on the tidal range and the size of the scheme.

The largest single area for tidal range resources in the UK is the Bristol Channel and Severn Estuary, which has one of the largest tidal ranges in the world while simultaneously providing a large basin area. Consequently, range

schemes in the area have been studied extensively, and a variety of different schemes has been proposed. In areas where the mean tidal range is less than 4 m, however, range schemes are thought to be economically undesirable (The Crown Estate, 2013). This is because they will require a prohibitively large basin area relative to their output, increasing the cost of the energy they provide to such an extent that it becomes uncompetitive, even though they may still be capable of generating MWs of power.

2.2.2 Tidal barrages

Barrages are long, dam-like structures built across the entrances to coastal bays or estuaries. This enables them to employ the surrounding land to create the impoundment basin, facilitating cheaper construction. Despite this, they still come with significant capital as well as environmental costs (Blunden and Bahaj, 2006), which can be difficult to overcome. Consequently, only five tidal barrages have been constructed globally, despite the many sites across the world that are considered suitable for exploitation (Charlier, 2007).

Table 2.2 provides a list of the barrages that have been constructed around the world. The largest example is the Sihwa Lake Power Station in South Korea, which has a rated capacity of 254 MW and was built into a seawall originally constructed for flood defence in 1994 (Bae et al., 2010).

While Sihwa Lake and La Rance can produce large amounts of power, their figures are dwarfed by the potential output of even larger scale schemes such as the proposed Severn Barrages presented in Table 2.1. In this region, a barrage would be capable of producing significantly more power than the predicted 154 MW maximum available to a tidal stream turbine array (Ahmadian et al., 2012). In fact, the annual energy yield of a Severn Outer Barrage is predicted to be greater than the estimated 12.7 TWh/year available from the entire Pentland Firth, which is arguably the UK's top tidal stream resource (Sustainable Development Commission, 2007).

Environmental impacts

Extracting such quantities of energy from the environment is predicted to cause significant impacts. These may be both positive and negative; for example, the construction of a Severn barrage would serve to reduce the strength of local tidal currents and reduce the concentration of sediment suspended in the water (Kirby and Shaw, 2005; Ahmadian et al., 2010a), encouraging the colonisation of an ecosystem that would otherwise remain highly supressed. At other sites however, the opposite may occur, since this effect is dependent

Table 2.2: List of barrages that have been constructed around the world.

Barrage	Inauguration date	Mean tidal range (m)	Basin area (km^2)	Capacity (MW)	Source
La Rance, France	1966	7.9	54	240	Frau (1993)
Sihwa Lake, South Korea	2011	7.8	23	254	Kim et al. (2012)
Annapolis Royal, Canada	1985	6.4	6	20	Frau (1993)
Jingxia, China	1980/86	5.0	2	3.2	Frau (1993)
Kislaya Guba, Russia	1968	2.4	2	0.4	Frau (1993)

upon the geology of the local seabed (Xia et al., 2010c). Barrages are also likely to increase the deposition of sediment in certain areas, depending upon their design and the prevailing direction of sediment transport (Kadiri et al., 2012).

In addition to affecting sediment transport, barrages are also predicted to impact water levels in the area surrounding the site, which may again have positive and negative consequences. For example, the construction of a Severn barrage has been predicted to reduce upstream water levels by 0.5 — 1.5 m (Xia et al., 2010a), indicating that such a barrage could additionally act as a flood defence. This is a particularly useful impact in the context of climate change and rising sea levels (Ahmadian et al., 2014), since it will reduce the amount of spending required on conventional flood defences (Parsons Brinckerhoff Ltd, 2010).

This reduction in water level may also lead to habitat loss, however. Numerical modelling suggests that the construction of a barrage between Cardiff and Weston-Super-Mare would result in the loss of 80.5 km^2 of intertidal habitats (Zhou et al., 2014). The same study predicted that the salinity of the water would also be reduced, which would reduce the concentrations of dissolved metals and nutrients in the (Kadiri et al., 2012). In addition, the local

wave climate may also be affected. A different numerical study has predicted that the construction of a Severn barrage would increase net wave heights by up to 20 % (Fairley et al., 2014), which would impact coastal erosion and sediment transport in the region.

Several methods have been proposed to overcome these impacts. For example, the Evans Engineering REEF system (Evans Engineering and Power Company, 2011) is designed to maintain a small but constant head difference across the barrage, rather than delaying the tides within the basin to generate a larger head. This is predicted to reduce the impact on water levels within the basin, reducing intertidal habitat loss. The use of bi-directional turbines and two-way generation has also been proposed as a means of reducing habitat loss by up to 60 % compared to an ebb only scheme (House of Commons Energy and Climate Change Committee 2013). Such generation schemes shave still been found to have significant environmental impacts (Xia et al., 2010a), illustrating the need for site specific research before the impacts of a particular scheme can be assessed with certainty.

2.2.3 Tidal lagoons

Tidal lagoons are extremely similar to tidal barrages and operate according to the same principles. Consequently, the power output is dependent upon the size of the basin and the local tidal range. Instead of blocking of an entire estuary or bay with a single structure, however, the impoundment basin of a lagoon is either entirely or mostly man-made. A larger structure is therefore required to construct a basin of comparable area to that of a barrage, which will increase the capital costs of a lagoon over a barrage of comparable output Baker et al. (2006); Entec UK Ltd (2007).

Environmental impacts

Without enclosing an entire bay or estuary, a tidal lagoon is likely to have comparatively smaller impacts on the hydrodynamics of the region outside the basin (Kadiri et al., 2012). For example, it is predicted that the hydrodynamics of the Severn Estuary will be hardly affect by the by a lagoon attached to the Welsh coast in the area (Xia et al., 2010c). Any impact of a lagoon on upstream water levels in this region is also predicted to be comparatively small next to those of a barrage (Kadiri et al., 2012). A numerical study of coastal tidal lagoons in North Wales, has shown that such impoundments also offer a level of reduced flood risk (Ahmadian et al., 2010b).

Within the basin of a lagoon, sediment deposition is likely to become an is-

sue due to the generation of strong recirculating currents that occur depending upon the placement of the turbines. Thus, lagoon basins are likely to require periodic dredging to maintain power output and ensure their performance is not reduced (Parsons Brinckerhoff Ltd, 2010).

2.3 Tidal stream power

Tidal stream devices generate power directly from the moving water of tidal currents, without the need for an impoundment basin or reservoir. Given that they extract energy from a moving fluid, many designs are considered analogous to wind turbines, and are planned to be deployed as part of larger farms or arrays (Hardisty, 2009). Before discussing tidal stream power in detail, it is therefore useful to briefly comment on the state of the art of wind power.

Commercial wind turbine design has converged toward the three bladed horizontal axis rotor for reasons of efficiency, noise, aesthetics, and an ability to survive and operate in a range of wind conditions through the use of yaw and pitch control (Schubel and Crossley, 2012). Given the dependence of turbine power output on rotor area from Equation 2.12, wind turbines are now growing ever larger to maximise power output per turbine and minimise costs (Schubel and Crossley, 2012).

The majority of future wind power development is expected to take place offshore (Ladenburg et al., 2013), where stronger winds compensate for the installation, operation and maintenance costs of operating in the marine environment (Sempreviva et al., 2008). The development of floating offshore turbines (Borg and Collu, 2014; Jeon et al., 2014), which would enable the devices to access extremely deep waters, is now an active area of research. Positioning turbines far offshore helps to overcome the NIMBY (not in my backyard) problem suffered by onshore wind developments (Premalatha et al., 2014), allowing extremely large devices to be designed and built. For example, the Vestas V164-8.0 MW has a diameter of 164 m and is capable of generating up to 8 MW (MHI Vestas, 2015) , while the proposed American Superconductor WindTec SeaTitan is 190 m in diameter and rated at 10 MW (AMSC, 2012).

But while the design of commercial wind energy devices has focussed on horizontal axis turbines in recent years, there is currently a wide variety of tidal stream technology under research and development. These include devices that closely resemble wind turbines, such as axial flow (horizontal axis) and cross flow (vertical and transverse horizontal axis) turbines, as well as the more

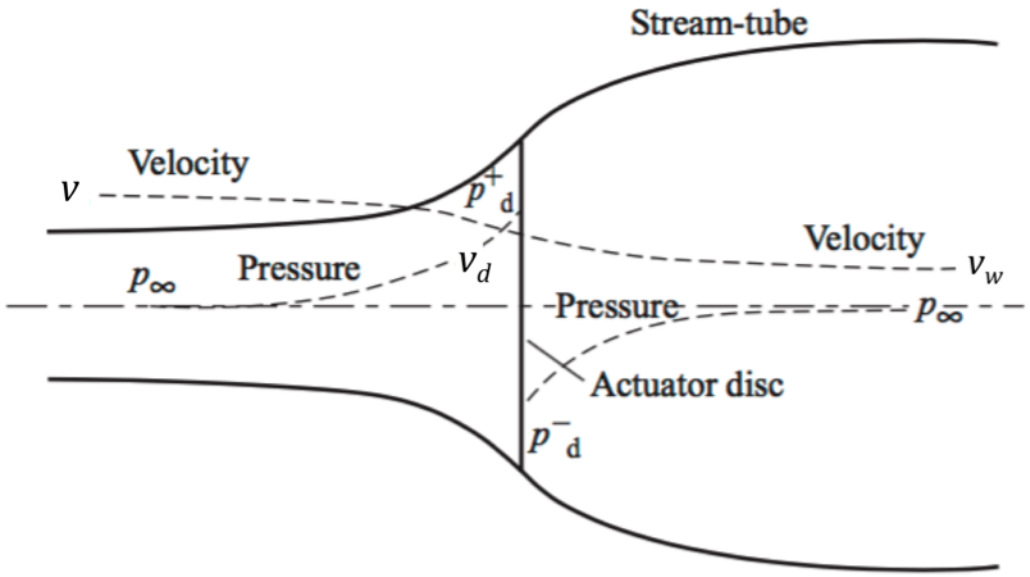

Figure 2.7: The single actuator disc concept. Adapted from Burton et al. (2001).

novel designs such as oscillating hydrofoils and tidal kites that are shown in Figure 2.1. Regardless of their design, all of these devices extract energy from a moving fluid. Linear momentum theory describes the generation of power from an unbounded fluid flow (Burton et al., 2001) by relating the power (P) available to a device to the speed (v) of the fluid that passes through its cross-sectional area (A_c). This is done by modelling the device as an infinitely thin, permeable disc, as illustrated in Figure 2.7.

The disc exchanges energy and momentum with the fluid, which is assumed to be inviscid, incompressible and of uniform speed across the area of the disc. A power coefficient (C_p) is defined to describe the hydrodynamic efficiency of the disc, enabling the power it generates to be described in terms of the kinetic energy of the fluid:

$$P = \frac{1}{2}\rho A_c v^3 C_p \tag{2.6}$$

As shown in Figure 2.7, the fluid speed is reduced as energy is extracted by the disc, causing the fluid to expand to conserve mass. This occurs equally upstream and downstream of the disc, and increases as more energy is extracted. Consequently, there is a maximum to the amount of power a disc can generate, as slowing the flow beyond a certain point results in the fluid expanding to such an extent that it stops passing through the disc. This maximum results in an efficiency limit of C_p=0.593, a value known as the Lanchester-Betz limit (Lanchester, 1915; Betz, 1920).

Linear momentum theory incorporating a single actuator disc is appropriate for axial flow turbines and other devices where energy is extracted from the

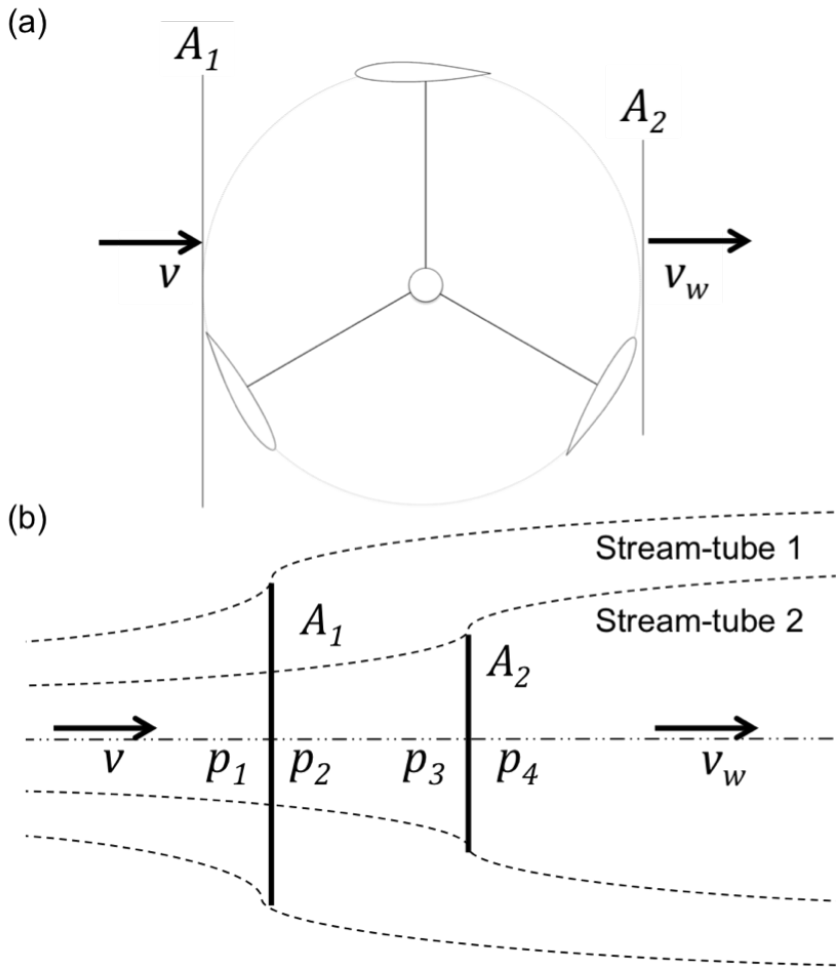

Figure 2.8: The double actuator disc concept. Adapted from Newman (1983).

flow in one region. Other devices extract energy from the flow in multiple regions, meaning a greater number of discs should be considered. In cross flow turbines, for example, a more reasonable assumption is that the fluid flows across the blades twice, and thus a double actuator disc is more appropriate (Newman, 1983). Positioning a second disc downstream of the first, as shown in Figure 2.8 enables slightly more power to be extracted from the flow, which increases the efficiency limit to C_p=0.640 (Newman, 1983). Adding further discs behind the second enables the efficiency limit to be increased towards C_p=0.667 at four discs. There is little increase in power beyond four discs however, as most of the power in the flow is absorbed by the upstream discs (Newman, 1986).

Dividing Equation 2.12 by A_c allows the theoretical power density of a tidal stream device to be calculated, enabling power output to be compared independently of size:

$$P_D = \frac{1}{2}\rho v^3 C_p \tag{2.7}$$

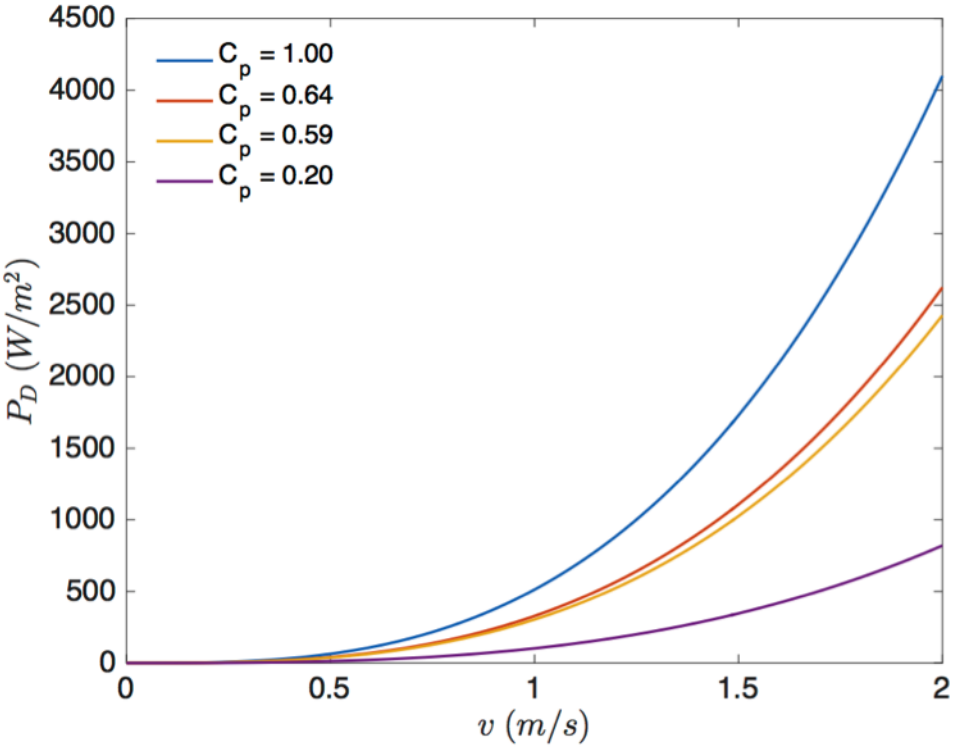

Figure 2.9: Theoretical power density available from tidal stream devices in flow speeds of 0 -– 2 m/s.

Figure 2.9 illustrates the theoretical power density for several values of C_p, including both the single and double actuator disc limits of 0.593 and 0.640, respectively. The higher efficiency limit of a double actuator disc suggests that devices which extract energy from the flow multiple times, such as cross flow turbines, are likely to generate more power than single disc devices like axial flow turbines. This small but additional amount of power per unit area will be advantageous for devices targeting shallow waters, where the maximum size of the device will be constrained by depth. Although Figure 2.9 shows power as a function of vertical cross-sectional area, rather than the horizontal area of a basin, comparing this plot with Figure 2.5 also suggests that tidal stream devices can produce more power relative to their size than tidal range devices. This suggests that tidal stream is more appropriate for pico scale power generation, since devices will not need to be as large and are therefore likely to be cheaper to install.

Figure 2.9 shows the minimum cross-sectional area necessary if tidal stream devices of various levels of efficiency are to extract 2 kW of power from flows of varying speed. This again illustrates that tidal stream devices are likely to be more suited for pico scale power. Even in a relatively weak flow of 0.5 m/s, an efficient tidal stream device will only need a cross-sectional area of around

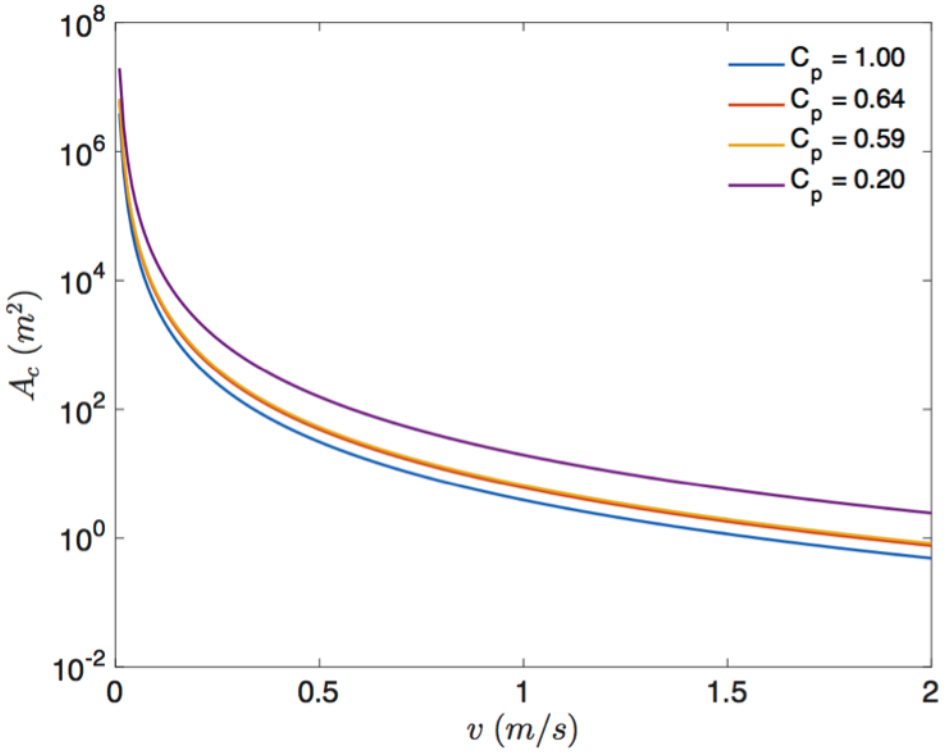

Figure 2.10: Minimum cross-sectional area necessary to generate 2 kW in flows of 0 – 2m/s.

50 m^2, compared to the minimum of 100 m^2 basin needed for a tidal range device in a 6 m tide.

While the theoretical actuator disc efficiency limits of 0.640 and 0.593 generally hold true for wind turbines in an unbounded flow, for devices operating underwater they are much less realistic (Garrett and Cummins, 2004). The extraction of energy from an open channel flow serves to deform the water surface (Whelan et al., 2009), reducing the downstream water depth due to the pressure drop that occurs across the device. This pressure drop increases as more energy is extracted, and the amount of power a device can generate is consequently affected by how much the free surface can be deformed.

The seabed and the water surface also act to constrain the flow (Bryden et al., 2007; Whelan et al., 2009), which hinders the expansion of the fluid as it is slowed by energy extraction. This effect, which is known as blockage, enables a greater portion of the power within the flow to be harvested. Devices that are of significant size relative to their surroundings can consequently exhibit C_p values that are greater than the theoretical limits for an unbounded flow. For example, several cross flow turbine configurations tested by McAdam et al. (2010) exhibited C_p values above the Lanchester-Betz limit, with the largest value found to be approximately 85 %.

Blockage is most noticeable in underwater channels, where the sides of the channel serve to constrict the flow even further. This enables the C_p of a single device within a channel to be increased above the Lanchester-Betz limit by a factor ϵ (Garrett and Cummins, 2007):

$$\epsilon = \frac{1}{(1-b)^2} \tag{2.8}$$

Where b is the blockage ratio of the channel, dependent upon the cross-sectional area of the disc A and the cross-sectional area of the channel A_c:

$$b = \frac{A}{A_c} \tag{2.9}$$

In reality, a device or array will never be able to fully block a channel. Instead, there will be gaps around each device according to the shape of the channel walls, as well as to permit marine life and watercraft to navigate. Downstream of where energy is extracted, the flow through these gaps will mix with the slower flow of the device wake, dissipating energy. This dissipation increases with the blockage ratio, meaning the increase in the power extracted by a device comes at the cost of reducing the overall efficiency of a channel (Garrett and Cummins, 2007). There is consequently a limit to the amount of power that can be extracted from such locations (Garrett and Cummins, 2008). Given that the presence of devices in the water also impacts upon the free-stream speed of the flow, it is crucial to tune the shape and size of an array of devices to the specific Vennell (2010).

Energy extraction using tidal stream devices is also predicted to have further impacts on the environment in addition to free surface deformation. For example, the reduction in upstream and downstream water velocities caused by power generation is predicted to negatively impact upon water quality and sediment transport Ahmadian et al. (2012). It is also predicted accelerated flow in the regions around a device will lead to scouring of the seabed and the device itself, which may negatively impact the lifespan and maintenance requirements (Shields et al., 2011). Other impacts during the operation phase of a device may include the alteration of habitats for marine organisms, noise pollution, the generation of electromagnetic fields and the striking of animals with rotor blades or other moving parts (Gill, 2005). These effects will scale according to the size and design of the device, and are therefore likely to be smaller than those of tidal range schemes due to the smaller size of tidal stream devices.

2.3.1 Tidal stream resources

The speed of an underwater current is dependent upon factors such as the distance from the seabed, whether the moving water is constrained by underwater channels or other bathymetric features, and the presence of other tidal devices nearby. Some early investigations into the tidal stream resource of the UK were conducted in the late 1970s. Fraenkel and Musgrove (1979) estimated the kinetic energy flux within major undersea channels using approximate mean depth and width values from navigational charts, and predicted an estimated average power of 14.7 GW available from tidal currents around the UK. Wyman and Peachey (1979) also used water depth and velocity information from navigational charts to estimate the average kinetic energy across whole areas of the sea, and predicted a slightly greater mean resource of 18.7 GW.

Later estimates conducted during the 1990s (ETSU, 1993; European Commission, 1996) continued to use navigational charts for water depth and flow speed data. These studies, which are summarised in Table 2.3, used this data to identify and select suitable sites based upon the depth and/or flow speed requirements of the technology available at the time. Sites were subdivided into plan areas so that the maximum number of installable devices could be calculated according to their size and spacing requirements. The power generated by individual devices was then calculated, enabling the estimation of the energy available from the arrays and single devices. ETSU (1993) assumed a constant value for device efficiency, while European Commission (1996) assumed a more realistic speed-efficiency curve based upon the performance of a wind turbine, with the latter providing more realistic estimates as a result.

One drawback of using navigational chart data is the fact that the flow speed data only applies to discrete points within a site. Neither ETSU (1993) or European Commission (1996) attempted to interpolate the data to calculate the flow speed between these points, which reduces the accuracy of their findings given that many of the chosen sites were on the scale of kilometres. Another drawback of these reports is that they did not account for the effect of energy extraction by other devices in the array on the local flow. This is vital to consider for projects involving arrays of devices and/or tidal channels, given that the extraction of energy from the flow results in a reduction of the flow speed (Bryden et al., 2004; Garrett and Cummins, 2005). Consequently, the power estimates of these early studies are now though to be much larger than what is realistically achievable.

Two more recent UK wide resource assessments (Black and Veatch Consulting Ltd, 2004, 2005) built upon the findings of these studies and attempted to

Table 2.3: Summary of UK tidal stream resource estimates from the past 25 years.

Study	ETSU 93	EC 96	B&V 04	B&V 05	B&V 11	CE 2012
Minimum site depth (m)	20	-	-	-	15	5
Minimum flow speed (m)	2	1.5	-	-	2.25	1.5
Sites assessed (-)	33	42	57	10	30	-
Total surface area (km^2)	1450	1330	-	-	-	-
Average available resource (GW)	6.9	3.9	2.5	2.1	-	32
Annual energy output (TWh)	57.6	30.9	22.0	16.0	20.6	95.0

improve the methodology by employing a significant impact factor to account for the effects of extracting energy from the flow. This factor described the proportion of energy within an undisturbed flow that could be extracted without significantly affecting flow conditions, and was defined for a one-dimensional channel as 'an acceptable percentage decrease in the upstream flow rate following energy extraction'. Since it was made in the absence of data regarding the impacts of devices on the flow, however, this definition is debatable (Blunden and Bahaj, 2007)

Black and Veatch Consulting Ltd (2004) used a somewhat arbitrary significant impact factor of 20 % of the maximum available energy for all of the sites investigated. The scope of Black and Veatch Consulting Ltd (2005) was limited to the 10 most energetic regions within the UK, which removed a number of smaller areas that may still be economically attractive for tidal power development (Blunden and Bahaj, 2007). For some of these regions, a smaller impact factor of 8 – 12 % of the maximum flow speed was used. Since both Black and Veatch Consulting Ltd (2004, 2005) relied upon the findings of studies from roughly a decade earlier to inform their site selection, they also neglected sites thought to be technologically inaccessible during the 1990s. This can be seen in how Black and Veatch Consulting Ltd (2005) categorises sites according to

depth and flow speed, with the shallowest, slowest sites considered to be less than 25 m deep with flows of less than 2.5 m/s.

An alternative method of quantifying the available tidal stream resource is to use numerical modelling. In addition to their data on tidal range, the models of ABP Marine Environmental Research Ltd (2008) also provide information on the distribution of the tidal stream currents around the UK. Due to the course grid resolution of 1.8 km^2 that this study used, localised high energy flows around headlands and through narrow straits and channels were missed (Blunden and Bahaj, 2007). This prevents the data from being useful for accurate local scale resource assessments.

The most recent analyses of the total tidal stream resource around the UK (Black and Veatch Consulting Ltd, 2011; The Crown Estate, 2012) still rely upon this data, acknowledging its poor resolution while simultaneously using it to assess the tidal stream resource of specific sites. Consequently, the results of these studies are subject to high levels of uncertainty. Black and Veatch Consulting Ltd (2011) studied waters that are on average deeper than 15 m, and which were found by ABP Marine Environmental Research Ltd (2008) to have a mean peak power density greater than 1.5 kW/m^2. Although the flow speed this corresponds to is not defined, all of the examined sites had a minimum mean spring peak flow speed of 2.25 m/s.

Sites falling out of these criteria were neglected as it was assumed most technology would not be capable of operating economically within them. A significant impact factor of 2 % was used to account for the difference between the available resource and that which can technically be extracted from tidal streams, resulting in an estimated extractable resource of 20.6 TWh/year (-50/+45 %), with a corresponding predicted cost of energy of £0.21/kWh (-25/+115 %).

The Crown Estate (2012) expanded the site selection criteria used by Black and Veatch Consulting Ltd (2011); investigating sites with a minimum depth of 5 m and with flow speeds greater than 1.5 m/s (corresponding to a power density of 0.5 kW/m^2). Again, an arbitrarily prescribed limit of 2 % was used to account for impacts of energy extraction on the flow, which was done due to the size of the study, the case-by-case nature of such impacts and a general lack of data regarding them. The total UK resource was estimated as 95 TWh of energy per year (-30/+45 %) and a maximum available power of 32 GW (-30/+45 %), figures that are significantly greater than the estimates of the previous studies. Given that The Crown Estate (2013) made the same allowances for the environmental effect of energy extraction as Black and Veatch Consulting Ltd (2011), this can only be ascribed to the much greater number

of sites that were assessed. Despite the large levels of uncertainty in these estimates, the difference between these figures suggests that there is a relatively large resource available to devices capable of functioning in what would otherwise be considered sub-optimal locations.

As is the case with tidal range, focussing on local areas allows for higher resolution numerical modelling to more accurately assess tidal currents over a prolonged period of time. For example, Blunden and Bahaj (2006) used a 2D finite element model to simulate tidal flows around the Portland Bill headland in Dorset. They found that their model accurately reproduced features of the tidal stream when compared with measured data, meaning their results could be used to confidently predict the performance of a single turbine located off the headline. Similar analyses have been conducted for arrays of devices in other locations, such as the Severn Estuary (Xia et al., 2010b) and the Ria de Muros in Spain (Carballo et al., 2009).

Other studies have attempted to account for the influence of devices on the flow by increasing the seafloor drag coefficient in the vicinity of a proposed farm (Walkington and Burrows, 2009). Employing an increased drag coefficient in a numerical model is arguably a more realistic method than imposing an arbitrary limit on the resource, since it can more readily account for differences in device design and deployment location.

Analytical models have also been developed that account for the retardation of the flow in tidal channels by tidal stream devices (Vennell, 2011a). These permit a more accurate assessment of tidal stream resources than those employing arbitrary efficiency limits, without the need for more computationally demanding numerical models. To maximise the tidal current resources available from a farm within a tidal channel, attention has to be given to the layout of a tidal stream array (Vennell, 2010).

An optimal arrangement is dependant not only on the layout and number of devices, but also the shape, size and depth of the channel. These variables all directly impact the power produced by the individual turbines and the farm itself (Vennell, 2011b, 2012a). Shallow channels, for example, which are already highly stressed due to friction with the seabed, are thought to produce proportionally less power as new devices are added to fill their cross-sectional area, due to increasing drag (Vennell, 2012a). In contrast, farms in larger tidal straits will produce more power as additional devices are added to the cross-section, with more power available per device and higher device efficiencies occurring due to blockage effects (Vennell, 2012a). As a result, adding new turbines to fill out a row of devices spanning the width of a channel is thought to be more economically viable than adding more rows behind the

first (Vennell, 2012b).

2.3.2 Tidal turbines

Tidal turbines are the tidal stream devices that most closely resemble wind turbines, as they consist of a rotor that is driven by the fluid flow. This is typically done through the use of hydrofoil shaped blades that operate according to the principles of hydrodynamic lift and drag (Hardisty, 2009). Tidal turbines can be classified according to their rotor design as either axial flow or cross flow, as illustrated in Figure 2.11.

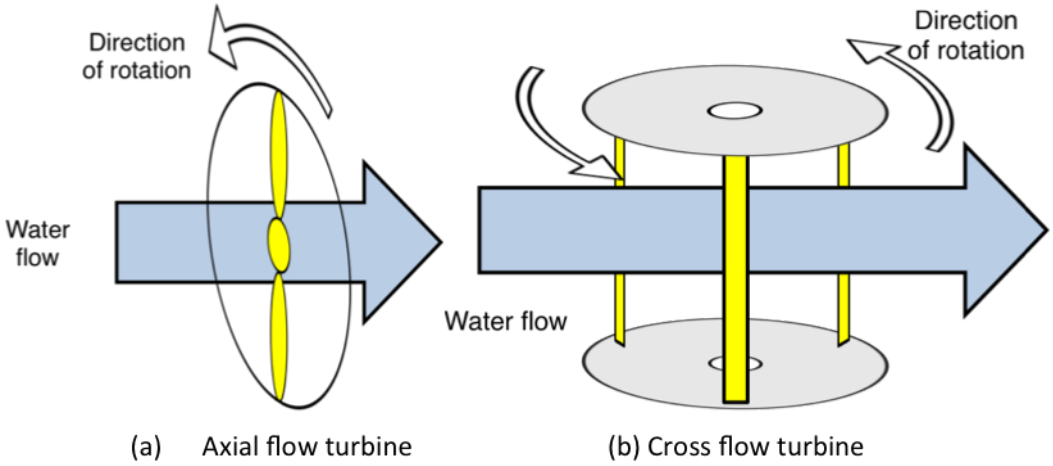

Figure 2.11: Tidal turbine rotor types.

Although the physics governing the behaviour of tidal turbines is identical to that of wind turbines, there are major differences between the two technologies. The most immediate of these are the differences between air and sea water; seawater has a density of approximately 1025 kg/m^3, compared to 1.25 kg/m^3 for air at standard temperature and pressure. This compensates for the fact that tidal currents are typically much slower than the wind, enabling tidal turbines and indeed all tidal stream devices to generate similar levels of power to wind turbines in the right conditions (Bahaj and Myers, 2003). In contrast to wind power, there are no extreme flow speeds due to the tides that could potentially damage underwater devices or force them to stop generating (Blunden and Bahaj, 2006), although tidal turbines must still be extremely durable to withstand the loading forces of the water and the harsh marine environment for prolonged periods of time. Further contrasts between wind and tidal turbines include free-surface effects (Whelan et al., 2009), the occurrence of cavitation and the bi-directionality of tidal currents (Batten et al., 2006), as well as the blockage effects discussed above.

The efficiency of a tidal turbine is primarily governed by the profile (Kadlec,

1978), pitch (Myers and Bahaj, 2006; Kirke and Lazauskas, 2008, 2011), shape (Baker et al., 2006) and surface roughness (Howell et al., 2010; Walker et al., 2014) of its hydrofoil blades, as well as flow characteristics including the Reynolds number Re (Consul, 2011; Roh and Kang, 2013) that a turbine is operating in. For a flow over a hydrofoil of chord length C, Re can be defined using the dynamic viscosity μ and density ρ of the fluid and the speed of the flow v_{rel} relative to the hydrofoil:

$$Re = \frac{\rho v_{rel} c}{\mu} \tag{2.10}$$

The Reynolds number directly affects the lift and drag coefficients of a hydrofoil blade and hence the power output of a turbine (Consul, 2011). It is crucial to consider Re in scale model testing aiming to quantify efficiency, since it is directly affected by the size and speed of the blades. Given the effect energy extraction has on the free surface (Whelan et al., 2009), it is also important to consider the Froude number Fr of the flow – a dimensionless quantity that relates the free-stream flow speed v_∞ to the water depth h_∞:

$$Fr = \frac{v_\infty}{\sqrt{g h_\infty}} \tag{2.11}$$

In higher Froude numbers, the free-stream flow speed is larger relative to the water depth. This can increase the power output of a single turbine, at a cost of reducing the overall basin efficiency (Consul, 2011). In turn, this may improve the effectiveness of an isolated device in shallow waters, while diminishing the overall amount of energy that may be extracted from the area.

The solidity of the turbine rotor is another important consideration in tidal turbine design (Consul et al., 2009; Consul, 2011). For a device of radius r with n blades, the solidity represents the ratio of total blade chord length to the rotor circumference:

$$\sigma = \frac{nC}{2\pi r} \tag{2.12}$$

If the support structure of a turbine is neglected, increasing the solidity of a rotor has been shown to increase the maximum power coefficient of the design (Consul et al., 2009). Higher solidity turbines have been found to generate more power from blocked flows in comparison to lower solidity designs (Schluntz and Willden, 2015) , suggesting that a shallow water design will need to be of higher solidity than a device designed to operate in deep waters. Care will need to be taken to minimise the drag created by the support structure, however, if these benefits are to be realised in practice.

Axial flow turbines

When generating power, axial flow turbines (aka horizontal axis turbines) sweep through a circular cross-section of the flow by rotating about an axis that is parallel to the flow direction. Since the flow passes over the blades only once, they are typically described by a single actuator disc, meaning their hydrodynamic efficiency in unbounded flows is constrained by the Lanchester-Betz limit.

Axial flow turbines are a very popular design with commercial developers, with the European Marine Energy Centre listing 30 different devices in development (European Marine Energy Centre, 2014). The performance characteristics of five commercial axial flow devices are summarised in Table 2.4: the MCT SeaGen S (Marine Current Turbines, 2016b), Atlantis Resource Corporation's AR1000 (EMEC, 2014), Bourne Energy's RiverStar Bourne Energy (2014), Verdant Power's Gen5 (Polagye et al., 2010), and Voith Hydro's 1 MW test device (Voith Hydro, 2014).

Table 2.4: Performance characteristics of selected commercial axial flow turbines.

Developer	Atlantis	Bourne	MCT	Verdant	Voith
Device	AR1000	RiverStar	SeaGen S	Gen5	1 MW test
Rated power (kW)	1000	50	2000	1.68	1000
Rated flow speed (m/s)	2.65	2.05	2.40	2.59	2.90
No. of rotors (-)	1	1	2	3	1
Rotor diameter (m)	18.0	6.09	20.0	5.00	16.0
Rotor swept area (m^2)	254	29	314	20	201
Rated C_p	0.41	0.39	0.45	0.35	0.40

The information presented in Table 2.4 provides an indication of the potential of commercial axial flow turbines, however since the information was primarily sourced from the developers it is difficult to accurately verify the performance data. Information on the performance of several smaller scale

Table 2.5: Performance characteristics of experimental axial flow turbines.

Study	O'Doherty et al. (2009)	Bahaj et al. (2007)	Myers and Bahaj (2006)	Coiro et al. (2006)
Rated power (W)	45	600*	460	800
Rated flow speed (m/s)	1.00	1.73	2.56	2.00
No. of rotors (-)	1	1	1	1
Rotor diameter (m)	0.50	0.80	0.40	0.80
Rotor swept area (m^2)	0.20	0.50	0.13	0.50
Rated C_p	0.41	0.46	0.44*	0.40

*figure not reported but calculated using Equation 2.12

experimental devices published in peer-reviewed studies is presented in Table 2.5. Comparing these tables shows that the commercial devices at least appear to be achieving comparable levels of efficiency to the small scale test devices. The dependence of the power output of a tidal stream device on both flow speeds and size is also apparent, with commercial devices apparently targeting much higher flow speeds than those of the experimental devices. Given the difference in device size and flow speed, the Reynolds numbers that the devices are operating in will also be different.

Cross flow turbines

Cross flow turbines rotate about an axis that is perpendicular to the flow direction, and therefore sweep through a rectangular cross-sectional area. As illustrated in Figure 2.12, the axis of rotation can be in either the vertical or horizontal plane, and cross flow turbines are frequently referred to as vertical axis or transverse horizontal axis turbines.

For both orientations, there are a number of subcategories, including straight-bladed Darrieus rotors, helical designs and devices designed to exploit channel blockage effects. Due to their orientation to the flow, cross flow turbines may

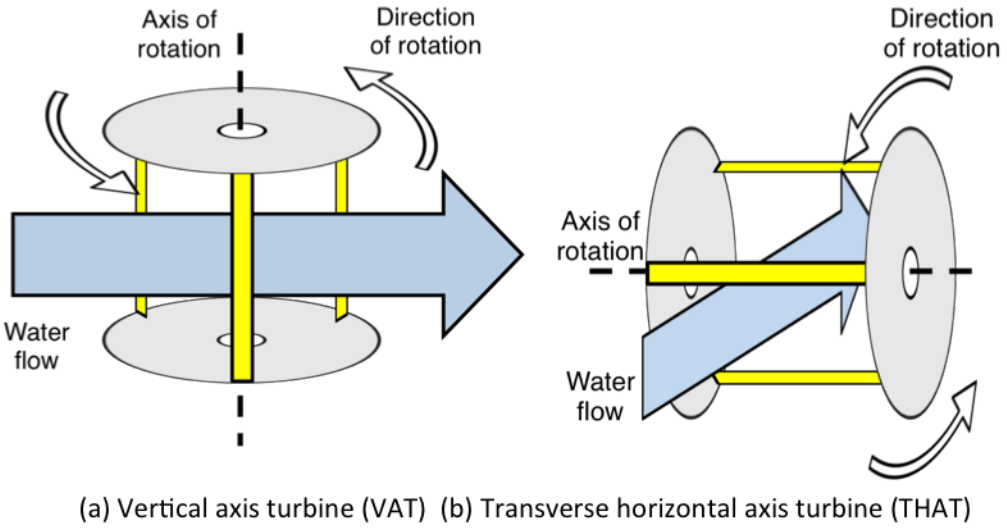

Figure 2.12: Cross flow turbine rotor classes.

be described using a double actuator disc (Newman, 1983), meaning they will have a slightly higher efficiency limit in unbounded flows compared to axial flow turbines. Given their rectangular swept area, cross flow turbines are more readily able to stretch across the width of a channel than axial flow turbines, enabling them to reach higher blockage ratios and thus achieve very high power coefficients (McAdam et al., 2010).

Although less popular than axial flow turbines among wind developers, vertical axis wind turbines have several advantages in addition to this higher efficiency limit. These include omni-directionality, no need for pitch regulation or a gearbox, lower maintenance requirements and better performance in severe wind climates (Eriksson et al., 2008). Many of these advantages translate directly to cross flow tidal turbines. For example, omni-directionality (for vertical axis turbines) or bi-directionality (for transverse horizontal axis devices) is of huge benefit in tidal flows. Cross flow tidal turbines are almost as popular with developers as axial flow designs, with 26 separate devices listed as in development by EMEC (European Marine Energy Centre, 2014).

Data on the performance of commercially developed cross flow turbines are less readily available than they are for axial turbines. Several small scale cross flow devices have been tested experimentally, however, and the performance characteristics of a selection of these devices is presented in Table 2.6.

The most efficient device shown (McAdam et al., 2010) was primarily designed to be large enough to take advantage of the blockage effects discussed in Section 2.3. Operating at a blockage ratio of 0.50, the high efficiency of the device shows the effectiveness of utilising blockage and deploying a device in a

Table 2.6: Performance characteristics of experimental cross flow turbines.

Study	Yang and Shu (2012)	McAdam et al. (2010)	Kyozuka (2008)	Coiro et al. (2005)	Shiono et al. (2000)
Device	Göttingen 623 hydrofoil	Truss** $B = 0.50$ $Fr = 0.09$			
Orientation	Horiz.	Horiz.	Vert.	Vert.	Vert.
Maximum power (W)	95	3	215*	160	16
Rated flow speed (m/s)	1.50	0.30	1.00	3.50	1.4
No. of rotors (-)	1	1	1	1	1
Rotor swept area (m^2)	0.14	0.44	0.19	30.0	0.06
Rated C_p (-)	0.41	0.53	0.43	0.24	0.19

* figure not reported but calculated using Equation 2.12.
** device designed to exploit blockage effects.

tidal channel. For this to happen effectively and reliably, however, the device will need to be tuned to operate within the specific constraints of an intended site.

The two lower efficiency devices are basic straight-bladed Darrieus rotors. These are relatively cheap and straightforward to construct, however at low rotational speeds their straight blades will suffer from a wildly fluctuating angle of attack (Kirke and Lazauskas, 2011). This reduces the efficiency of the devices and makes them liable to stall, while also hindering their ability to self-start. The blades of Darrieus devices are also subject to much higher levels of stress due to the rapidly fluctuating levels of torque they generate.

Using a pitch control system to adjust the angle of attack of a blade over the course of a revolution is, in principle, one method of minimising these issues. Two types of pitch control system may be used, active pitch control, which forces the blade pitch to follow a predetermined regime, or passive pitch control, which uses the forces acting on the blades control the pitch. Due to the mechanical complexity of active pitch control and the dubious effectiveness of passive pitch control, however, variable pitch Darrieus wind turbines have never reached commercial production (Kirke and Lazauskas, 2011). Despite this, efficient Darrieus designs can still be developed (Kyozuka, 2008), although the Reynolds number and blockage ratio of that experiment, which will affect the efficiency of the design, were not reported.

An alternative to the straight bladed Darrieus is a helical rotor (Gorlov, 1995; Gorban et al., 2001), as employed by Yang and Shu (2012). By design, the angle of attack varies along the length of a helical blade, smoothing out the torque pulsations (Kirke and Lazauskas, 2008), reducing the tendency to stall, increasing starting torque and improving overall efficiency (Baker, 1983), at the cost of more difficult and expensive blade manufacture.

Ducted turbines

Adding a duct to either an axial or cross flow turbine accelerates the flow through the device, increasing efficiency by allowing a rotor to produce more power for its size (Shives and Crawford, 2010). The definition of efficiency typically neglects the additional area required by the duct, however, and comparing devices of equal total size shows that ducted turbines may actually be less efficient than their unducted counterparts (Belloni, 2013), apart from when the flow into the device is yawed.

Turbine ducts are generally designed to increase the expansion of the fluid downstream of the rotor and hence reduce the downstream velocity due to conservation of mass. This in turn increases the reduction in the downstream

Table 2.7: Performance characteristics of selected commercial ducted turbines.

Developer	Clean Current	Tidal Energy Pty Ltd	OpenHydro
Device	CC035B	DHV 170 kW	200 kW Demo
Rated power (kW)	65	170	200
Rated flow speed (m/s)	3.00	3.00	2.50
No. of rotors (-)	1	1	1
Rotor diameter (m)	3.50	5	10.0
Rotor swept area (m^2)	10.0	19.6	79.0
Rotor C_p	0.49	0.63	0.32
Assumed total area (m^2)	20.0	41.2	158
Total device C_p	0.23	0.29	0.16

pressure, accelerating the flow across the rotor and hence increasing the available power (Consul, 2011). The effect of a duct or diffuser on device performance is dependent upon its size and angle, with each having an optimum value (Gaden and Bibeau, 2010). The extra structure of the duct also serves to increase the overall drag coefficient of the device, which will reduce the effectiveness of turbine arrays (Shives and Crawford, 2010). This is likely to be more noticeable in regions of constrained flow, such as channels, or shallow regions that are already highly stressed due to seabed friction.

Ducted devices appear less popular with commercial organisations than their unducted counterparts. EMEC currently list 8 different developers working on ducted devices. Table 2.7 provides details on two axial flow commercial devices, a 200kW OpenHydro demonstrator device (Polagye et al., 2010) and the small Clean Current CC035B (Clean Current Power Systems Inc 2012) and one ducted cross-flow device, the 170 kW Davidson-Hill Venturi turbine (Ltd, 2015). Two calculated power coefficient values are also provided, the first de-

termined according to the rotor diameter described by the developers, and the second assuming a total device diameter approximately 1.45 times that of the rotor. This ratio of total to rotor diameter is in line with the of values of other ducted devices in development (Belloni, 2013), however it varies according to device design. Regardless of the value used, accounting for the extra area of the duct will naturally result in a reduction in power coefficient, as shown by Table 2.7.

2.3.3 Oscillating hydrofoils

Oscillating hydrofoils consist of a wing attacked to a level arm, and make use of the principles of hydrodynamic lift and drag to create a reciprocating motion that is ultimately used to drive a generator via hydraulics or a cam-rocker mechanism (Xu and Sun, 2015). A simple illustration of an oscillating hydrofoil is provided in Figure 2.13.

The flow of water across the wing generates lift on one side, enabling the lever to rise or fall at some frequency (f) with a sinusoidal motion that is a combination of heave (y) and pitch (θ):

$$y(t) = y_0 \sin(2\pi f t + \phi) \tag{2.13}$$

$$\theta(t) = \theta_0 \sin(2\pi f t) \tag{2.14}$$

This motion is illustrated in Figure 2.14 for a system where the phase ϕ between the heave and pitch motions is 90 degrees. Due to this combination of linear and rotary motion, the instantaneous power generated by an oscillating hydrofoil at a time t may be expressed as (Xu and Sun, 2015):

$$P(t) = F_y(t)\dot{y}(t) + \tau(t)\omega(t) \tag{2.15}$$

Where F_y is the vertical force acting on the wing, $\dot{y}$ is its linear speed, τ is the torque generated about the pivot point and ω is the angular frequency of the wing. The mean power generated over a time T is given by:

$$\overline{P} = \frac{1}{T}\int_0^T P(t)\mathrm{d}t \tag{2.16}$$

The varying position and pitch of the wing changes the angle-of-attack of the flow relative to the hydrofoil. As a result, the lift generated by the wing varies with time eventually changes direction, reversing the motion as shown in Figure 2.15. Depending upon the design, a second wing on a second arm may be positioned behind the first to create a see-saw arrangement that enables

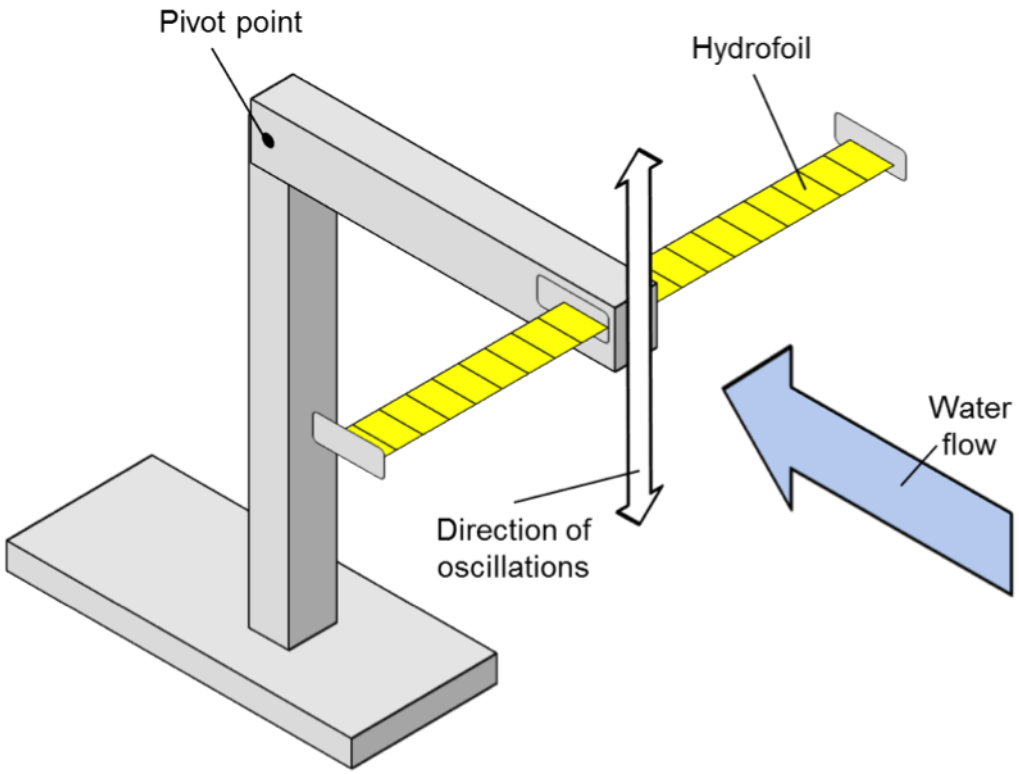

Figure 2.13: Illustration of a single wing oscillation hydrofoil.

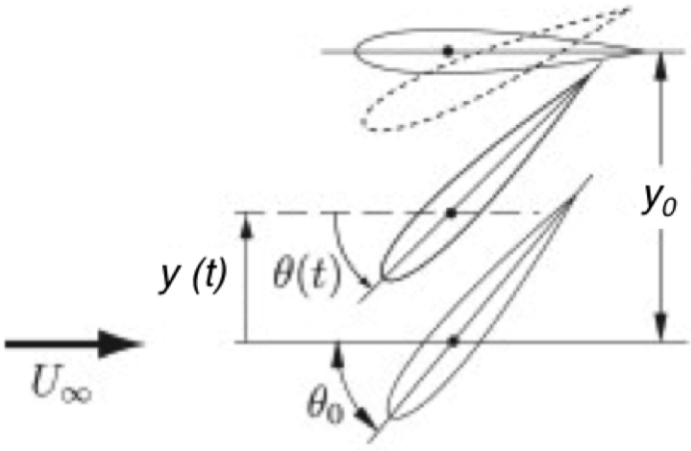

Figure 2.14: Heaving and pitching motion of an oscillating hydrofoil wing with a 90 degree phase angle. Adapted from Kinsey et al. (2011).

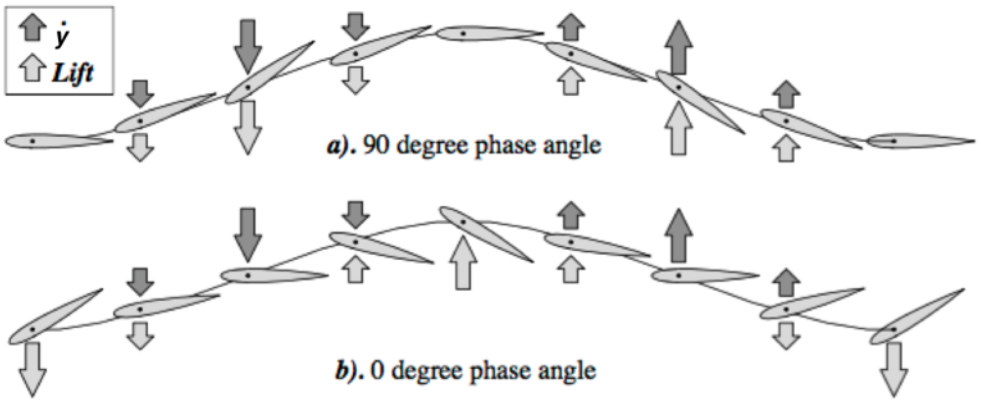

Figure 2.15: Variation in lift and velocity of oscillating hydrofoil wing. Adapted from Jones et al. (2003).

energy to be extracted from the flow twice.

The power that an oscillating hydrofoil extracts from a tidal current may be non-dimensionalised in a virtually identical manner to that of a turbine (Kinsey et al., 2011). An oscillating hydrofoil sweeps through a rectangular area of water, which is the product of the extent of the vertical motion ($2y_0$ referring to Figure 2.14) and the wingspan d. Hence, from Equation 2.12:

$$C_p = \frac{P}{\rho y_0 d v^3} \tag{2.17}$$

Oscillating hydrofoils have been described as suitable for the exploitation of shallow water tidal currents (Kinsey et al., 2011), since the amount of energy they can extract from the flow is dependent upon blade length and not strictly constrained by depth. As the relative speed of the flow, and therefore angle-of-attack, over the length of the oscillating hydrofoil blade remains uniform, they do not require twisting, unlike axial turbine blades. Compared to a straight-bladed cross flow turbine like a Darrieus rotor, the variation in the angle-of-attack experienced by the blades over the course of an oscillation is relatively small, reducing the magnitude of the torque pulsations and reducing issues with fatigue. Oscillating hydrofoil blades are therefore cheaper and easier to produce than those of most turbine designs, although very long blades may suffer issues such as flexing.

Oscillating hydrofoil efficiency can be poor due to the time required to reverse the direction of oscillation (O Rourke et al., 2010). This is exemplified by the fact that the most well developed commercial oscillating hydrofoil, known as Stingray (The Engineering Business Ltd, 2003, 2005), was shelved due to poor performance. A second commercial oscillating hydrofoil is under

Table 2.8: Performance characteristics of oscillating hydrofoils.

Device	Kinsey et al. (2011)	Stingray
Maximum power (kW)	2.00	8.53*
Number of wings (-)	2	1
Required flow speed (m/s)	1.99	2.00
Blade span (m)	1.68	15.5
Extent of vertical motion (m)	0.61	12.6**
Swept area (m^2)	1.02	195
Total power density (kW/m^2)	1.96	0.04
Total rated C_p	0.40	0.12
Wing power density (kW/m^2)	0.98	0.04
Wing C_p	0.20	0.12

* mean hydraulic power produced over 30 minute period (The Engineering Business Ltd, 2005).
** calculated from arm length and operating angle values (The Engineering Business Ltd, 2003).

development by Pulse Tidal (Pulse Tidal, 2014) although there is currently little data available on the performance of this device.

Table 2.8 summarises the characteristics of the cancelled Stingray device and the experimental oscillating hydrofoil tested by Kinsey et al. (2011), illustrating a huge difference in the efficiency of the two devices. In addition to the differences in Reynolds number and blade profile between the devices, this is partly because the device of Kinsey et al. (2011) featured two hydrofoil wings, while Stingray only had one. Calculating values of power density and C_p per wing suggests that the performance of the devices is more similar than it first appears, suggesting that such devices are less efficient than their conventional turbine counterparts.

2.3.4 Tidal kites

Tidal kites consist of a small axial flow turbine attached to a hydrofoil wing that is tethered to the seabed. Lift is created by water flowing over the wing, which pushes the kite through the water. The motion is controlled through a combination of a rudder and tether tension, enabling the device to be guided along a given trajectory, such as the figure-of-eight shown in Figure 2.16b for the Minesto Deep Green tidal kite (Minesto, 2013). A schematic of the this

device is shown in Figure 2.16a.

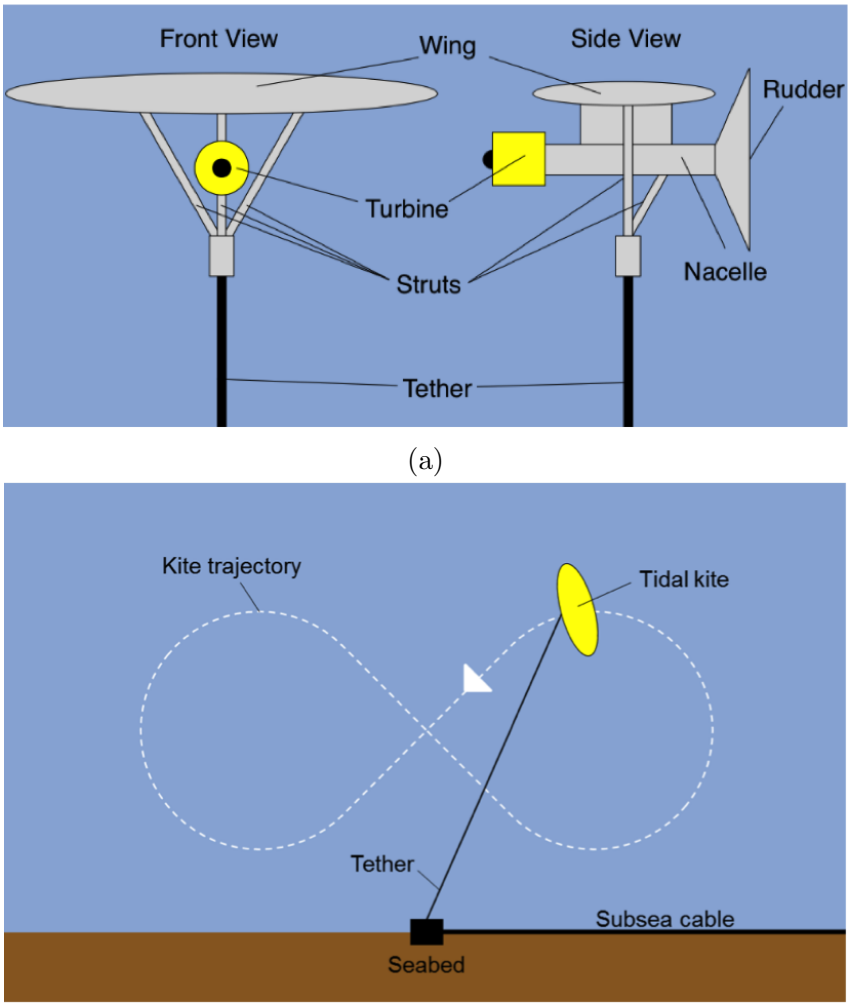

Figure 2.16: Schematic (a) and motion (b) of the Minesto Deep Green tidal kite. Adapted from Minesto (2013).

The movement of the kite through the water increases the flow speed through the turbine below the wing, allowing a smaller rotor to generate greater amounts of power from weaker flows. The turbine is typically a horizontal axis axial flow turbine, meaning the flow kinematics is identical to that of a more conventional design. A direct-drive generator attached to the kite is used to generate electricity, which is transmitted through a cable in the tether to a station on the seabed, and then onto the shore.

Table 2.9 details the specifications of several variants of the Minesto Deep Green device. The power coefficient estimates were calculated using Equation 2.12, the provided rotor diameters and Minesto's claim that the device moves at a speed 10 times greater than the water current. For the calculated power density values, the rated power was divided by the total device swept area. This was estimated as a semi-circle with the minimum tether length as its

Table 2.9: Minesto Deep Green specifications. Sourced from Minesto (2014).

Device	DG-8	DG-10	DG-12	DG-14
Rated power (kW)	110	220	500	850
Rated speed (m/s)	1.30	1.40	1.60	1.73
Rotor diameter (m)	0.67	0.83	1.00	1.15
Tether length (m)	60 – 80	75 – 100	85 – 120	110 – 140
Installation depth (m)	50 – 65	60 – 80	75 – 100	90 – 120
Wing span (m)	8.00	10.0	12.0	14.0
Weight (tonnes)	2	4	7	11
Devices / km^2 (-)	50	30	25	16
Power / m^2 (W/ m^2)	5.50	6.60	12.5	13.6
Estimated swept area (m^2)	5700	8840	11400	19000
Estimated P_d (W/m^2)	19	24	44	45
Estimated rotor C_p (-)	0.28	0.29	0.30	0.31

radius, resulting in the very low values shown. In practice, the swept area is likely to be much smaller than this.

In water depths appropriate for the technology, tidal kites appear capable of producing great amounts of power for the size of their rotors. The devices are also likely to be easy to maintain, given that the kites can be detached from their tethers and floated to the surface for easy recovery. In shallow waters, however, the requirement to sweep through a large vertical area to reach a speed necessary to generate their power output is likely to make them rather unfeasible.

2.4 Hydraulic ram pumps

Hydraulic rams are cyclic water pumps that were first developed during the 18th and 19th centuries (Young, 1995), and are still employed today in rural and remote locations due to their reliability and lack of moving parts. Although they are not a conventional tidal power device, it was suggested during the early stages of this research to use them for pumping water into storage. The stored water could then be released across turbines later on, generating power as desired.

Hydraulic rams work by using water at one head to propel a smaller amount of water to a much greater head, without any need for an external fuel supply (Mohammed, 2007). A basic overview of their mode of operation is provided in Figure 2.17. Water enters the drive pipe at the inlet (1) and flows all the way to the waste valve (4). The drag force of the water acting on the valve (2) causes it to slam shut, which changes the momentum of the water within the drive pipe. This generates a pressure surge known as a water hammer (see Section 2.4.1 below), which opens the delivery valve (5) and forces water into the delivery pipe. The excess pressure is contained within the pressure chamber (6), which features a bleed valve to ensure there is a cushion of air within.

As water leaves the system through the delivery pipe, the pressure inside begins to diminish. Some of the pressure propagates up the drive pipe to the inlet, causing the flow into the system to reverse. This reduces the pressure within the system to such an extent that the delivery valve closes and the waste valve reopens, enabling the process to begin again. The valves are therefore the only moving parts in the entire device.

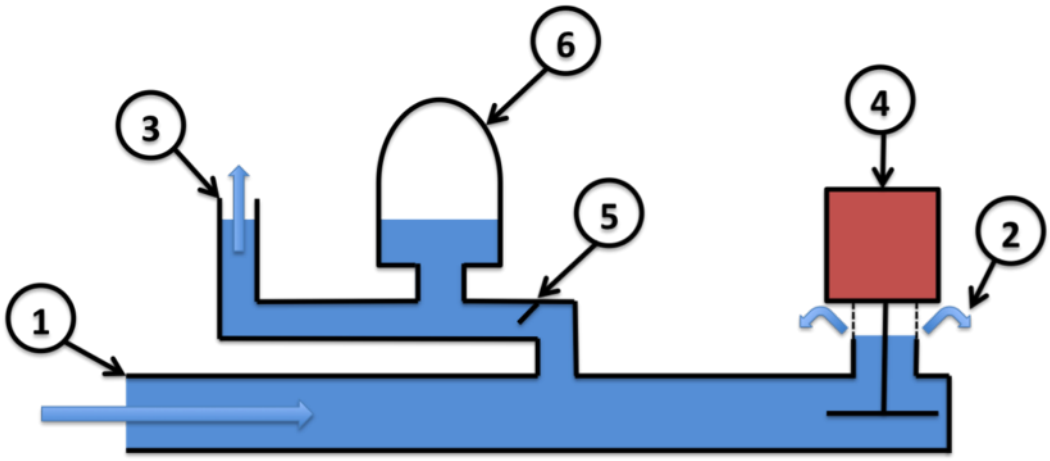

Figure 2.17: Overview of hydraulic ram pump operation.

2.4.1 The water hammer effect

Hydraulic ram pumps operate using the water hammer effect, a time varying pressure surge that occurs when a fluid experiences a sudden change in momentum (Chaudhry, 2014). The water hammer typically occurs in pipelines when valves are closed rapidly, and can create excessive high or low pressures capable of damaging or even destroying a hydraulic system (Bonin, 1960). As a result of this destructive potential, the water hammer is generally regarded as problematic, and much work has been done on minimising and mitigating its effects, such as developing surge tanks and spring loaded check valves to slow valve closures (Ghidaoui et al., 2005).

A basic description of the water hammer is provided by rigid water column theory; the following derivation is based on that found in Stephenson (1984). If there is a pressure difference Δp between the upstream and downstream ends of a pipe of cross-sectional area A and length l, the fluid within will experience a net force:

$$F = (p_u - p_d)A = \Delta pA \tag{2.18}$$

Assuming that the fluid is incompressible, this pressure difference can be related to the change in momentum experienced by the water through Newton's Second law:

$$\Delta p = \rho l \frac{\mathrm{d}v}{\mathrm{d}t} \tag{2.19}$$

Equation 2.19 shows how any abrupt changes in the flow speed within a pipe will generate a corresponding change in pressure. Accelerating the flow will produce a positive pressure difference, meaning the downstream pressure has become smaller than the upstream pressure (since Δp is defined as $p_u - p_d$). Conversely, a deceleration in the flow will result in a negative pressure difference, meaning the downstream pressure has increased. Both instances

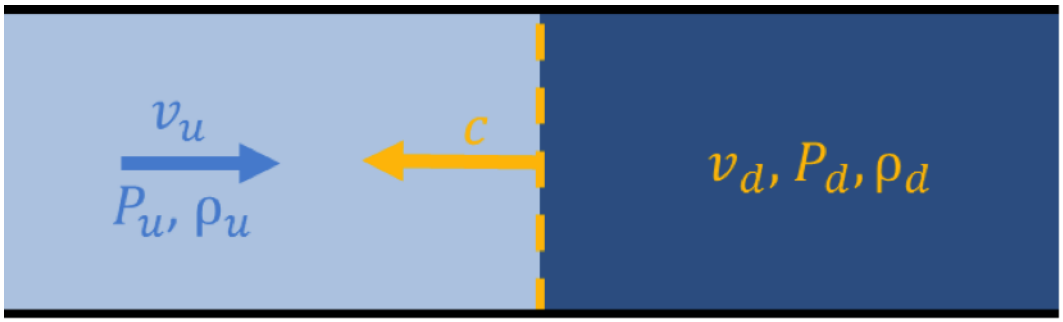

Figure 2.18: Propagation of excess pressure up pipeline. Adapted from Apsley (2013).

can occur due to valve operations; opening a valve will accelerate the flow, while closing a valve will decelerate it, with the magnitude of both depending upon the time required for the valve to complete its operation.

In reality, the excess pressure Δp will propagate through the pipeline at a speed c Chaudhry (2014), as illustrated in Figure 2.18. The front of the wave is known as the shock, and the properties of the fluid change as it passes across this region, becoming $v_d = v_u + \Delta v$, $p_d = p_u + \Delta p$ and $\rho_d = \rho_u + \Delta\rho$ (Chaudhry, 2014).

The speed c of the pressure surge is dependent upon the elasticity of the fluid and whether the pipeline can be considered rigid. The compressibility of a material is described by its bulk modulus K, which relates how much the material will be compressed when subject to a change in pressure Δp. The bulk modulus can be expressed in terms of either volume V or density ρ:

$$\Delta p = K\frac{\Delta V}{V} = K\frac{\Delta\rho}{\rho} \tag{2.20}$$

If the fluid is only slightly compressible, the increase in mass of a control volume due to changing density will be negligible. Equating the upstream and downstream mass flow rates from the reference frame of the shock therefore allows conservation of mass to be considered:

$$\rho_u A(v_u + c) = (\rho_u + \Delta\rho)A(v_u + \Delta v + c) \tag{2.21}$$

Assuming that $v_u + \Delta v \ll c$, this can be rearranged to find Δv:

$$\Delta v = -\frac{\Delta\rho}{\rho_u}c \tag{2.22}$$

Applying Newton's second law across the shock allows conservation of mo-

mentum to be considered:

$$(p_u - p_d)A = -p_u(v_u + c)A\Delta v \tag{2.23}$$

Assuming that $v_u \ll c$ (which will typically be the case for water and other liquids) and rearranging shows that:

$$\Delta p = -\Delta v_u \rho_u c \tag{2.24}$$

Equation 2.24 is commonly known as the Joukowsky equation (Joukowsky, 1900; Tijsseling and Anderson, 2004), and shows that, for a compressible fluid, the magnitude of a pressure surge is still dependent upon any change in flow speed.

Substituting Equations 2.23 and 2.24 into the density form of Equation 2.20 allows the calculation of the speed of the pressure surge in a rigid pipeline:

$$-\Delta v \rho_u c = -K\left(\frac{\Delta v}{c}\right) \tag{2.25}$$

$$c = \sqrt{\frac{K}{\rho_u}} \tag{2.26}$$

Any deformation of the pipe will absorb some of the energy of the pressure surge and reduce its speed, however. The rigidity of the pipe walls must be considered to find the change in the area of the pipeline ΔA. This is dependent upon the diameter D, wall thickness e and Young's modulus Y of the pipe, as well as the pressure acting upon it:

$$\Delta A = \frac{AD\Delta p}{Ye} \tag{2.27}$$

Considering conservation of mass when the pipe area varies across the shock:

$$\rho_u A(v_u + c) = (\rho_u + \Delta\rho)(A + \Delta A)(v_u + \Delta v + c) \tag{2.28}$$

Rearranging Equation 2.28 (again assuming that $v_u + \Delta v \ll c$) and neglecting the second order terms shows that:

$$\frac{\Delta v}{c} = \frac{\Delta A}{A} + \frac{\Delta \rho}{\rho_u} \tag{2.29}$$

Hence, from Equations 2.20, 2.23 and 2.30:

$$\frac{\Delta p}{\rho c^2} = \frac{D\Delta p}{Ye} + \frac{\Delta p}{K} \tag{2.30}$$

$$c = \sqrt{\frac{1}{\rho\left(\frac{D}{Ye} + \frac{1}{K}\right)}} \tag{2.31}$$

Equation 2.31 describes the speed that the pressure surge will propagate up a non-rigid pipeline. This can be used to determine the time required for the pressure surge to travel from the valve to the pipe inlet:

$$t = \frac{l}{c} \tag{2.32}$$

When a surge reaches the inlet, the pressure within the pipe itself is greater than the external pressure. This forces the flow to reverse, causing the pressure within the pipe to drop as flow leaves the system. The pressure surge is then reflected and travels back to the valve, whereupon the pressure in the pipe will be equal to the external pressure. Flow will still be leaving the system, however, and the pressure will therefore fall further, creating a negative pressure surge that returns to the inlet. This process of reflection and alternating between positive and negative pressure continues until the excess energy of the pressure surge is dissipated due to friction (Chaudhry, 2014).

2.5 The Water Hammer Energy System

Although the idea of using hydraulic rams to pump water into storage was not considered feasible (due to the size of the reservoir that would be required to generate meaningful amounts of power), it was realised at the same time that the principle behind their operation could be adapted to generate power directly from water hammer pressure surges. Figure 2.19 provides an overview of how such a system (hereafter referred to as the Water Hammer Energy System, or WHES) would operate. Reviewing the literature indicates that such a system would be a novel method for generating either mechanical or electrical power from a fluid.

The WHES effectively consists of an upturned T-shaped section of pipe with a valve located at the downstream end. In a similar fashion to a hydraulic ram pump, water enters the system at the inlet and flows down the drive pipe and through the check valve, eventually causing it to close. This reduces the momentum of the water still within the pipe, creating a pressure surge that propagates back up the drive pipe towards the inlet. This causes the water level within the vertical section of pipe (hereafter referred to as the chamber) to rise to some maximum value as the pressure wave passes underneath.

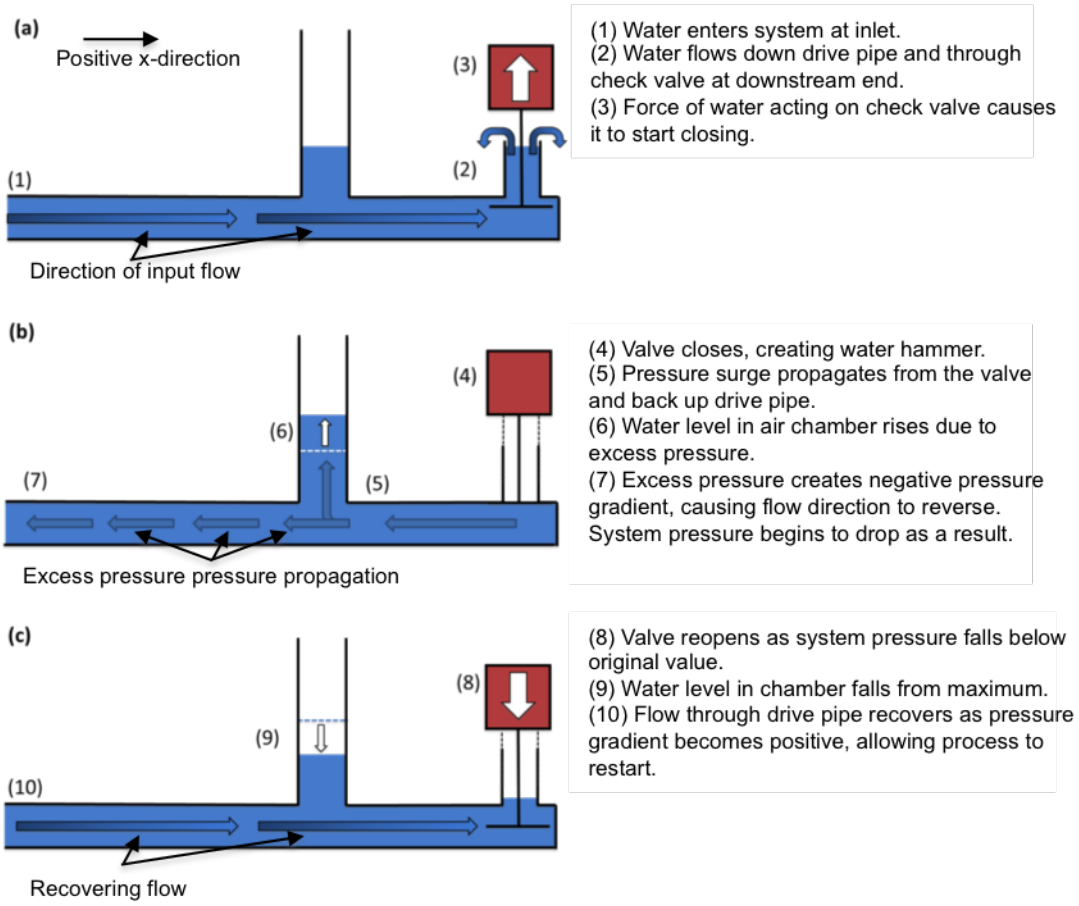

Figure 2.19: Mode of operation of the Water Hammer Energy System.

When the surge reaches the inlet, the pressure within the pipe will be greater than that outside, creating a negative pressure gradient. This forces water to flow out the drive pipe through the inlet and the pressure wave is reflected back towards the valve, in accordance with the discussion of the water hammer in Section 2.4.1. When the pressure within the system falls sufficiently, the check valve reopens, which permits the flow through the drive pipe to recover and the process to restart. In this way, vertical oscillations can be generated from a horizontal flow of water.

Energy can be extracted from these oscillations using a variety of techniques. Several methods are already employed by wave energy convertors (WECs), which harness the energy of ocean surface waves for electricity generation. Devices such as oscillating water columns (OWCs) (Heath, 2012) and heaving bodies (Waters et al., 2007) generate power from a similar vertical movement of water.

Figure 2.20 illustrates three proposed methods of generating power using the WHES. The first method (Figure 2.20a) is virtually identical to that employed by an OWC, as the vertical motion of the water in the chamber would

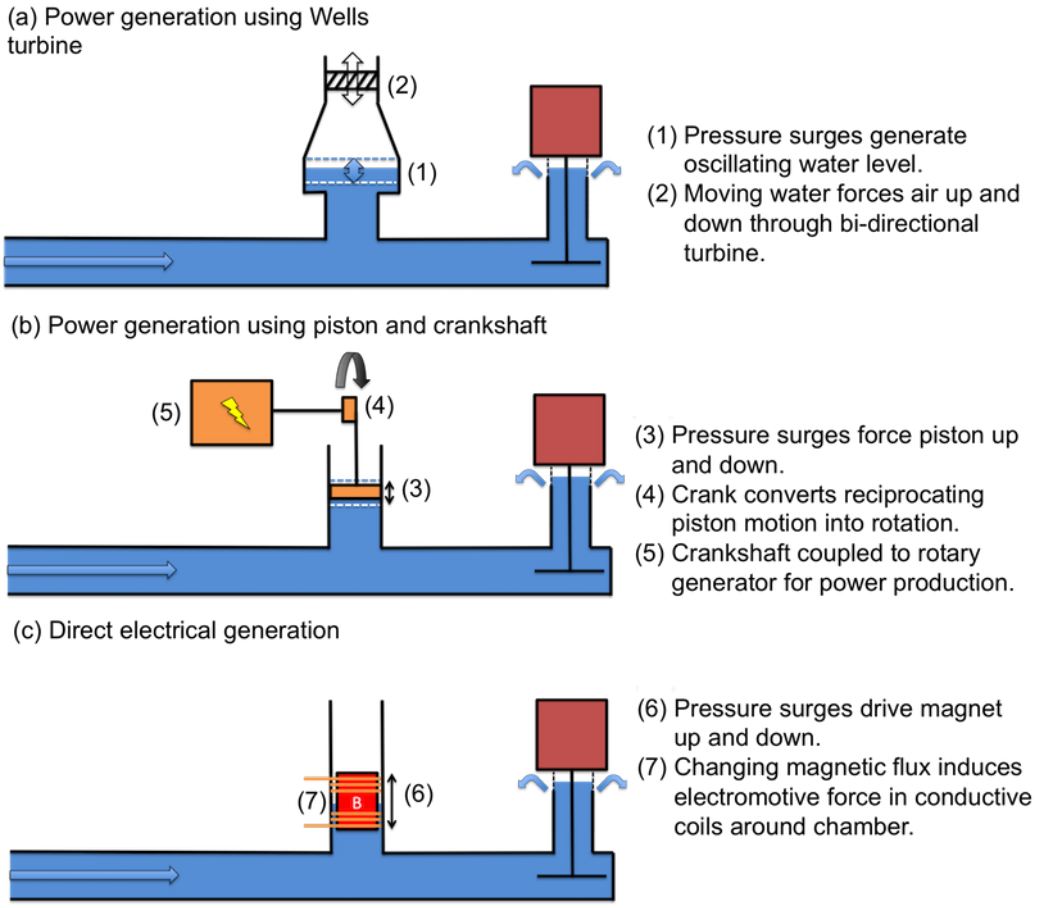

Figure 2.20: Methods of generating power from the WHES.

pump the air above back and forth across a turbine Evans and Porter (1995). Many OWC designs feature a bi-directional Wells turbine that is combined with an induction generator to minimise the efficiency losses that occur in mechanical power transmission (Heath, 2012). This serves to limit the number of moving parts, improving reliability and ease of maintenance.

The electrical power output of an OWC depends upon the amount of energy absorbed from the incident waves and the efficiency of its conversion into electrical energy (Falcão, A., 2002). Viscous effects in the water within the chamber, such as the formation of vortices and sloshing Zhang et al. (2012), are a major factor in efficiency. The aerodynamics of the turbine, bearing friction and electrical resistance also effect the power output of an OWC. It is reasonable to assume that these factors would also govern the efficiency of a WHES driving an air turbine.

In the second power generation method (Figure 2.20b), the pressure surges of the WHES are used to drive a piston up and down. The piston is connected to a crankshaft via a connecting rod, turning the reciprocating motion into rotary motion that could is used for useful work. Multiple devices may be

attached to a single crankshaft to increase power if desired. The crankshaft can then be used to drive a generator or provide mechanical power. The effectiveness of a piston and crank will depend upon the amount of pressure generated by the WHES, which will govern the force applied to the piston and hence the torque on the crankshaft. The frequency of the valve closures will also be an important factor.

The third method (Figure 2.20c) is a linear alternator. A floating magnet is positioned inside the chamber using a float, with coils of conductive wire wound around the exterior. The oscillating water level inside the chamber would then propel the magnet up and down, varying the magnetic flux Φ_B cutting through the wire and inducing an electromotive force ξ in accordance with Faraday's law of induction. For a tightly wound coil with N turns of wire, this is given by:

$$\xi = -N\frac{\mathrm{d}\Phi_B}{\mathrm{d}t} \tag{2.33}$$

From Faraday's law, the effectiveness of this method would primarily depend upon the strength of the magnet and the speed with which it could be forced up and down.

Regardless of their potential efficiency, all three methods allow the power take-off subsystem of a WHES device to be above water. This would enable the device to access shallow waters and would also serve to simplify maintenance work, since the valve would be the only moving component located underwater. The fact that the crank could provide both electrical and mechanical power makes it a particularly useful option; however it is also likely to be the most complex given it requires the most moving parts.

From Equations 2.19 and 2.24, the magnitude of the pressure generated by the WHES will be proportional to the change in momentum experienced by the water, rather than the flow speed itself. Although the maximum momentum change will be dependent upon the flow speed, this suggests that the device should be capable of functioning reasonably well in low input conditions. These two advantages combined may make the WHES a suitable method for generating pico scale power from low input, shallow water sites.

2.6 Technology discussion

There are various criteria that will govern the success of a pico scale deployment in low input, shallow water conditions. These include:

- Power density: how much power a technology can generate for its size.

- Scalability: the ability to increase the size of a device within the confines of shallow waters to reach a desired power output.
- Durability: the ability of a device to survive for prolonged periods of time within the marine environment.
- Maintainability: the ease with which a technology can be maintained and repaired.
- Economic potential: the cost of construction, maintenance and decommissioning a technology and whether it is financially attractive for the level of energy it provided.
- Environmental impacts: the scale of the effects a given technology has on its surrounding environment.

Of the various technologies discussed in this chapter, tidal range devices arguably have the worst power density. This is partly because they are characterised by relatively low levels of efficiency in comparison to tidal stream devices, and partly because their power is proportional to tidal range squared, rather than flow speed cubed. The will consequently need relatively large basins to generate a given amount of power. This size requirement will serve to increase not only construction and decommissioning costs, but also the magnitude of their environmental impacts, and indicates that barrages and lagoons are not as appropriate for pico scale generation as tidal stream devices. The main advantages small scale range schemes would have over tidal stream is durability and ease of maintenance. This is illustrated by the projected 120 year lifespan of the Severn Barrage, which is six times the 20 year design life of the MCT SeaGen tidal turbine (Kelly, K., McManus, M. and Hammond, G., 2012).

In contrast, an efficient hydrokinetic device designed to operate in low speed waters will likely possess lower capital and environmental costs, improving economic potential over tidal range schemes. Given the constraints that shallow waters place on maximum device size, some tidal stream technologies appear more suitable than others. Tidal kites require extremely deep waters to operate effectively, for example. Although they target relatively low flow speeds compared to other devices, they require a large amount of space to sweep through, which reduces their power density. One advantage they do possess is the ability to be easily detached and recovered on the surface. This would make them significantly easier to maintain than a bottom mounted turbine.

Ducted turbines are also deemed unsuitable for shallow water generation. Although ducts are designed to accelerate the flow through the rotor and

thus improve power output, the extra space they require is likely to negate the benefits of improved rotor efficiency. Given the constrains shallow waters impose on maximum device size, this limits the scalability of a ducted device. Ducts do offer some benefits, including an element of protection to the rotor and improved efficiency in yawed flow, however an efficient unducted device will capable of generating just as much, if not more, power than a ducted design.

Axial flow turbines are a well developed and understood technology and can extract energy from a flow with a high efficiency. They are not without their limitations, however. The fact that they sweep through a circular area limits their maximum size and output in shallow water locations, making them less capable of exploiting blockage effects.

Oscillating hydrofoils have been described as suitable for shallow water deployments as they sweep through a rectangular swept area. They can be stretched laterally across the water column to increase size and (depending upon the site) blockage ratio, to boost power output if required. Dual-wing oscillating hydrofoils also extract energy from the flow twice (lift is generated at both the upstream and downstream wings, contributing to the power that is generated), enabling them to reach a higher theoretical efficiency limit than axial turbines in unbounded flows.

Despite this, the efficiency of oscillating hydrofoils is somewhat debatable. Cross flow turbines, which also sweep through a rectangular area and can be designed to exhibit large C_p values, are therefore likely to be the most effective of the current tidal stream technologies for generating pico scale power from low input, shallow waters. Although difficult to manufacture, helical blades improve the durability and efficiency of a cross flow turbine over a conventional Darrieus design without the need for mechanically complex pitch control systems. Given that blockage is likely to be a factor in a shallow water deployment, an effective design should also be of a reasonably high solidity to further increase the power captured from the flow.

In comparison to these devices, the WHES is a relatively unknown quantity. The power-take off can be located above the water surface, reducing the impact shallow waters would have on its maximum size while permitting easier maintenance work. Depending upon the power take-off, it would also have relatively few moving parts under the water. This could make it a relatively durable design, as exemplified by the fact that hydraulic ram pumps can operate for years without requiring maintenance work.

The power density, economic potential and environmental impact of such a device, however, are complete unknowns at this stage. The fact that water

hammer pressure surges depend upon the change in fluid momentum, rather than the initial momentum itself, indicates that the device may be capable of functioning effectively in low input conditions. Whether it is economically viable will depend upon the amount of energy that can be extracted from the generated pressure surges. In terms of environmental impacts, the most serious is likely to be underwater noise, given that the system is generating pressure surges. The severity of these impacts will depend upon how the excess pressure dissipates once it leaves the system at the inlet, and the effectiveness of any methods designed to minimise its effect.

2.7 Review conclusions

In this chapter, the state of the art of tidal power has been reviewed and the suitability of various tidal power technologies for pico scale generation in shallow water, low input conditions discussed. While there is a wide range of technology available, not all of it is appropriate for the criteria of interest.

For example, even though tidal range devices can generate power independently of water depth and flow speed, they are likely to require large basins that will increase their capital and environmental costs, rendering them less suitable than a smaller, efficient hydrokinetic design. Among the tidal stream technologies, dual-wing oscillating hydrofoils and cross flow devices appear the most suitable. Both are capable of extracting energy from the flow twice, enabling them to reach a higher efficiency limit than other tidal stream designs and thus generate more power from their size. Both also sweep through a rectangular area, meaning their maximum size would not necessarily be constrained by water depth. The low efficiency values exhibited by current commercial oscillating hydrofoils suggests that cross flow turbines are the most appropriate of the current mainstream technologies, however.

In addition to these devices, the Water Hammer Energy System has also been introduced. The WHES is speculated to have several desirable features from a design point of view, including an above surface power take-off and an ability to generate power independently of flow speed. Whether it is an appropriate device or not, however, will depend upon the magnitude of the power it can generate.

As a result of its perceived advantages and its novel nature, it was decided to investigate and develop the WHES to identify whether or not it is a suitable system for generating pico scale hydropower. This was to be achieved using a mixture of experimental and theoretical methods to identify the behaviour of the device, demonstrate it is capable of generating power and quantify its

hydrodynamic efficiency. This information would then be used to assess how much energy it could provide if operating in a range of input conditions.

Chapter 3

Experimental investigation of WHES

In Chapter, 2 the state of the art of tidal energy was reviewed and the Water Hammer Energy System was introduced. Its potential for generating hydropower from low input conditions (including the ability to access shallow waters and the potential to generate power independently of flow speed) was outlined and compared with that of conventional tidal devices.

Given its novelty and potential advantages, it was decided to investigate the WHES through a mixture of physical experimentation and mathematical modelling. The purpose of these studies was to identify the behaviour of the device, quantify its efficiency, demonstrate that it can generate power and evaluate how much energy it might be capable of providing.

This chapter presents the methods and results of the physical experiments that were conducted to assess the hydrodynamic behaviour of the system. The aim of these experiments was to:

- Study the oscillations generated by the system and measure the power available from them.
- Identify the variables affecting system performance and provide information for designing an optimised device.

To achieve these aims, a small scale test rig was constructed from standard PVC pipe fittings and subjected to a series of tests in laboratory conditions. The test rig was driven by a static head of water from a reservoir, and its performance was assessed by tracking the motion of objects within the chamber as they were driven by the vertical oscillations. This enabled the velocity, acceleration, force and power of the objects to be calculated and thus the performance of the test rig to be assessed. The results and conclusions of

these experiments inform the mathematical studies presented in Chapter 4 and the design of the power take-off systems discussed in Chapter 5.

3.1 Methodology

3.1.1 Experimental set-up

To study the oscillations generated by the WHES and to identify the variables affecting its performance, a small scale system was constructed using threaded PVC British Standard pipe components. This type of pipe was chosen as it is relatively cheap and facilitated rapid construction and easy modification. The pipe used in the scale model had an outer diameter of 20 mm and an internal diameter of 16 mm.

The flow into the test rig was provided by a static head of water from a reservoir situated 345 mm above the level of the valve, as illustrated in Figure 3.1. The reservoir, which had a maximum capacity of 0.084 m^3, was connected to the model via a 1 m long PVC hose pipe of the same diameter as the rigid pipe. A ball valve was positioned between the reservoir and the hose to control the input flow into the system. The water level within the reservoir was set to between 165 and 225 mm before the beginning of each test run, providing a total input head of 510 – 570 mm. This was not kept constant over the course of a test run, however, meaning the input head and flow rate into the scale model gradually diminished with time during each test.

A threaded 3/4 inch brass swing-check valve was positioned vertically at the downstream end of the system to generate the water hammer pressure surges. The discharge from the valve was directed into a 0.015 m^3 bucket that served as a sump via an elbow and a hose barb. A 1 m length of 20 mm diameter clear PVCu pipe (again with an internal diameter of 16 mm) was used as the vertical chamber. This allowed a 13 mm diameter wooden float, which was painted bright red, to be visible when placed inside.

The test rig was attached to a white wooden back board using pipe clips, to create a contrast between the float and its surroundings. Motion tracking was used to capture the behaviour of the float and measure how its position varied as a function time during test runs. This was felt to be an advantageous method since the behaviour of the system was not interfered with in any way during testing. During the latter stages of the experiments, the float was replaced by a piston of 15 mm diameter to capture more of the pressure generated by the valve closures. A photograph of the test rig is shown in Figure 3.2.

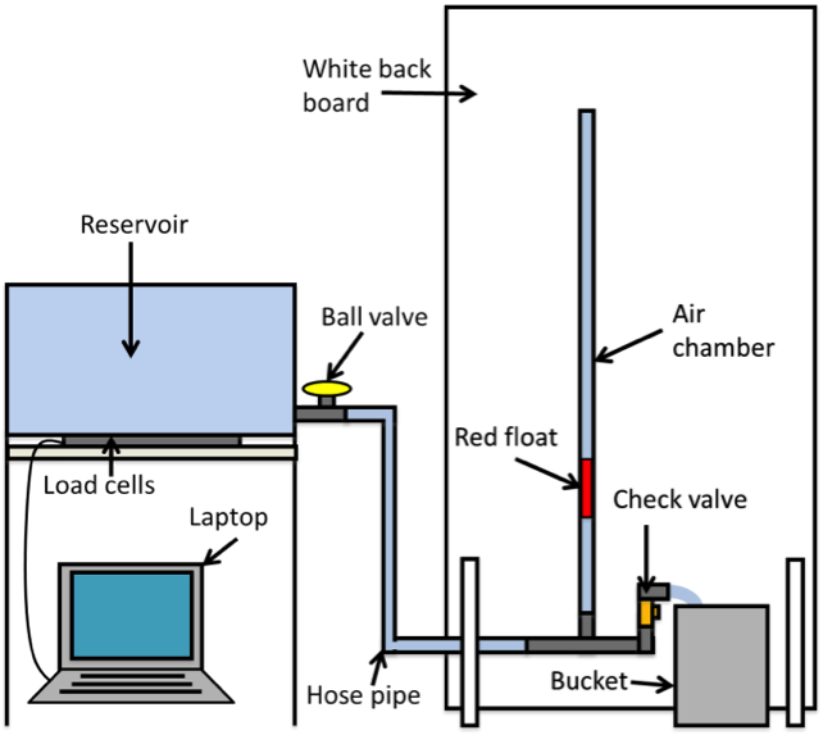

Figure 3.1: Experimental set-up for the system characterisation tests.

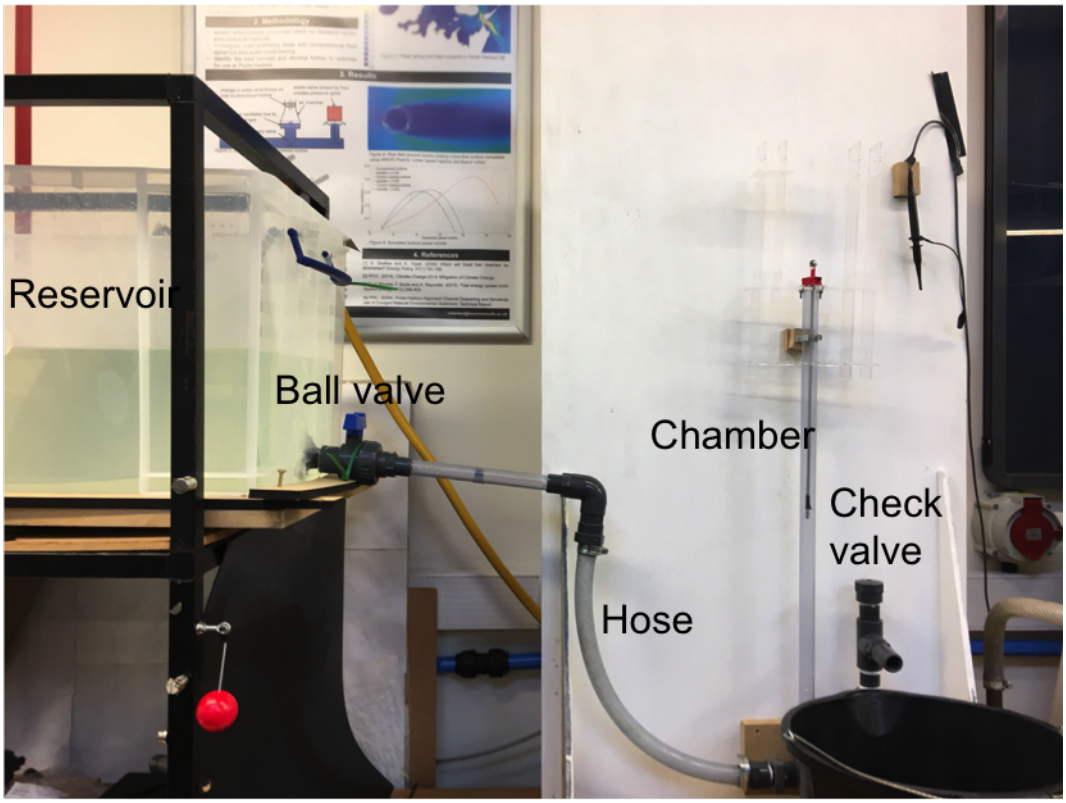

Figure 3.2: Photograph of the test rig used for the system characterisation tests.

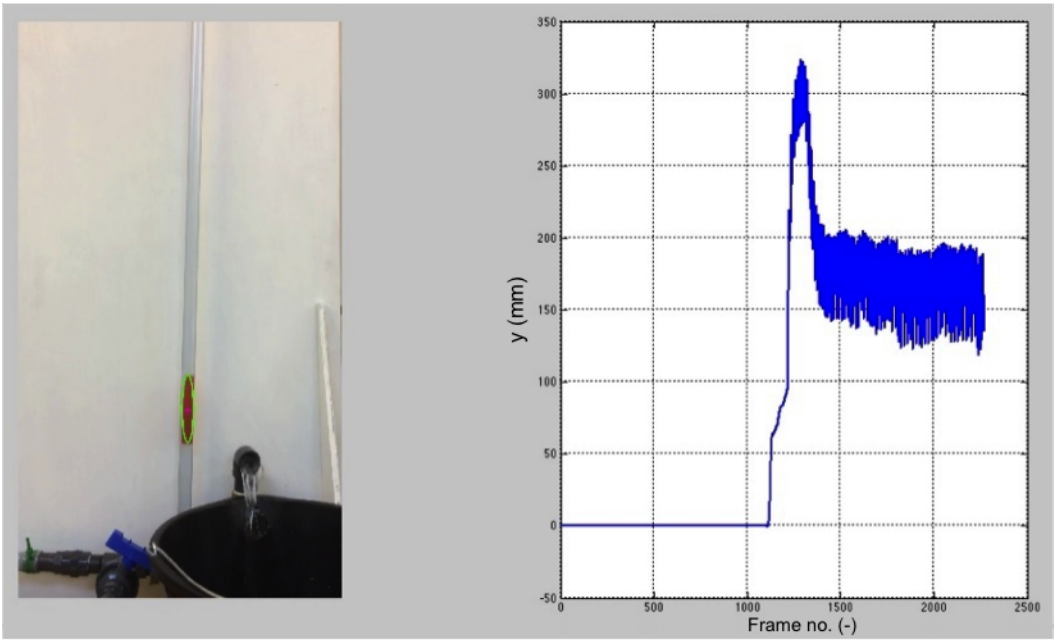

Figure 3.3: Screenshot showing the MATLAB program extracting position data from a particular test run.

A 1280 x 720 pixel high definition camera operating at 240 frames per second (i.e. a sample rate of 240 Hz) was positioned directly in front of the test rig and used to film each test run. The videos were later processed with a motion tracking program in MATLAB (MathWorks, 2015). This program was written at Bournemouth University and has previously been used successfully for measuring leg motion in a gait analysis study (Aslani et al., 2016). Figure 3.3 shows a screenshot of the motion tracking program in operation, including the test rig as seen from the position of the camera.

Four half bridge load cells were used to determine the mass of the reservoir as a function of time and hence calculate the flow rate into the test rig. The load cells were positioned underneath the reservoir and connected to an Arduino Uno micro-controller (Arduino LLC, 2017). This was connected via a USB cable to a laptop computer that served as a data logger.

The load cells consisted of a half Wheatstone bridge electrical circuit, and measured the changing resistance of two strain gauges as they are deformed under a load. An example circuit diagram for a half Wheatstone bridge is provided in Figure 3.4. The resistance of the upper (tension) and lower (compression) strain gauges is signified by R_u and R_l; R_W indicates the resistance of the wires within the circuit itself, R_1 and R_2 are completion resistors of known resistance, and V_{ex} and V_{out} signify the excitation and output voltages.

Each of the cells used for the flow rate sensor could operate individually under anything up to a maximum load of 50 kg. Combining them together

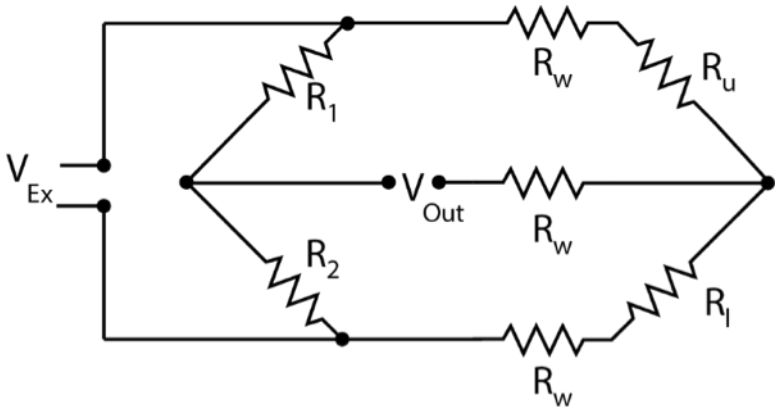

Figure 3.4: Circuit diagram of the half Wheatstone bridge used by the load cells.

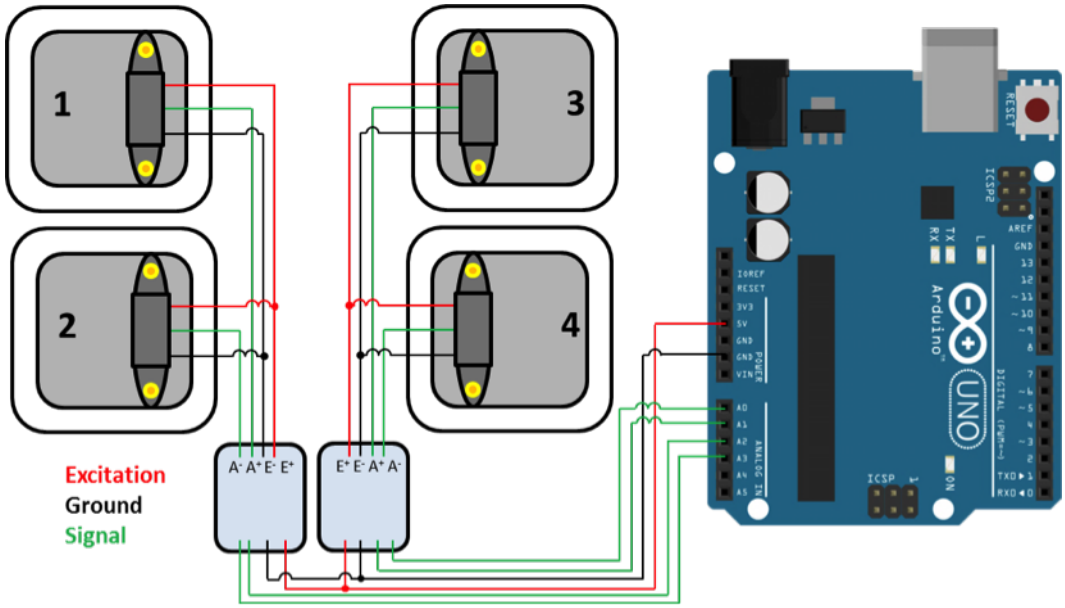

Figure 3.5: Illustration showing the four load cells connected to the Arduino UNO micro-controller via the two HX711 ADCs. The Arduino image was sourced from Werkstatt Workshop (2016).

according to the diagram shown in Figure 3.5 enabled measurements of up to 200 kg. This upper limit is greater than the maximum mass of the reservoir, which was 84 kg if completely filled with water.

As shown in Figure 3.5, the Arduino Uno micro-controller was used to supply an excitation voltage to the load cells while simultaneously measuring their output. An Arduino Uno board can safely handle up to 5 V and features 14 analogue input pins that can be read at up to 10 kHz (Arduino LLC, 2017). The board also features a 10 bit analogue to digital converter (ADC), which enables it to convert an input voltage into a numerical value between 0 and 1023, yielding a precision of 4.9 mV by itself. This was improved upon by connecting two 24 bit HX711 ADCs between the load cells and the Arduino

board. These converted the output voltage from the load cells into a number between 0 and 2^{24}, resulting in an uncalibrated measurement resolution of approximately 300 nV.

The Arduino was connected to a laptop computer via a USB cable. A computer program, written in C, was uploaded to it so that the signal voltages from the load cells could be read and output to the laptop via the serial port. A second program, written in MATLAB, was used to log the values reported by the Arduino and convert them into mass measurements using calibration data. The MATLAB program also determined the time at which the voltages were recorded so that mass flow rate could be determined later. The codes are provided in Appendix A.

3.1.2 Instrument calibration

Motion tracking

To account for the angle and position of the camera relative to the float, two calibration videos were recorded in addition to the test runs themselves. These were analysed prior to the test run videos so that the motion tracking program could be calibrated for the position of the camera.

The first of these calibration videos involved filming a black and white chequerboard, consisting of 25 mm wide squares, while it was being rotated in 3 dimensions. The calibration code tracked the position of the vertices of each square, measuring how the apparent distance between them varied from frame to frame. By relating this apparent distance to the real distance of 25 mm, a correction factor was calculated for each pixel and applied to all subsequently analysed videos to convert pixel position into length.

Following this, a second video was recorded in which a red object was moved vertically up and down in fixed intervals of 25 mm. This video was then analysed to identify a second linear correction factor to ensure vertical position was measured correctly. These calibration methods resulted in a maximum measurement uncertainty of $\pm$ 0.2 mm for pixels in the central region of the video (corresponding to where the float was located), with the maximum uncertainty growing to $\pm$ 0.8 mm at the video edges.

Load cells

To calibrate the load cells, the raw signal values from the Arduino were recorded as water was gradually added to the reservoir in measured intervals of 3 kg. A funnel and hose pipe were used to minimise both sloshing and the impact of the water influencing the voltages output by the load cells.

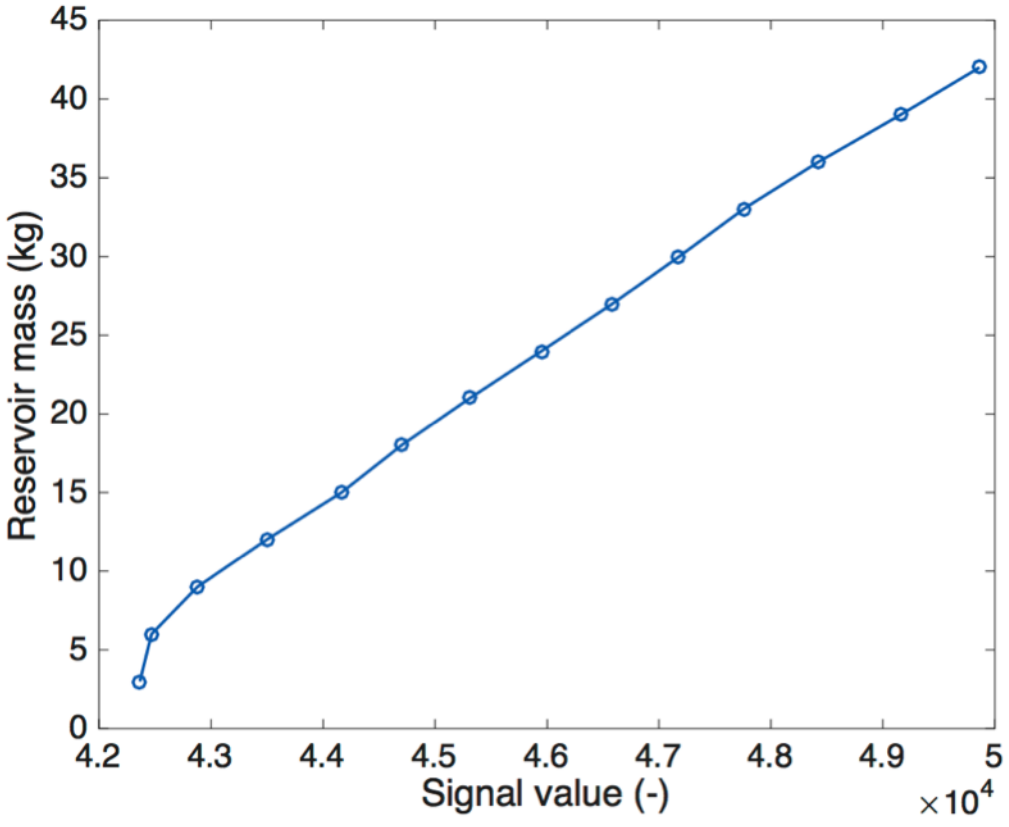

Figure 3.6: Reservoir mass as a function of load cell signal.

Figure 3.6 illustrates the mass of water within the reservoir as a function of the values reported by the Arduino during this calibration, and shows that the relationship between mass and output signal is broadly linear above 9 kg.

This information allowed the relationship between the load cell signal and the mass of water within the reservoir to be determined, and thus the signal values to be converted into kg. Once this was done, water was released from the reservoir and allowed to flow into the sump. The mass of the water within the sump was measured using laboratory scales with a precision of 100 mg, and the figures were compared to the total change in mass measured by the load cells. This process was repeated 5 times, allowing an additional small correction factor to be determined. To account for any drift in the values reported by the sensor due to changes in temperature and the cells being constantly under the load of the reservoir, this second calibration procedure was repeated before each new series of experiments were conducted.

3.1.3 Experimental schedule

The aim of the experiments presented in this chapter was to characterise the performance of the test rig and identify how different variables govern its hy-

drodynamic behaviour. Initially, the motion of an 8.9×10^{-3} kg mass float was measured so that its velocity, acceleration, force and power could be determined. 10 separate test runs were conducted, with the angle of the ball valve regulating the flow into the system reduced from one run to the next to alter the input conditions.

Following this, the test rig was used to drive 3 different wooden floats of equal diameter but different mass (4.5×10^{-3}, 8.9×10^{-3} and 13.9×10^{-3} kg, respectively) so that the effect of float mass and size on power output could be investigated. Again, 10 test runs were conducted per float, with the angle of the ball valve altered from one run to the next to change the input flow. The 8.9×10^{-3} kg float was tested a second time so that the data was collected over the same period, to account for any variations in light levels and small changes in camera position and calibration.

After these tests, the input into the system was further varied by adjusting the reservoir head in 30 mm intervals. The motion of the 4.5×10^{-3} kg float was recorded in each of these input heads, so that their effect on system performance could be determined. Lastly, the floats were replaced by a 0.015 kg piston, with a red marker on its upper end as shown in Figure 3.7. The piston was made from laser cut acrylic discs of 15 mm diameter that were pressed onto a 4 mm diameter aluminium rod. Unlike the float, the piston discs were wide enough to capture almost all of the pressure generated by the valve closures. To prevent it from sinking, the piston was held in place using the acrylic structure of the piston-crank discussed in Chapter 5, sliding on a plastic bushing to minimise friction.

For each of the test runs, the camera was operated for roughly 30 s, with the system oscillating freely for 15 s of this time. The experimental data was used for analysis was collected from this period of free oscillation. Each set of experiments was also repeated to check the validity of the results.

3.1.4 Data analysis

Following testing and calibration, the video files were processed in MATLAB to extract the raw data for the position y of the float against time t. An example image of the code in action is shown in Figure 3.3.

To minimise the effect of the diminishing input head during data analysis, the position data for each run were subdivided into 8.3 s windows (corresponding to 2000 data points at 240 FPS). The corresponding float velocity $\dot{y}$ and acceleration $\ddot{y}$ for each data window could then be computed via numerical

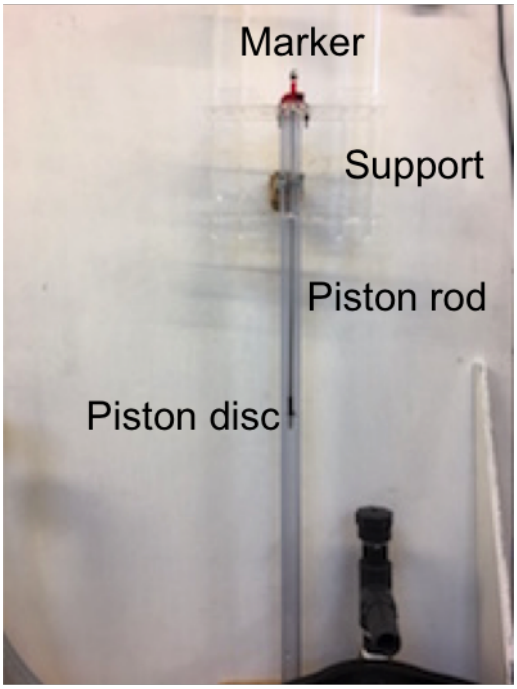

Figure 3.7: Uncoupled piston sitting in chamber.

differentiation:

$$\dot{y}(t) = \frac{y_t - y_{t-1}}{t_t - t_{t_1}} \tag{3.1}$$

Basic numerical differentiation using Equation 3.1 has the unfortunate drawback of amplifying any noise present in a signal, which will reduce the accuracy of the results. This is unavoidable, even if the data is filtered before it is differentiated. Regularising the differentiation process so that the computed derivative has some degree of smoothness provides better results (Chartrand, 2011). One method is total variation regularisation, which has the advantage of suppressing noise without suppressing real discontinuities in the signal. Chartrand (2011) offer a MATLAB algorithm to accomplish this, which is provided in Appendix B and used for the numerical differentiation of the data in this thesis.

The float velocity and acceleration were used to compute its vertical force and power:

$$F_y = m\ddot{y} \tag{3.2}$$

$$P = F_y\dot{y} \tag{3.3}$$

A peak analysis code (again written in MATLAB) was also employed to investigate the amplitude (a) and frequency (f) of the oscillations. The peak analysis function in MATLAB can identify the location and value of maxima and minima within a signal, which can then be used to determine the total amplitude and frequency of oscillations as well as any variation between the

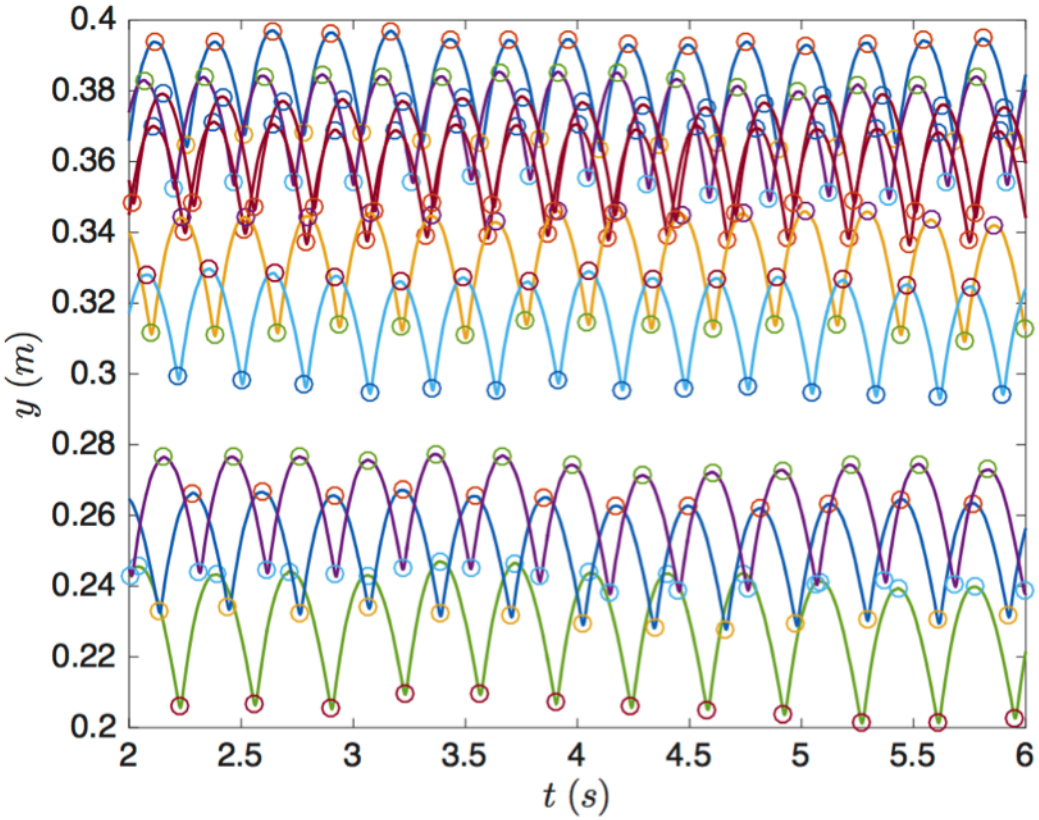

Figure 3.8: Maxima and minima of float oscillations as identified by peak analysis code for a range of different input head cases.

upstroke and downstroke. The peak analysis code, which is included in Appendix C, was embedded within a loop so that it could batch process a series of test runs in succession, as shown in Figure 3.8.

The position data windows were further analysed using a Fast Fourier Transform (FFT) algorithm, to investigate any harmonics within the position signal and their corresponding amplitudes and frequencies. Given the sample rate of 240 FPS and the 2000 data points in each sample window, the bin width generated by the FFTs was 0.120 Hz.

Meanwhile, the mass flow rate $\dot{m}$ through the test rig was calculated from the measurements of the reservoir mass. This was again achieved via numerical differentiation, with the difference in reservoir mass Δm from one reading to the next divided by the time difference Δt between the readings:

$$\dot{m} = \frac{\Delta m}{\Delta t} \tag{3.4}$$

3.2 Flow rate

An example of how the reservoir mass varied as a function of time is shown in Figure 3.9. The load cells were activated before the test run began, during which time they measured the mass of the reservoir for 30 s before taking an average to zero the measured data. Following this, the mass of the reservoir was logged at a frequency of approximately 11.5 Hz. The reservoir valve was opened at 8 s, creating the first vertical spike. After this point, the measured mass decreases as water flows into the test rig. The valve was adjusted for about 3 s, after which the water drained freely from the reservoir for a period of 15 s. Following this, the valve was shut at 25 s, creating a second spike in the mass signal. These are due to the force on the valve handle as it was turned, and are therefore useful for aligning the data recorded by the flow sensor to the position data recorded by the camera.

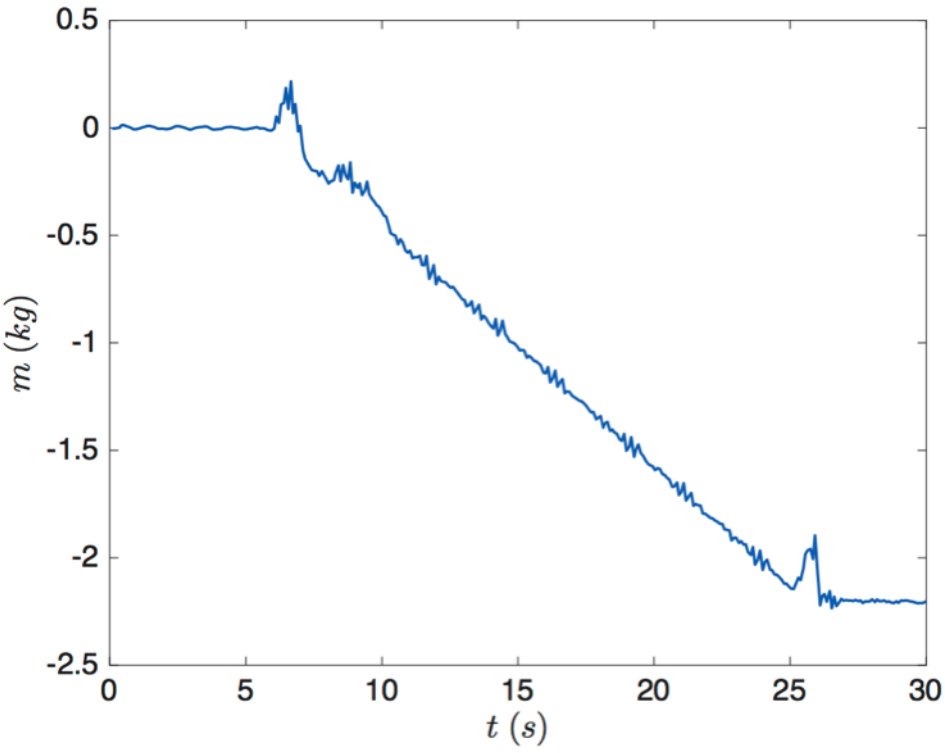

Figure 3.9: Example of the mass measurements recorded by the flow sensor over the course of a test run.

Following the valve closure, the flow sensor continued to measure the mass of the reservoir for a few seconds before it was deactivated. During this period, and prior to the valve being opened, a small wave like motion is visible in the mass-time data. This is due to a slight movement of the water within the reservoir, which is a result of refilling it after the previous test run and the

movement of the water as it flows out of the check valve.

Figure 3.9 shows that the variation in the reservoir mass was not constant while the valve was open, since smalls spikes can be seen in the data between 11 and 25 s. These occur because the discharge out of the system – and hence the flow out of the reservoir – vary due to the check valve at the downstream end.

This can be seen in the computed mass flow rate $\dot{m}$ out of the reservoir. Figure 3.10 illustrates $\dot{m}$ over the 11 – 24 s period of Figure 3.9 as calculated using Equation 3.4, and shows the oscillatory nature of the input flow rate due to the periodic check valve. Using an FFT algorithm to identify the frequency components, the frequency of the oscillations in Figure 3.10 was 3.63 Hz, which broadly corresponds to the 3.58 Hz chamber oscillation frequency for this test run.

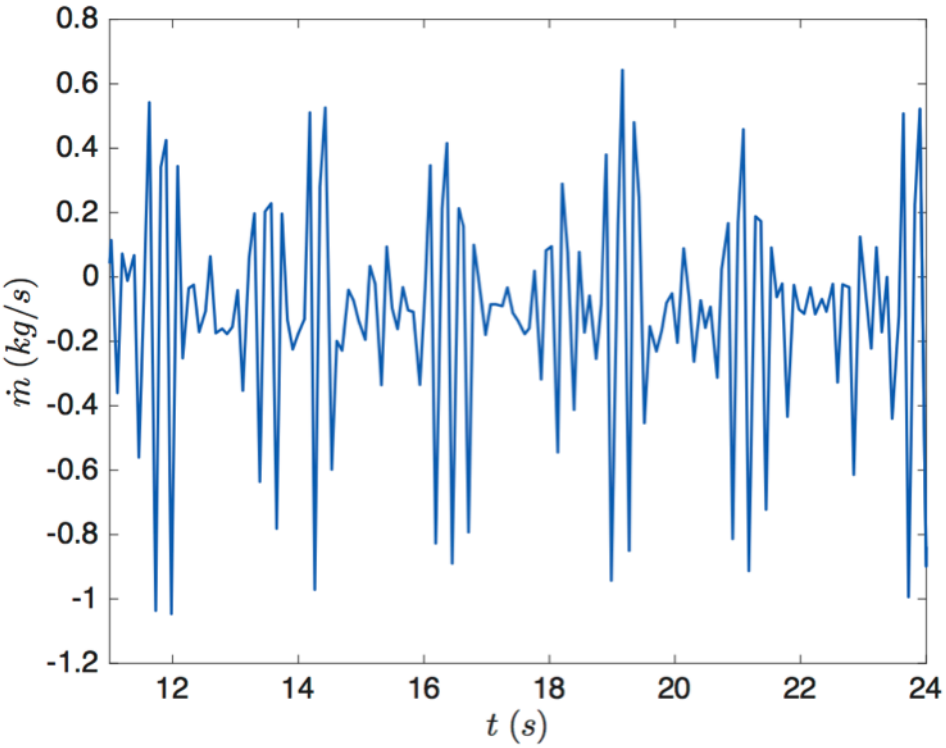

Figure 3.10: Computed mass flow rate during the 11 – 24 s period shown in Figure 3.9.

Their variation in $\dot{m}$ appears inconsistent, with periods of smaller and larger oscillations visible in the signal. This is due to the movement of the water within the reservoir from refilling it. Since the purpose of these experiments was to identify how the system is influenced by the input conditions (i.e. the mean flow rate), these variations were not deemed problematic. The variation in the flow rate through the system is studied in the mathematical investigation

of Chapter 4.

The mean flow rate ($\bar{\dot{m}}$) was calculated by dividing the mass-time data into the same 8.3 s windows as the position data for each test run. Linear trend lines were fitted to these data windows, and their gradient was taken as corresponding to the mean mass flow rate. Assuming the density of the water in the system to be constant at 998.2 kg/m^3 enabled the mean volumetric flow rate to be determined from mass flow rate. This could then be used to calculate the mean flow speed ($\bar{v}$) into the system. For the test run shown in Figure 3.9, the mean mass flow rate $\bar{\dot{m}}$ into the system was found to be 0.115 kg/s, corresponding to a mean flow speed of approximately 0.57 m/s. These values are at the upper limit of those measured during the test runs presented in this section.

3.3 Float position, velocity and acceleration

Figure 3.11 shows an example of raw position data for the duration of an entire test run using an 8.9×10^{-3} kg float. During the first 5 s the float remains stationary, as the camera was activated prior to flow entering the system. The ball valve was opened gradually between 5 – 7 s, with the float rising as water began to flow through the system. At approximately 7 s, the flow became sufficiently strong to close the check valve, resulting in the first pressure surge. This caused the water level within the chamber, and hence the float, to abruptly accelerate upwards. As it did so the check valve reopened, and the float briefly began to fall from its peak position before the check valve closed a second time. This second closure created another pressure surge that forced the float back upwards.

From 7 – 10 s the ball valve was opened further, increasing the mean position of the float $\bar{y}$ within the chamber. From 10 s onwards, the position of the ball valve was held constant and the system was allowed to oscillate naturally. During this period, $\bar{y}$ gradually fell because of the diminishing head within the reservoir. Although some small variations in the amplitude and the position of the minima and maxima occur from one oscillation to the next, the general shape of the oscillations appears to remain relatively consistent throughout this period. The variations are ascribed to the presence of higher order frequencies within the signal, which are discussed in greater detail below.

At 27 s, the ball valve was quickly shut, which caused the float to rapidly drop towards its initial position. During this period the check valve closed once more, creating a tiny final oscillation before the flow through the system ceased. This reduction in the momentum of the fluid in the pipe, coupled

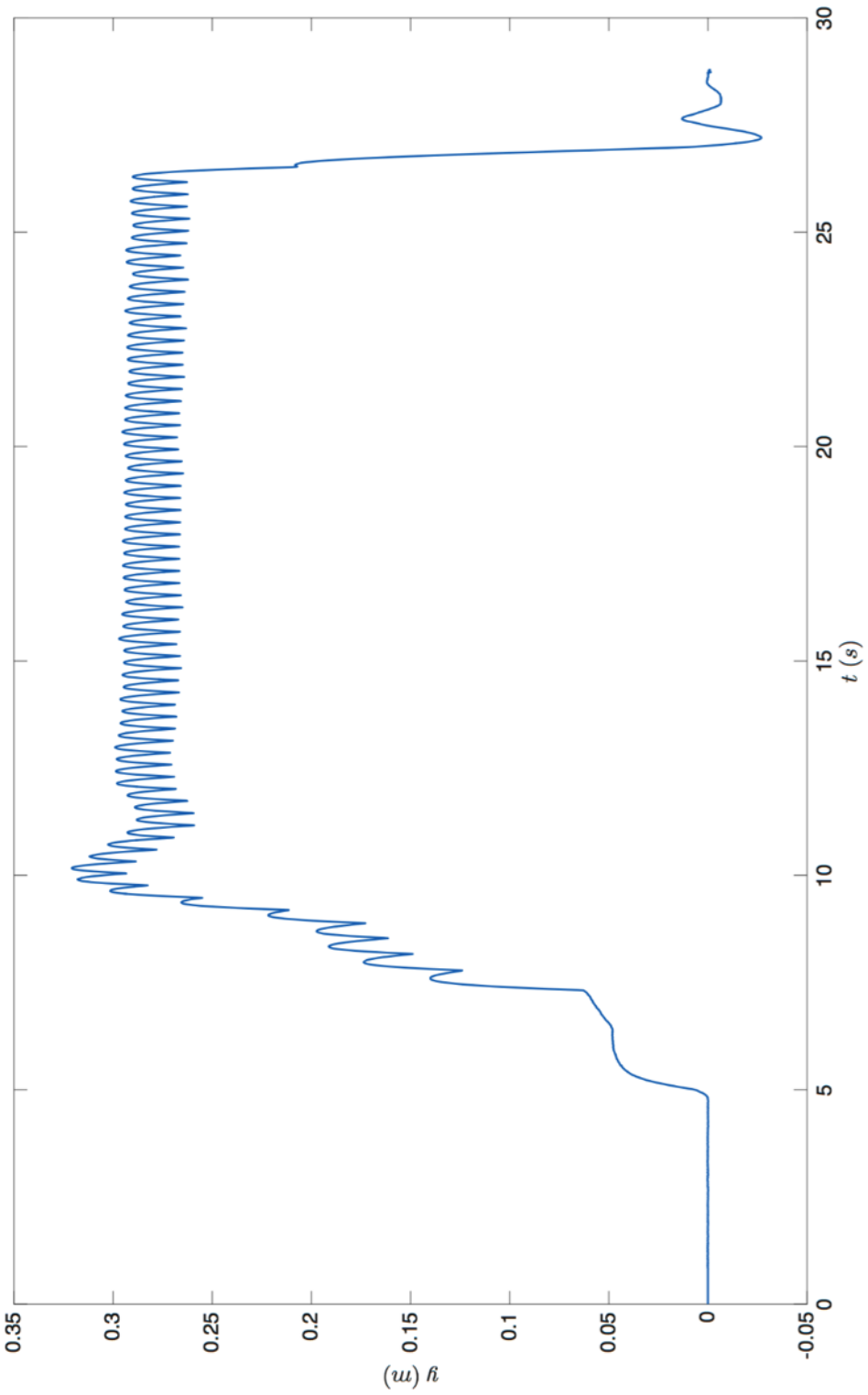

Figure 3.11: Example position data showing the oscillations of the 8.9×10^{-3} kg float over the course of a test run.

with the buoyancy and free surface forces acting upon the float, caused it to oscillate briefly about its minimum position before it finally came to a rest at the end of the test run.

Figure 3.12a shows the position of the float between 15 – 20 s for the same test run, providing a more detailed view of its motion. The shape of the oscillations is somewhat like those of a $\sin(t)$ wave, as they feature short, sharp minima that contrast with the relatively smooth, broad maxima. Each minima corresponds to a pressure surge generated by a valve closure passing underneath the chamber. The excess pressure serves to force both the float and the water within the chamber sharply upwards, abruptly changing their trajectory. Due to its high speed (calculated to be approximately 530 m/s from Equation 2.31 in Chapter 2) the pressure surge passes the chamber extremely quickly, meaning the excess pressure is only acting upon the float for a brief period.

For most of the oscillation period, the main forces acting upon the float are weight, buoyancy, free surface forces and friction from the pipe walls. Since the water level is moving independently of the float, the float buoyancy will be slightly greater than weight on the upstroke. This is because the water will begin to rise before the float (due to the float's inertia) meaning slightly more of the float will be submerged than it would otherwise be during static conditions. Meanwhile, the opposite will be true on the downstroke.

The combination of weight and friction diminishes the upwards momentum of the float and eventually reverses its direction, creating the broad peaks that can be seen in Figure 3.12a. The oscillations are slightly skewed in shape, with the upstroke period smaller than the downstroke period. This can be seen more clearly below in Figure 3.17 and is due to the difference in the forces acting on the float between the upstroke and downstroke. In this case, the mean oscillation amplitude was found to be 0.042 ± 0.001 m, and the mean total frequency 3.288 ± 0.004 Hz.

The behaviour of the float can be studied further by examining Figure 3.12b and c, which illustrate the corresponding velocity and acceleration of the float. From Figure 3.12b, the velocity of the float changes dramatically following a valve closure event, going from 0.4 m/s downwards to around 0.5 m/s upwards. This maximum occurs shortly after the float has reversed direction. Given the small range of motion it is a rather large number, suggesting that the float undergoes significant acceleration. Figure 3.12c shows that the peak acceleration of the float is typically over 50 m/s^2 and in some cases approaches 100 m/s^2. Although this value is sustained only very briefly, it is extremely large; to put it into context, the NASA space shuttle was limited to 30 m/s^2

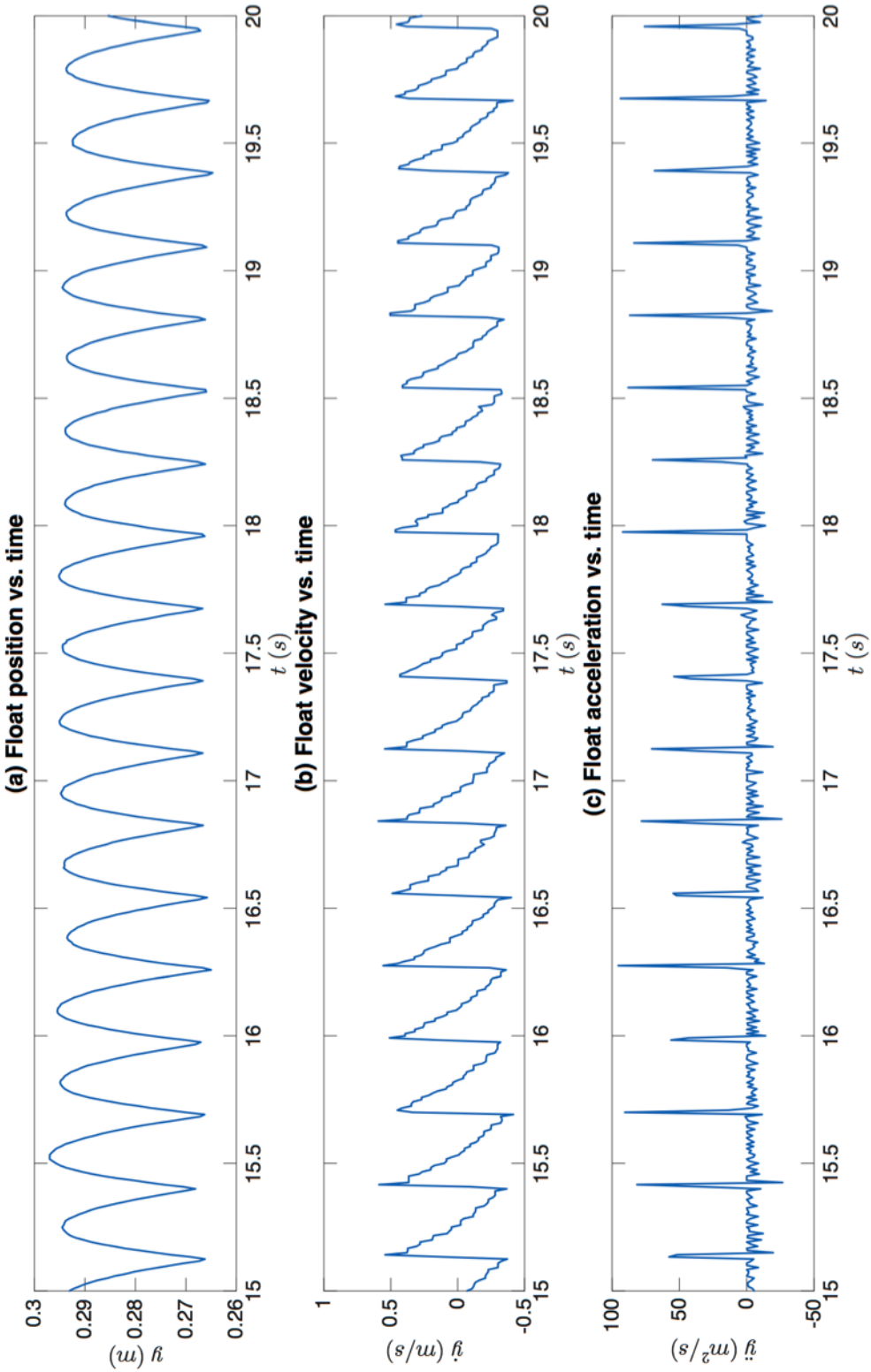

Figure 3.12: Float position, velocity and acceleration between 15 – 20 s of the test run shown in Figure 3.11.

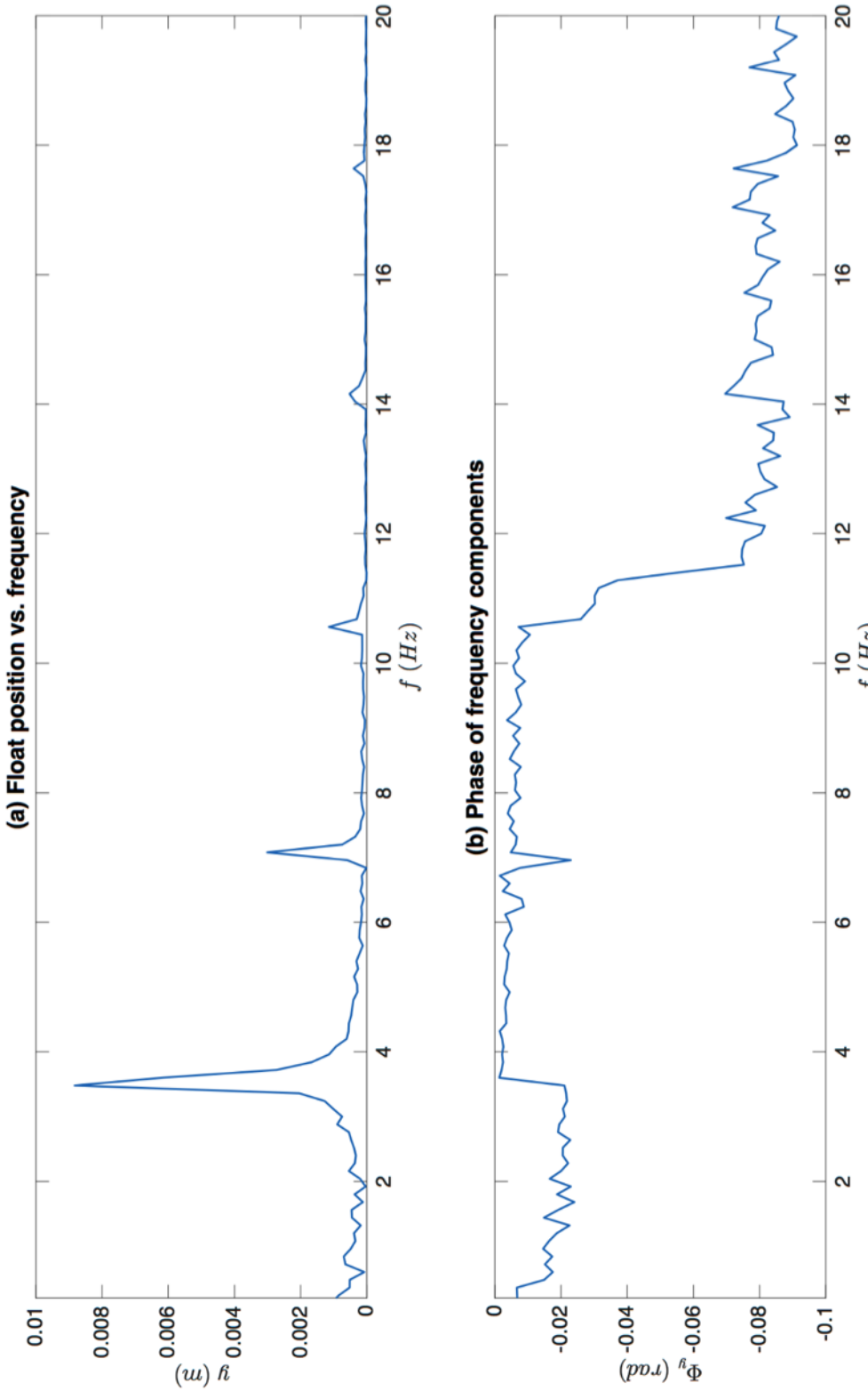

Figure 3.13: Float position from Figure 3.12 in the frequency domain.

to ensure the safety of the astronauts (NASA, 2011).

The float acceleration during the rest of the oscillation is significantly lower than the peak value. It is also highly variable, which indicates the presence of higher order frequencies within the overall position-time signal. Figure 3.13 presents the data shown in Figure 3.12 in the frequency domain, as determined using the FFT algorithm in MATLAB. The main component of the position signal can be seen at 3.480 Hz, although its magnitude of 0.009 m is significantly smaller than the value of 0.026 ± 0.001 m that was determined from the data in the time domain. This is because of the relatively wide frequency bin width of 0.120 Hz, and the fact that the magnitude of any frequency that does not directly correspond to a multiple of the bin width is underreported by an FFT.

While identifying the main frequency component of the oscillations, the FFT also shows the higher order frequencies in the signal. These occur at integer multiples of the main component, with their magnitude decaying with increasing frequency. From Figure 3.13b, which shows the phase angle of these frequency components, the main components within the signal are typically out of phase with one another.

These higher order frequencies are the reflected remains of previous pressure surges generated by preceding valve closure events. As discussed in Section 2.4.1, these do not simply disappear after propagating up the drive pipe, but linger within the system as their intensity is gradually diminished by friction from the pipe walls. There is more than one type of reflected pressure wave within the system, since the pressure will not only be reflected at the inlet and valve, but also by the chamber. Waves are therefore reflected between the valve and the chamber, the chamber and the inlet and the valve and the inlet.

These waves are important because they affect the pressure inside the system, and hence the flow rate through the device and the forces acting upon the valve. In doing so they alter the valve behaviour and affect the magnitude of the pressure surges in the chamber. It is hypothesised that this is the reason the peak acceleration values shown in Figure 3.12c fluctuate to the extent that they do, as exemplified by the fact that the mean of the peak values is 73.5 ± 15.0 m/s^2, a relative standard deviation of 20.4 %.

3.4 Oscillation characteristics

The mean oscillation amplitude of the 4.5×10^{-3} kg float is shown in Figure 3.14 as a function of input flow rate and head. The effect of the input head on the flow rate through the system can clearly be seen, however it is the opposite

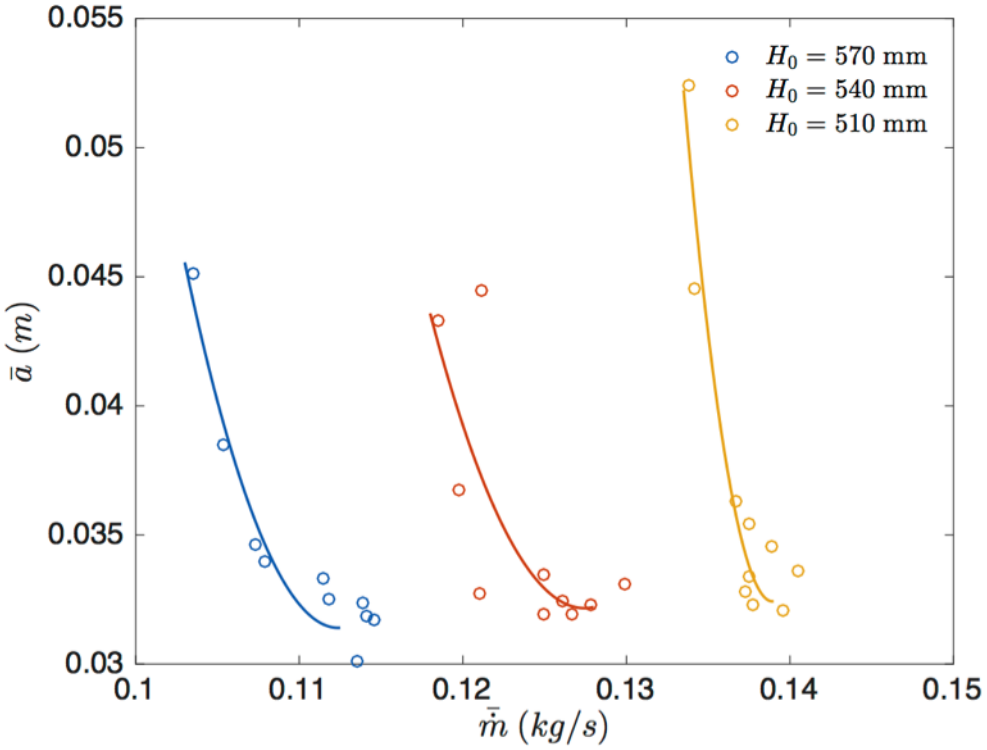

Figure 3.14: Mean oscillation amplitude of the 4.5×10^{-3} kg float as a function of mean input flow rate and head.

of what would be expected if water were simply allowed to drain freely from the reservoir. The largest input head resulted in the lowest mean flow through the system, and vice versa. This behaviour is ascribed to the check valve, which effectively chokes the flow exiting the WHES and therefore regulates the flow into the system. The pressure forces acting on the flap of the valve are greater in a larger head, meaning it will close in a weaker flow and choke the outflow to a greater extent. Conversely, in a lower head, a faster flow will be required to compensate for the lower pressure.

The other notable feature shown in Figure 3.15 is the inversely proportional relationship between the mean oscillation amplitude and the mean flow rate, which indicates that the pressure surges generated by the WHES are larger in weaker flows. This can be explained by considering the frequency of the chamber oscillations and hence the frequency of the valve closures, which are presented in Figure 3.15.

Figure 3.15 shows that the oscillation frequency is directly proportional to the mean flow rate, illustrating that the valve is more willing to close in a larger input. If the frequency of the valve closures is lower, it is open for a greater period on average, enabling the flow to recover by a greater extent from one closure to the next. The flow therefore experiences a greater momentum change

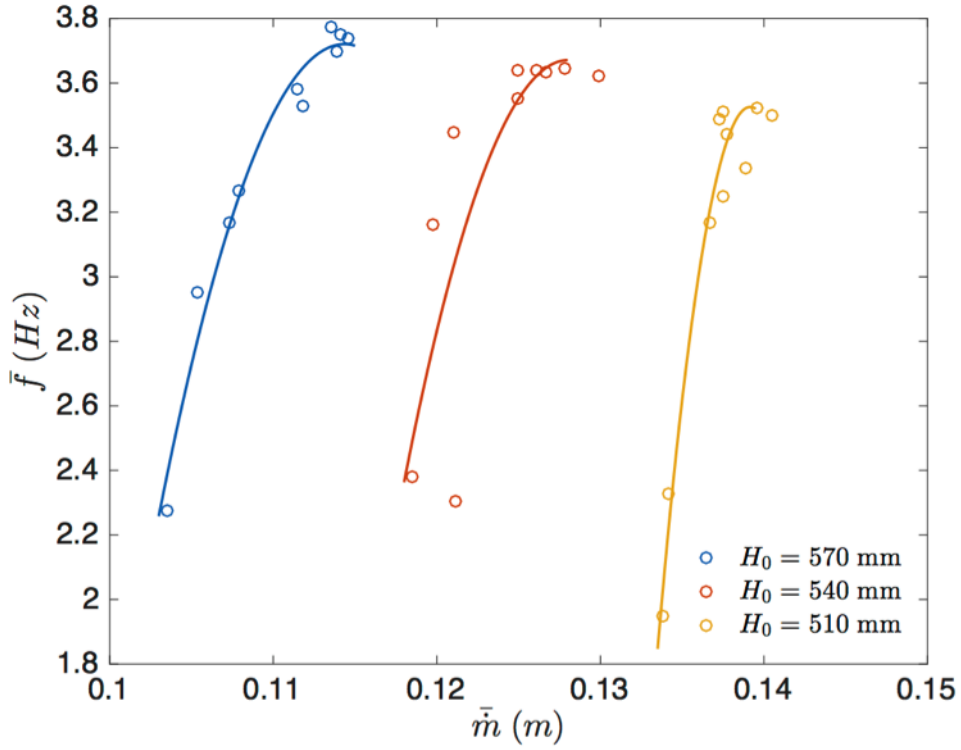

Figure 3.15: Mean oscillation frequency of the 4.5×10^{-3} kg float as a function of mean input flow rate and head.

when the valve does close, generating a larger oscillation within the chamber. In higher mean flow rates, the valve closes more readily, preventing the flow from recovering as much following each closure event. Although the mean flow rate may be slightly larger, this will reduce the peak flow rate through the valve, resulting in a smaller momentum change and lower amplitude oscillations. This behaviour is studied in further detail during the mathematical investigation of Chapter 4.

Given their respective relationships with the flow rate into the system, the amplitude and frequency of the oscillations are inversely proportional to one another. This is shown in Figure 3.16, which again illustrates how infrequent valve closures cause larger chamber oscillations. This behaviour is also visible in the mathematical predictions of Chapter 4, however the relationship shown by the experimental data is linear, unlike that seen in the mathematical study. This is because the peak outflow rate was kept constant in the mathematical study, whereas it will naturally vary in a physical system due to the input conditions and valve behaviour. The relationship shown in Figure 3.16 may be quantified as:

$$\bar{a} = \frac{\beta_1 \bar{f} + \beta_2}{H_0} \tag{3.5}$$

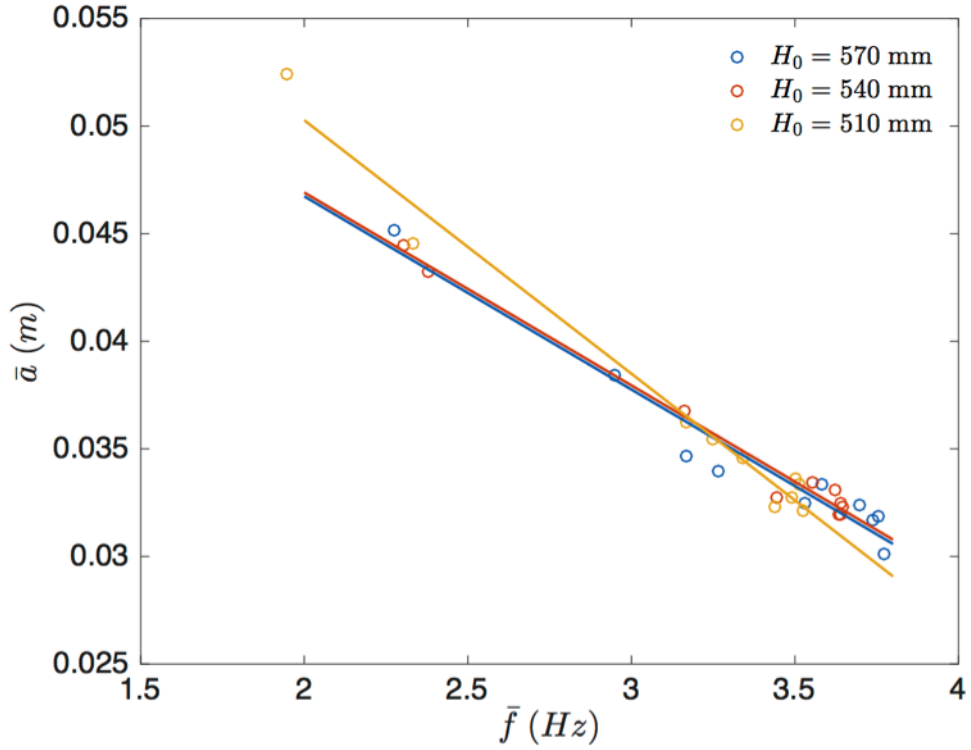

Figure 3.16: Mean oscillation amplitude of the 4.5×10^{-3} kg float as a function of mean frequency.

Where β_1 and β_2 are constants equal to -0.005 ± 0.001 m^2s and 0.036 ± 0.001 m^2, respectively.

As already discussed in Section 3.3, an important feature of the chamber oscillations is the difference between the upstroke and downstroke behaviour. Figure 3.17 illustrates this relationship and shows that the downstroke period is consistently larger than the upstroke period. This highlights the asymmetrical nature of the oscillations, which as already discussed is due to the varying forces acting on the float. This suggests that the power available from the upstroke and downstroke will be different. The relationship shown in Figure 3.17 may be quantified as:

$$\bar{T_D} = \frac{\beta_1 \bar{T_U} + \beta_2}{H_0} \tag{3.6}$$

Where the constants β_1 and β_2 equal -0.900 ± 0.040 m and -0.150 ± 0.050 m, respectively.

The effect of input on system behaviour can also be seen by examining the mean water level within the chamber. Figure 3.18 illustrates this against the mean flow rate and input head. The mean water level within the chamber increases proportionally with both flow rate and head, which is again due to

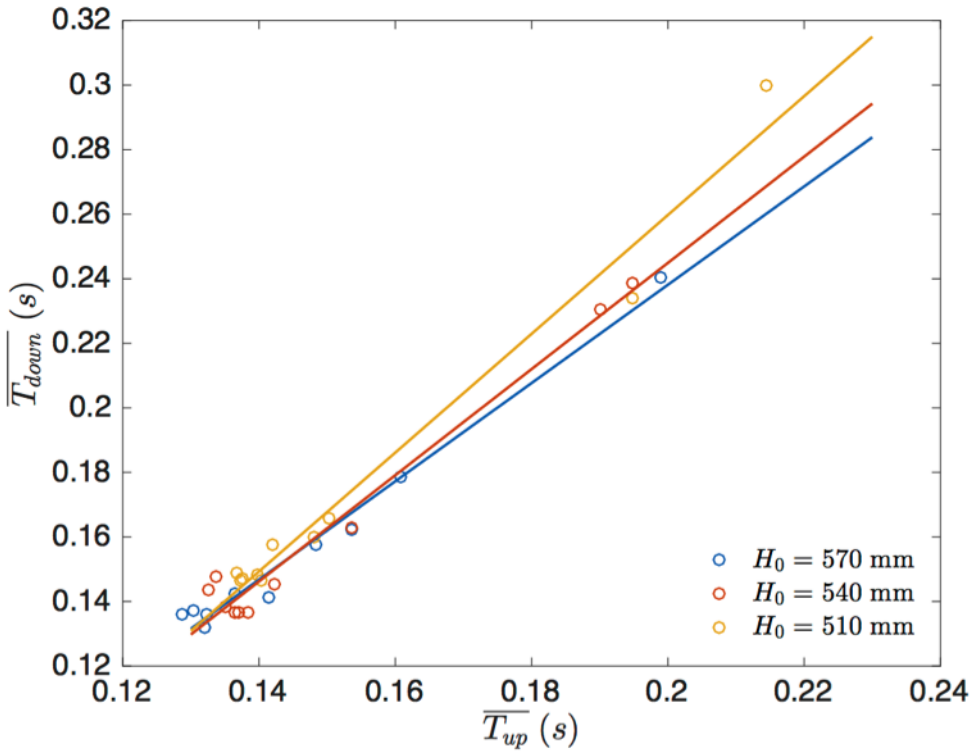

Figure 3.17: Relationship between mean upstroke and downstroke oscillation periods.

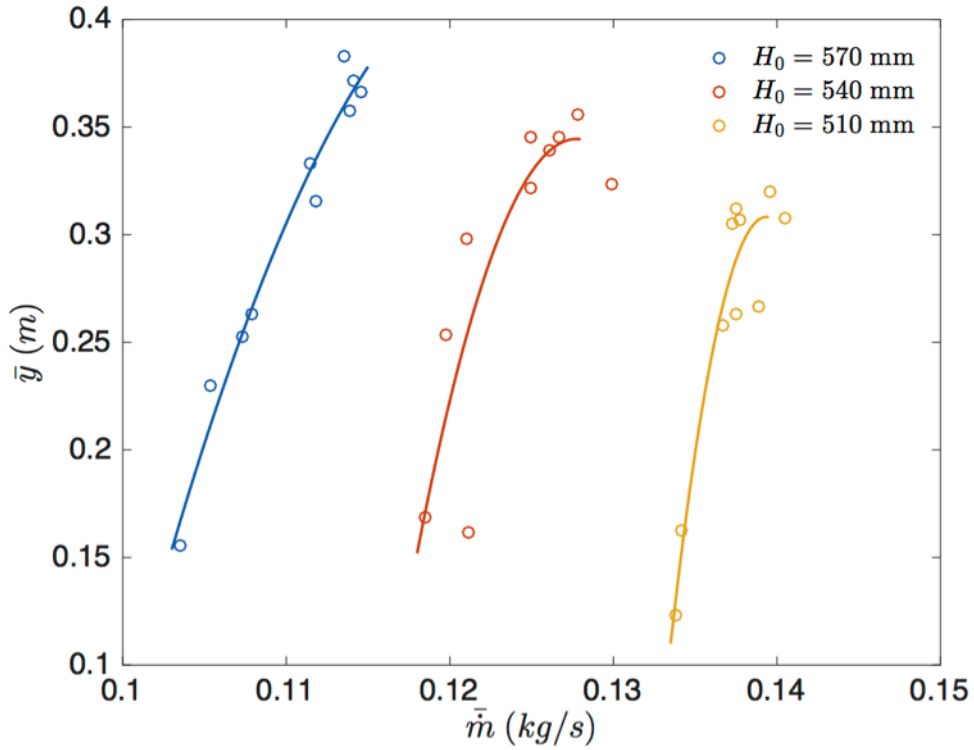

Figure 3.18: Mean chamber water level as a function of flow rate and input head.

the behaviour of the valve. In lower flow rates when the valve is closing less frequently, the outflow is choked to a lesser extent and more closely corresponds to the mean inflow. As the input is increased, the valve chokes the outflow by a greater extent, creating a larger difference between the two and a higher water level within the chamber due to conservation of mass. As the head within the chamber increases, the pressure gradient in the drive pipe is diminished, limiting the maximum input flow rate.

The relationship shown in Figure 3.18 is somewhat similar to that determined by the mathematical study in Chapter 4, insofar as the water level within the chamber increases as a function of the input conditions. Unlike the mathematical results, however, the chamber water level also increases with the valve closure frequency. This again illustrates how the frequency of the valve closures affects the peak outflow rate, since this variable was kept constant in the mathematical study but not in the experimental one.

3.5 Power

The velocity and acceleration data can be used to calculate the net force and power of the float per Equations 3.2 and 3.3, respectively. Figure 3.19 provides an example power curve for the 8.9×10^{-3} kg float data presented in Figure 3.12.

Figure 3.19 shows that the power of the float is subject to sudden, sharp peaks. These correspond to the minima of each oscillation, where the float is forces upwards by a pressure surge. In this case, the magnitude of the peaks varies from roughly 140 – 450 mW, with a mean of 283 $\pm$ 87.2 mW. Between the pressure surges, however, the power available from the system is much lower. In this case the mean overall power available from the system was 15.6 $\pm$ 51.2 mW. On average, the mean peak stroke power was found to be 15.5 times greater than the mean overall power.

Figure 3.20 plots the mean peak stroke power $\overline{P_s}$ of the float as a function of the mean overall power $\overline{P}$ for the different mass floats. The disparity between the peak stroke power and mean overall power can be seen by comparing the magnitudes of the two axes. This suggests that increasing the frequency at which the valve closes may provide more power on average, since it will result in more frequent peaks. Whether or not this is true will depend upon how the strength of the pressure surges is affected by the valve closure frequency. These effects are studied in further detail below and in Chapter 4, where it is shown that low frequency, high power oscillations will provide the most power on average.

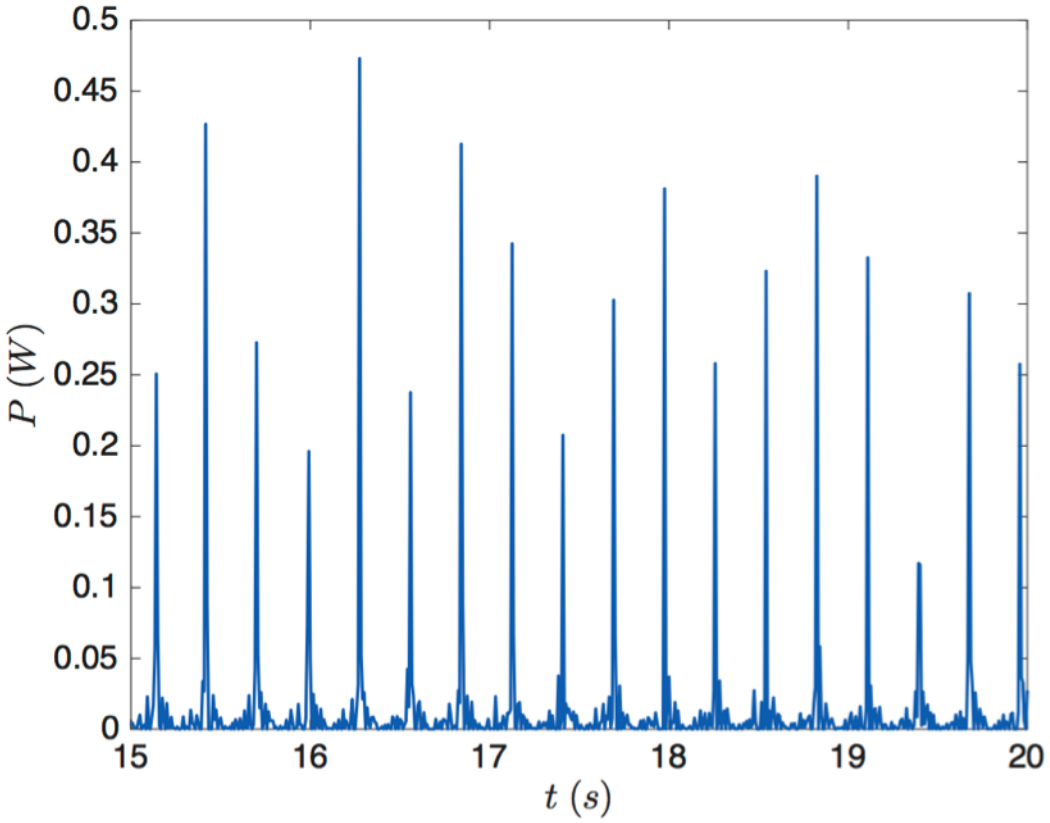

Figure 3.19: Mechanical power of the 8.9×10^{-3} kg float during 15 – 20 s of the test run presented Figure 3.11.

Using linear regression, a basic relationship between the mean stroke power and the mean overall power can be determined from the data presented in Figure 3.20:

$$\overline{P_s} = m(\beta_1 \overline{P} + \beta_2) \tag{3.7}$$

Where β_1 and β_2 are constants equal to 590 ± 70.6 kg^{-1} and 13.8 ± 3.51 W/kg, respectively.

These values are likely dependent upon the parameters of the system and what it is driving. Equation 2.31 shows that changing the material that the system is made from will vary the speed of the pressure waves, affecting the behaviour of the system. Equation 3.7 also does not consider the difference between the surface area of the floats and the cross-sectional area of the pipe. A larger diameter float will have a greater cross-sectional area and hence capture more of the available pressure. This is demonstrated by the comparisons between the floats with the piston below.

Figure 3.20 and Equation 3.7 also show that increasing the mass of the float increases its power. This is because the weight of the float, which acts in opposition to the force arising from the water hammer pressure pulse, is

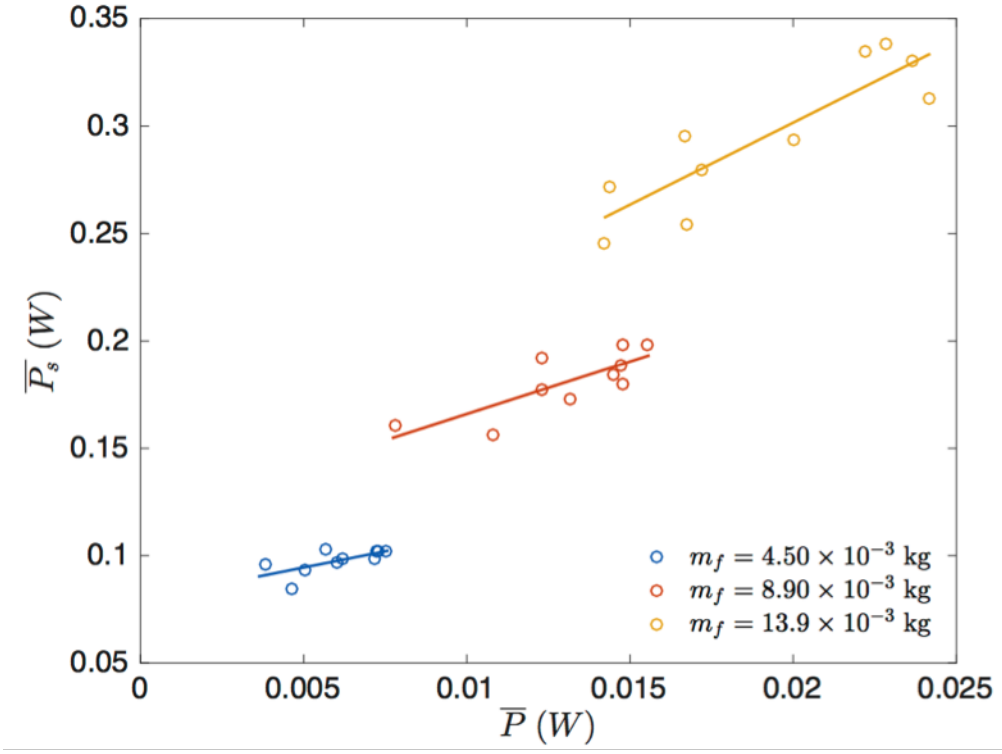

Figure 3.20: Relationship between mean overall power and mean peak stroke power for each test run.

compensated for by the buoyancy force of the displaced water. The greater surface area of the larger floats will also enable them to capture slightly more pressure. There will be a limit to this however, since the maximum size of the float will be limited by the size of the device. Figure 3.21 plots the mean peak velocity and acceleration of the float (i.e. the mean of the values that correspond to each power spike), and suggests that the mean peak acceleration experienced by the float decreases with increasing mass, as one would expect.

Given that the input conditions affect the behaviour of the valve and the form of the oscillations within the chamber, they also affect the power generated by the WHES. Figure 3.22 illustrates how the mean overall and stroke power of the 4.5×10^{-3} kg float are affected by the input conditions.

The mean overall power is directly proportional to the input flow rate, which follows from the fact that the oscillations and hence the power peaks become more frequent. The relationship between the mean flow rate and the mean power shown in Figure 3.22a can be quantified as:

$$\bar{P} = H_0(\beta_1 \bar{\dot{m}} + \beta_2) \tag{3.8}$$

Where β_1 and β_2 are constants equal to 0.224 $\pm$ 0.088 m/s^2 and -0.025 $\pm$

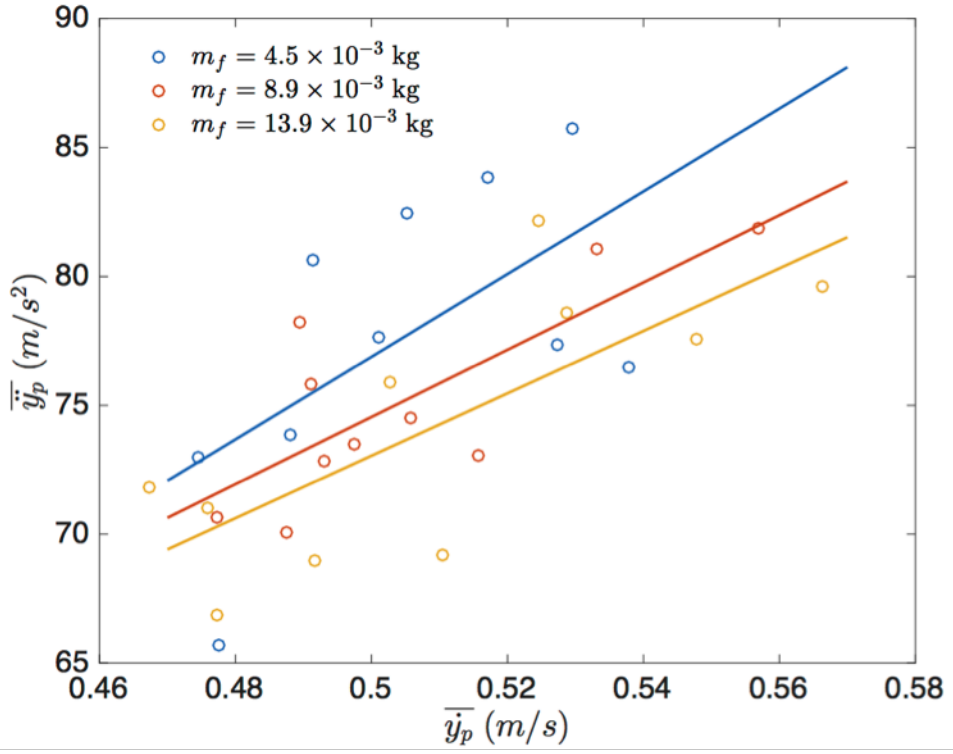

Figure 3.21: Relationship between mean peak float acceleration and and velocity for each test run conducted with the varying float masses.

0.014 kg·m/s^3, respectively. Examining the mean peak stroke power in Figure 3.22b is less informative than the time-averaged power, beyond the fact that it is significantly larger, since the correlation between the variables is much weaker. This can be examined using the coefficient of determination R^2:

$$R^2 = 1 - \frac{(\sum_{i=1}^{n} y_i - \hat{y}_i)^2}{(\sum_{i=1}^{n} y_i - \bar{y}_i)^2} \tag{3.9}$$

Where $\hat{y}$ represents the value of y predicted by a model (i.e. the trend line). An R^2 value of 1 indicates that a model is capable of perfectly predicting measured behaviour, while smaller values indicate that it is less accurate.

Table 3.1 presents R^2 values for the data sets shown in Figure 3.22. While the measured mean flow rate appears to correlate reasonably well with the time-averaged power for all 3 input heads, there is little to no correlation between the mean peak power and the flow rate. Consequently, no attempt is made to quantify the relationship between the two variables.

This is contrary to what was expected. Since the oscillation amplitude is inversely proportional to mean flow rate, it was thought that a lower mean flow rate would provide more powerful strokes. A larger amplitude oscillation should indicate the generation of a larger pressure surge, resulting in more

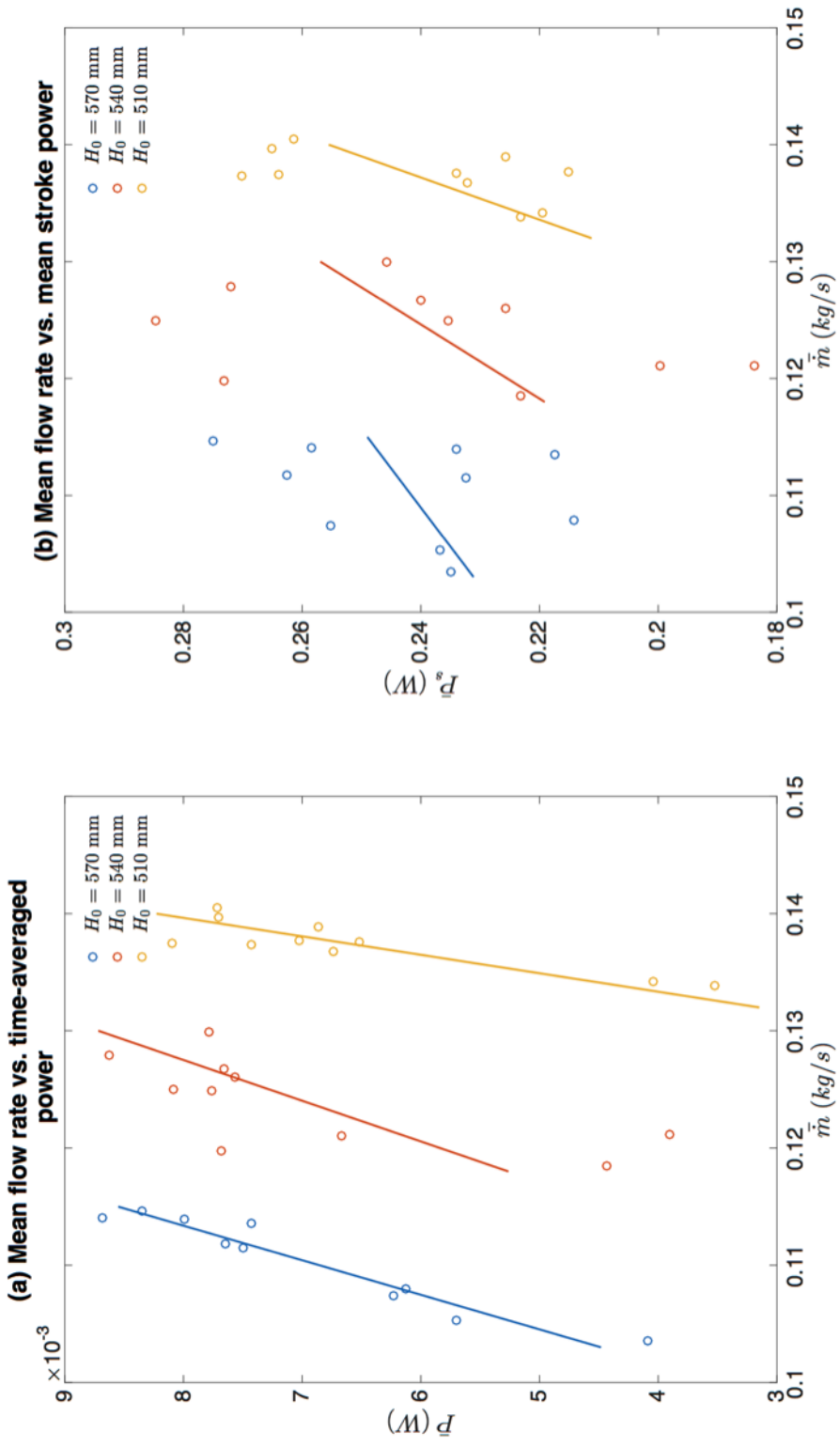

Figure 3.22: Effect of input flow rate and head on the time-averaged and mean stroke power of the 4.5×10^{-3} kg float.

Table 3.1: Coefficients of determination of the data sets presented in Figure 3.22.

Input head (mm)	R^2 mean overall power	R^2 mean peak power
510	0.929	0.091
540	0.472	0.135
570	0.747	0.294

force and power. The reason for this is the use of a floating body that is relatively narrow compared to the chamber diameter, which allows much of the pressure generated by the valve closures to escape.

Replacing the float with the piston shows that there is a correlation between the mean stroke power and the amplitude of the oscillations. This is illustrated by Figure 3.23, which shows the relationship between oscillation amplitude and peak stroke power for ten test runs conducted using the piston. The relationship shown has an R^2 value of 0.830, which is significantly greater than the R^2 value for the floats summarised in Table 3.1. This is because the piston has a much wider diameter than the floats, and is therefore capable of capturing more of the excess pressure generated by the valve closures. Given its much greater weight, free-surface forces and buoyancy also play a relatively smaller role in its behaviour. The relationship shown in Figure 3.23 may be quantified as:

$$\bar{P}_s = 60.8\bar{a} - 3.13 \tag{3.10}$$

The other noteworthy feature of Figure 3.23 is the magnitude of the mean peak power, which can be seen through comparisons with Figure 3.20b and Figure 3.22b to be significantly greater than the power available from any of the floats. Although this is partly due to the extra mass of the piston (which was 15.0×10^{-3} kg compared to the 13.9×10^{-3} kg of the heaviest float), it is again indicative of the piston capturing more of the excess pressure generated by the valve closures.

The greater diameter of the piston enables it to reach much higher peak velocity and acceleration values in comparison to the floats, as illustrated by Figure 3.24. The various floats that were tested reached a mean peak velocity of 0.45 to 0.58 m/s and a mean peak acceleration of 65 – 85 m/s^2. Yet the piston, which had the greatest mass of all of the bodies tested, reached a mean peak velocity between 0.74 to 0.85 m/s and a mean peak acceleration between 85 – 125 m/s^2. This demonstrates that using a body with as wide a diameter as possible within the chamber will be the most effective way of capturing the power generated by the WHES.

This point is further illustrated by Figure 3.25, which plots the mean stroke

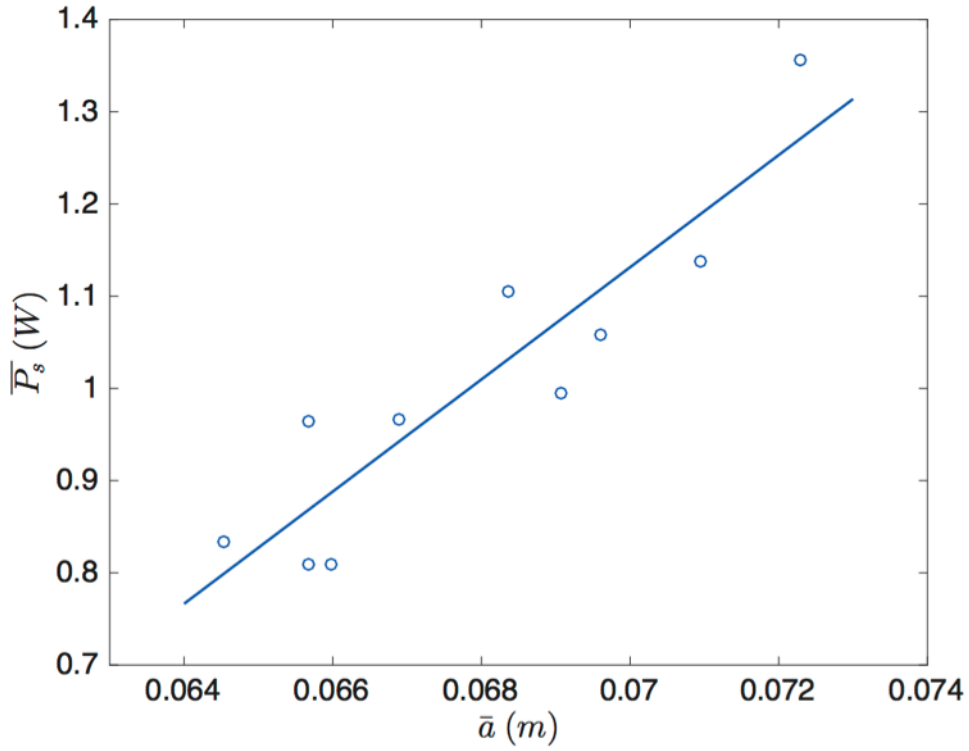

Figure 3.23: Peak stroke power of the piston as a function of stroke amplitude.

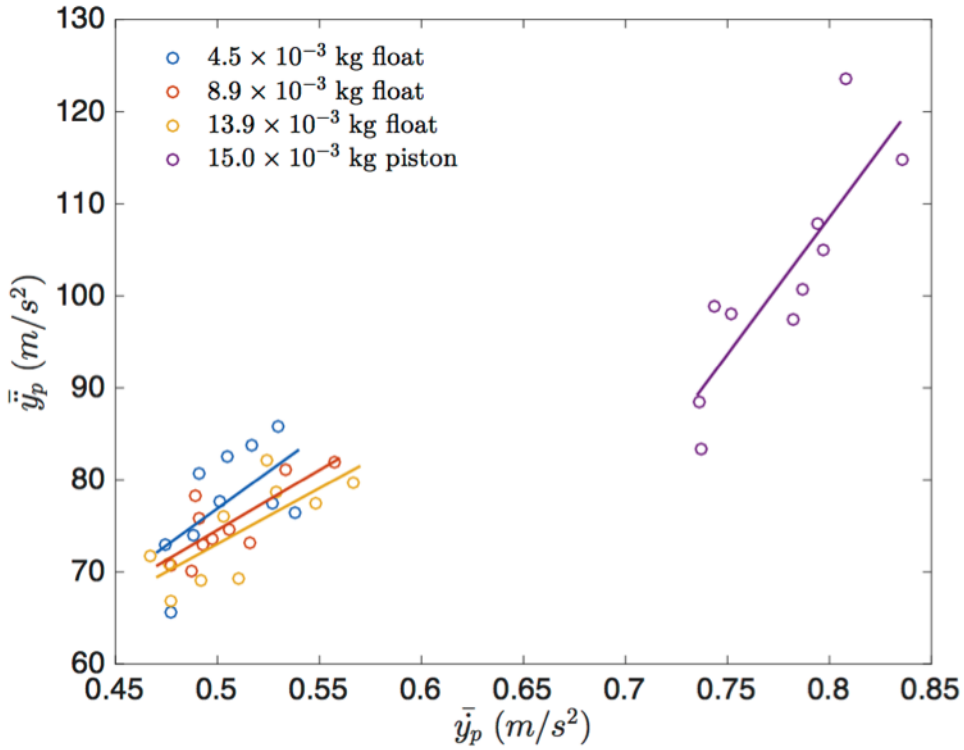

Figure 3.24: Relationship between peak velocity and acceleration for the various bodies driven by the WHES.

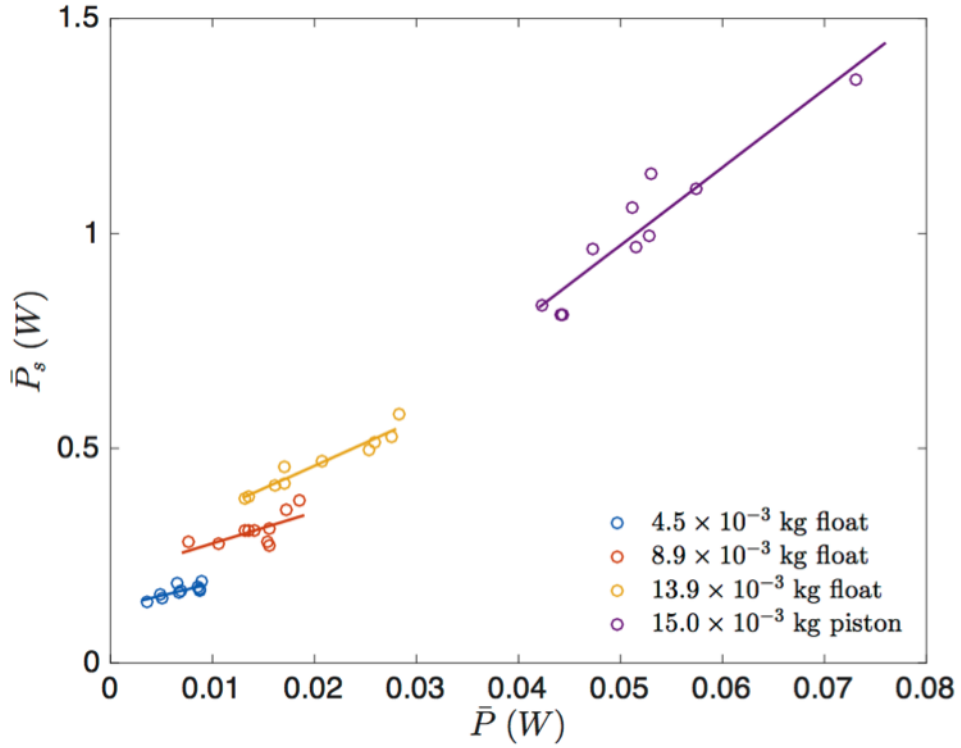

Figure 3.25: Relationship between mean overall and mean stroke power for the various bodies driven by the WHES.

power available from the various driven bodies as a function of their mean overall power. The piston can again be seen to provide the most power, both in terms of the peak power available per stroke and the average power available over the course of a test run.

The relationship shown in Figure 3.25 between the mean and peak piston power may be quantified as:

$$\bar{P}_s = 18.2\bar{P} + 0.06 \tag{3.11}$$

The R^2 value for this relationship is 0.980, which indicates a high correlation between the two variables. Equation 3.11 quantifies the ratio of mean stroke power to mean overall power, demonstrating that the power available from the pressure surges is 18.2 times that available on average.

Given that the mean overall power is directly proportional to the mean peak power, Equation 3.11 suggests that increasing the magnitude of the pressure surges will be the most effective way of maximising the power output from the system. Since the piston stroke power is greater at larger amplitudes and low frequencies, a low frequency system generating large amplitude oscillations will likely be the most effective. Controlling the behaviour of the valve may permit

large amplitude oscillations to be generated at a higher frequenecy, however.

Equation 3.11 also indicates that the power take-off system will need to be capable of conditioning the power available from the device into a smoother form, given that the mean stroke power is 18.2 times greater than the time-averaged power. This could be done electrically, however any power conditioning circuit will depend upon the method used to extract energy from the chamber. This is investigated in Chapter 5, which presents details of two different power take-off systems: a linear alternator and a piston-crank mechanism.

3.6 Discussion

The results of these experiments show that it is possible to use the WHES to generate vertical oscillations as intended, and that these oscillations can be used to drive either a floating body or a piston up and down. The available power occurs in brief peaks, which correspond to the pressure surge generated by a valve closure. Although the pressure is only available for a very brief period, it provides enough force to reverse the trajectory of a body within the chamber and propel it back upwards to a speed that is large relative to the distance travelled.

Once the pressure surge has passed, the power available over the remainder of the oscillation is significantly lower. This is due to the smaller forces that act on the body during this period. Although there are reflected pressure waves from previous valve closures still within the pipe, their magnitude is reduced by friction to such an extent that they contribute little to the available power. Maximising the magnitude of the pressure surges will therefore maximise the average power available. If a float is used, increasing the valve closure frequency may also be advantageous. However, it is shown in Chapter 4 that increasing frequency actually reduces the average available hydrodynamic power by diminishing the pressure surge strength.

The behaviour of the system is influenced by several factors, including the input head and flow rate, which govern the oscillation frequency and amplitude. These factors alter the forces on the valve, changing its behaviour and hence impacting the momentum changes experienced by the water within the drive pipe. Interestingly, there appeared to be no correlation between oscillation amplitude and power when the system was used to drive a floating body. Yet when the piston was used, there was a clear correlation between the two variables. The piston serves captures much more of the excess pressure generated by the valve closures than a narrow floating body, suggesting that a piston-crank mechanism will be a suitable method for generating power from

the device.

The hydrodynamic effectiveness of the device can be explored by comparing the power available from the scale model to the performance of conventional tidal stream devices. For the floats, the maximum available mean peak power was 0.581 ± 0.080 W, which occurred for the heaviest float oscillating in the highest input flow rate. The corresponding mean overall power value was computed as 0.028 ± 0.006 W. Normalising the power output for the cross-sectional area of the pipe provides a mean peak power density of 2.887 ± 0.250 kW/m^2, with a corresponding mean overall power density of 0.141 ± 0.021 kW/m^2.

For the piston, the maximum mean peak power was 1.356 ± 0.353 W and the mean overall power was 0.073 ± 0.018 W. The corresponding mean peak power density is 6.744 ± 1.753 kW/m^2, and the mean overall power density is 0.363 ± 0.087 kW/m^2. Comparatively, the MCT SeaGen S device generates an average 3.18 kW/m^2 based on the power output and rotor sized reported in Chapter 2. Although this is a crude comparison, given that it does not account for effects of scale or the input power, it indicates that the WHES may be capable of producing reasonable amounts of power for its size, provided that an efficient power take-off system can be designed.

The results suggest several ways of maximising the power available from the WHES. A piston or similarly wide object should be used in the chamber to capture as much of each pressure surge as possible. If such an object is used, then increasing the magnitude of the pressure surges will result in a greater overall power output. For the uncontrolled valve used in this experiment, oscillation amplitude was inversely proportional to closure frequency. This suggests that maximising the pressure surges will require a low frequency system. Increasing the cross-sectional area of the drive pipe and chamber should also increase the power available from the system, since a larger diameter will enable more of the force available in the pressure surges to be captured. This is studied in further detail in Chapter 4.

Other topics that have arisen from this investigation include the higher order components within the position-time signal. These are the remains of pressure surges generated by previous valve closures, which are reflected up and down the drive pipe as they decay. It is hypothesised that these waves have a small impact on the behaviour of the check valve, altering the magnitude of the pressure surges it generates. Additionally, the fact that altering the input conditions affects the behaviour of the valve suggests that a given valve design will only be capable of operating within a specific range of input conditions. Controlling the behaviour of the valve is therefore likely to be a necessity if

the WHES is to behave consistently and reliably. Given the variable nature of the tides, a WHES operating in a tidal stream will be more likely to require a controlled valve, which would come at the cost of increasing the complexity of the system. If a WHES were operating in a more predictable environment, such as an elevation head provided by a river or reservoir, and an appropriate valve was chosen, a control system may not be strictly necessary for the device to function, as demonstrated by this experiment and hydraulic ram pumps.

3.7 Chapter conclusions

This chapter has presented the methods and results of an experimental investigation into the hydrodynamics of the Water Hammer Energy System. The results indicate that the WHES is capable of functioning as intended and may have the capacity to generate reasonable amounts of power if scaled up and combined with an effective power take-off system.

When driving a float, the scale model tested in this chapter was calculated to provide a maximum mean stroke power of 0.581 $\pm$ 0.080 W, and 0.028 $\pm$ 0.006 W on average. Normalising the power output for the size of the device indicates a mean peak power density of 2.887 $\pm$ 0.250 kW/m^2 and a mean overall power density of 0.141 $\pm$ 0.021 kW/m^2, suggesting the device may have potential for generating power in a real world setting. This is particularly true when considering the mean peak and overall power density that would be available from a piston, which was found to be significantly larger at 6.744 $\pm$ 1.753 kW/m^2 and 0.363 $\pm$ 0.087 kW/m^2, respectively. Several empirical relations, capable of predicting the power from the tested device and various other parameters, have also been derived, although these are thought to be device specific.

The results suggest that a piston will be more effective than a floating body for extracting energy from the system. Given that more powerful pressure surges are generated by lower valve closure frequencies, it is hypothesised that a low frequency, high pressure system will be the most efficient design. This would occur in lower input rates if a freely closing check valve is used, again indicating that the system will be effective in low input conditions.

Further studies need to be conducted before the effectiveness of the WHES can be assessed with any certainty, however. These include how parameters that were not tested during these experiments (such as valve behaviour and system size) influence performance. The hydrodynamic efficiency of the device (i.e. the efficiency at which the power in the input flow can be converted to hydraulic power within the chamber) must also be quantified. These factors

are assessed in Chapter 4, which uses a mathematical model to investigate variables that would otherwise prove too difficult, costly or time-consuming to test experimentally. The main variables investigated are:

- The effect of valve behaviour and outflow on the magnitude of the pressure surges and the hydrodynamic efficiency of the device.
- The effect of input conditions on performance if the valve behaviour is held constant.
- The effect of device diameter on performance.

Chapter 4

Mathematical model & parametric study

Chapter 3 detailed an experimental investigation into the performance of the Water Hammer Energy System, providing details on the basic behaviour of the device and the how varying the input affects system performance. Many variables that will impact upon the system were not investigated, however, due to the difficulty of doing so. The hydrodynamic efficiency of the system was not quantified either, since the power measurements depended upon the object the system was driving.

This chapter presents a mathematical investigation into the hydrodynamics of the water hammer energy system. The aims of this study were to identify how the behaviour of the system is governed by variables that were not tested in the previous chapter and evaluate the hydrodynamic efficiency of the system, which is defined as the ratio of the hydraulic power available in the chamber to the power available from the input flow.

To achieve this, the study was split into three separate parts:

- Outflow behaviour in fixed input conditions.
- Input conditions when outflow remains constant.
- System size with constant input and outflow velocity.

These topics were investigated using the ordinary differential equations that describe the behaviour of simple surge tanks. These are vertical pipes of water located upstream of a valve, and therefore very similar to the Water Hammer Energy System. Four periodic functions were used to approximate the oscillatory flow through the valve, enabling the effect of outflow behaviour to be studied. Following this, the outflow was approximated using a sawtooth wave (which provided the closest match to the experimental observations of

Chapter 3) to investigate the effects of varying input conditions and system size on performance.

4.1 Governing equations

The chamber in the Water Hammer Energy System is an open standpipe located upstream of the valve, making it very similar to a simple surge tank. The equations governing surge tank behaviour are therefore an ideal starting point for predicting the performance of the WHES. This section presents a derivation of the momentum and continuity equations for a simple surge tank, based on that found in Chaudhry (2014).

Figure 4.1 illustrates a reservoir of head H_0 connected to a rigid pipe of length l and cross-sectional area A_p. Water flows through this pipe at a volumetric flow rate Q_p towards the vertical chamber of cross-sectional area A_c. Downstream of the chamber is the valve, which opens and closes periodically and thus governs the volumetric flow rate Q_v that passes through it.

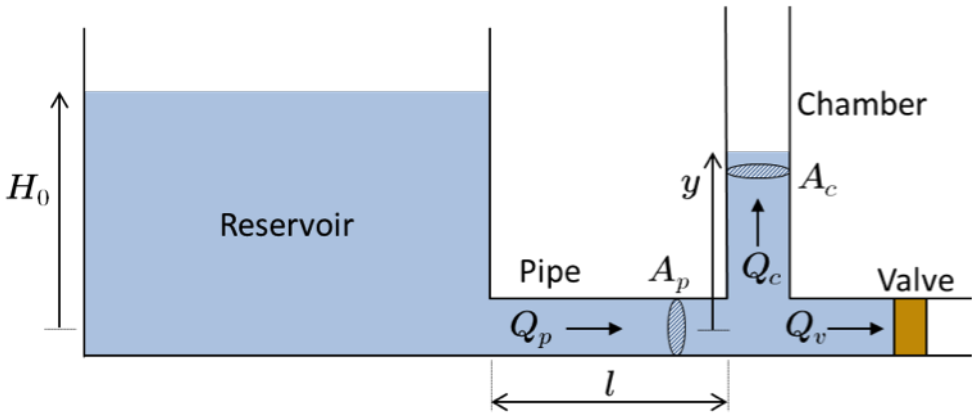

Figure 4.1: Reservoir, chamber and valve system.

4.1.1 Conservation of momentum

To calculate the variation in the chamber water level, it is first important to consider the forces that act upon the water within the pipe. These are illustrated in the free body diagram of Figure 4.2: force F_1 is due to the pressure of the water within the reservoir, F_2 results from the water pressure within the chamber, F_3 represents the friction between the water and the pipe walls, and F_4 corresponds to the weight of the water within the pipe.

As previously static fluid in the reservoir flows into the pipe at a velocity v_p, some of the input head is lost as pressure energy is converted into kinetic

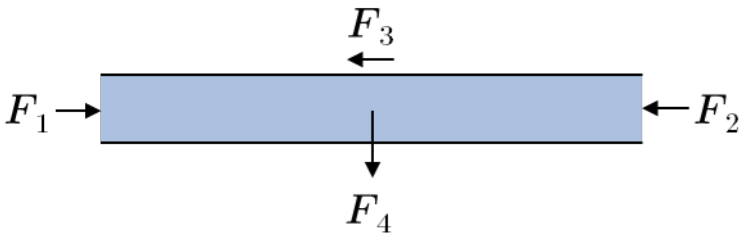

Figure 4.2: Free body diagram showing the forces in the pipe between the reservoir and chamber.

energy. This pressure drop is equivalent to the velocity head H_v, given by:

$$H_v = \frac{{v_p}^2}{2g} \tag{4.1}$$

Further head losses H_l occur as fluid leaves the reservoir and enters the pipe. These are governed by the geometry of the inlet:

$$H_l = k\frac{{v_p}^2}{2g} \tag{4.2}$$

Where k is a loss coefficient that is determined by the shape of the inlet. Inside the pipe, friction causes a further head loss h_f, which can be determined according to the Darcy-Weisbach equation:

$$H_f = \frac{\Lambda {v_p}^2 l}{2gD} \tag{4.3}$$

Where D is the pipe diameter and Λ is the Darcy-Weisbach friction factor, which is dependent upon the roughness of the pipe and whether the flow is laminar, transitional or turbulent. This is dependent upon the Reynolds number Re, which for pipe flow is given by:

$$Re = \frac{\rho v_p D}{\mu} \tag{4.4}$$

Where μ is the dynamic viscosity of the fluid.

In laminar flow ($Re < 2300$), the roughness of the pipe can be neglected, allowing Λ to be calculated trivially:

$$\Lambda = \frac{64}{Re} \tag{4.5}$$

For turbulent flow ($Re > 4000$), Λ can be calculated using the Colebrook-

White equation:

$$\frac{1}{\sqrt{\Lambda}} = -2\log_{10}\left(\frac{2.51}{Re\sqrt{\Lambda}} + \frac{\varepsilon}{3.71D}\right) \tag{4.6}$$

Where ε is the absolute roughness of the pipe wall. In transitional flow ($2300 < Re < 4000$), Λ is subjected to large uncertainties and can be difficult to accurately determine. In this region, it may be estimated using a Moody diagram if the flow is fully developed.

Considering these head losses, the forces in the pipe shown in Figure 4.4 are:

$$F_1 = \rho g A_p (H_0 - H_v - H_l) \tag{4.7}$$

$$F_2 = \rho g A_p y \tag{4.8}$$

$$F_3 = \rho g A_p H_f \tag{4.9}$$

$$F_4 = \rho g A_p l \tag{4.10}$$

Where density $\rho = 998.2$ kg/m^3 for fresh water, acceleration due to gravity $g = 9.81$ m/s^2 and y is the water level within the chamber, which is considered to be positive in the upwards direction.

If fluid that is propagating towards the downstream end of the pipe shown in Figure 4.2 is considered to be travelling in the positive direction, the net horizontal force acting upon the flow is given by:

$$\sum F_h = \rho g A_p \left(H_0 - H_v - H_l - H_f - y\right) \tag{4.11}$$

By Newton's second law, this force is equivalent to the fluid's rate of change of momentum:

$$\sum F_h = m\frac{\mathrm{d}v_p}{\mathrm{d}t} \tag{4.12}$$

The mass m of the water within the pipeline is given by:

$$m = \rho A_p l \tag{4.13}$$

While the water velocity v_p is given by the volumetric flow rate and the cross-sectional area of the pipe:

$$v_p = \frac{Q_p}{A_p} \tag{4.14}$$

Therefore:

$$m\frac{\mathrm{d}v_p}{\mathrm{d}t} = \rho l\frac{\mathrm{d}Q_p}{\mathrm{d}t} \tag{4.15}$$

Hence, from Equation 4.12:

$$\frac{\mathrm{d}Q_p}{\mathrm{d}t} = \frac{gA_p}{l}\left(H_0 - H_v - H_l - H_f - y\right) \tag{4.16}$$

$$\frac{\mathrm{d}Q_p}{\mathrm{d}t} = \frac{gA_p}{l}\left(H_0 - y - \frac{Q_p|Q_p|}{2g{A_p}^2}\left(1 + K + \frac{\Lambda l}{D}\right)\right) \tag{4.17}$$

Equation 4.17 is the momentum equation, which shows that any change in the momentum of the fluid in the drive pipe is caused by a difference in the water level between the reservoir and the chamber. What would otherwise be a ${Q_p}^2$ term is written as $Q_p|Q_p|$ to account for any reversal in the flow direction.

A constant β may be defined for a given system and Reynolds number to simplify Equation 4.17 further:

$$\frac{\mathrm{d}Q_p}{\mathrm{d}t} = \frac{gA_p}{l}\left(H_0 - y - \beta Q_p|Q_p|\right) \tag{4.18}$$

Where:

$$\beta = \frac{1}{2g{A_p}^2}\left(1 + K + \frac{\Lambda l}{D}\right) \tag{4.19}$$

For a system driven by a static reservoir or a pure elevation head, the input head H_0 is equivalent to the level of water above the inlet. For a system operating in a dynamic input such as a tidal stream, however, the flow into the system will already be moving at a velocity v. Therefore, from Bernoulli's principle:

$$H_0 = H + \frac{v^2}{2g} \tag{4.20}$$

Where H is the water level above the inlet. For a dynamic input flow, Equation 4.17 will therefore become:

$$\frac{\mathrm{d}Q_p}{\mathrm{d}t} = \frac{gA_p}{l}\left(H + \frac{v^2}{2g} - y - \frac{Q_p|Q_p|}{2g{A_p}^2}\left(1 + K + \frac{\Lambda l}{D}\right)\right) \tag{4.21}$$

4.1.2 Conservation of mass

By conservation of mass, the amount of fluid flowing into the junction shown in Figure 4.1 from upstream Q_p must be equal to the amount flowing out of the downstream end through the valve Q_v, plus the amount flowing into the chamber Q_c. Hence:

$$Q_p = Q_v + Q_c \tag{4.22}$$

The flow rate in the chamber Q_c can be determined from the area of the chamber A_c and the flow speed v_c within. The latter will be equal to the rate

of change of the water level $\frac{\mathrm{d}y}{\mathrm{d}t}$:

$$Q_c = A_c \frac{\mathrm{d}y}{\mathrm{d}t} \tag{4.23}$$

Therefore:

$$\frac{\mathrm{d}y}{\mathrm{d}t} = \frac{1}{A_c}\left(Q_p - Q_v\right) \tag{4.24}$$

Equation 4.24 is the continuity equation, and shows how the water level within the chamber is governed by the difference between the flow rate in the drive pipe and the discharge through the valve. Both will depend upon the input conditions and the behaviour of the valve.

4.1.3 Pressure, power and efficiency

To determine the hydraulic power P in the chamber, it is first necessary to know the pressure p of the water within. This can be determined using the unsteady form of Bernoulli's principle (Equation 4.27). A derivation for this, based upon that provided by Massachusetts Institute of Technology (2013), is summarised here and subsequently used to determine the chamber pressure.

Beginning with Euler's equation of motion for a one-dimensional, transient flow (Equation 4.25), and integrating between two points along a streamline s (illustrated in Figure 4.3) shows that:

$$\rho\frac{\partial v_s}{\partial t} + \rho v_s\frac{\partial v_s}{\partial s} = -\frac{\partial p}{\partial s} - \rho g\frac{\partial z}{\partial s} \tag{4.25}$$

$$\int_1^2 \rho\frac{\partial v_s}{\partial t}\partial s + \int_1^2 \rho v_s\frac{\partial v_s}{\partial s}\partial s = p_1 - p_2 + \rho g\left(z_1 - z_2\right) \tag{4.26}$$

$$\int_1^2 \rho\frac{\partial v_s}{\partial t}\partial s + \left(p + \frac{1}{2}\rho {v_s}^2 + \rho g z\right)_2 = \left(p + \frac{1}{2}\rho {v_s}^2 + \rho g z\right)_1 \tag{4.27}$$

From Figure 4.3, the integral on the left hand side of Equation 4.27 can be split into several terms:

$$\int_1^2 \rho\frac{\partial v_s}{\partial t}\partial s = \int_1^a \rho\frac{\partial v_s}{\partial t}\partial s + \int_a^b \rho\frac{\partial v_s}{\partial t}\partial s + \int_b^2 \rho\frac{\partial v_s}{\partial t}\partial s \tag{4.28}$$

If the area of the reservoir is assumed to be much greater than that of the pipe, and the pipe entry region is small compared to its length, then the transient velocities between (1) and (a) and (a) and (b) will be negligible

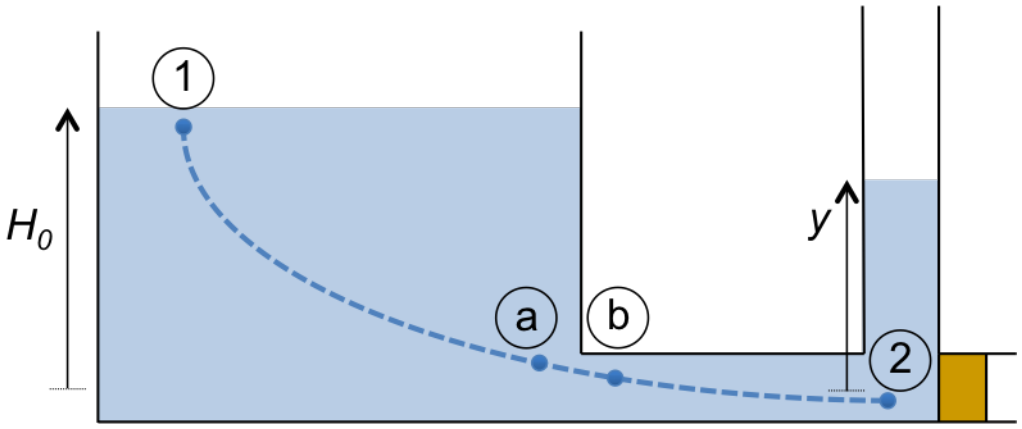

Figure 4.3: Streamline in the reservoir, chamber and valve system. Adapted from Massachusetts Institute of Technology (2013).

compared to those between (b) and (2). Therefore:

$$\int_1^2 \rho \frac{\partial v_s}{\partial t} \partial s \approx \int_b^2 \rho \frac{\partial v_s}{\partial t} \partial s = \int_b^2 \rho \frac{\partial v_2}{\partial t} \partial s = \rho \frac{\partial v_2}{\partial t} l \tag{4.29}$$

Combining Equation 4.29 with Equation 4.27 shows that:

$$\rho \frac{\partial v_2}{\partial t} l + \left(p + \frac{1}{2} \rho {v_s}^2 + \rho g z \right)_2 = \left(p + \frac{1}{2} \rho {v_s}^2 + \rho g z \right)_1 \tag{4.30}$$

Assuming that $v_{s1} = 0$ m/s, taking atmospheric pressure as gauge pressure (i.e. $p_1 = 0$ Pa), and rewriting in terms of pipe flow rate ($Q_p = v_p / A_p$), reservoir head (H_0) and chamber head (y):

$$\frac{\rho l}{A_p} \frac{\partial Q_p}{\partial t} + p_2 + \frac{\rho {Q_p}^2}{2 {A_p}^2} + \rho g y = \rho g H_0 \tag{4.31}$$

Given that the only derivative term in Equation 4.31 is with respect to time, the pressure at the chamber can therefore be computed as:

$$p_2 = \rho \left(g(H_0 - y) - \frac{{Q_p}^2}{2 {A_p}^2} - \frac{l}{A_p} \frac{\mathrm{d}Q_p}{\mathrm{d}t} \right) \tag{4.32}$$

The hydraulic power of the fluid in the chamber may be calculated according to its pressure and flow rate:

$$P = p_2 A_c \frac{\mathrm{d}y}{\mathrm{d}t} \tag{4.33}$$

Finally, the efficiency ϵ of the system can be defined as the ratio between

the power in the chamber and that available from the input flow:

$$\epsilon = \frac{P}{P_{av}} = \frac{P}{\rho g Q_0 H_0} \tag{4.34}$$

Where Q_0 represents the flow rate available from the input water supply. Given the behaviour that was observed during Chapter 3, the hydraulic power available on the downstroke is ignored during this analysis.

4.1.4 Valve behaviour

Solving Equations 4.17 and 4.24 is commonplace in the design of surge tanks for systems where a valve may close abruptly and then remain closed, such as shutting off the flow to a turbine in a conventional hydropower plant. In the WHES, however, a valve will repeatedly open and close at some frequency f, causing Q_v to vary periodically. It is therefore possible to approximate Q_v using a variety of different periodic waveforms, such as the sine, triangular, square and sawtooth waves illustrated in Figure 4.4.

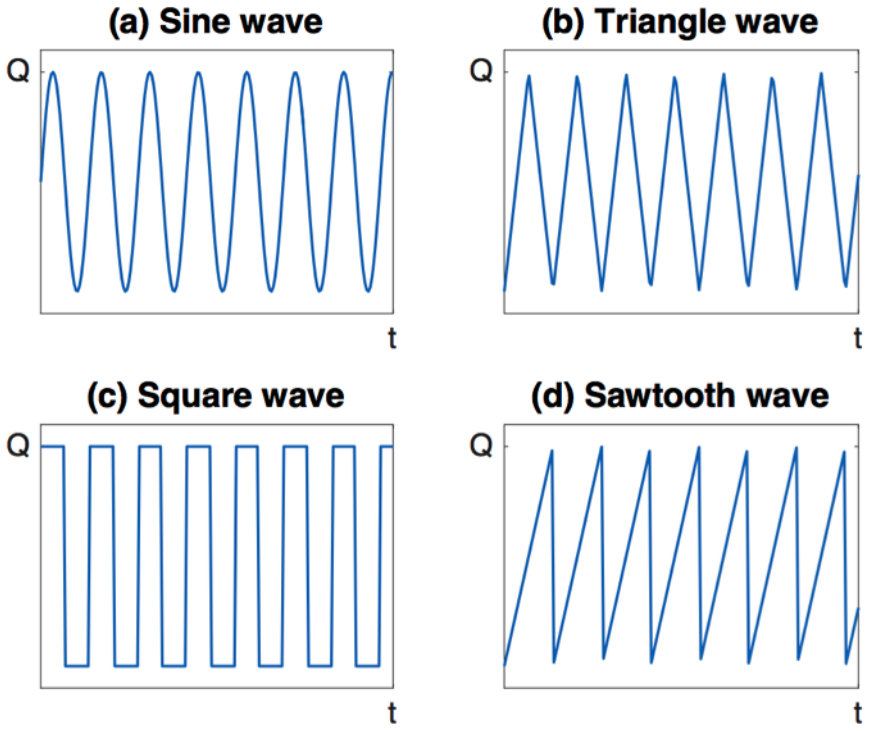

Figure 4.4: The four different waveforms used to approximate Q_v.

Approximating the flow rate in this manner dispenses with the need to directly model the valve, enabling the hydrodynamics of the system to be investigated independently of valve design. The waveforms shown in Figure

4.4 can be generated using Equation 4.35 for the sine wave, Equation 4.36 for the triangular wave, Equation 4.37 for the square wave and Equation 4.40 for the sawtooth wave.

$$Q_v = Q \sin(2\pi f t) \tag{4.35}$$

$$Q_v = Qf\left(t - \frac{f}{2}\left\lfloor 2ft + \frac{1}{2}\right\rfloor\right)(-1)^{\left\lfloor 2ft+\frac{1}{2}\right\rfloor} \tag{4.36}$$

$$Q_v = Q\left(2\lfloor ft\rfloor - \lfloor 2ft\rfloor + 1\right) \tag{4.37}$$

$$Q_v = 2Q\left(ft - \left\lfloor ft + \frac{1}{2}\right\rfloor\right) \tag{4.38}$$

Where Q is the peak discharge rate and f is the frequency of valve closure events. The symbol $\lfloor n \rfloor$ represents the floor function, which maps a given number n to the largest previous integer m:

$$\lfloor n \rfloor = \max\{m \in \mathbb{Z} | m \leq n\} \tag{4.39}$$

4.2 Methodology

4.2.1 Equation solution

If the frictional terms are included in the governing equations then cannot be solved analytically; numerical methods must be employed instead. The commercial software MATLAB (MathWorks, 2015) features a range of algorithms for solving ordinary differential equations numerically. One is *ode45* (MathWorks), which is a versatile algorithm and the one employed for the purposes of this investigation. The *ode45* algorithm is based on the Dormand-Prince method, one a family of explicit Runge-Kutta methods (Dormand and Prince, 1980). For a system of first order ordinary differential equations where the initial conditions are known:

$$\frac{\mathrm{d}y}{\mathrm{d}x} = F[x, y(x)], \qquad y(x_0) = y_0 \tag{4.40}$$

The general explicit Runge-Kutta method allows the value of y at a certain value of x to be calculated through the definition of a step of size $h > 0$:

$$y_{n+1} = y_n + h\sum_{i=1}^{8} b_i k_i \tag{4.41}$$

Where:

$$k_s = F[x_n + c_s h, y_n + h(a_{s1}k_1 + a_{s2}k_2 + \ldots + a_{s,s-1}k_{s-1})] \tag{4.42}$$

Particular Runge-Kutta methods are defined according to the number of solution stages s, the coefficients a_{ij} of the Runge-Kutta matrix, and the values of the coefficients b_i and c_i. One method of displaying these coefficients is to use a Butcher tableau, such as the example shown in Table 4.1.

Table 4.1: Example Butcher tableau illustrating the coefficients used by the general Runge-Kutta method.

0					
c_2	a_{21}				
$\vdots$	$\vdots$	$\ddots$			
c_s	a_{s1}	a_{s2}	$\dots$	$a_{s,s-1}$	
b_i	b_1	b_2	$\dots$	b_{s-1}	b_s

Table 4.2: Butcher tableau for the Dormand-Prince method (Dormand and Prince, 1980).

0							
$\frac{1}{5}$	$\frac{1}{5}$						
$\frac{3}{10}$	$\frac{3}{40}$	$\frac{9}{40}$					
$\frac{4}{5}$	$\frac{44}{45}$	$-\frac{56}{15}$	$\frac{32}{9}$				
$\frac{8}{9}$	$\frac{19372}{6561}$	$-\frac{25360}{2187}$	$\frac{64448}{6561}$	$-\frac{212}{729}$			
1	$\frac{9017}{3168}$	$-\frac{355}{33}$	$\frac{46732}{5247}$	$\frac{49}{176}$	$-\frac{5103}{18656}$		
1	$\frac{35}{384}$	0	$\frac{500}{1113}$	$\frac{125}{192}$	$-\frac{2187}{6784}$	$\frac{11}{84}$	
b_i^*	$\frac{35}{384}$	0	$\frac{500}{1113}$	$\frac{125}{192}$	$-\frac{2187}{6784}$	$\frac{11}{84}$	0
b_i	$\frac{5179}{57600}$	0	$\frac{7571}{16695}$	$\frac{363}{640}$	$-\frac{92097}{339200}$	$\frac{187}{2100}$	$\frac{1}{40}$

The Dormand-Prince method evaluates six functions to provide accurate

fourth and fifth order solutions, with an estimate of the solution error given as the difference between the two. If the value of the lower order step is defined as:

$$y_{n-1}{}^{*} = y_n + h\sum_{i=1}^{8} b_i{}^{*}k_i \tag{4.43}$$

The general error may be defined as:

$$e_{n+1} = y_{n+1} - y_{n+1}{}^{*} = h\sum_{i=1}^{8}(b_i - b_i{}^{*})k_i \tag{4.44}$$

A Butcher tableau can be extended to illustrate the values of $b_i{}^{*}$. Table 4.2 illustrates the coefficients used by the Dormand-Prince method.

An example of the MATLAB code employing *ode45* to solve Equations 4.17 and 4.24 is provided in Appendix D. The code was run using a laptop computer with 4 GB of RAM and a 2.7 GHz dual-core processor.

4.2.2 Investigation overview

The main aim of this study was to investigate variables that would otherwise prove too difficult, time consuming or expensive to investigate via physical experimentation. These include the behaviour of the flow through the check valve and device size.

The check valve is responsible for altering the momentum of the water within the drive pipe, and its behaviour is therefore a crucial factor in the performance of the WHES. Consequently, the first part of the mathematical study examined how device hydrodynamics are affected by varying the flow through the valve in fixed input conditions. This was achieved by investigating:

- The form of the flow rate through the valve (i.e. the four periodic wave functions described in Section 4.1.4) when it is closing at a fixed frequency and peak outflow rate.
- The frequency of the valve closures when the peak outflow rate is fixed.
- The peak flow rate through the valve when the closure frequency remains constant.

The system parameters were chosen to reflect those of the test rig discussed in Chapter 3 for the purposes of validation. These are presented in Table 4.3, along with the initial conditions used for solving the governing equations.

The initial flow rate within the drive pipe was set as 0.00 m^3/s to fully reflect the experiments presented in Chapter 3, where the water within the

Table 4.3: Summary of the parameters of the modelled system and the initial conditions used during equation solution.

Cross-sectional area of chamber A_c (10^{-4} m^2)	2.01
Cross-sectional area of pipe A_p (10^{-4} m^2)	2.01
Pipe diameter D (10^{-2} m)	1.6
Drive pipe length l (m)	1.30
Reservoir head H_0 (m)	0.50
Inlet head loss coefficient K (-)	0.50
Reynolds number Re (10^3)	8.40
Darcy friction factor Λ (10^{-2})	4.52
Initial chamber head y (m)	0.00
Initial pipe flow rate Q_p (m^3/s)	0.00

system was static until the ball valve between the drive pipe and reservoir was opened. The Reynolds number was calculated according to the diameter of the pipe and a mean flow speed of 0.50 m/s, which was determined from the flow rate measurements of Chapter 3.

Following this, attention was turned to the effect the input conditions have when the behaviour of the outflow remains constant. For this section of the study, the system parameters were kept identical to those shown in Table 4.3. The effect of input head was tested by varying H_0 in 0.25 m intervals, from 0.25 m to 0.75 m, respectively. A velocity input case, with $H = 0$ m and v = 0.5 m/s, was also simulated.

Finally, the effect of system size on performance was investigated. Table 4.4 summarises the parameters of the three system sizes that were tested during this study.

4.3 Validation

Before conducting a numerical analysis, it is important to check whether the solution of the governing equations produces results that are physically valid. This can be achieved by ensuring the step size of the solver is sufficiently small to accurately capture physical behaviour, and subsequently comparing the mathematical predictions to experimental data.

Table 4.4: Summary of parameters used for testing the effects of system size on performance.

System size	Small	Medium	Large
Drive pipe length (m)	1.30	1.30	1.30
Drive pipe diameter (cm)	1.60	3.20	4.80
Chamber diameter (cm)	1.60	3.20	4.80
Peak valve discharge (10^{-4} m^3/s)	2.01	8.04	18.1
Reservoir head (m)	0.50	0.50	0.50
Inlet head loss (-)	0.50	0.50	0.50
Reynolds number (10^3)	8.40	16.8	33.6
Darcy friction factor (10^{-2})	4.33	4.04	3.88
Initial chamber head (m)	0.00	0.00	0.00
Initial pipe flow rate (m^3/s)	0.00	0.00	0.00

4.3.1 Solution convergence

If the step size used during equation solution is too large, then details will be missed and the results less accurate. If the step size is too small, however, the solution process will take a longer period of time and may be computationally inefficient. A convergence study identifies an optimal step size by repeatedly solving a problem while systematically reducing the step size from one solution to the next. The difference between the predictions of one solution and the previous are quantified, allowing an acceptable step size to be chosen based on the increase in accuracy against computational cost. This process is most useful in the numerical solution of partial differential equations where step sizes are required for multiple variables; however it is still worthwhile to conduct when solving ordinary differential equations.

Table 4.5 details the results of the convergence study conducted prior to the rest of this investigation. Equations 4.17 and 4.24 were solved using a sawtooth function to approximate Q_v; the amplitude of this function Q was set to 2×10^{-4} m^3/s and the frequency was set to 2.5 Hz. The predictions for the chamber water level as a function of time were then studied using a peak analysis code to determine the mean amplitude of the oscillations within

the chamber. The accuracy of the different time-steps was quantified as the percentage difference between the mean amplitude predicted by one time-step and that predicted by the following case.

Table 4.5: Summary of the solution convergence study.

Solution number	Time-step size (ms)	Steps per second (-)	Mean oscillation amplitude (mm)	Solution error (%)
1	1000	1	47	0
2	500	2	47	29.8
3	250	4	33	-8.64
4	125	8	35.9	23.1
5	64	15.6	44.2	-9.22
6	32	31.3	48.2	-2.1
7	16	62.5	49.2	-0.1
8	8	125	49.3	N/A

Table 4.5 shows that the time-step can have a significant impact on the accuracy of the results, highlighting the importance of choosing an appropriate step size before conducting the investigation. A time-step of 16 ms was chosen for the rest of the study, due to the relatively low error of 0.10 % in the mean amplitude predictions as well as the manageable number of steps per second.

4.3.2 Comparison of results with experimental data

Figure 4.5 compares values of y that were computed through the solution of Equations 4.17 and 4.24 with data from one of the experimental runs with the 4.5×10^{-3} kg float discussed in Chapter 3. Although the equations predict the motion of water. rather than a floating body, the mass of the float was deemed sufficiently small for inertial effects to be neglected. A sawtooth wave was used to approximate the flow through the valve, with the frequency term set to that of the main frequency component seen in the data (3.6 Hz). The maximum flow rate through the valve set at 90 % of that available from the input head to account for the retardation of the flow by the valve. The remaining parameters used in the Equation salutation are equal to those shown in Table 4.4.

The predictions using the sawtooth wave appear to show good agreement with the observed float behaviour, with a root mean square error of 0.0138 m between the predictions and the observations, corresponding to 3.37 % of the median float position between 10-12 s. The agreement is also visible in Figure 4.5; the predicted oscillations feature both the same broad peaks and sharp

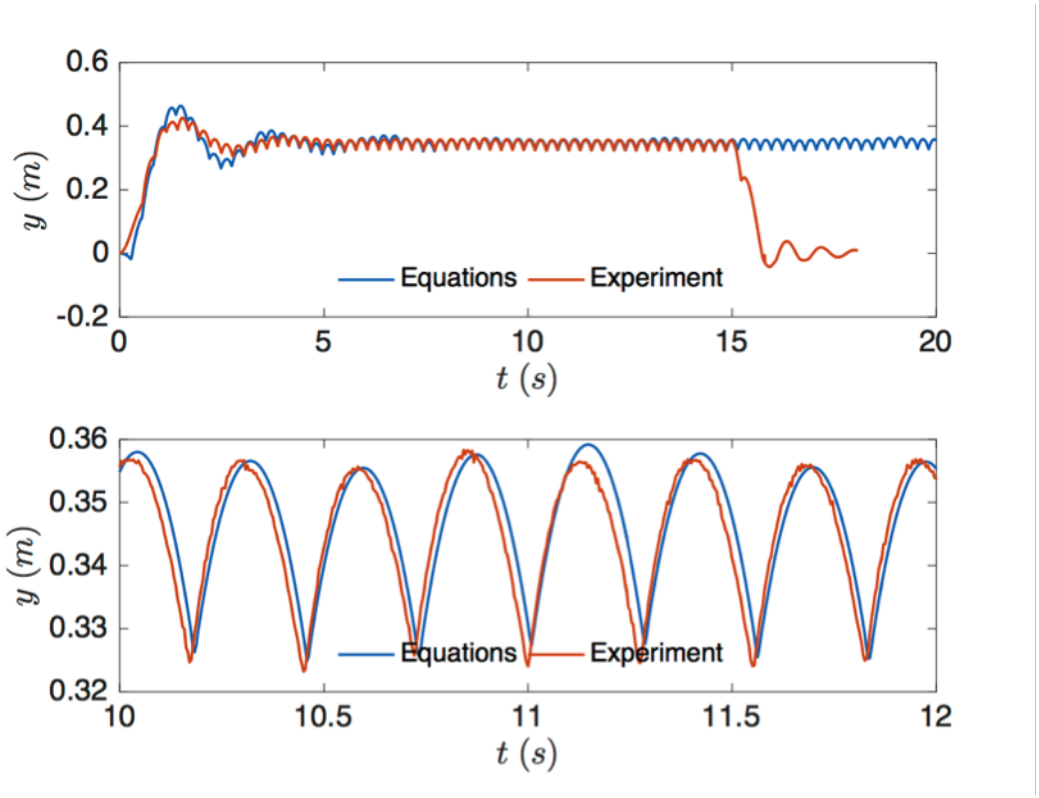

Figure 4.5: Comparison of sawtooth wave boundary condition predictions with experimental data.

troughs visible in the experimental data. This indicates that the equations are capable of accurately replicating physical behaviour and that they are a valid method for investigating the hydrodynamics of the WHES.

One difference between the equations and the experimental data can be seen in the time required for flow to reach a steady periodic state. This took approximately 10 s for the mathematical predictions, compared to the 5 s seen in the experimental data. This is due to the assumption of a constant maximum flow rate through the valve and an instantaneous increase in the flow rate into the system, rather than the gradual one that occurred in reality.

4.4 Study results

4.4.1 Effect of outflow rate

This section presents the effects of the outflow rate on the performance of the WHES. All of the initial conditions and system parameters were kept constant for each case; Equations 4.17 and 4.24 were solved according to the numerical methods described in Section 4.2.1 using a time-step of 16 ms.

Form of Q_v

In a conventional surge tank, the valve chokes the discharge out of the pipe rather than generating periodic flow. It is therefore useful to discuss the oscillations generated by a single closure before investigating those caused by a periodic valve. Figure 4.6 illustrates how the water level within the chamber will vary following a single valve closure (either full or partial) that chokes the discharge to a greater or lesser extent.

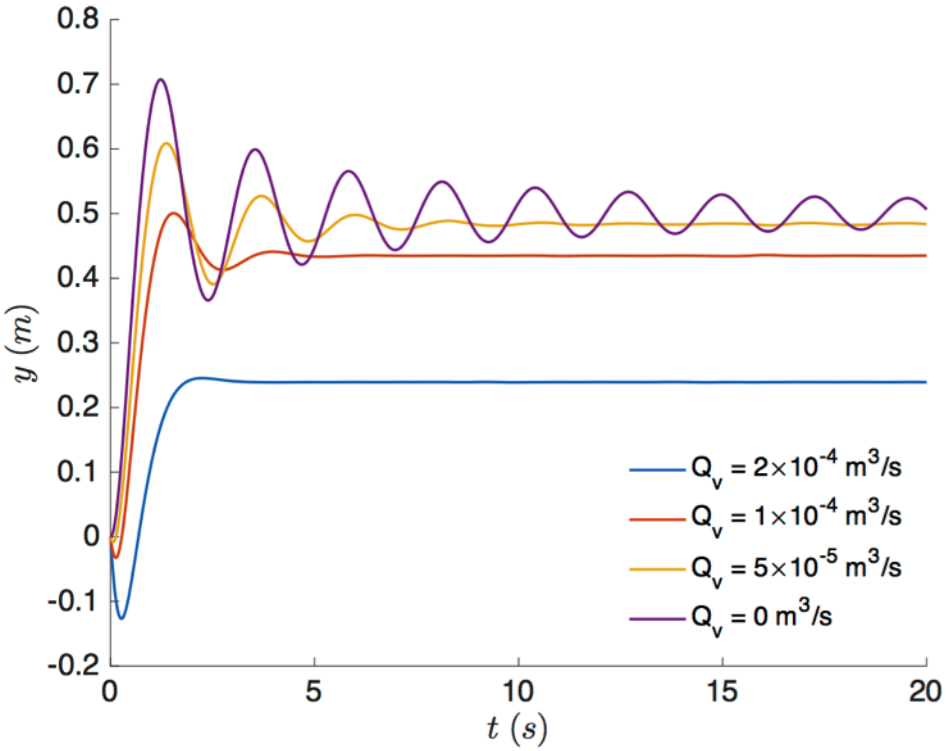

Figure 4.6: Chamber water level predictions for various constant values of Q_v.

The curves shown in Figure 4.6 are damped sine waves, the typical shape of the pressure oscillations generated by a partial or full valve closure (Chaudhry, 2014). The amplitude of the oscillations is dependent upon Q_v, with the largest surges occurring when Q_v= 0 m^3/s and the smallest when the outflow is largest ($Q_v = 2 \times 10^{-4}$ $m3$/s). This is because the water within the pipe experiences the greatest change in momentum in former case and thus a larger pressure surge, to the extent that the water level within the chamber exceeds the input head during some of the initial oscillations. The mean value of y ($\bar{y}$) also increases as Q_v is reduced due to conservation of mass, eventually matching the input head of 0.50 m at Q_v= 0 m^3/s.

Figure 4.7 illustrates the corresponding predictions for the pipe flow rate Q_p. Again, the largest oscillations occur when Q_v= 0 m^3/s; in this case, Q_p

reverses direction due to the large head in the chamber rising above that of the reservoir. The reduction in the peak flow rate from 1.86×10^{-4} m^3/s to -9.38×10^{-5} m^3/s in a time of 1.28 s corresponds to a linear deceleration of approximately 1.10 m/s^2. As with the surface elevation, the flow rate decays with time due to frictional damping.

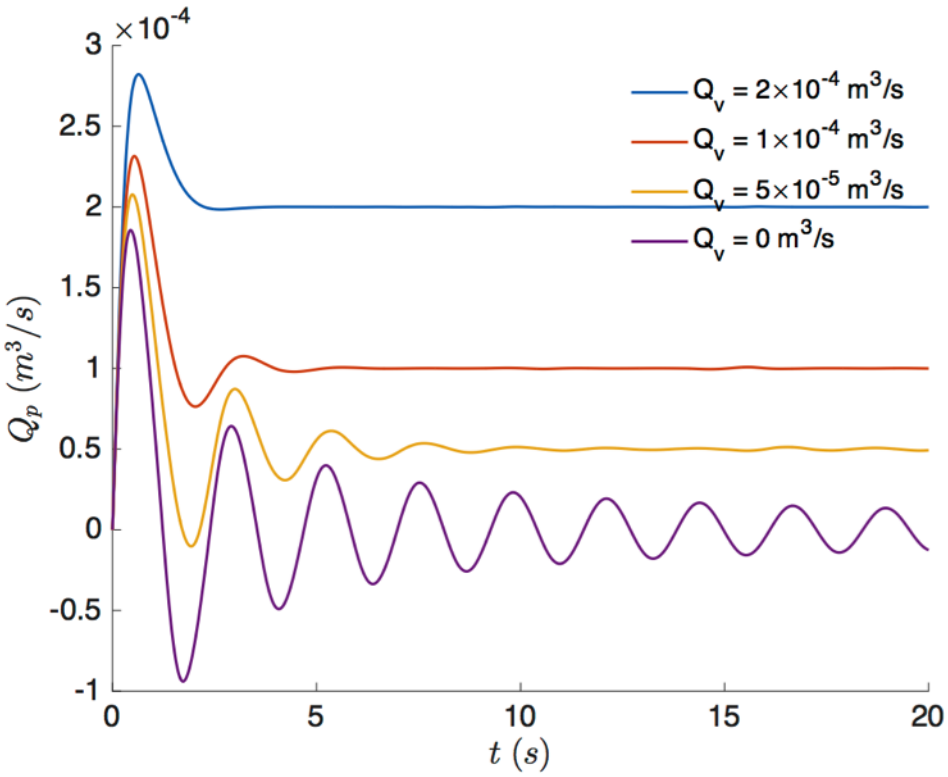

Figure 4.7: Drive pipe flow rate predictions for various constant values of Q_v.

The predictions shown in Figure 4.6 and Figure 4.7 indicate that the amplitude of the oscillations generated by a periodic Q_v will be governed by how the discharge out of the system varies with time. This will depend upon factors such as the maximum discharge permitted by the valve, the frequency of the valve closures and the overall form of the flow rate as a function of time.

Figure 4.8 presents predictions of the water level within the chamber for a system where Q_v is modelled using sinusoidal, triangular, square and sawtooth functions. The four different Q_v waves were generated with Equations 4.35 – 4.40, with Q set to $2 \times 10^{-4} m^3$/s and $f = 3$ Hz for each case. A second plot shown in Figure 4.9 presents a scaled view of these predictions between 15 – 20 s. The corresponding pipe flow rate Q_p, chamber pressure p and hydraulic power P predictions between 15 – 20 s are shown in Figures 4.10, 4.11 and 4.12 respectively.

Figure 4.8 and Figure 4.9 show that the oscillations generated by periodic discharge are quite different to those generated by constant outflow, as they

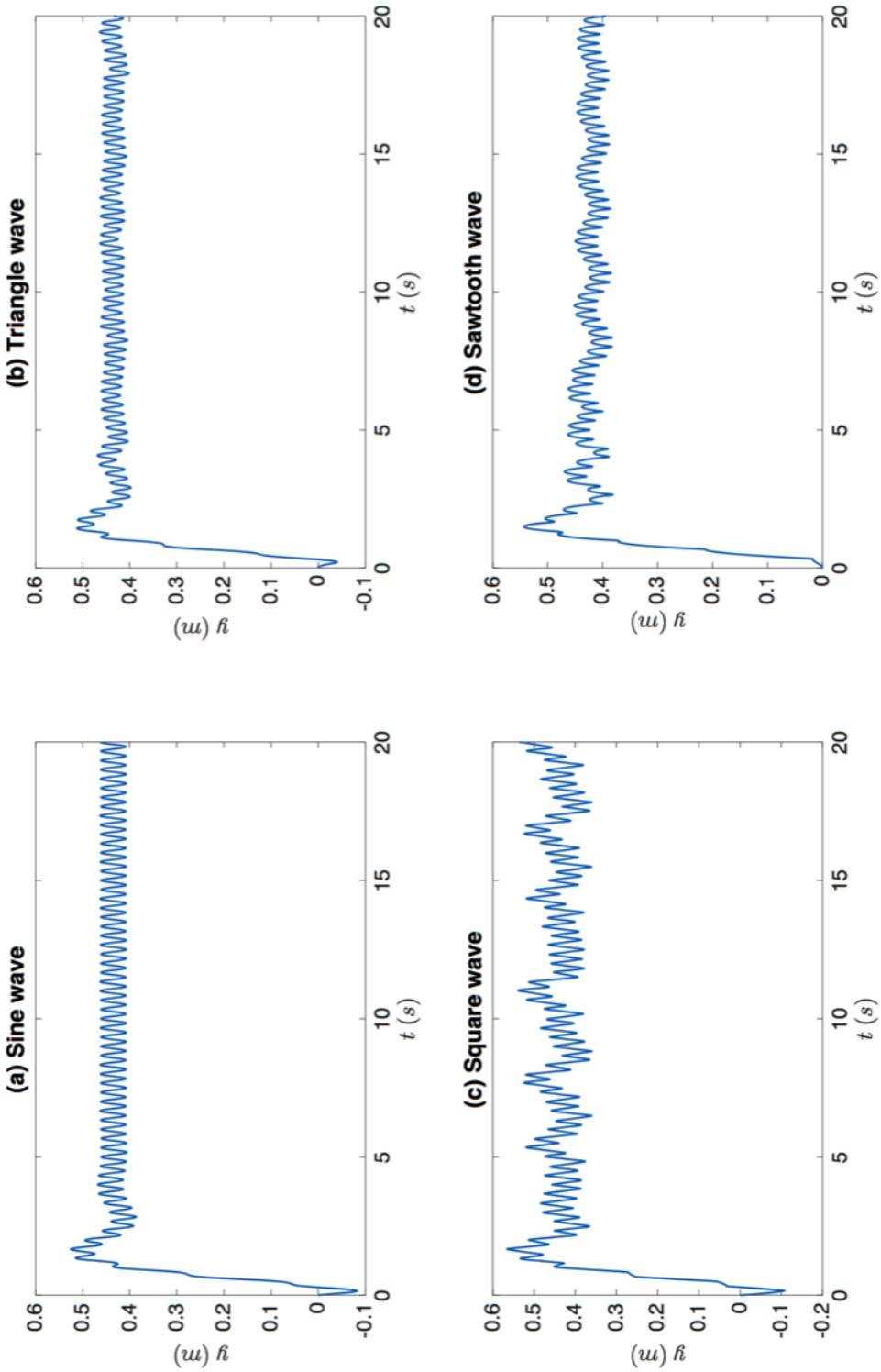

Figure 4.8: Chamber water level predictions for four different periodic functions representing Q_v.

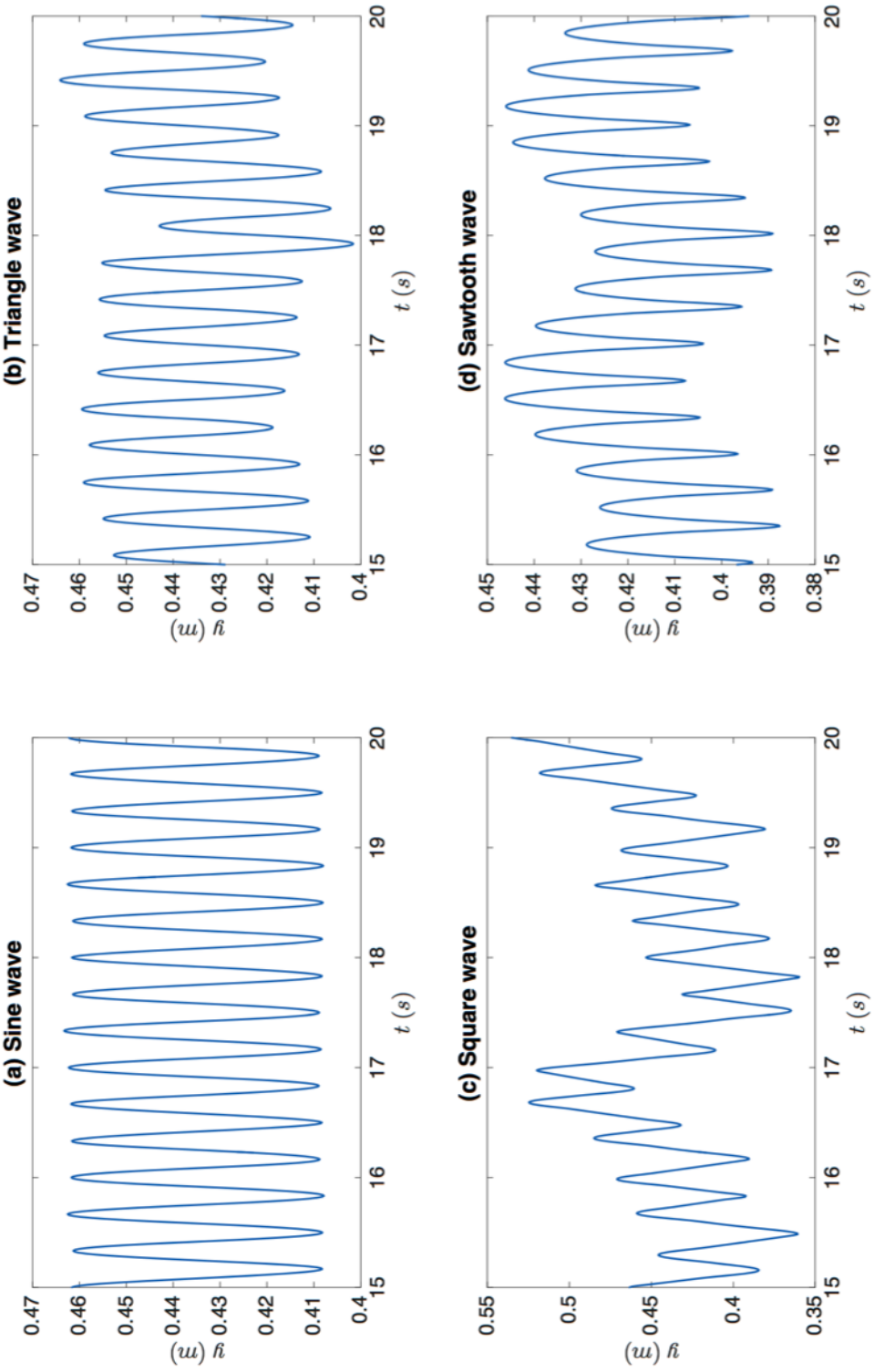

Figure 4.9: Scaled view of the chamber water level predictions shown in Figure 4.8

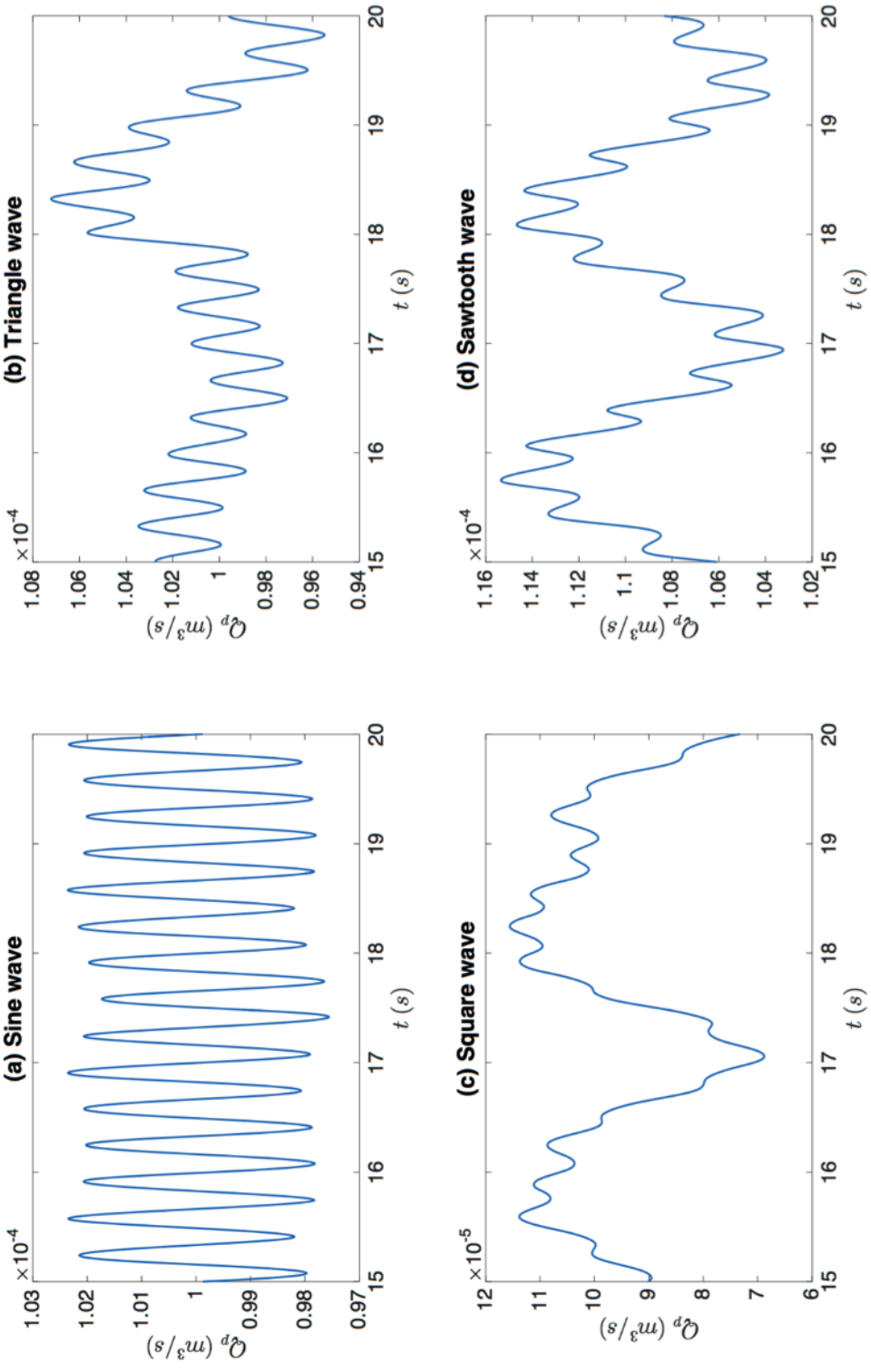

Figure 4.10: Drive pipe flow rate predictions for predictions for four different periodic functions representing Q_v.

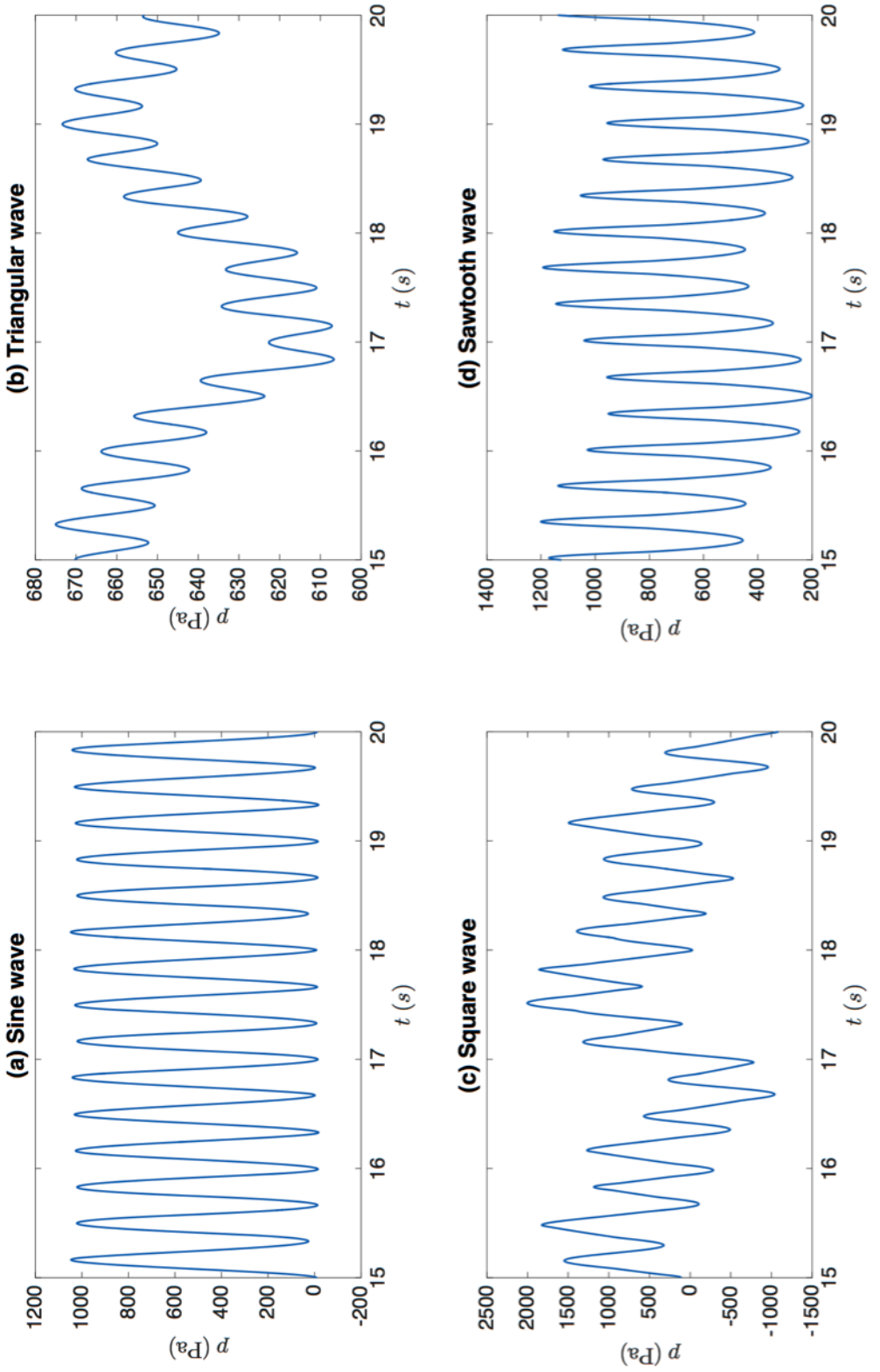

Figure 4.11: Chamber pressure predictions for four different periodic functions representing Q_v.

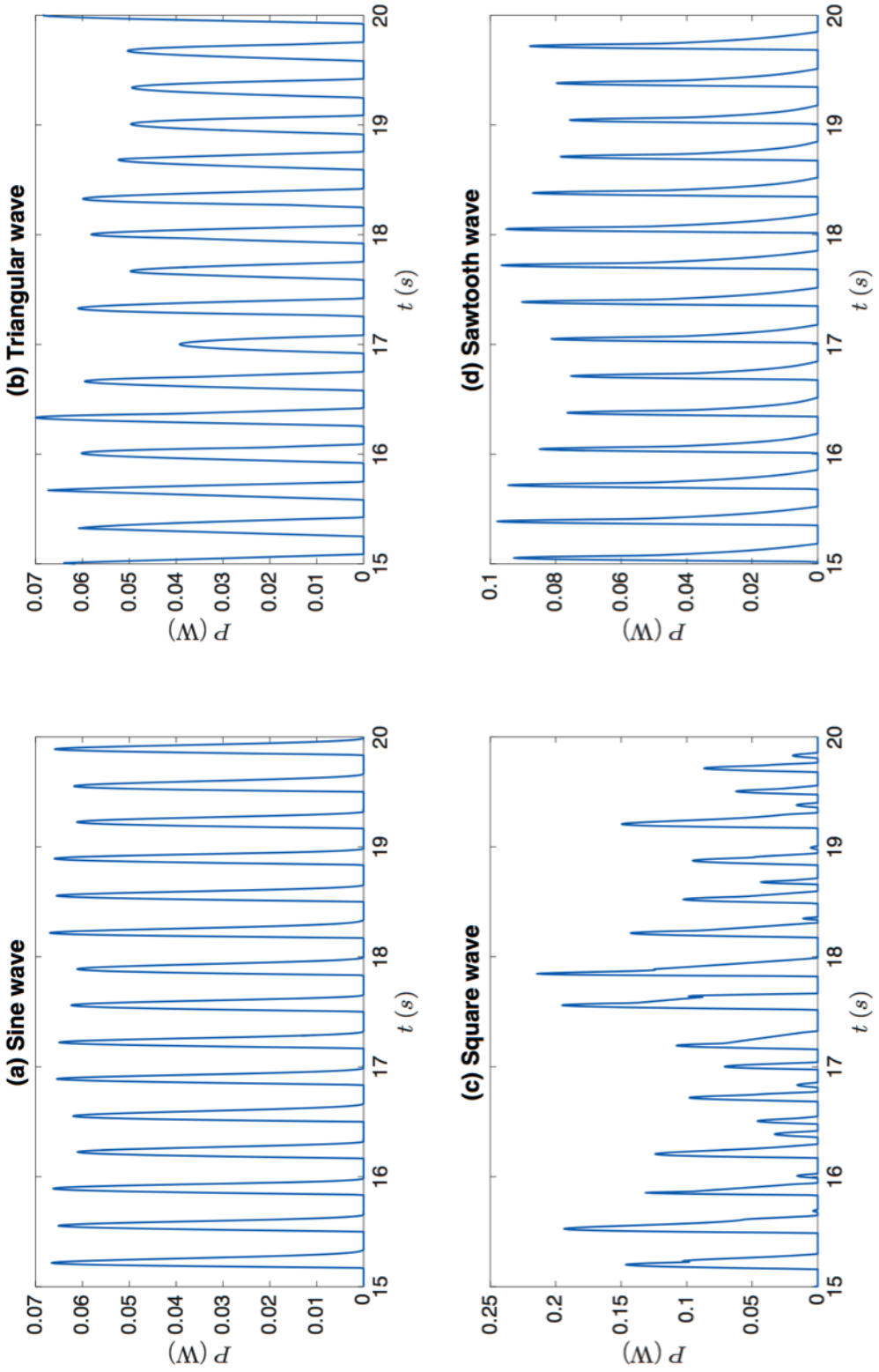

Figure 4.12: Hydraulic power predictions for four different periodic functions representing Q_v.

Table 4.6: Summary of the characteristics of the oscillations and pressure surges generated by the four periodic outflow functions between 15 – 20 s.

Sine	Sine	Triangle	Square	Sawtooth
$\bar{y}$ (m)	0.44 ± 0.02	0.43 ± 0.02	0.44 ± 0.04	0.42 ± 0.01
$\bar{a}$ ($\times 10^{-3}$ m)	52.8 ± 0.68	42.7 ± 3.00	78.6 ± 14.7	38.1 ± 2.90
$\overline{Q_v}$ ($\times 10^{-4}$ m^3/s)	1.00 ± 0.71	0.99 ± 0.58	1.02 ± 0.99	0.98 ± 0.58
$\overline{\Delta Q_p}$ ($\times 10^{-6}$ m^3/s)	4.13 ± 0.05	3.32 ± 1.17	10.0 ± 15.3	2.90 ± 1.21
$\overline{\Delta p}$ ($\times 10^{2}$ Pa)	10.3 ± 0.10	6.55 ± 0.16	11.9 ± 5.38	10.1 ± 0.91
$\overline{P}$ ($\times 10^{-2}$ W)	1.54 ± 2.26	1.70 ± 2.14	2.76 ± 4.51	1.63 ± 2.54
$\overline{P_{max}}$ ($\times 10^{-2}$ W)	6.42 ± 0.22	5.68 ± 0.81	8.63 ± 6.23	8.63 ± 0.81
$\bar{\epsilon}$ (%)	3.13 ± 4.59	3.45 ± 4.35	5.62 ± 9.16	3.31 ± 5.17
$\overline{\epsilon_{max}}$ (%)	13.0 ± 0.46	11.5 ± 1.65	17.8 ± 12.5	17.5 ± 1.64

are comparatively small in amplitude. From Figure 4.8, these smaller oscillations become apparent for each periodic function as y approaches its initial maximum of around 0.5 m. After this, $\bar{y}$ oscillates briefly before settling to a relatively consistent value. Although the maximum flow rate for all of the periodic cases is 2×10^{-4} m^3/s, equivalent to the least choked flow case presented in Figure 4.6, for all of the periodic cases $\bar{y}$ is much greater than the 0.24 m of the constant case.

This can be seen more clearly in Table 4.6, which summarises the data presented in Figures 4.9 to 4.12. This includes the mean water level $\bar{y}$, the mean oscillation amplitude $\bar{a}$, the mean valve discharge $\overline{Q_v}$, the mean variation in the drive pipe flow rate $\overline{\Delta Q_p}$, the mean pressure surge $\overline{\Delta p}$, the mean hydraulic power $\overline{P}$ and the mean peak hydraulic power $\overline{P_{max}}$ for each of the four periodic cases. The mean efficiency $\bar{\epsilon}$ and mean peak efficiency $\overline{\epsilon_s}$ values, calculated according to the input head and a mean input flow speed of 0.5 m/s, are also presented.

The difference in $\bar{y}$ between the periodic and constant discharge cases is due to the lower mean outflow rate created by the periodic discharge, which increases the mean water level due to conservation of mass. This will be of importance during the design of a power take-off for the system, since the mean water level within the chamber will govern the positioning and size of the generator components. Given that the mean outflow rate is broadly similar for each of the periodic functions, there is little difference in the mean water level between them. The effect of the peak outflow rate and valve closure

frequency on $\bar{y}$ are discussed below.

Another subject of interest is the shape of the oscillations. From Figure 4.9, the oscillations generated by the periodic functions are different to one another and those of the constant outflow cases presented in Figure 4.6. While the sinusoidal Q_v term produces sinusoidal oscillations in the chamber, the other waveforms generate different shape oscillations of varying amplitude. For example, the triangular Q_v function produces oscillations that are similar in shape to the sinusoidal function, however their mean amplitude is smaller and there is a subtle variation in the position that their minima and maxima occur. This variation can be seen in the order of magnitude difference between the amplitude standard deviations for the two functions.

From Table 4.6, the square wave Q_v term, which generates waves that are roughly triangular with rounded minima and maxima, produces the largest amplitude oscillations. Although the frequency is constant at the 3 Hz that was set in the boundary condition equation (as it is for all of the periodic functions), the square wave amplitude varies considerably from one oscillation to the next. This can be seen in the standard deviation, which is the largest of all of the periodic functions, indicating that the square wave oscillations are the most widely distributed around the mean. The square wave generates the largest amplitude oscillations since, from Figure 4.4, it is the function in which Q_v is at its maximum and minimum for the longest period. Thus, the flow rate within the drive pipe is subject to the greatest changes and the largest pressure surges are generated. As a result of this, the square wave boundary condition also provides the greatest hydraulic power and efficiency.

The sine wave produces the second largest amplitude oscillations and pressure surges, again because Q_v is close to its maximum and minimum values for a longer period. The triangle and sawtooth waves produce the lowest amplitude oscillations, because Q_v is only very briefly at its maximum and minimum. It is interesting to note that, while the four periodic functions affect the shape of the oscillations within the chamber, the fluctuations of the flow rate within the pipe are all of similar shape. The only differences are in the magnitude and variation from one flow rate oscillation to the next.

For each wave function, the power is produced in sharp spikes that correspond to the generation of a pressure surge. The predicted values yield a mean hydraulic efficiency of between 3.13 – 5.62 %, depending upon the valve flow rate function. The magnitude of the hydraulic power peaks relative to the mean is between 2.99 to 4.33, which is smaller than the 18.2 found for the piston during the experiments of Chapter 3. This is ascribed to the difference in the power between the water itself and an object it is driving, as well as

measurement inaccuracy from the motion tracking method.

Of all of the periodic functions, the sawtooth wave produces the oscillations that most closely resemble those generated by the test rig of Chapter 3. This can be seen in Section 4.3.2, where the water level predictions of the sawtooth wave closely match the experimental data. In a real system, the outflow rate will suddenly drop to zero following a valve closure, however it will take a longer time to recover to its maximum when the valve reopens. This is most closely approximated by the sawtooth wave, and hence this function is used for the remainder of the analysis presented in this section.

Valve closure frequency and discharge flow rate

Figure 4.13 illustrates the effect that the valve closure frequency f_{valve} and the peak outflow rate Q have on the mean amplitude of the oscillations within the chamber. The sawtooth function was used to approximate the flow rate through the valve, with Q varied in 0.5×10^{-4} m^3/s intervals from 1.5×10^{-4} to 2.5×10^{-4} m^3/s. For each value of Q, f_{valve} was varied in 0.1 Hz intervals from 0.1 to 5 Hz. The mean oscillation amplitude was computed over a 10 s period following the convergence of the solution to periodic flow.

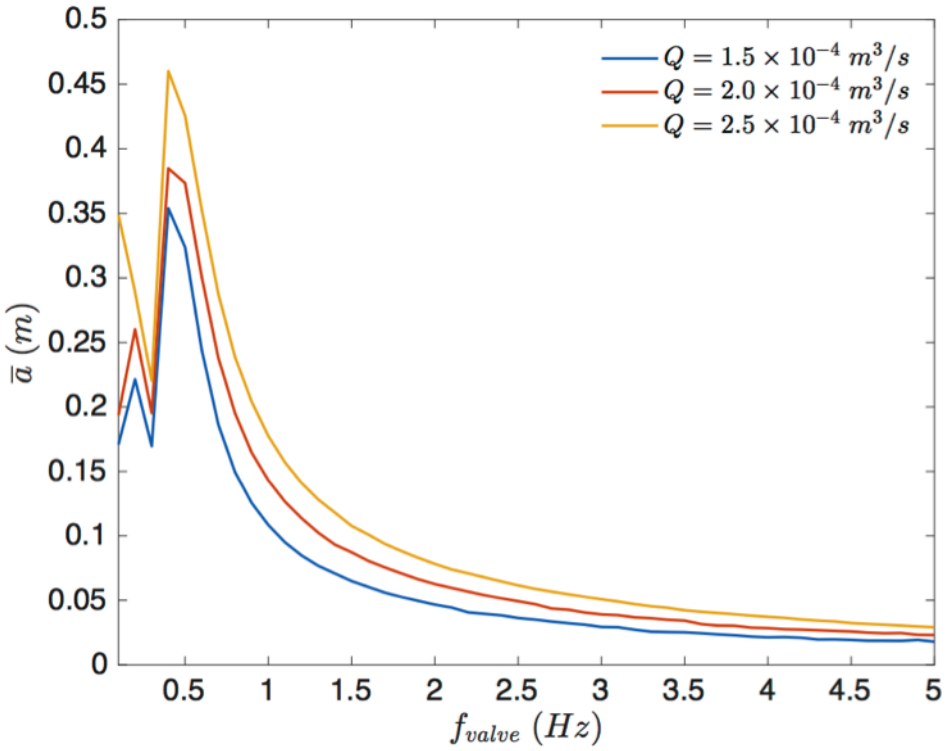

Figure 4.13: Effect of maximum outflow rate and valve closure frequency on oscillation amplitude.

Figure 4.13 shows that the valve closure frequency and peak outflow rate

have a significant impact on the oscillation amplitude. For each outflow case, the largest oscillations are generated when the valve closure is around 0.4 – 0.5 Hz, with smaller oscillations generated as the valve frequency is increased further. The relationship above 0.50 Hz can be quantified as:

$$\ln(\bar{a}) = \ln(Q)(\beta_1 \ln(\bar{f}) + 1) + \beta_2 \tag{4.45}$$

Where β_1 and β_2 are constants equal to 0.131 ± 0.019 and 6.543 ± 0.011, respectively. These values are somewhat arbitrary, since they will be affected by parameters such as input head and chamber area that Equation 4.45 does not consider.

The reason a higher Q generates larger amplitudes is due to the momentum changes experienced by the water within the drive pipe. A greater Q creates a larger change in momentum when the outflow drops to zero, generating a larger pressure surge and a larger oscillation. Lower values of f_{valve} enables the flow rate within the drive pipe to recover by a greater extent from one valve closure to the next. This results in a larger difference between the inflow and outflow when the valve does close, creating a bigger momentum change and larger oscillations. If the frequency is too low, however, then the chamber water level will oscillate a second time at a lower amplitude (similar to Figure 4.6), diminishing $\bar{a}$.

The magnitude of the pipe flow rate oscillations $\overline{\Delta Q_p}$ are illustrated in Figure 4.14. The relationship is very similar to that between the chamber water level oscillations and frequency, with the largest values occurring at 0.4 – 0.5 Hz. Increasing the valve discharge rate serves to increase $\overline{\Delta Q_p}$, since it enables the drive pipe flow rate to reach a higher value before a valve closure.

Unlike the $\bar{a}$, there is some variation at the higher frequencies shown in Figure 4.14. This is because $\overline{\Delta Q_p}$ is much less consistent at higher frequencies, which negatively affects the ability of the peak analysis code to identify the peaks within the signal. This is highlighted by Table 4.7, which provides the calculated mean, standard deviation and relative standard deviation for $\overline{\Delta Q_p}$ for selected values of f_{valve} for the $Q = 2.0 \times 10^{-4}$ m^3/s case.

Varying the outflow rate and closure frequency also serves to alter the mean water level $\bar{y}$ within the chamber. As illustrated by Figure 4.15, when the outflow rate is largest, the mean drive pipe flow rate $\overline{Q_p}$ is larger and the mean water level in the chamber is relatively low. This is due to conservation of mass; when the peak outflow rate is lower, less of the water within the drive pipe can escape the system. This causes the $\bar{y}$ to rise and thus increases the resistance to the flow in the drive pipe, reducing $\overline{Q_p}$. The relationship between

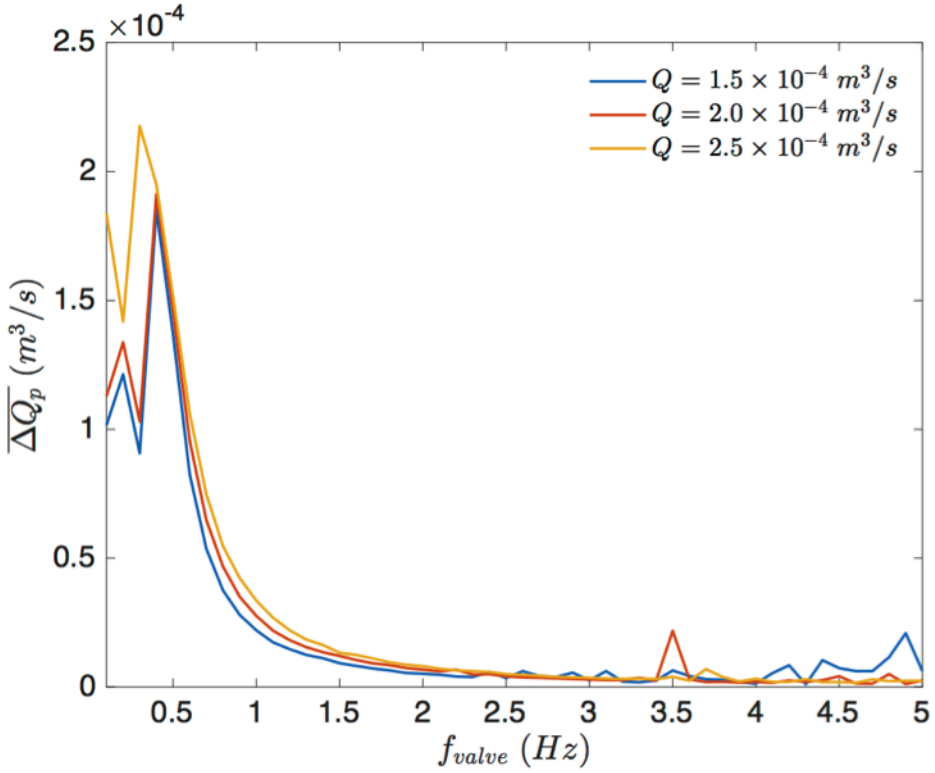

Figure 4.14: Effect of maximum outflow rate and valve closure frequency on variation in input flow rate.

Table 4.7: Mean, standard deviation and relative standard deviations of the amplitude of the flow rate oscillations for the $Q = 2.0 \times 10^{-4}$ m^3/s case.

$f_{valve}(Hz)$	$\overline{\Delta Q_p}$ $(\times 10^{-6} m^3/\mathrm{s})$	σ $(\times 10^{-6} m^3/\mathrm{s})$	σ (%)
0.5	146	2.15	1.48
1.0	27.6	3.60	13.0
1.5	12.0	4.37	36.3
2.0	6.73	2.01	29.8
2.5	4.11	0.82	19.9
3.0	2.92	0.67	23.1
3.5	21.7	23.0	106
4.0	1.98	2.44	123
4.5	4.08	6.50	159
5.0	2.54	4.23	167

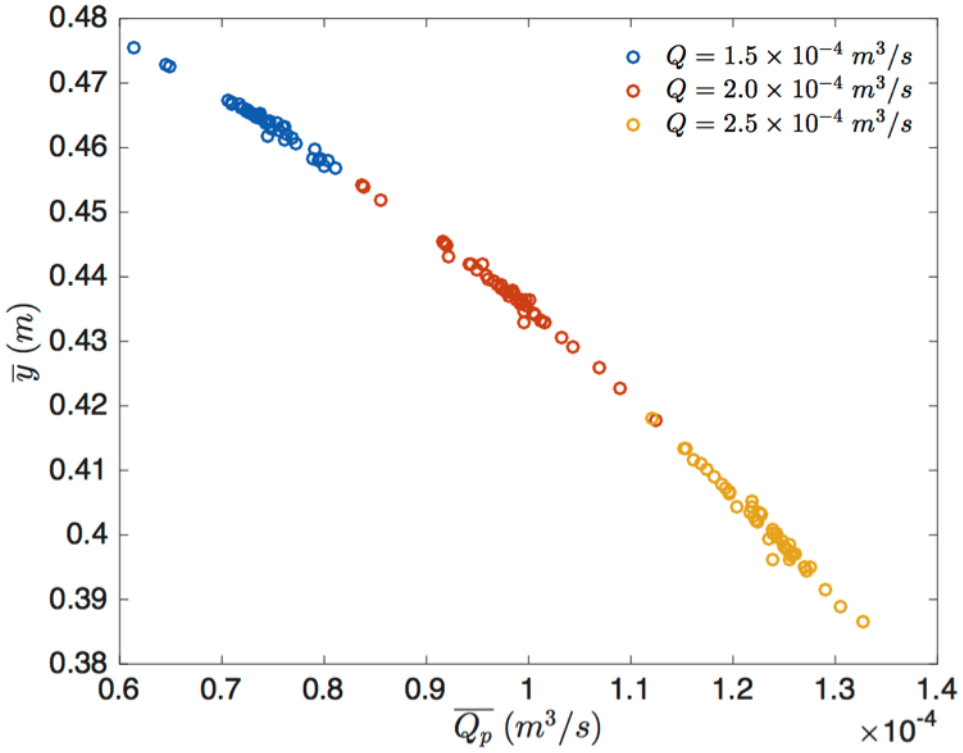

Figure 4.15: Relationship between maximum outflow rate, mean drive pipe flow rate and mean chamber water level.

mean drive pipe flow rate and mean chamber water level can be quantified as:

$$\bar{y} = Q(\beta_1 \overline{Q_p} + 1) + \beta_2 \tag{4.46}$$

Where the constants β_1 and β_2 are equal to $-7.215 \pm 0.438 \times 10^{-6}\ s^2/m^5$ and $0.582 \pm 0.042\ s/m^2$, respectively.

The effect of outflow rate and valve closure frequency on the magnitude of the pressure surges is illustrated in Figure 4.16. The relationship is again very similar to that shown in Figures 4.13 and 4.14. The largest pressure surges are available when the valve closes less frequently, with the peak value occurring at around 0.60 Hz. Above this value, the relationship between the variables can be quantified as:

$$\ln(\overline{\Delta Q_p}) = \ln(Q)\left(\beta_1 \ln(\bar{f}) + 1\right) + \beta_2 \tag{4.47}$$

Where the constants β_1 and β_2 are equal to 0.14 ± 0.01 and -16.4 ± 0.05, respectively.

Given that the outflow rate and valve closure frequencies govern the chamber water level, flow rate oscillations and pressure surges, they will also affect the power and thus the efficiency of the WHES. This is illustrated in Figure

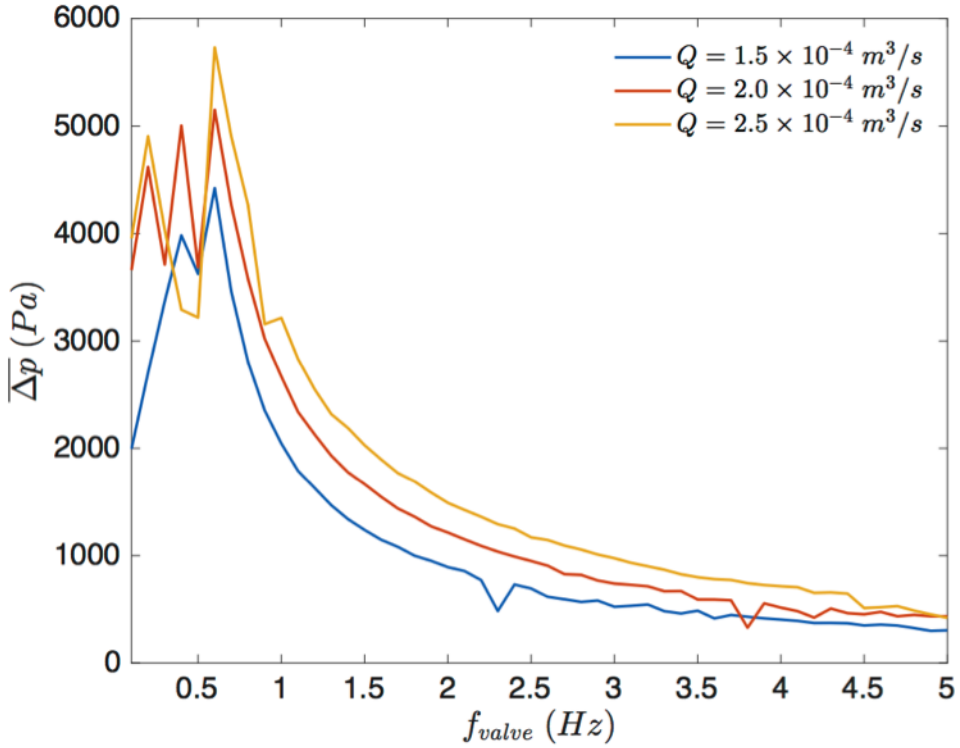

Figure 4.16: Effect of maximum outflow rate and valve closure frequency on the mean pressure surge.

4.17, which shows the mean hydrodynamic efficiency $\bar{\epsilon}$ as a function of the various valve closure frequencies and outflow rates. The hydraulic efficiency of the system is greatest at around 0.50 Hz, when the pressure surges are at their strongest and the amplitude of the oscillations is largest. The extra power this provides per oscillation more than compensates for them occurring less frequently.

Increasing the peak outflow rate through the valve serves to increase the efficiency of the system; the $Q = 2.5 \times 10^{-4}$ m^3/s case has a mean efficiency of 10.3 % at 0.60 Hz, which is significantly greater than the 6.29 % of the $Q = 1.5 \times 10^{-4}$ m^3/s case. This suggests that an infrequently closing valve, which impedes the flow as little as possible when it is open, will be necessary if the efficiency of the system is to be maximised.

4.4.2 Input conditions

Static input head

The effect of reservoir head level H_0 on the amplitude of the oscillations within the chamber is shown in Figure 4.18. Using the sawtooth boundary condition, the peak discharge rate was kept constant at $Q = 2.0 \times 10^{-4}$ m^3/s while the

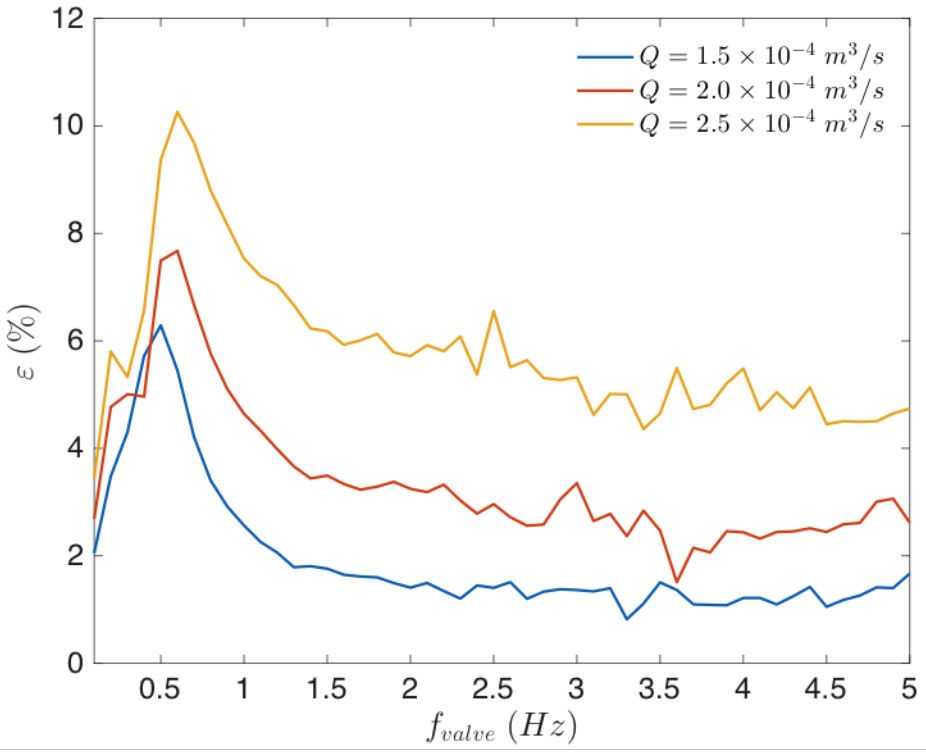

Figure 4.17: Effect of maximum outflow rate and valve frequency on hydraulic efficiency.

valve closure frequency was again increased in 0.1 Hz intervals from 0.1 – 5 Hz.

From Figure 4.18, varying the input into the system has very little effect on the oscillations within the chamber, provided that the valve behaviour remains constant. This indicates that the hydrodynamic behaviour of the system is almost entirely dependent upon the valve; with an appropriate control system and valve design, it should be possible to control the power output relative to the input conditions.

This can be seen in Figure 4.19, which illustrates the effect of input head and valve closure frequency on the mean hydraulic power available in the chamber. Although there is some variation between the three input heads, Figure 4.19 shows that the mean chamber power is broadly independent of the input conditions if the valve behaviour remains constant, particularly around the peak values at 0.5 Hz. This is because the momentum changes experience by the water remain constant, and hence the same pressure surges are generated.

As shown in Figure 4.20, the main variable governed by altering the input is the mean chamber water level $\bar{y}$. Since a larger input head provides a greater mean flow rate within the drive pipe while the outflow rate is held constant, $\bar{y}$ increases to conserve mass. The power take-off of a physical device operating

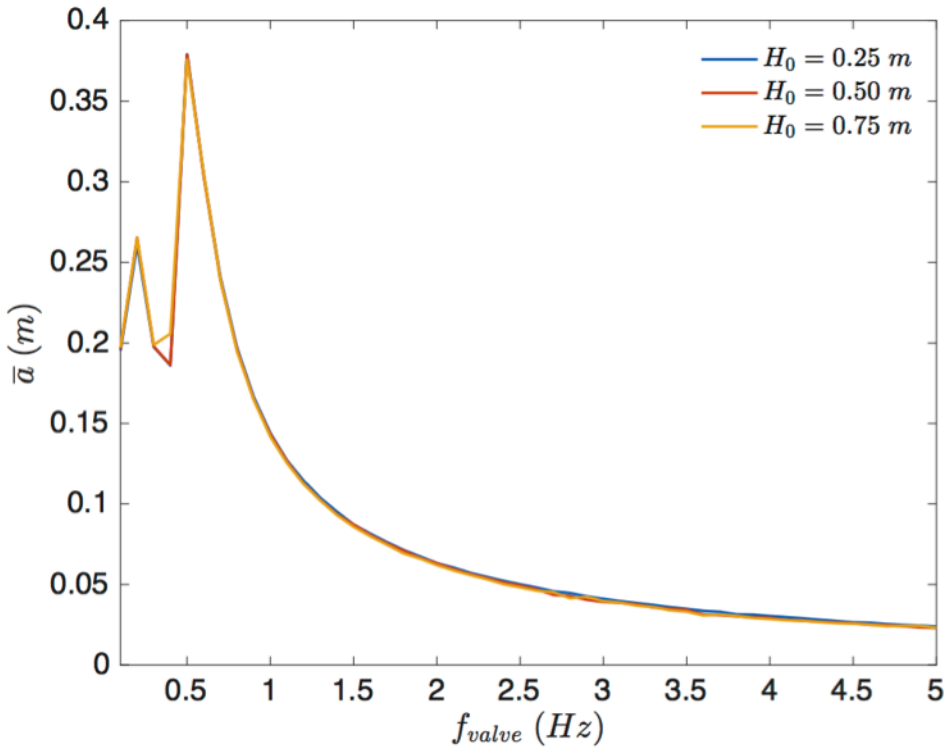

Figure 4.18: Effect of input head and valve closure frequency on chamber oscillation amplitude.

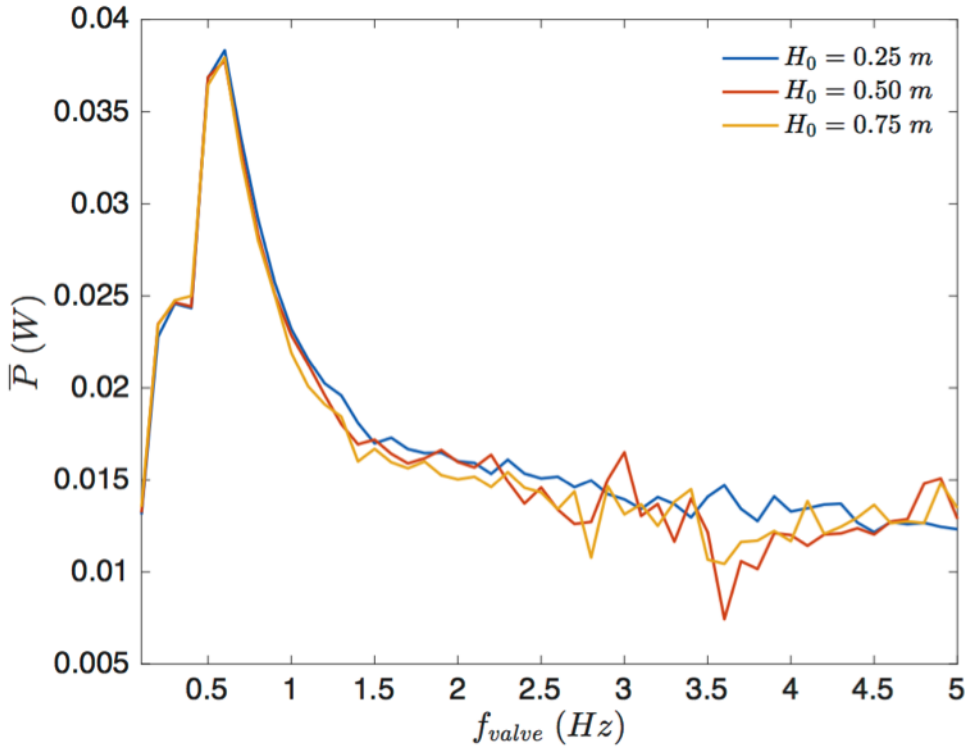

Figure 4.19: Effect of input head and valve closure frequency on hydraulic power.

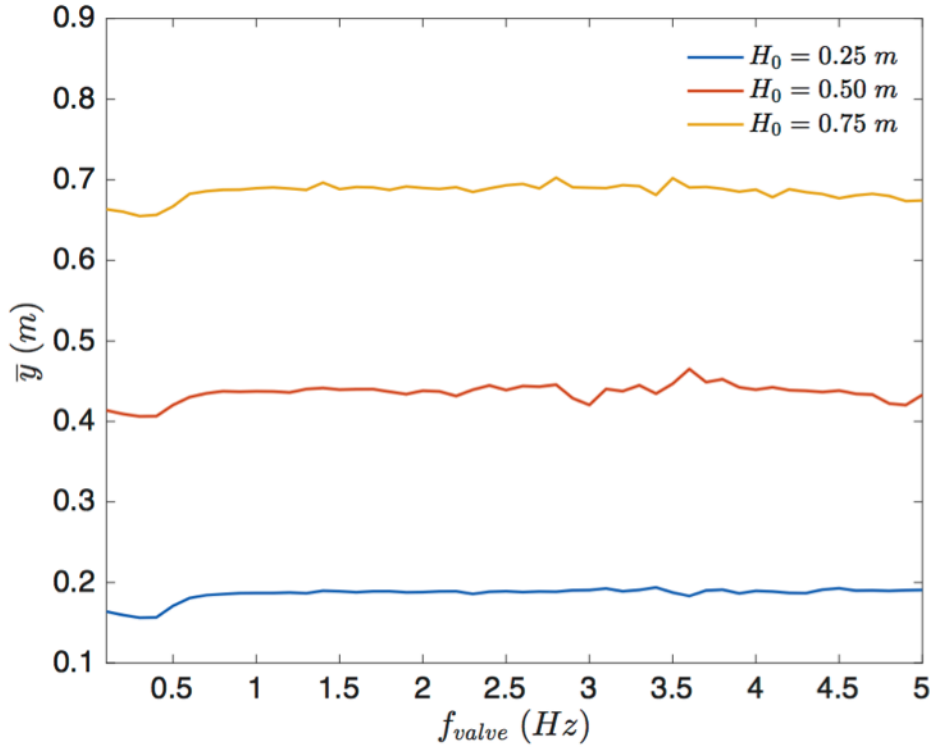

Figure 4.20: Effect of input head and valve closure frequency on mean chamber water level.

in variable input conditions, such as those provided by tidal currents, will therefore need to be capable of dealing with a varying mean chamber water level if the discharge through the valve is kept constant.

The relationship between mean water level and input head shown in Figure 4.20 can be quantified as:

$$\bar{y} = H_0 - \beta \tag{4.48}$$

Where the constant β is equal to 0.062 ± 0.006 m.

It is also important to consider how the system will behave if the input is provided purely by a velocity head, which will be the case for a system operating within a tidal stream. This is because a velocity head (given by $\frac{v^2}{2g}$) will be significantly smaller than any reasonable elevation head. Figure 4.21 shows a comparison of the chamber water level predictions for one system driven by a 0.50 m static head and one by a 0.50 m/s velocity head, with the valve discharge behaviour the same for both cases. This was predicted in 0.5 Hz intervals of valve closure frequency in the range 1 - 5 Hz. The greater input of the static head results in a much higher water level within the chamber, yet the oscillations themselves remain the same for both cases. This can be seen clearly in Figure 4.22, which shows mean oscillation amplitude as a function of mean oscillation frequency.

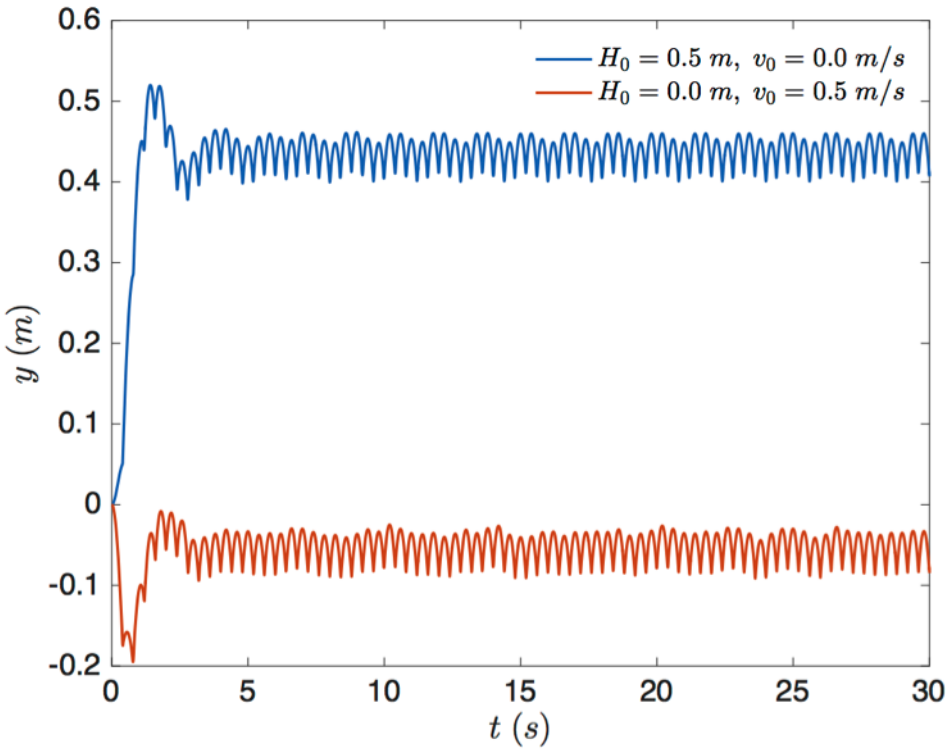

Figure 4.21: Comparison of chamber water level provided by 0.5 m/s velocity head and 0.5 m static head.

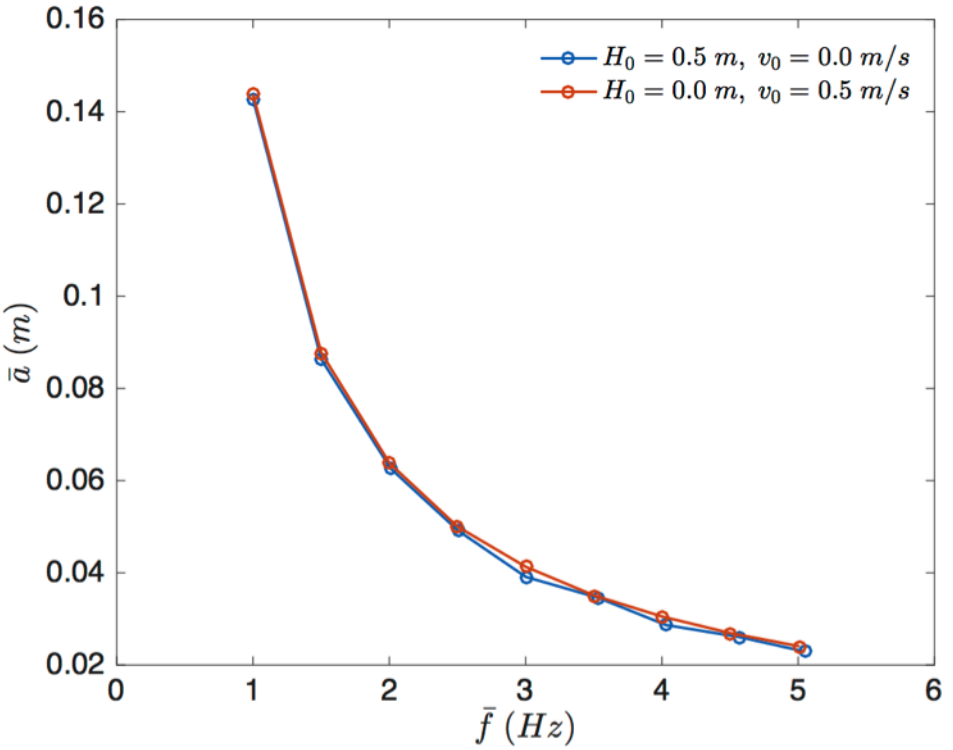

Figure 4.22: Comparison of oscillation amplitudes provided by 0.5 m/s velocity head and 0.5 m static head.

Again, this indicates that the WHES should be capable of functioning just as well in a low input head as it is in a high head, provided the valve discharge remains constant. Whether or not this can be achieved will depend on the conditions, since the maximum possible flow rate through the device, and hence the valve, will be limited in lower heads.

This difference between the inflow rate is the reason why the velocity head oscillations shown in Figure 4.21 occur below $y = 0$ m. In both cases, the maximum outflow was set as 2×10^{-4} m^3/s, however the maximum flow into the system (given the 0.5 m/s velocity and the 2.01×10^{-4} m^2 cross-sectional area) is only 1×10^{-4} m^3/s in the velocity head case. The chamber water level therefore has to become negative to maintain mass conservation. In a real system, Q would have dropped to a lower value, preventing a negative water level while reducing the oscillation magnitude.

4.4.3 System size

Figure 4.23 shows the effect of device cross-sectional area on mean oscillation amplitude and the mean pressure surge magnitude. For each case, Q was set according to the cross-sectional area of the drive pipe so that the peak outflow speed was held constant. Doing so enabled oscillations and pressure surges of virtually identical magnitude to be generated above 1 Hz, regardless of device size. Below 1 Hz, the bigger devices are capable of generating even larger amplitude oscillations and stronger pressure surges. This is because the larger flow rates within a bigger device enable greater changes in fluid momentum to be achieved.

There is consequently more power available from the larger devices, as shwown in Figure 4.24. This illustrates the corresponding power and efficiency predictions for the three different device areas over the range of valve closure frequencies. The large system produces the greatest amount of hydraulic power on average, providing a peak of 0.79 W at 0.40 Hz, falling to 0.07 W at 5 Hz. In contrast, the small system is predicted to produce an average of 0.04 W at 0.50 Hz and 0.01 W at 5 Hz.

Despite this, the small system is actually predicted to be slightly more efficient than the medium and large systems at higher frequencies. At 5 Hz, the smallest system has an efficiency of 2.45 %, compared to the 1.54 % of the largest system. At lower frequencies, however the large system not only produces more power but is also more efficient, with a peak efficiency of 17.8 % at 0.40 Hz contrasting with the predicted 7.75 % efficiency of the small system at 0.6 Hz.

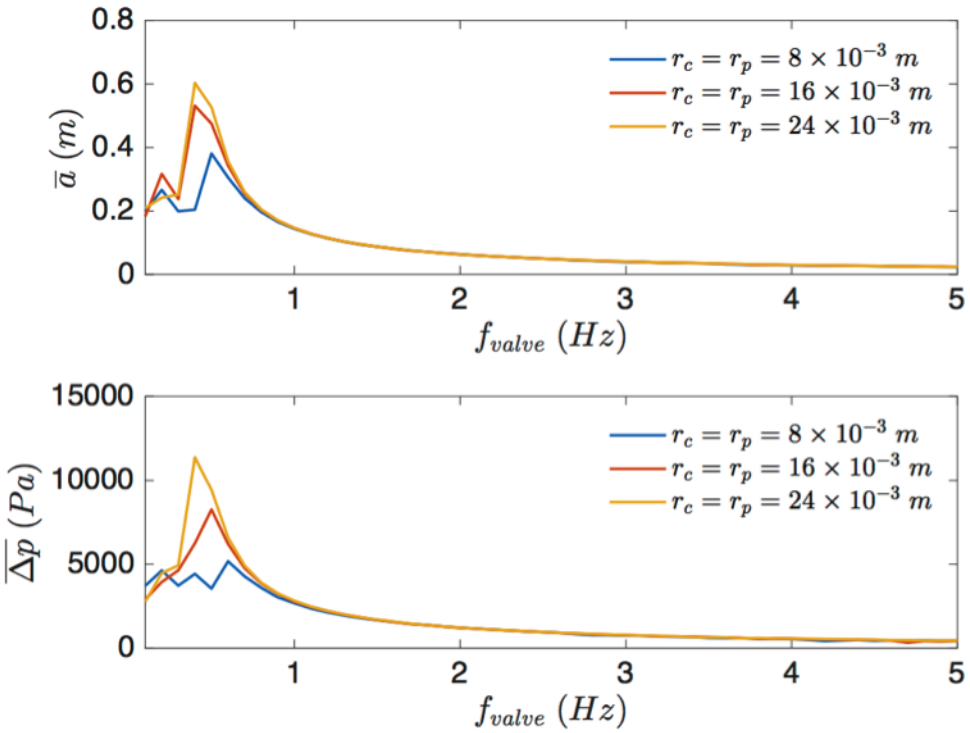

Figure 4.23: Effect of device size on (a) mean oscillation amplitude and (b) mean pressure surge.

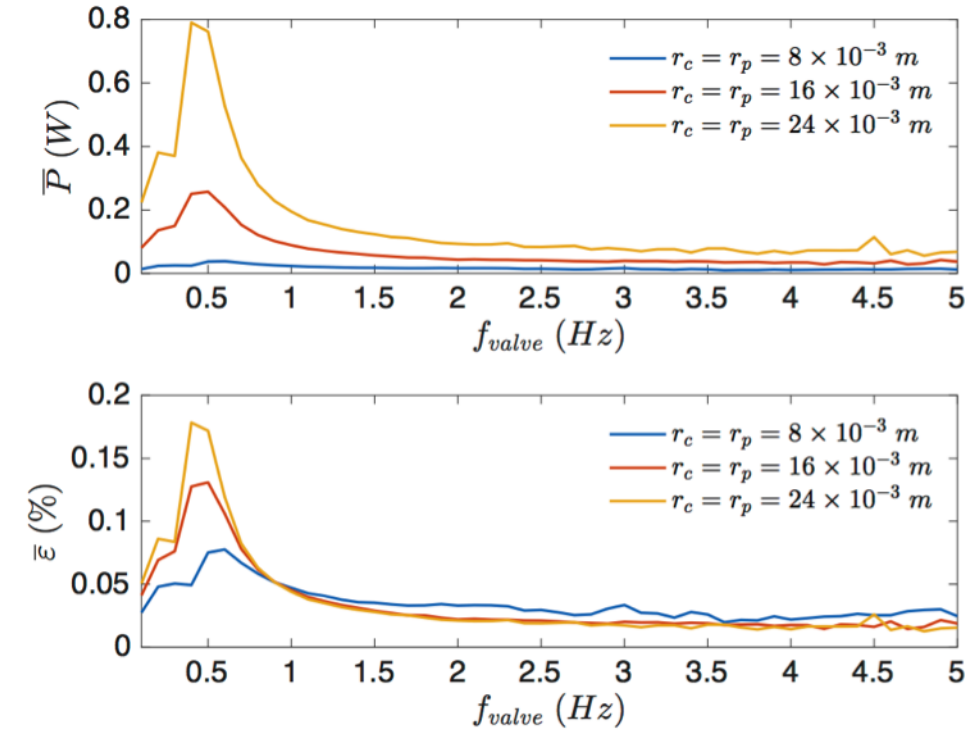

Figure 4.24: Effect of device size on (a) mean hydraulic power and (b) mean hydrodynamic efficiency.

These factors suggests that a large, low frequency system will be the most effective at converting horizontal power into vertical power. The valve will therefore need to be controlled to ensure it closes at the correct operating frequency, while the power take-off will need to be designed to operate effectively at low frequency values.

4.5 Chapter conclusions

The theoretical study presented in this chapter has investigated the effects of several parameters on the hydrodynamic behaviour of the WHES. These include the outflow when the input conditions are held constant, varying the input when the outflow remains constant, and the effects of device size. Of the various waveforms used to approximate the outflow (in the absence of directly modelling the valve), the sawtooth wave found to produce results that most closely matched the behaviour of the scale model tested in Chapter 3.

The results of the study indicate that the discharge out of the system – and hence the behaviour of the valve – is the most important factor affecting the hydrodynamics of the system. The discharge affects all aspects of system performance, including the shape, amplitude and frequency of the oscillations, the mean water level within the chamber, the magnitude and frequency of the pressure surges and the change in momentum experienced by the water within the drive pipe.

Increasing the peak outflow through the valve was found to increase the size of the oscillations and pressure surges. The closure frequency of the valve is also a crucial factor, with the simulated systems at their most efficient with a valve frequency of around 0.5 Hz. This occurs because the drive pipe flow rate can recover to the greatest extent at this frequency, enabling the largest fluid momentum changes to be generated. This behaviour matches that measured during Chapter 3, where the average power of the piston was greatest in the largest amplitude, lowest frequency oscillations. As a result of this, controlling the behaviour of the valve will be crucial to designing an effective system. The peak hydrodynamic efficiency of the various systems tested in this chapter was found to be 17.8 % at a valve closure frequency of 0.4 Hz and a peak outflow rate of 1.81×10^{-3} m^3/s.

The results also suggest that the input into the system will have little impact on the oscillations within the chamber, provided that the flow through the valve remains constant. In such cases, the only factor that the input head will affect is the mean water level within the chamber. Since varying the valve behaviour also affects the mean chamber water level, the power take-off

of a physical WHES will need to be capable of handling different operating conditions.

Finally, the study investigated the effects of device size on system performance. It was found that, if the peak outflow speed through the valve remains constant, increasing the size of the system will increase the oscillation amplitude and pressure surge strength at lower (< 1 Hz) valve frequencies. At higher valve frequencies, pressure surges of similar magnitude are generated, irrespective of device size. These factors mean that more power is available from larger devices, and that larger devices are the more efficient choice at low valve frequencies. At higher frequencies, a smaller device may actually be more efficient than a larger one. This suggests that the largest possible device for a given site, operating with a low valve closure frequency, will be the most effective design for converting the power available from the horizontal flow into hydraulic power within the chamber

One drawback of the methodology used during this study was the governing equations themselves, which are simplified versions of the full partial differential equations describing the propagation of a water hammer within a pipeline. As a result, spatial effects (such as the location of the chamber on the drive pipe and the speed at which the pressure surges will propagate through the system) have been neglected by this analysis. These effects may influence the performance of the device and the most efficient operating frequency, and should therefore be the subject of further study in future.

Despite this, the results have identified the most significant factors governing the performance of the WHES. This information, combined with experimental data from Chapter 3, is used in the next chapter to develop a mechanical power take-off system to extract energy from the device.

Chapter 5

Power generation

Chapter 3 demonstrated the concept behind the Water Hammer Energy System and showed that it is possible to use the pressure surges to drive either a float or a piston. Chapter 4 studied the effects of a range of variables on system performance, illustrating that the discharge through the valve is the most important factor affecting system efficiency.

To provide proof of concept, however, it is necessary to show that the WHES can generate useful power. The purpose of this chapter is to demonstrate that this can be achieved and to identify the factors that will influence the choice of power take-off design, rather than developing a fully optimised system.

There are a variety of methods that may be used to extract energy from the WHES. Three of these were first mentioned in Chapter 2:

- A bi-directional turbine to extract energy from the movement of either air or water within the chamber.
- A piston-crank mechanism to capture the pressure generated by the valve closures and create rotary power.
- A linear alternator to directly generate electrical power from the oscillations.

Of these methods, a linear alternator and piston-crank were investigated during the research presented within this thesis. The turbine method was neglected because the investigations relied upon the small test-rig of Chapter 3, and it was felt that building a turbine capable of functioning in such a small cross-sectional area would be unfeasible.

5.1 The linear alternator

A linear alternator converts the energy of a reciprocating linear motion into electricity, without the need for an intermediate mechanical stage. A basic design was built and tested as part of a preliminary study into the feasibility of the WHES, since it was deemed the most simple method for demonstrating that the system can generate power. This section provides a brief overview of the basic design, manufacture and performance of the alternator as a qualitative demonstration of its characteristics.

5.1.1 Design and manufacture

To keep the design as simple as possible, it was envisaged that the magnets of the alternator would float within the chamber, with the oscillating water level driving them up and down. This was achieved by placing the magnets within an air filled plastic cylinder that floated within the chamber. N42 Neodymium circular disc magnets were used, due to their strength and small diameter of 12 mm. Four magnets were used inside the tube, each 3 mm thick and capable of lifting 2.5 kg. Since the WHES was driving a float, rather than a piston, the velocity and acceleration experienced by the magnets (and hence the time rate of change of the magnetic flux experienced by the wire coils) were not maximised, which is an obvious drawback of this particular design.

Figure 5.1: Copper coil winding.

The coils, which were designed to wrap around the exterior of the chamber, were manufactured from 0.15 mm diameter copper magnet wire. This was achieved using the purpose-built CNC coil winding machine shown in Figure 5.1, which consisted of 2 DC motors controlled by an Arduino UNO micro

controller. While one motor rotated a plastic drum of equivalent diameter to the chamber, the rotary motion of the second motor was converted into linear motion using a lead screw. Controlling the RPM of each rotor through the Arduino enabled the position of the wire feeder to be continuously adjusted so that a tightly wrapped coil could be created, with each individual turn of wire as close as possible to the previous one. The coil winding machine enabled the length and total number of each coil to be determined according to the motor speeds and the thread pitch of the lead screw, and was capable of reversing direction so that more turns could be positioned in a small length. This machine was used to manufacture several types of coil. The first that was used to test the system consisted of 2000 turns in a 2 cm long coil. The second design consisted of 400 turns in the same length, with 5 coils connected together in parallel.

5.1.2 Performance

Figure 5.2 shows an image from one of the first tests using the 2000 turn coil, where it was used to illuminate an LED and demonstrate that the WHES can provide useful power.

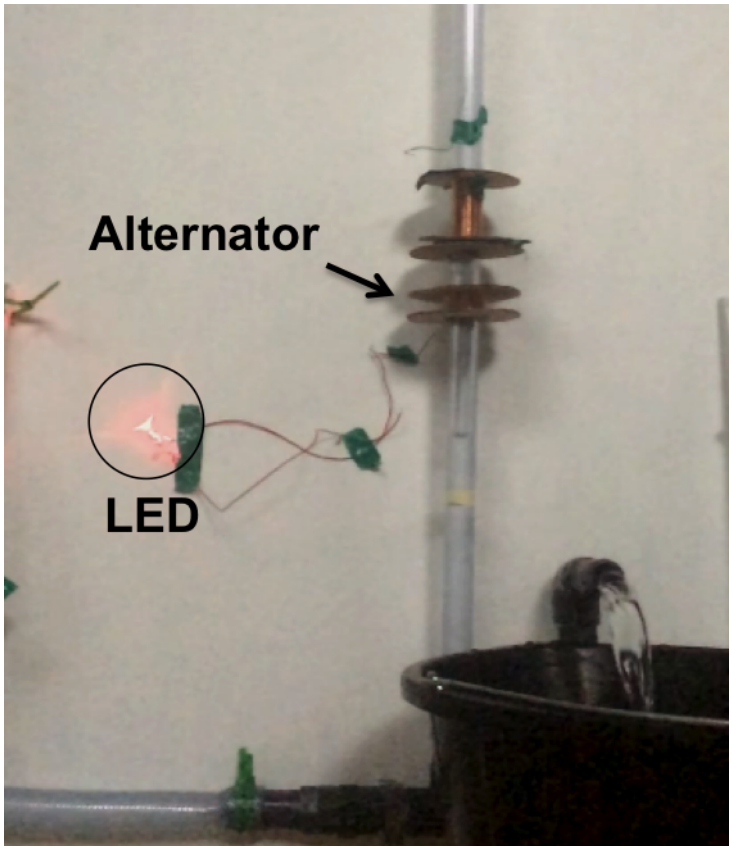

Figure 5.2: Illumination of LED using a linear alternator prototype.

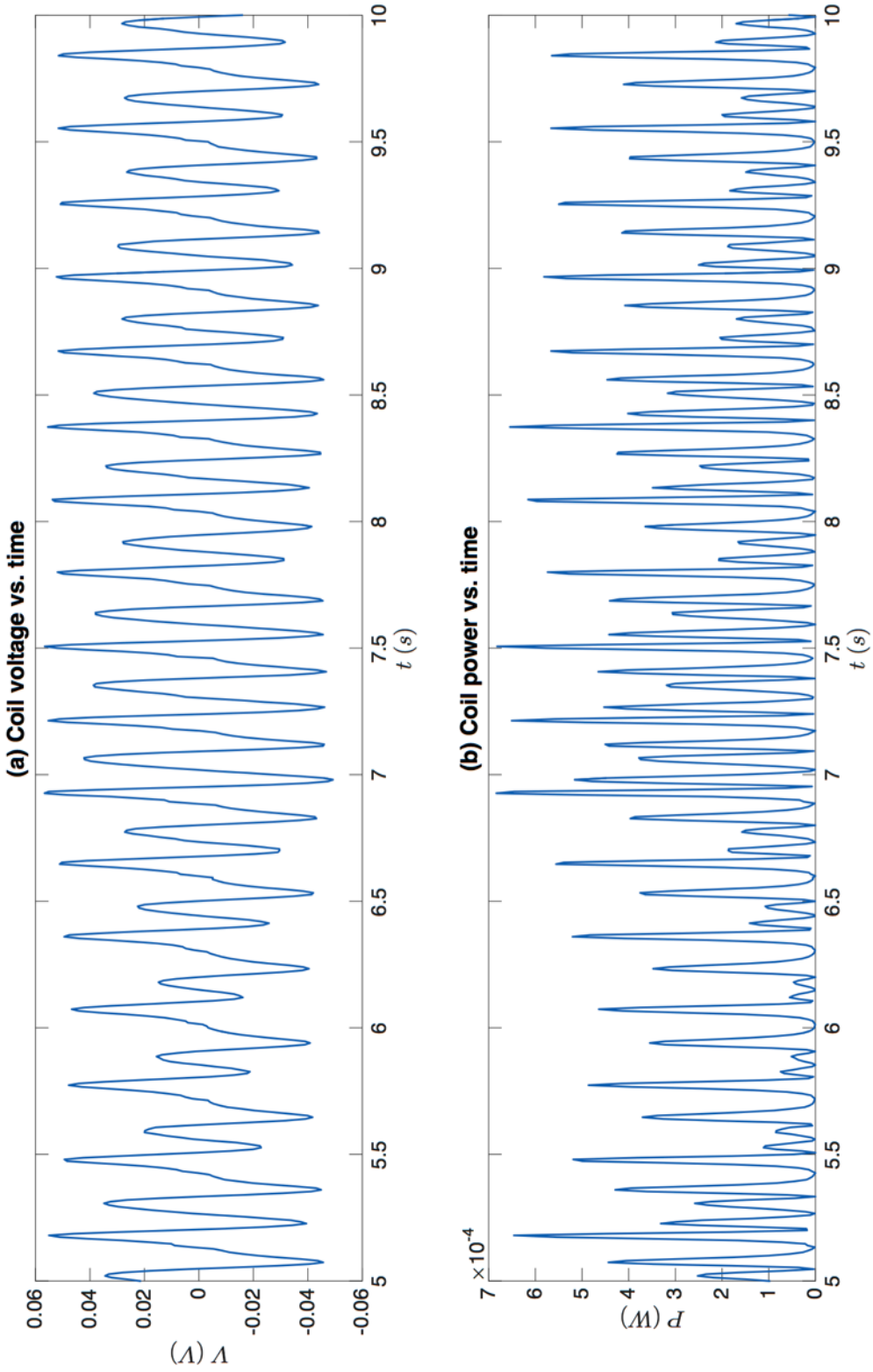

Figure 5.3: Voltage and power supplied to 4.7 Ω resistor by 400 turn coils.

A drawback of the alternator method is that the power supplied is inconsistent, however. This can be seen in Figure 5.3, which shows both the voltage and power supplied by the 400 turn coils to a 4.7 Ω resistor. From Figure 5.3a, the voltage can be seen to oscillate between positive and negative values as the magnets move up and down, which is indicative of the alternating current that is generated. The upstroke produces a slightly larger voltage since, from Chapter 3, the upstroke velocity is slightly greater than the downstroke velocity. At the top and bottom of its motion, however, when the magnet is briefly stationary, no power is produced, resulting in the inconsistent power that can be seen in Figure 5.3.

There are several ways that electrical power can be conditioned so that the quality of the power supplied is more consistent. Such methods are out of the scope of this thesis, however. It was decided instead to design and test a piston-crank mechanism in an attempt to provide a more consistent power output.

5.2 The piston-crank mechanism

A mechanical crank is an arm that may be used to convert reciprocating motion into rotary motion, or vice versa. Figure 5.4 provides an illustration of the basic geometry of a piston-crank mechanism, where a crank is used to connect a reciprocating piston to a rotary shaft. The piston itself is positioned inside a chamber, and is free to move vertically should any forces act upon it. The upper face of the piston is pinned to the lower end of a connecting rod of length l; as the piston moves, the rod is forced to rotate, forming an angle φ with the vertical. The upper end of the connecting rod is pinned to the crank; the distance between the centre of the crankshaft and the end of the connecting rod forms the crank radius R, which by geometry should be equal to $S/2$.

5.2.1 Piston motion

Since the piston is coupled to the crank via a connecting rod, its motion is dependent upon the crank radius and connecting rod length (Nigus, 2015). Figure 5.4 shows that x, l and R form the sides of a triangle. The cosine rule shows that:

$$l^2 = R^2 + x^2 - 2Rx\cos(\theta) \tag{5.1}$$

Equation 5.1 may be used to predict the variation in x as a function of θ.

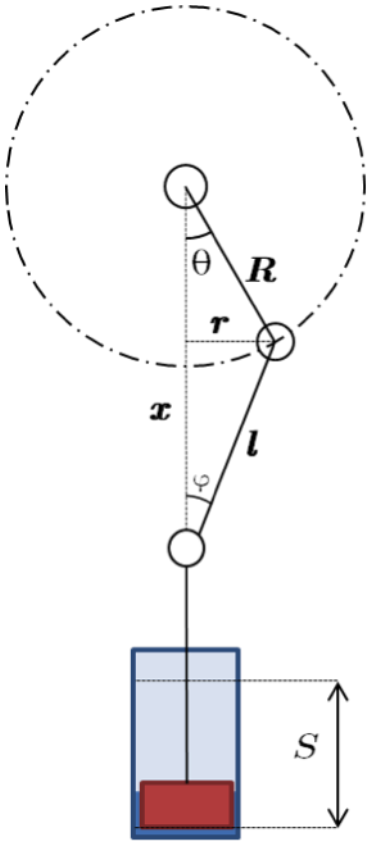

Figure 5.4: Overview of a piston-crank mechanism.

Using the trigonometric identity $\sin^2(\theta) + \cos^2(\theta) - 1 = 0$ and rearranging:

$$l^2 = R^2 + x^2 - 2Rx\cos(\theta) + R^2(\sin^2(\theta) + \cos^2(\theta) - 1) \tag{5.2}$$

$$x = R\cos(\theta) + \sqrt{l^2 - R^2\sin^2(\theta)} \tag{5.3}$$

Equation 5.3 enables the piston position y to be defined as a function of crank angle:

$$y(\theta) = x(0) - x(\theta) \tag{5.4}$$

$$y(\theta) = l + R(1 - \cos(\theta)) - \sqrt{l^2 - R^2\sin^2(\theta)} \tag{5.5}$$

5.2.2 Torque and inertia

Any force applied to the piston will be transmitted through the connecting rod to the crank. Since this force is applied at a distance it will generate a torque $\boldsymbol{\tau}$, which will depend upon the force $\boldsymbol{F}$ acting on the crank and the perpendicular distance $\boldsymbol{r}$ between the end of the connecting rod and the centre of the crank:

$$\boldsymbol{\tau} = \boldsymbol{r} \times \boldsymbol{F} \tag{5.6}$$

From Figure 5.4, $\boldsymbol{r}$ is dependent upon both $\boldsymbol{R}$ and θ, as well as $\boldsymbol{l}$ and φ:

$$\boldsymbol{r} = \boldsymbol{R}\sin(\theta) = \boldsymbol{l}\sin(\varphi) \tag{5.7}$$

Hence, from Equations 5.6 and 5.7:

$$\boldsymbol{\tau} = ||\boldsymbol{R}||||\boldsymbol{F}||\sin(\theta)\cos(\varphi)\hat{\boldsymbol{n}} \tag{5.8}$$

The unit vector $\hat{\boldsymbol{n}}$ is perpendicular to the plane of the crank, with a direction given by the right-hand rule. From Equation 5.6 $\varphi = \sin^{-1}(\boldsymbol{r}/\boldsymbol{l})$, which combined with the trigonometric identity $\cos(\sin^{-1}(x)) = \sqrt{1-x^2}$ yields:

$$\boldsymbol{\tau} = ||\boldsymbol{R}||||\boldsymbol{F}||\sin(\theta)\sqrt{1-\left(\frac{\boldsymbol{r}}{\boldsymbol{l}}\right)^2}\hat{\boldsymbol{n}} \tag{5.9}$$

$$\tau = RF\sin(\theta)\sqrt{1-\frac{R^2\sin^2\theta}{l^2}} \tag{5.10}$$

Equation 5.10 shows how the magnitude of the torque acting on the crank will vary over the course of a revolution. If a constant force is applied, the peak torque will occur at $\theta = \pi/2$ and $3\pi/2$ rad. No torque will be generated at $\theta = 0$ and π rad (known as bottom dead centre and top dead centre, respectively), since the force will be directed straight through the pivot point.

If a piston-crank mechanism driven by a WHES is to self-start, it will need to generate enough torque from a single pressure surge to overcome its inertia and accelerate to its operating angular frequency, as shown by by Newton's second law for rotating bodies:

$$\tau = I\alpha \tag{5.11}$$

Since Chapter 3 showed that the pressure surges act upon a body in the chamber for only a very short period of time, the required acceleration α will be very high. The inertia I of the piston-crank will therefore need to be minimised during design to ensure it can self-start.

5.3 Design considerations

Given its reliance on a piston, it was decided to design the piston-crank according to the behaviour of the freely oscillating piston observed during Chapter 3. Figure 5.5 illustrates a sample force time-curve from one of the piston test runs, which featured a mean oscillation amplitude of 72.3 ± 7.2 mm and a mean frequency of 2.93 ± 0.06 Hz. This particular test run was chosen as it

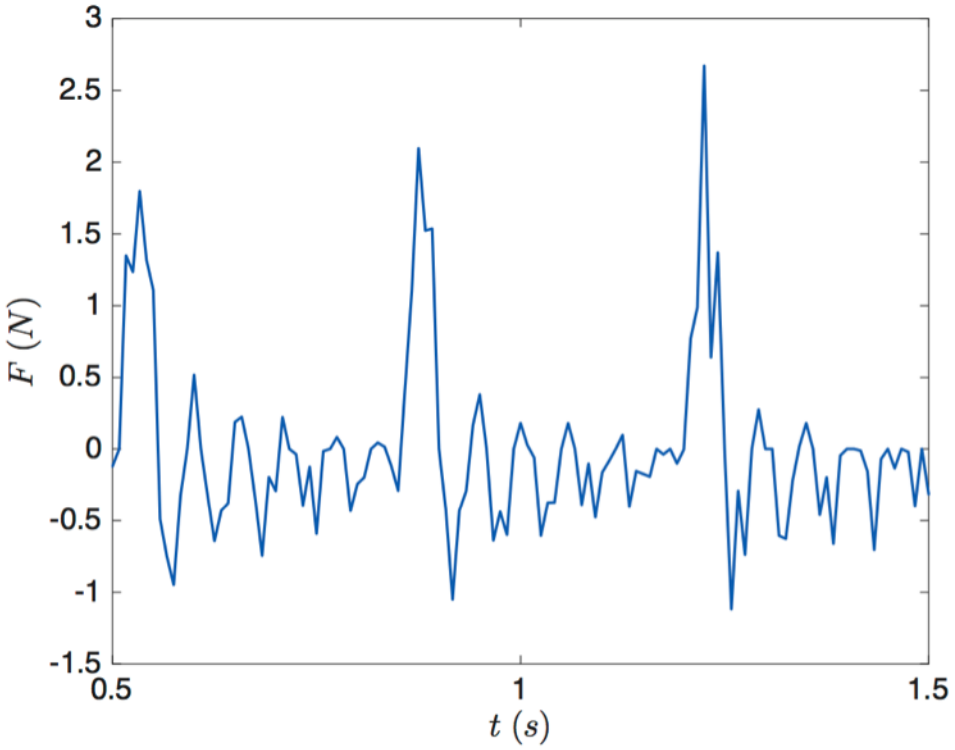

Figure 5.5: Force-time data used for predictions during crank design.

occurred when the ball valve controlling the flow between the reservoir and the system was fully open, meaning the input conditions would be straightforward to replicate during power take-off testing.

5.3.1 Connecting rod length

From Equation 5.10, the main factors that affect the torque generated by the crank are its radius, its angular position and the connecting rod length. While the crank radius is governed by the stroke length of the piston, the length of the connecting rod may be varied according to design. To visualise how this affects the torque on the crank, the values of F shown in Figure 5.5 were combined with Equation 5.10. To convert the force data from the time domain to that of the crank angle, the angular frequency ω of the crank was predicted from the valve closure frequency.

Table 5.1 summarises the predicted maximum and mean torque values for 9 different connecting rod lengths. It shows that increasing the length of the connecting rod will result in small gains in both the maximum torque available to the crank, although the magnitude of the gain begins to fall as L is increased further. In contrast, the shorter connecting rods are predicted to supply the greatest mean torque, since they will minimise the effect of the force that acts

Table 5.1: Effect of connecting rod on maximum and mean torque available to crank.

Case	L (mm)	τ_{max} (mNm)	$\bar{\tau}$ (mNm)
1	36.2	35.70	1.734
2	41.2	37.68	1.656
3	46.2	38.99	1.646
4	51.2	39.91	1.644
5	56.2	40.58	1.645
6	61.2	41.09	1.647
7	66.2	41.48	1.649
8	71.2	41.79	1.650
9	76.2	42.04	1.651

in the opposite direction to the motion (i.e. the piston weight on the upstroke and the reflected pressure surges on the downstroke).

From Equation 5.5, the length of the connecting rod will also affect the motion of the piston. This is illustrated in Figure 5.6, which shows the piston position as a function of crank angle for various connecting rod lengths. A shorter connecting rod forces the piston to remain near the peak of its stroke oscillation over a greater range of crank angles (and, by extension, time). As l is increased and becomes much greater than R, the piston will spend less time at the peak of each oscillation and the overall shape of the curve will tend towards a sinusoid.

Given the shape of the oscillations generated by the WHES, a relatively short connecting rod will therefore provide a piston motion that is closer to the natural system behaviour. Comparing the RMS errors of the measured piston motion with various predictions suggests that a connecting rod of 49 mm would enable the power take-off to most closely match the natural behaviour of the experimental test-rig.

5.3.2 Valve control system

Since the force generated by the water hammer system is time-dependent, with a large but brief peak occurring at the beginning of each oscillation, the value of θ that the peak force occurs at will be extremely important if a crank is to be used to for power generation. If the peak force is generated when θ is extremely small, the resulting torque may be insufficient to fully overcome the inertia of the crank. This may prevent the crank from completing a full revolution, or result the device being unable to self-start. Conversely, if the maximum force occurs when θ is too large, the crank may be incapable of completing a full upwards stroke. This could potentially jam or even break

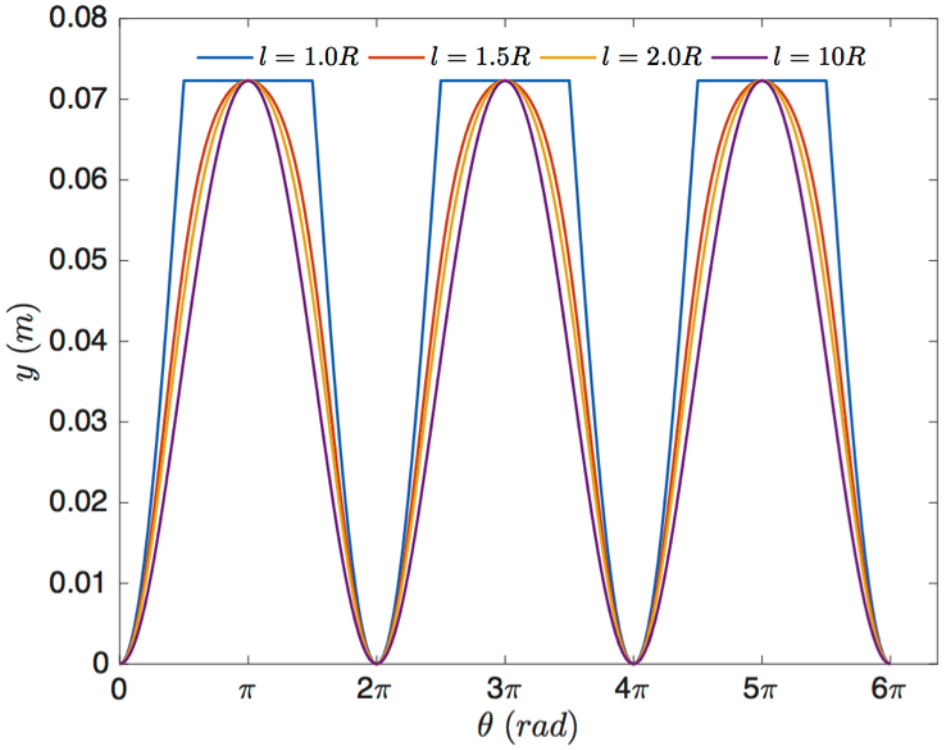

Figure 5.6: Piston position as a function of crank angle and connecting rod length.

the system, as the piston would still want to travel upwards with the crank at top dead centre.

It is therefore necessary to control the valve to ensure it closes when the crank is at a specific angle. To visualise how the torque on the crank varies with its position when the valve closes, the force-time values shown in Figure 5.5 were combined with Equation 5.10. Table 5.2 summarises the various cases that were predicted, detailing the value of θ at which F_{max} was set to occur (θ_F), the maximum stroke length available for F_{max} occurring at this angle (a_F), which is given by $R(1+\cos(\theta_F))$, the maximum torque τ_{max} on the crank over the course of one revolution, and the mean torque $\bar{\tau}$ on the crank over one revolution.

Table 5.2 shows that increasing θ_F results in greater values of both τ_{max} and $\bar{\tau}$, although this naturally reduces S_F. The relatively small difference in S_F between Case 1 and 2 suggest that an angle of up to 0.15 rad (8.6 deg) may be achievable without overly impacting the behaviour of the system.

5.3.3 Crank inertia

If a piston-crank system driven by the water hammer system is to self-start, the crank will have to accelerate from rest to its angular velocity over the time

Table 5.2: Effect of crank angle at valve closure on the maximum and mean torque available.

Case	θ_f (rad)	τ_{max} (mNm)	$\bar{\tau}$ (mNm)
1	0.00	72.3	12.7
2	0.15	71.9	22.8
3	0.31	70.6	33.0
4	0.46	68.5	42.0
5	0.61	65.7	49.6
6	0.77	62.2	55.7
7	0.92	58.1	60.3
8	1.07	53.4	63.6
9	1.23	48.4	65.5

Table 5.3: Estimated values of S_F, τ_{max} and I_{max} for $0 \leq \theta_F \leq 0.16$

Case	θ_F (rad)	S_F (mm)	τ_{max} (mNm)	I_{max} (10^{-5} kgm^2)
1	0.00	72.3	12.7	3.45
2	0.02	72.3	13.2	3.59
3	0.04	72.3	14.6	3.97
4	0.06	72.2	16.1	4.38
5	0.08	72.2	17.5	4.76
6	0.10	72.1	19.0	5.16
7	0.12	72.0	20.4	5.54
8	0.14	71.9	21.8	5.92
9	0.16	71.8	23.2	6.30

period that the pressure surge is applied to the piston. If this is not achieved, the pressure in the pipe may not be able to dissipate freely and the valve may jam shut. For the test run shown in Figure 5.5, the piston accelerated from rest to 18.4 rad/s in just 0.05 s, equivalent to a constant angular acceleration of 368 rad/s^2.

Combining this value of α with predicted values of τ_{max} permits the calculation of the maximum inertia I_{max} of the entire crank shaft system as a function of θ_F. Predictions of I_{max}, using a peak force of 2.09 N, a crank radius of 36.15 mm and a connecting rod length of 75 mm are summarised in Table 5.3 for $0 \leq \theta_F \leq 0.16$.

Table 5.3 shows that the inertia of the power take-off system will need to be extremely low if it is to be capable of self-starting. Increasing the angle of the crank at which the peak force is provided will allow for more inertia in the power take-off, again illustrating the importance of controlling the valve behaviour if a piston-crank system is to be used.

5.4 Experimental system

5.4.1 Design

To facilitate accurate and rapid construction of the power take-off, it was decided to manufacture as many components as possible using laser cut acrylic. Although acrylic is relatively brittle and lacks the strength of other materials, its low cost and the ease of making relatively complex shapes via computer aided design and manufacturing make it an ideal material for rapid prototyping. A superstructure made of 3 mm thick acrylic (visible in Figure 5.9) was manufactured to support the crankshaft above the chamber.

Given the low levels of inertia required for the power take-off to self-start, it was decided to minimise the amount of material used in the crank while maintaining the necessary radius to accommodate the piston stroke. The resulting shape is shown in Figure 5.7, which has an inertia of 1.21×10^{-6} kgm^2 if made from 3 mm thick acrylic. One end of the crank was coupled to the connecting rod, which was 75 mm long to ensure the pin coupling the connecting rod with the piston rod did not hit the crank. Although this was longer than the predicted optimum of 49 mm, it was necessary to prevent the piston from clipping the crank.

The same 15×10^{-3} kg piston used in Chapter 3 was used again in this design, with a 4 mm spherical bearing used to connect the 4 mm aluminium piston rod to the connecting rod pin. To ensure the crank was balanced, a steel counterweight was mass of 18×10^{-3} kg was added to the far end of the crank. Two M3 bolts were used to connect the crank to a small acrylic flange, which in turn was positioned on the crankshaft and secured using M4 locknuts.

The crankshaft itself was made from a 4 mm diameter stainless steel rod. Despite its greater inertia relative to materials such as aluminium, steel was chosen due to the ease with which it can be machined as well as its strength. This ensured that the threaded section of the crankshaft would not be stripped by adding and removing the nuts holding the other components in place. The crankshaft was supported in the superstructure by plastic bushings to minimise the friction between it and the acrylic.

One of the additional components held in place with locknuts was a snail drop cam, which was used to control the valve by actuating a push rod. This was felt to be a reasonably straightforward way of ensuring the valve closed when the crank angle was most appropriate. As illustrated in Figure 5.8, the snail drop cam keeps the valve open for most of a crank revolution; the angle of the flat edge of the cam relative to the crank defines the position at which the valve is permitted to close, and hence the crank angle at which the peak

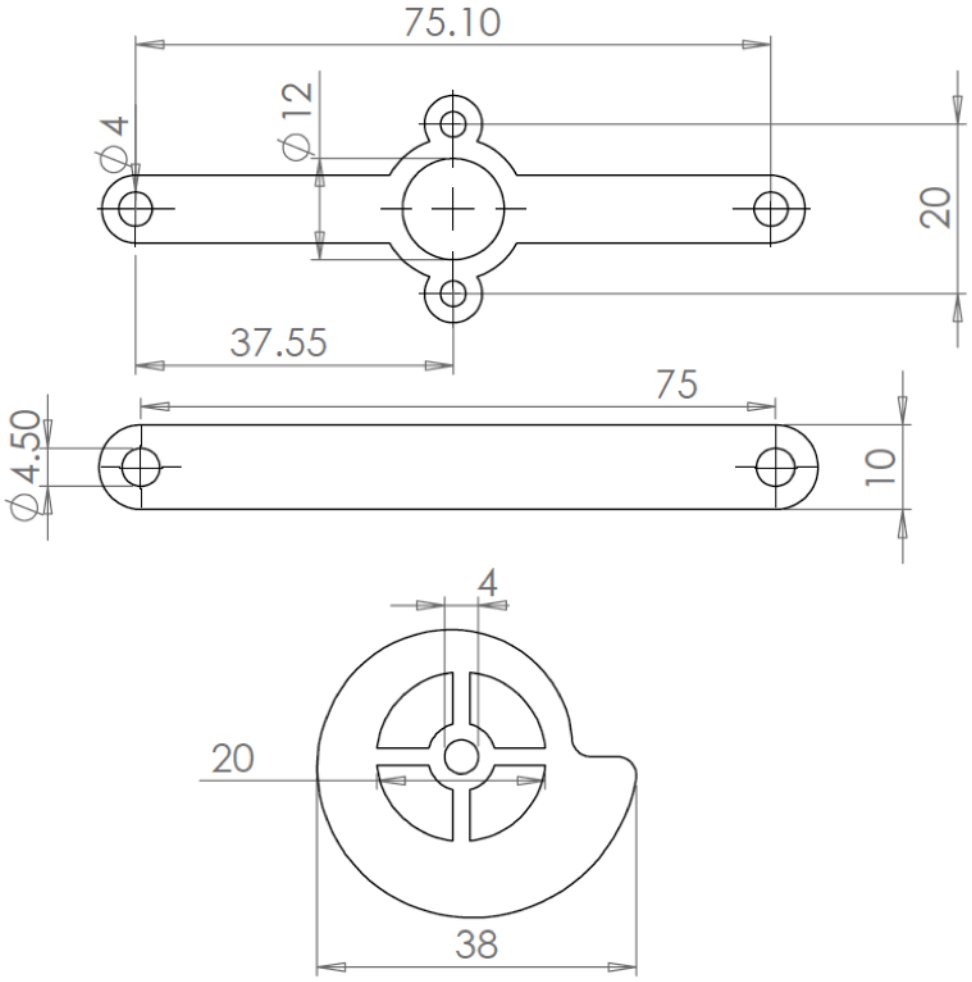

Figure 5.7: CAD drawing of crank, connecting rod and cam. Dimensions are in millimetres and based on the piston motion, crank torque and inertia predictions of Section 5.3.

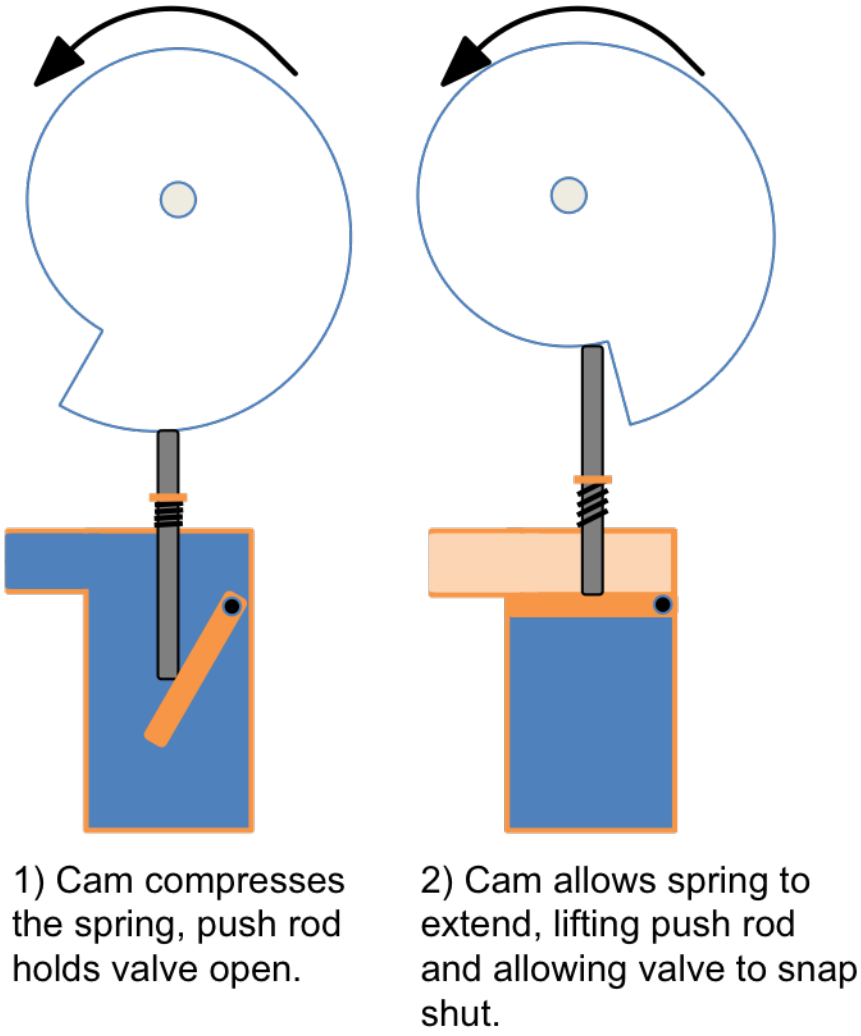

Figure 5.8: Overview of valve control mechanism operation

force is applied to the piston.

Figure 5.7 includes a CAD drawing of the cam, which was cut from 5 mm acrylic rather than 3 mm to ensure good contact with the push rod follower. The shape of the cam is given by an Archimedan spiral, the maximum radius of which was 38 mm. To reduce the inertial mass, some of the interior of the cam was removed, resulting in a total inertia of 4.47×10^{-7} kgm^2.

The push rod was made from a solid 4 mm diameter carbon fibre rod, which due to the distance between the power take-off and the valve had a length of 720 mm. This gave it a mass of 14×10^{-3} kg and a weight of 0.137 N, significantly more than the water force on the check valve flap could overcome. Three springs were positioned on the lower end of the rod to support this weight and ensure the valve flap remained open. Below this, the rod was fed through a pipe plug to ensure it remained in position on the valve flap. At its upper end, the rod was supported by the crankshaft support structure.

One drawback with this design is a relatively high amount of friction be-

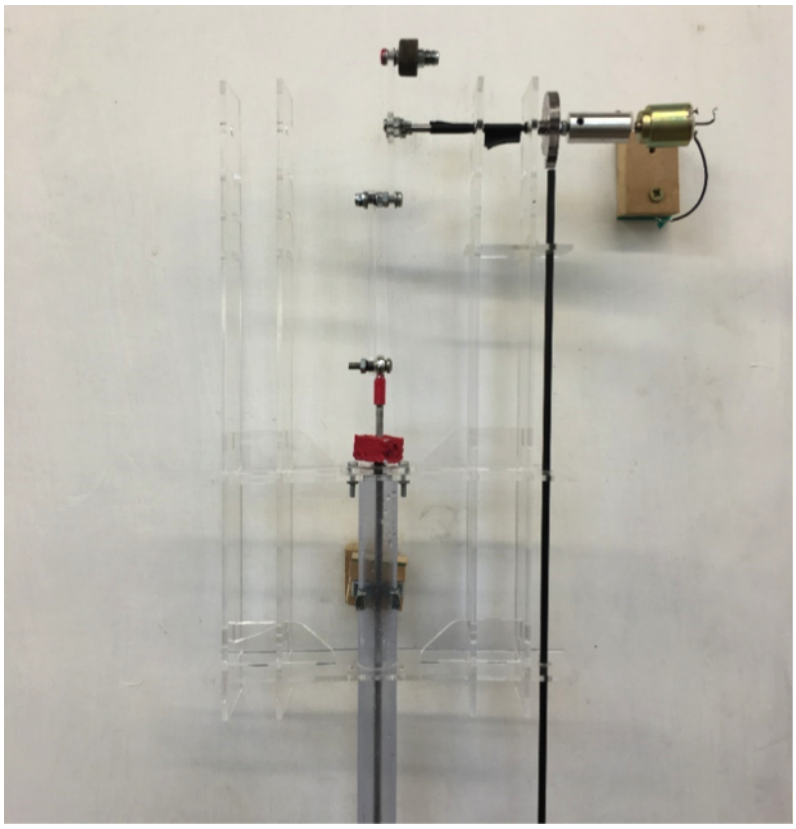

Figure 5.9: Photograph of the mechanical power take-off.

tween the cam and push rod. This was noticed during preliminary testing of the power take-off, when the friction between the cam and the push rod served to prevent the crank from completing a full rotation. To overcome this, a low friction acetyl cap was added to the upper end of the push rod. During testing, the cam was frequently lubricated to further minimise friction.

To measure the power output from the crankshaft, an aluminium coupling was used to connect one end to a 2V brushless DC motor that served as a generator. The motor was chosen due to the predicted low levels of torque the scale model would generate and the small size of the crankshaft. A drawback with this is that small DC motors are typically designed to operate at high RPMs, and are therefore extremely inefficient when running at low speeds, particularly if in reverse as a generator. Despite this, it was felt the motor would still produce sufficient voltage to measure the power output and prove the overall concept of the system.

A photograph of the completed experimental design is shown in Figure 5.9. In addition to the power take-off components, this also illustrates the red marker that was attached to the piston rod so that its motion could be tracked during the operation of the system.

5.4.2 Testing methodology

To prove the concept behind the WHES and ascertain the effectiveness of the designed power take-off, a set of experiments were run to determine the power available from the piston itself and the electrical output of the generator. This was achieved using a similar experimental set-up to that presented in Chapter 3. One modification was made to its design, which was to position a 24 W electric water pump in the sump to create a recirculating test-rig. This enabled the power take-off to be run for prolonged periods of time, at the cost of preventing the flow rate through the system from being determined. Several test runs were conducted with the pump switched off so that the flow rate could be measured. In every case, the input was kept at 570 mm, which was the head used to determine the motion of the piston in Chapter 3.

The behaviour of the power take-off was measured in two ways. In the first, the motion of the piston and its mechanical power were determined using the motion tracking techniques of Chapter 3. The same camera set-up (720 p at 240 FPS) was used to record the position of the piston marker as a function of time. The same calibration techniques were also used, and as such they are not covered here. In the second method, the terminals of the motor were connected in series to a 4.7 Ω resistive load. The voltage across the load was measured using a PicoScope 4224 digital oscilloscope and data logger at a sample frequency of 1 kHz, allowing the electrical power to be calculated using the combination of Joule's law and Ohm's law:

$$P = \frac{V^2}{R} \tag{5.12}$$

A photograph of the complete power take-off test rig, which shows the voltage probe running to the resistive load the pipe from the pump, is provided in Figure 5.10.

5.4.3 Piston motion

Figure 5.11 illustrates how the position, velocity and acceleration of the piston varied as a function of time. Comparing these plots with the ones shown in Figure 3.12 in Chapter 3 shows the influence the crank has on the behaviour of the system. From Figure 5.11a, the motion of the piston is much more triangular due to the influence of the crank, which also serves to smooth out the minima. The asymmetrical motion of the piston is also a lot more apparent, which is due to the friction between the push rod and the cam slowing the system down on the downstroke.

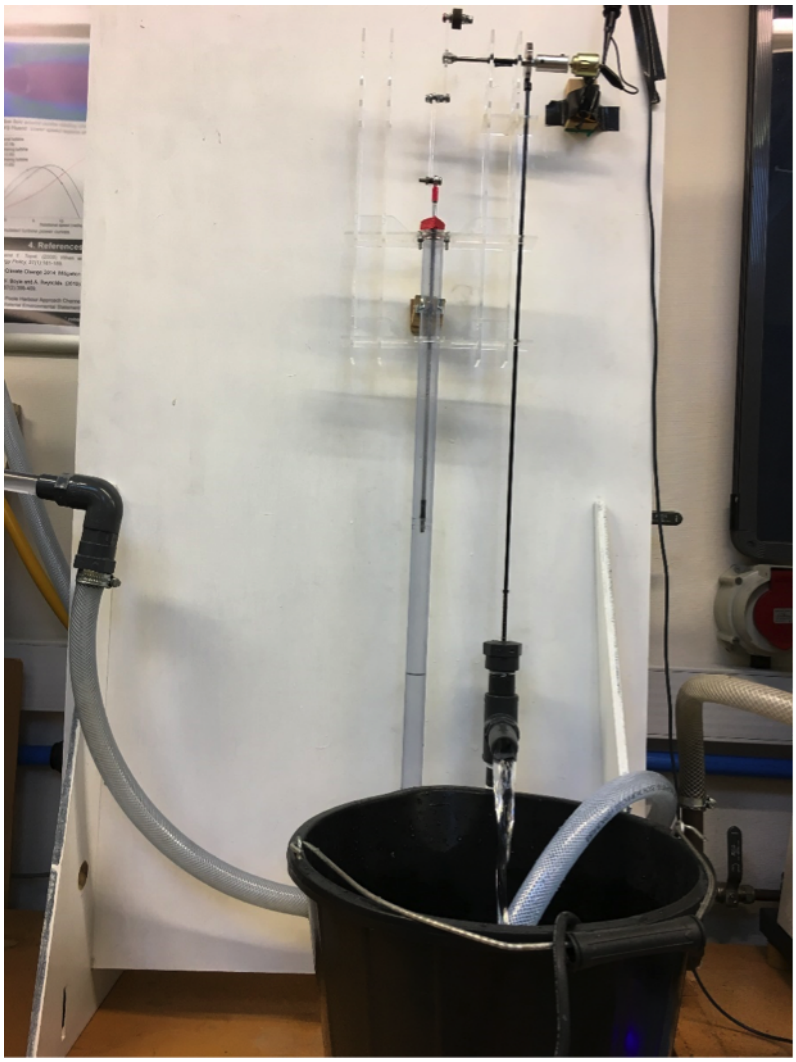

Figure 5.10: Overview of power take-off test rig.

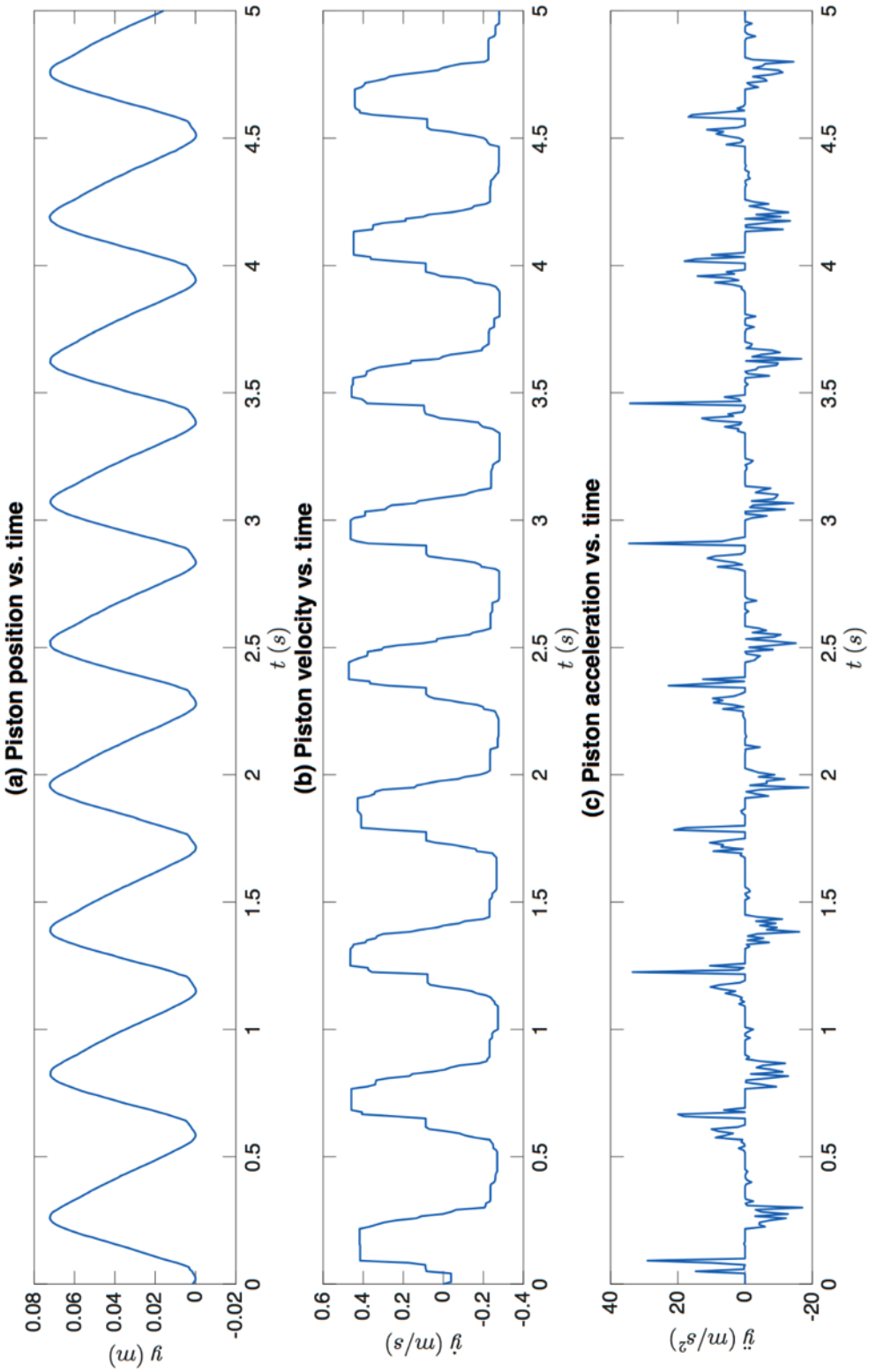

Figure 5.11: Position, velocity and acceleration of piston as a function of time.

The frequency of the piston oscillations was 1.76 Hz, resulting in the crank rotating at 105.6 RPM. This is lower than the 2.92 Hz frequency of the uncoupled piston shown in Figure 5.5, even though the input conditions in terms of the reservoir head and ball valve angle were the same. Additionally, the mean input flow rate into the system, measured across several test runs when the pump was switched off, was found to be 0.130 kg/s, which is higher than that recorded for the piston when the valve was not controlled. Both factors are due to valve being held open for a much greater period of time with the control system in place. From the mathematical results of the previous chapter, this indicates that the strength of the pressure surges was be greater than in the uncoupled case.

The timing of the valve relative to the piston position is also visible in 5.11a, since it causes a small but abrupt upwards step shortly after the minimum of each oscillation. This can be seen more clearly in the velocity data in Figure 5.11b. At the end of each revolution, the speed of the piston becomes positive once again as the inertia of the crank begins to lift it upwards. During this time the valve closes, creating the pressure surge that kicks the piston upwards. This causes its velocity to dramatically increase to a peak of approximately 0.6 m/s. In contrast with the uncoupled case of Figure 3.12, this velocity is maintained for the duration of the upwards motion and only changes once the crank has passed top dead centre. The velocity on the downstroke remains constant as well, however its magnitude of 0.4 m/s is smaller than that of the upstroke.

Examining the acceleration of the piston provided in Figure 5.11c shows that the peak upwards acceleration varied between $20 - 30$ m/s^2. This is again smaller than that experienced by the uncoupled piston, and occurs due to the additional resistive forces imposed by the crank. The deceleration experienced by the piston when it reverses direction is also much more significant than it is in the uncoupled case, as the piston is forced downwards by the inertia of the crank rather than simply falling downwards under gravity.

5.4.4 Power

An example plot of the piston position alongside the instantaneous mechanical power (computed from its velocity, acceleration and mass) is shown in Figure 5.12. Comparing Figure 5.12a with Figure 5.12b shows that the large spikes that occur at the beginning of each oscillation correspond to the water hammer pressure surges forcing the piston upwards. Unlike the uncoupled case shown in Figure 3.19 spikes in the power output can be seen in each oscillation. These

occur when the piston is rapidly decelerated as the crank passes through top dead centre, with further small spikes occurring when the crank swings through bottom dead centre prior to the next pressure surge. In this case, the mean peak power available from the piston was 106 ± 49.6 mW, while the mean overall power was 7.94 ± 20.9 mW. These figures are lower than the power available from the uncoupled piston due to the resistive forces opposing the motion of the crank.

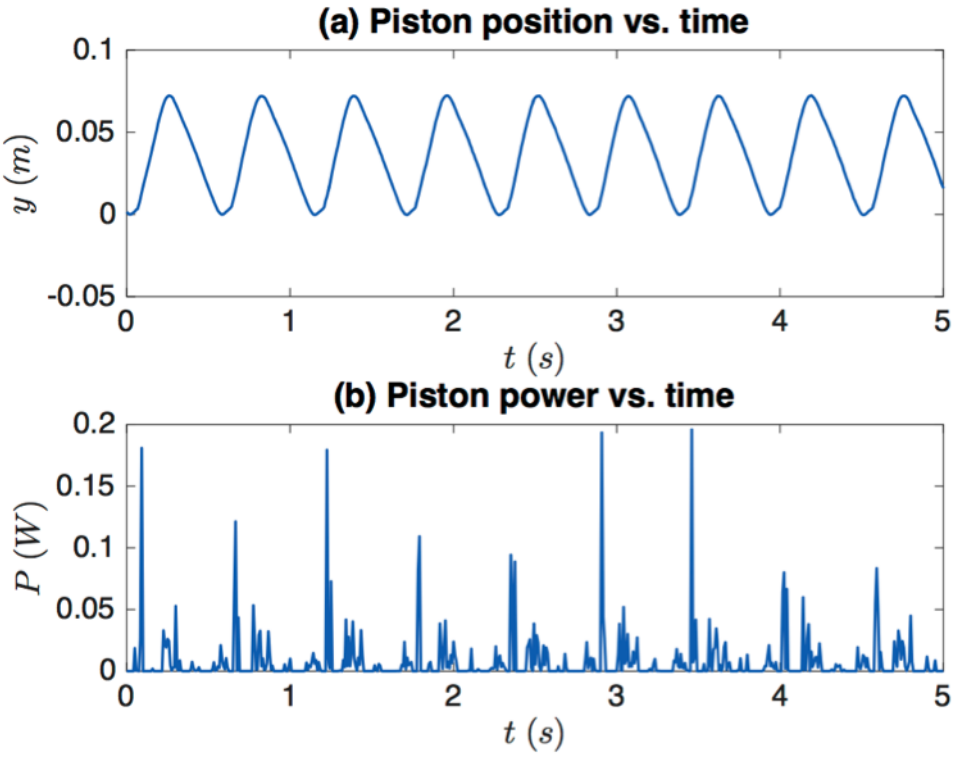

Figure 5.12: Computed instantaneous mechanical piston power as a function of time.

Despite this, the mean power available from the piston is much closer to that available from the peaks. This can be seen by comparing the ratio of the mean peak to mean overall power, which was found to be 18.2 for the floats and uncoupled piston, but only 8.70 for the coupled piston shown in Figure 5.12. This indicates that using the crank for power generation provides a more consistent output.

The input head of 570 mm and the mean mass flow rate through the device of 0.130 kg/s (1.302×10^{-4} m^3/s) put the test rig firmly within the input condition range defined in Figure 1.2. These values also allow the power available to the system P_{av} to be determined, in turn allowing mechanical efficiency ϵ to be calculated according to Equation 4.34 of Chapter 4.

The instantaneous efficiency of the piston is shown in Figure 5.13. The

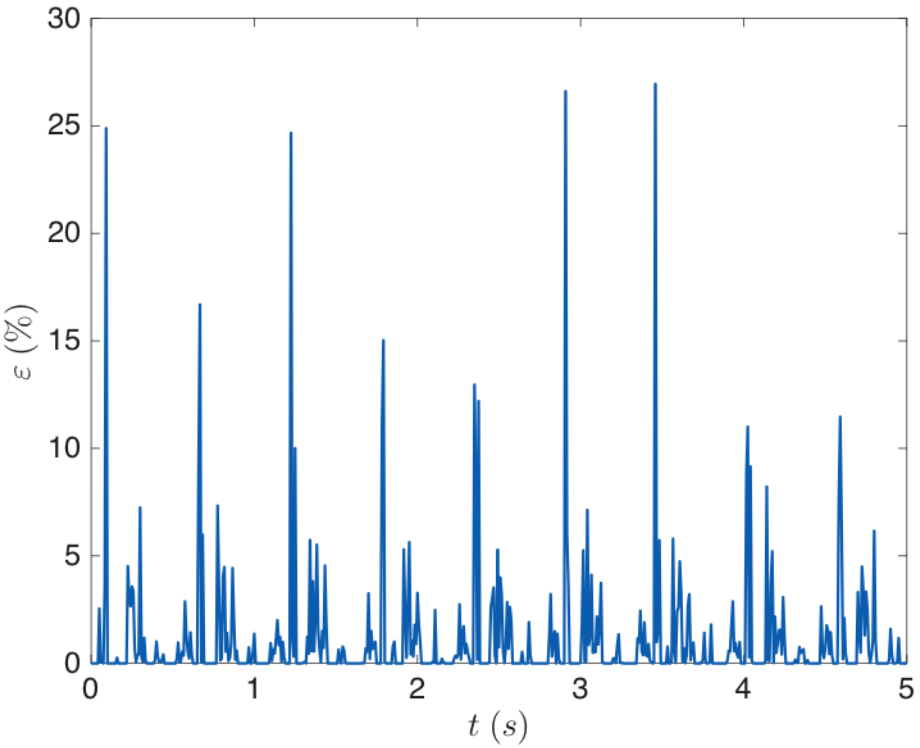

Figure 5.13: Instantaneous mechanical efficiency of the crank as a function of time.

peak efficiency, corresponding to the times at which a pressure surge acts upon the piston, can be seen to vary between 10-25 %, although the time-averaged efficiency value was smaller at 1.09 %. These facts indicate that the WHES can operate within the low input conditions targeted by this research, however they also show that further optimisation work will be required to maximise the effectiveness of both the hydrodynamic and power take-off subsystems.

The voltage and power supplied by the generator to the 4.7 Ω resistor over an entire test run are shown in Figure 5.14a and b, respectively. Both the voltage and the power occur in brief spikes that correspond to the piston being forced upwards by the pressure surges generated by the valve. The mean peak voltage supplied by the motor was 31.38 ± 2.629 mV, with an overall average of 12.33 ± 7.223 mV. The corresponding mean peak power was 179.3 ± 40.17 μW and the time-averaged power was 43.45 ± 47.71 μW.

These power values are smaller than those computed from the motion of the piston, as well as those predicted for an uncoupled piston or float. This is due to the extremely poor efficiency of the motor when operating at the low RPM of the crankshaft. Despite this, the form of the power is similar to that calculated from the motion of the crank. The bulk of the power is generated on the upstroke, when the crank is moving at a greater angular velocity, with

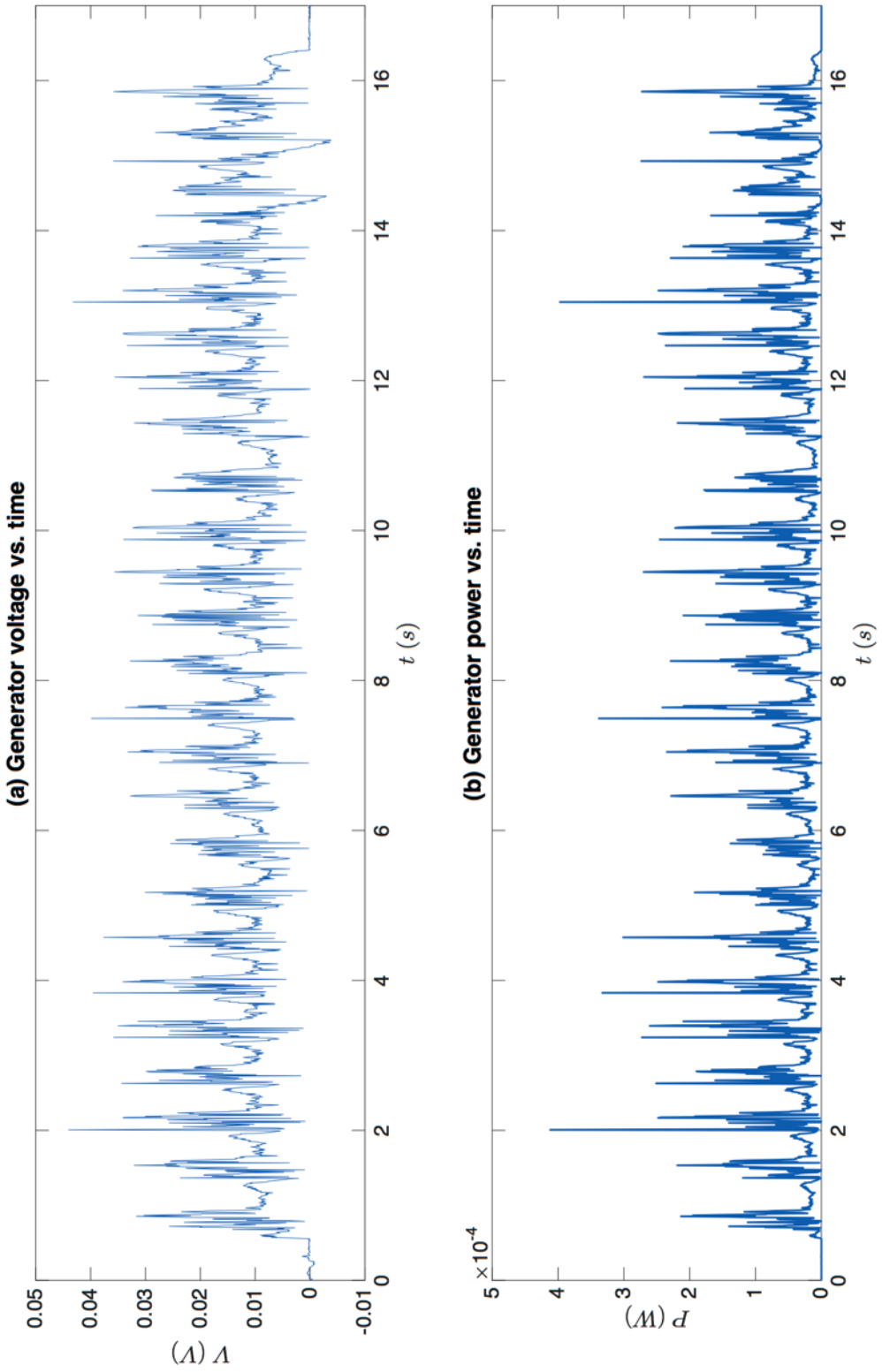

Figure 5.14: Voltage and power supplied to 4.7 Ω load by the 2 V DC motor.

a much smaller amount supplied during the downstroke.

A method for providing even more consistent power output would be to couple multiple pistons onto a single crankshaft, with each piston driven by its own valve to ensure the pressure surges in each chamber are consistent. The valves could be timed by a single camshaft to ensure they closed out of phase with one another, creating a system that is analogous to an internal combustion engine. This would provide a more consistent torque on the crankshaft, which may also serve to improve the efficiency of the generator.

5.5 Chapter conclusions

This chapter has presented two methods for generating electricity from the Water Hammer Energy System. The first was a linear alternator system, which used the WHES to drive a magnet up and down within coils of copper wire. This system was used to illuminate an LED, qualitatively demonstrating that the WHES can provide useful power. Following this, the coils were connected to a 4.7 Ω resistive load, with the voltage across the load measured using a digital oscilloscope so that the power could be determined. This results show that both the voltage and power supplied by the coils occurred in brief spikes, which correspond to the motion of the magnets in the chamber. Brief lulls in the power output occur at the top and bottom of the magnet's motion. This suggests that a WHES driving an alternator will require a conditioning system to improve the quality of the power that is supplied.

The mean power provided by the 400 turn coils over a 30 s period was calculated as 149 μW, which corresponds to 4.47 mJ of energy. Increasing the number of turns of wire in the coils, as well as amount of magnetic flux passing through them, would enable a much more efficient alternator to be developed and significantly more energy to be extracted from the chamber. This is demonstrated by the 2000 turn coil that illuminated the LED, which typically have a voltage drop of 1.7 V. Such work has not been attempted in this chapter, however, since it would fall out of the scope of the thesis.

The second power generation method presented was a piston-crank mechanism. This was developed in an attempt to improve the consistency of the power supplied by the WHES, and was designed according to the behaviour of the uncoupled piston tested in Chapter 3. The final design featured a piston with a 72.5 mm stroke length, a 75 mm long connecting rod, and a snail drop cam actuating a carbon fibre push rod to ensure the valve closed at the correct crank angle. The crankshaft was coupled to a 2 V brushless DC motor that was wired in series to a 4.7 Ω resistor, so that the voltage and power generated

by the motor could be determined using a digital oscilloscope. The motion of the piston was also filmed, so that its kinematic behaviour could be studied.

Using the motion tracking data, the piston was found to produce a mean power of 7.90 mW over 20 seconds, corresponding to 158 mJ of energy. The ratio of mean overall to mean peak power was found to be 8.7, which is much smaller than the 18.2 for the uncoupled piston. This shows that the crank provides a more consistent level of power, however its output is still far from constant. Given these values and the input conditions used during the experiment (a 570 mm head and a 0.130 kg/s mass flow rate), the crank was found to have a maximum efficiency of between 10 - 25 %. These peak efficiency values occurred when a pressure surge forced the crank upwards – given their periodic nature, the overall time-averaged efficiency was found to be 1.09 %. These values suggest that the system can operate in the low input conditions targeted by this research, however they also show that further research, development and optimisation of both the hydrodynamic and power take-off subsystems is required if the WHES is to become an effective generation system.

The electrical power available from the crank was found to be 43.45 $\pm$ 47.71 μW, which is smaller than that produced by the multiple coils of wire and lower than that determined from the piston motion. This is due to the extremely poor efficiency of the generator that was used. The power output would naturally be significantly improved by designing an appropriate generator and/or transmission system, however such work falls out of the scope of this thesis. The ratio of peak to mean electrical power as measured by the oscilloscope was 4.13, again indicating that the crank and a rotary generator will improve the consistency of the power supplied.

Given the complexity of their respective designs and the variables influencing their effectiveness, a well-designed linear alternator may be more suited to extracting energy from a WHES deployed in a tidal stream. This is mainly due to its simplicity. The lack of additional mechanical components will greatly improve durability and reduce maintenance requirements. The use of floating magnets, when combined with the fact that the velocity and acceleration experienced by a float should enable a linear alternator to function effectively in a wide range of input conditions, provided an appropriate valve is selected. The biggest issue with varying input conditions for an alternator will be the varying water level within the chamber, however this could be designed for by building multiple coils and connecting them in parallel. The power generated would require conditioning so that it was of suitable quality for consumption.

Meanwhile, the mechanical system is likely to be more effective in a system driven by an elevation head than it is in a tidal stream. This is because it

is a more complex system with multiple moving parts. It will also be less capable of dealing with varying input conditions, since the diameter of the crank must equal the stroke length. The crank does provide a more consistent power output, and may also offer mechanical, rather than electrical power. This second advantage will naturally be of much greater use on land than it is out to sea.

Although the output of the crank is more consistent than that of an uncoupled piston, it still struggles to produce comparable power on the downstroke as it does on the upstroke. This could be compensated for by coupling multiple cranks onto a single shaft to create a multi-cylinder device. Ultimately the choice and design of the power take-off will depend upon the desired output and the conditions that the device has to operate in.

Chapter 6

Case study

Chapters 3 and 4 illustrated the hydrodynamics of the Water Hammer Energy System and identified the variables governing its efficiency. Chapter 5 demonstrated its capability to generate electricity, demonstrating that the concept has the potential to generate useful power with further research and development. For the system to be effective in the real world, however, it will need to provide meaningful amounts of renewable energy from low speed, shallow water flows. Whether or not this is possible is dependent upon the effectiveness with which it can convert the power of a horizontal flow into hydraulic power within the chamber.

The purpose of this chapter is to identify the efficiency of a Water Hammer Energy System operating in a variety of real world locations, and thus provide an indication of the energy it could provide. This is achieved by computing the efficiency curve of a 1 m^2 device operating with a range of valve closure frequencies in flow speeds of 0 to 2 m/s. The predicted efficiency values are multiplied by the power available from a variety of flows to compute the power and energy that would be supplied.

The flow data used in this chapter comes from a hydrodynamic model of Poole Harbour in Dorset, UK. This model was created by the commercial company HR Wallingford (Posford Haskoning and HR Wallingford, 2004) as part of a study into the effects of deepening the main shipping channel in the harbour, and the results were used with their permission. Several sites around Poole Harbour are selected according to their flow rate and depths, which are all significantly smaller than those targeted by commercial tidal stream devices. Following this, an assessment of how much energy would be supplied by a WHES operating in flows of constant velocity is also provided.

6.1 Poole Harbour

Named after the nearby town of Poole that is situated on its northern shores, Poole Harbour is a large natural harbour located in Dorset, England. It was formed at the end of the last ice age approximately 7000 years ago, when rising sea levels broke through a chalk ridge which had connected Old Harry Rocks in Studland Bay with the Needles in the Isle of Wight (Posford Haskoning and HR Wallingford, 2004). An overview of the harbour is provided in Figure 6.1.

Figure 6.1: Location of Poole Harbour in the United Kingdom. Created using Google Maps.

At high water on spring tides, Poole Harbour has a surface area of 36 km^2, making it the largest natural harbour in the UK and one of the largest in Europe (Humphreys and May, 2005). The shoreline of Poole Harbour is over 100 km long, however it is only 0.48 m deep on average. There are five large islands (Brownsea, Furzy, Green, Round and Long) within the harbour, which serves as the estuary of four rivers (the Frome, Piddle, Corfe and Sherford). There is a single seaward entrance that is 370 m across at its widest point. The north and east sides of the harbour, incorporating the areas of Poole and Sandbanks, are highly urbanised and developed, while the south and west areas are more natural and rural.

6.1.1 Tidal climate

The tides inside Poole Harbour are governed by those of the adjacent English Channel. As discussed in Chapter 2, the tides can be described as standing waves of water. The nodes of a standing tidal wave are called amphidromic points, and although there are no such points within the English Channel, the tides act as if there is one inland of Bournemouth. Due to its proximity to this point, the tidal range in Poole Harbour is extremely small; around 1.8 m on spring tides and 0.6 m on neap tides (Humphreys, 2005).

Poole Harbour is consequently classified as a micro tidal area. Despite this, its large area results in an estimated 7.13×10^7 m^3 of water leaving the harbour on an ebbing spring tide, around 45 % of the total spring high water volume. On neap ebb tides this figure is around 22 % of the total neap high water volume. The geomorphology of the harbour is such that 80 % of the harbour bed is periodically exposed by the ebb tide.

In a low amplitude tidal regime, local effects become more pronounced relative to the primary lunar and solar tidal constituents. For Poole Harbour, this results in the unusual phenomenon of double high waters, which can be seen in Figure 2.2 of Chapter 2. Low water is followed by the flood tide and high water, before a brief ebb tide known as the "fore-ebb" generates a subsidiary low water. This is then brought back up to high water by a second flood tide known as the "half-flood", before the full ebb tide returns the water to the low level. For spring tides, the level of the first high water is typically greater than that of the second, while the reverse occurs for neap tides (Humphreys, 2005).

A consequence of the double high tide is a relatively long period of high water, with the water level above the mean value for roughly 16 hours out of every 24. This affects the quality of the tidal power resources available, since the tidal currents in Poole Harbour reverse direction 8 times a day compared to the more usual 4 times of a typical semi-diurnal location.

Over the winter of 2005/2006, 2.12×10^6 m^3 of material was dredged from the approach to deepen the channels to a navigation depth of 7.5 m below Chart Datum and widen the Middle Ship Channel to 100 m (Ramsbottom, 2012). As part of the channel deepening work, a study was undertaken to assess the environmental impacts of the dredging and subsequent use of the dredged material (Posford Haskoning and HR Wallingford, 2004). This included a numerical simulation of the harbour to predict the tidal flow and assess the impact of channel deepening on it. The predictions of this model were validated against Acoustic Doppler Current Probe observations of the water flow in the harbour entrance during the spring and neap tides of 8 April and 13 April

2004.

6.2 Case study methodology

To investigate the feasibility of using the WHES for generating pico scale electricity from the tides, it was decided to investigate its hydrodynamic performance in the conditions of various sites within Poole Harbour. To achieve this, flow velocity data from the HR Wallingford model was combined with efficiency predictions from the mathematical model of Chapter 4, to estimate the hydraulic energy a WHES could provide at a range of sites throughout Poole Harbour. Following this, the study is repeated using consistent flow values to illustrate how the WHES might perform in a conventional hydropower scenario.

6.2.1 Site selection

Seven sites were selected according to their location, depth and flow speeds. These are summarised in Table 6.1, which demonstrates that all of these sites are significantly smaller in terms of both flow speed and water depth than those targeted by the conventional tidal stream devices discussed in Chapter 2. The location of the sites around Poole Harbour can be seen in Figure 6.2. With the exception of Site G, they are all clustered about harbour mouth, which experiences the strongest flows due to its relatively narrow size and the volume of water that enters and leaves with the tides.

Table 6.1: Summary of selected sites.

Site	Name	Mean flow speed (m/s)	Peak flow speed (m/s)	Maximum depth (m)
A	East Looe Channel	0.42	1.14	2.60
B	South Haven Point	0.33	1.29	1.50
C	Swash Channel	0.48	1.46	7.50
D	Chapmans Peak	0.59	1.69	5.70
E	Northhaven Point	0.36	1.40	1.50
F	Brownsea East Pier	0.39	1.40	12.0
G	Little Channel	0.31	0.93	6.00

Given that it is the only seaward entrance, this area of the harbour is extremely busy with marine traffic. The Bramble Bush chain ferry also crosses the harbour mouth between Sandbanks in the north and Shell Bay in the south. Sites C and D, which from Table 6.1 will provide the most power due to their high mean and peak flow speeds, are in the middle of the harbour

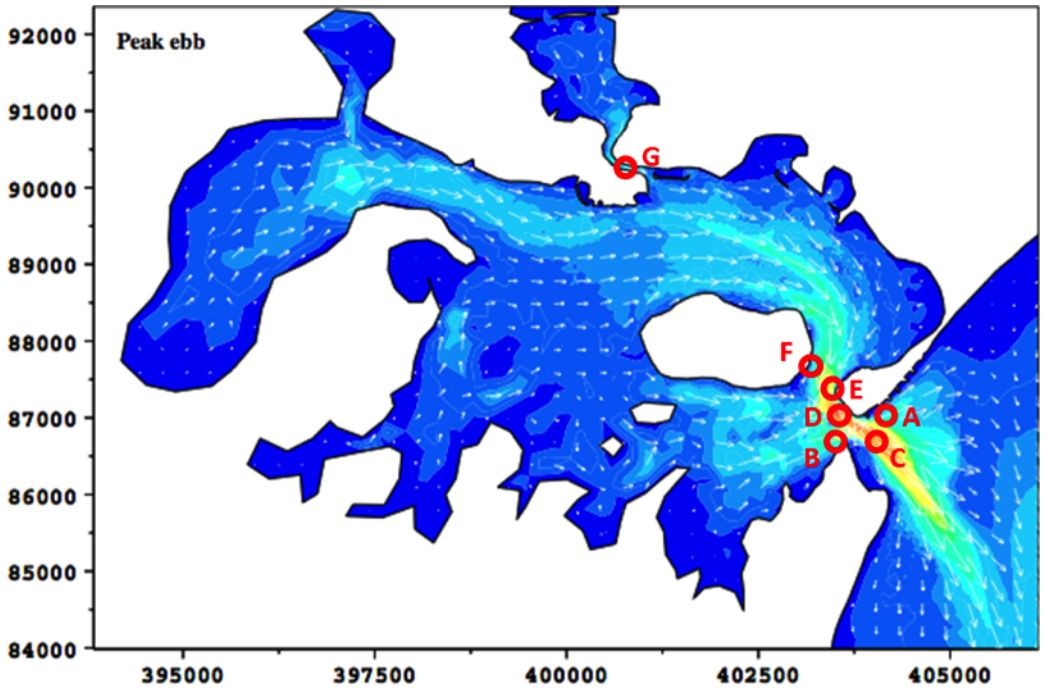

Figure 6.2: Location of selected sites in Poole Harbour and the peak flows of the ebb tide. Tidal flow map sourced from Posford Haskoning and HR Wallingford (2004)

entrance and therefore unlikely to be useable in reality. The other sites are all located just off the shoreline, which would make them easily accessible for maintenance work and reduce the amount of infrastructure required to transmit the generated power to a point of demand. This, combined with the low input head conditions, makes them ideal for investigating the effectiveness of the Water Hammer Energy System in pico scale applications.

6.2.2 Power output

To estimate the energy that a WHES could supply from each site, the power available from the flow was calculated according to the available velocity and head. This was then multiplied by the hydrodynamic efficiency of a theoretical WHES with a 1 m^2 drive pipe and chamber operating in identical conditions. The efficiency values were calculated using the mathematical model of Chapter 4; a sawtooth wave was used to approximate the flow through the valve, with a peak outflow rate equal to the available inflow rate (i.e. the input flow speed multiplied by the device area). The efficiency of the system was determined from the predicted chamber power relative to the input, and was calculated over a range of closure frequencies and input flow speeds to produce the plot shown in Figure 6.3.

Figure 6.3 shows that the theoretical device is at its most efficient at a

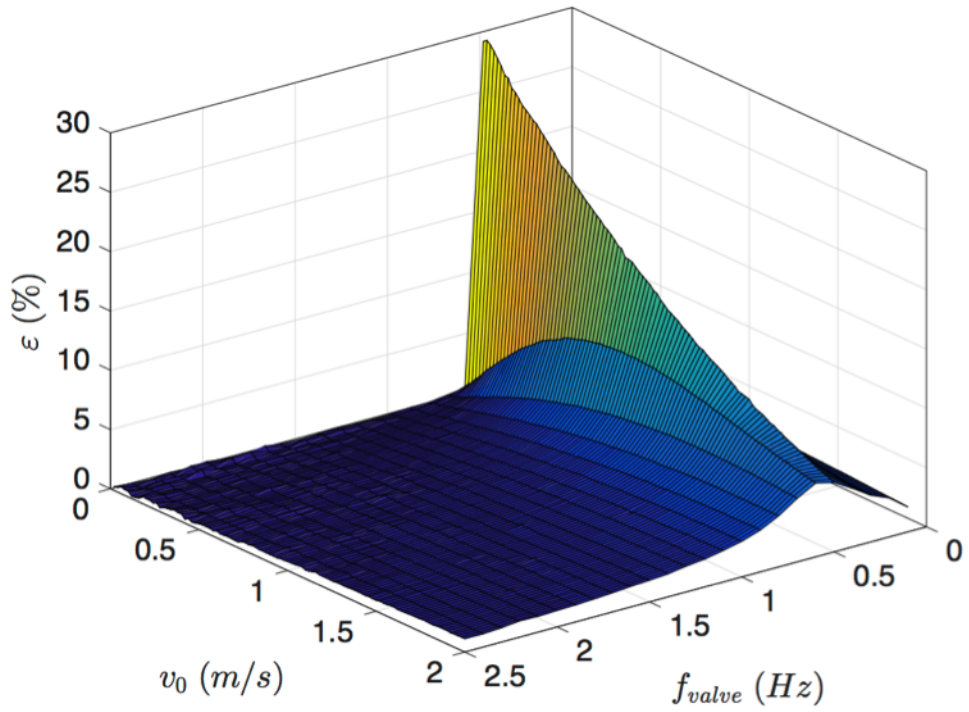

Figure 6.3: Theoretical hydrodynamic efficiency curve for a 1 m^2 WHES.

closure frequency of 0.5 Hz, as from Chapter 4 this is the frequency at which the water within the drive pipe experiences the greatest momentum changes. The device is at also at its most efficient in the lowest input speeds; as the input is increased, the flow cannot recover to its peak value following each valve closure, meaning the momentum change, pressure surges and power generated by subsequent valve closures are not as great relative to the available power.

A fixed operating frequency of 0.5 Hz was chosen for this study, given that it is the ideal operating frequency of the system shown in Figure 6.3. The minimum operating speed of the device was set as 0.4 m/s, although in practice this value will depend upon the design of the valve. These figures resulted in a hydrodynamic efficiency range of 23.1 % at the cut-in speed to 5.83 % in a 2 m/s flow.

The predicted flow velocities at the various selected sites were divided into 0.02 m/s bins (corresponding to the intervals of predicted device efficiency) so that the power available from the flow could be calculated. This was then multiplied by the predicted device efficiency at that velocity to compute the hydraulic power it could provide. It was assumed that the system was capable of yawing into the flow so that it always captured the full magnitude of the velocity. Since the velocity data from the model was split into 15 minute intervals, it was also assumed that the velocity and power remained constant

over that time for the purposes of estimating the mean power $\bar{P}$ the device could supply. This was calculated by summing the energy extracted in each 15 minute time interval and dividing the result by the total time period of 26760 minutes:

$$\bar{P} = \frac{1}{T} \sum_{1}^{n} P_n \Delta t_n \tag{6.1}$$

Where n is the number of time steps (i.e. 1784), Δt is the size of a time interval (i.e. 15 minutes) and T the total time (i.e.26760 minutes).

Annual energy predictions were calculated by summing the energy available from each time bin, and then assuming that the 18.6 days worth of flow data available from the model would be repeatedly consistently over the course of a year:

$$E_{an} = \frac{365}{18.6} \sum_{1}^{n} P_n \Delta t_n \tag{6.2}$$

For the constant flow cases, the peak flow velocity at each site was assumed to remain constant over the course of a year.

6.3 Case study results

The amount of power available from the Poole Harbour sites is summarised in Table 6.2, alongside the mean hydrodynamic efficiency and power output of the theoretical WHES. The results show that the design would be capable of producing a mean power output of 0.77 to 3.81 kW, with a peak power output in the strongest flows of between 6.86 to 19.5 kW, depending upon the site. Although these are small values when compared with the power output of the large scale commercial devices discussed in Chapter 2, they are not insignificant given the level of power available from the low head conditions of Poole Harbour.

Net values, representing the amount of power that would be provided if WHES devices were positioned at each site, are also shown. These figures suggest that up to 94.5 kW of hydraulic power would be provided by 7 single chamber WHES devices located around Poole Harbour in peak flows, with 13.3 kW produced on average. These figures do not account for the influence each individual device would have on the surrounding flow field, however given their relatively small size in comparison to the area they are operating in (the theoretical devices have a diameter of 1.28 m compared to the 370 m width of the harbour entrance), there is likely to be a minimal impact on the flow if only a handful of devices are deployed.

The usefulness of generating such small levels of power is illustrated Table

Table 6.2: Summary of power available from the various sites and what would be provided by the theoretical WHES.

Site	Mean site power (kW)	Peak site power (kW)	Mean WHES power (kW)	Peak WHES power (kW)	Mean WHES efficiency (%)
A	10.7	76.5	1.69	10.0	8.92
B	8.84	111	1.26	13.0	5.85
C	18.1	160	2.54	15.7	8.99
D	30.0	241	3.81	19.5	9.97
E	10.9	140	1.47	14.7	5.66
F	12.2	140	1.74	14.7	7.38
G	5.14	43.4	0.77	6.86	6.30
Mean	13.7	130	1.90	13.5	7.58
Net	95.8	655	13.3	94.5	14.4

Table 6.3: Summary of the hydrodynamic energy available from the WHES across Poole Harbour.

Site	Monthly energy output (kWh)	Annual energy output (kWh)	No. of houses supplied (-)	CO_2 offset from natural gas (tonnes)
A	1240	14800	3.22	8.21
B	922	11100	2.40	6.12
C	1860	22300	4.84	12.3
D	2780	33400	7.25	18.5
E	1070	12900	2.80	7.13
F	1270	15300	3.32	8.45
G	561	6730	1.46	3.72
Mean	1390	16600	3.62	9.20
Net	9700	116000	25.3	64.4

6.2, which summarises the amount of hydrodynamic energy that the theoretical system could provide at each site. The monthly figures range from a minimum of 561 kWh at Site G, to a maximum of 2780 kWh in the harbour entrance at Site D.

These values can be put into context by demonstrating how many UK households (which have a typical average annual electrical energy consumption of 3300 kWh (ofgem, 2011)) each site could sustain, as well as the annual CO_2 savings that would be provided if the site were to offset combined cycle natural gas generation. The latter figure is calculated according to estimated 0.55 kg of CO_2 per kWh produced by gas-fired power stations (US Energy Information Administration). Doing so suggests that, if all seven sites across Poole Harbour were utilised, enough energy could be extracted per year to sustain 25 average households while offsetting 64.4 tonnes of CO_2 from natural gas generation.

Table 6.4: Effect of device cut-in speed on operating time in Poole Harbour flows.

Site	Operating time (%)			
	$v_c = 0.2$ m/s	$v_c = 0.4$ m/s	$v_c = 0.6$ m/s	$v_c = 0.8$ m/s
A	75.0	46.3	26.7	11.4
B	59.4	30.8	16.1	9.96
C	75.7	49.9	32.1	21.0
D	80.1	58.8	40.4	29.4
E	64.7	30.8	17.5	11.8
F	66.3	39.4	22.1	12.0
G	66.4	30.5	10.6	1.06

These figures do not account for the conversion of hydrodynamic energy into electricity, however. If an arbitrary 30 % conversion efficiency is considered, 7.5 houses might be sustained with 19.3 tonnes of CO_2 offset. Although these figures are quite low, they suggest that an efficiently designed WHES may be capable of providing pico scale tidal power to coastal homes and communities. If this was done at many sites around the coastline, it could provide a small but meaningful contribution to the UK's renewable energy targets.

Although tidal power is predictable well into the future, it still suffers the drawback of providing variable power, with very little flow occurring at high and low water when the tidal currents reverse direction. This is illustrated by Table 6.4, which summarises how the minimum system operating speed v_c will govern the percentage of time it could operate in the flows of Poole Harbour.

Depending upon the site, the WHES would only be capable of generating power 60 to 80 % of the time, even with an extremely low cut-in speed of 0.2 m/s. This will naturally diminish the energy that can be supplied. Rivers provide more constant input conditions in the form of a less variable flow and accessible static head. Tables 6.5 and 6.6 summarise the amount of power and energy that the WHES could supply from the Poole Harbour sites if their peak flow speeds remained constant, reflecting the output that may be available from rivers in such flow speeds.

Tables 6.5 and 6.6 suggest that if the WHES were operating on a river, it may be capable of enough hydrodynamic energy to meet the electrical energy consumption of 25 – 26 typical UK homes. This figure would be sufficient to offset around 65.5 tonnes of CO_2 that would otherwise be generated by burning natural gas. If device were deployed at all seven sites, up to 458 tonnes of CO_2 from natural gas generation could be offset. If a 30% conversion factor is again assumed for electricity generation, these figures would obviously fall: a single device might provide enough electrical energy for approximately 8

Table 6.5: Summary of power available from the WHES at the various Poole Harbour sites if the flow speed were constant.

Site	Flow speed (m/s)	Site power (kW)	WHES power (kW)	WHES efficiency (%)
A	1.14	76.5	10.0	13.1
B	1.29	111	13.0	11.7
C	1.47	160	15.7	9.80
D	1.69	241	19.5	8.09
E	1.40	140	14.7	10.5
F	1.40	140	14.7	10.5
G	0.93	43.4	6.86	15.8
Mean	1.33	130	13.5	11.4
Net	N/A	655	94.5	13.1

Table 6.6: Summary of energy available from the WHES at the various Poole Harbour sites if the flow speed were constant.

Site	Monthly energy output (kWh)	Annual energy output (kWh)	No. of houses supplied (-)	CO_2 offset from natural gas (tonnes)
A	7330	88000	19.1	48.7
B	9460	114000	24.9	62.8
C	11500	138000	30.0	76.3
D	14300	171000	37.2	94.7
E	10800	129000	28.1	71.4
F	10700	128000	27.9	71.1
G	5010	60100	13.1	33.3
Mean	9860	118000	25.7	65.5
Net	69000	828000	180	458

homes, offsetting nearly 20 tonnes of CO_2 in the process. If all seven sites were utilised, 54 homes might be supplied and 137 tonnes of CO_2 offset.

These figures again illustrate the potential impact that generating hydropower from shallow water, low flow speed sites could have on renewable energy and climate change targets. Although small by themselves, if they were repeated at a number of site across the country they could result in a small but meaningful contribution.

6.4 Case study conclusions

This chapter has predicted the theoretical hydrodynamic efficiency of a 1 m^2 Water Hammer Energy System operating at various valve closure frequencies in a range of flow speeds. This information has been combined with tidal stream velocity predictions (from a numerical model of Poole Harbour provided by HR Wallingford) to predict the amount of power and energy the theoretical system could supply in a range of conditions.

The results suggest that a system operating with a valve closure frequency of 0.5 Hz would be the most efficient, with hydrodynamic efficiency values ranging between 23.1 % at the cut-in speed to 5.83 % in a 2 m/s flow. One of these systems in Poole Harbour would be capable of providing 3.81 kW of hydraulic power on average if it were positioned in the harbour entrance. Over the course of a year, this would be sufficient to satisfy the electrical energy demand of about 7 average UK households and could offset 18.5 tonnes of CO_2 from gas-fired generation. If such a system were placed in a constant flow speed of 1.69 m/s, it could be capable of providing up to 19.5 kW of hydrodynamic power. The annual energy this equates to would be sufficient to supply 37 annual UK households and offset 94.7 tonnes of CO_2 from natural gas generation.

These figures do not account for the conversion of chamber power into electricity, however. This is because an efficient power take-off system for the WHES is yet to be designed. If an arbitrary 30 % efficiency value is assumed for this process, then the device operating in the mouth of Poole Harbour would provide 1.14 kW on average. Over the course of a year, this would provide enough energy to supply 2 houses and offset 5.55 tonnes of CO_2. Using the same generator efficiency factor, 5.85 kW would be generated in a constant 1.69 m/s flow. This would be sufficient to supply the annual electricity usage of 11 typical UK households and offset nearly 30 tonnes of CO_2 from natural gas.

These figures were computed using the mathematical model of Chapter 4,

and are therefore subject to the assumptions used in the derivation of those equations. These include incompressible flow and a completely rigid system, neither of which will be true in practice. Despite this, the values suggest at the potential of using the Water Hammer Energy System to generate pico scale power from shallow, low flow sites. If multiple devices were deployed around the country in such areas, then the power they would supplied would be sufficient to make a small but meaningful contribution to the UK's climate change and renewable energy targets. At the same time, using the devices as part of a distributed grid would also improve the resilience of the electricity network and reduce transmission losses, further improving sustainability.

Chapter 7

Conclusions and future work

The development of renewable energy sources is being driven by the issue of climate change and the consequent need to develop sustainable energy supplies. Hydropower is one of the few renewables to provide predictable power, making it an attractive option, particularly for smaller scale generation in a decentralised power network. Yet there are currently few hydropower devices that can operate effectively in sites with very low heads (< 1 m) and flow rates (< 1 m^3/s). This is particularly true for generating power from the tides; most tidal stream devices in development target flows >2 m/s in waters that are deeper than 15 m, while tidal range devices typically require at least moderate heads (> 4 m). Due to these technological limitations, many small scale local resources are currently unable to be exploited.

7.1 Conclusions

The aim of this thesis was to develop a device capable of operating in shallow waters and low input conditions, with flow rates under 2 m^3/s and input heads under 1 m. This was to be achieved by

1. Reviewing the state of the art of tidal power to identify the factors that affect pico scale generation and assessing the suitability of current tidal technologies for this application.

2. Designing a device that is capable of generating electrical power from a range of sites based on this information.

3. Studying the hydrodynamics of this device to identify the criteria that govern its efficiency through mathematical modelling and scale model testing.

4. Proposing an efficient design and and evaluating its annual energy output in a range of input conditions.

Objective 1 was met in Chapter 2 by assessing the state of the art of tidal energy. The factors that govern the resources available to major tidal technology types were reviewed alongside the devices themselves, to assess which would be most effective for generating power from low head and low flow rate sites. The assessed technologies included both tidal range and tidal stream systems, including a mixture of conventional hydrokinetic turbines and more novel designs such as oscillating hydrofoils. Of these technologies, cross-flow turbines were deemed the most suitable for pico scale applications, due to their relatively high hydrodynamic efficiencies and the fact that their maximum size is not constrained by water depth.

A novel device for generating power from low head, low flow speed sites is detailed during the second part of Chapter 2. Referred to as the Water Hammer Energy System (WHES), the device uses a periodically closing valve to generate pressure surges and create an oscillating water level within a vertical chamber, from which energy may be extracted. This enables the power take-off system to be located above the water surface, meaning the size of the device can be maximised while also providing easier maintenance.

The fact that the magnitude of a water hammer pressure surge is dependent upon the deceleration experienced by the flow, rather than the flow rate itself, meant the WHES appeared particularly well suited to low flow speed sites in comparison to a conventional turbine. Although the hydrodynamic effectiveness of the WHES was completely unknown, its potential advantages in shallow waters and low input conditions were deemed sufficient for it to be capable of fulfilling Objective 2. This resulted in it being taken forwards for further investigation, so that the factors governing its performance could be assessed. This was achieved in Chapters 3 and 4 through a mixture of experimental and mathematical methods, completing Objective 3.

The experimental investigations focussed on characterising the performance of a scale model test rig. The model was built from threaded PVC pipe parts, and driven by a head of water from a reservoir located 350 mm above the outlet of the test rig. The experiments found the pressure surges generated by the WHES are capable of driving both a floating body and a piston. Since the valve used in these experiments was not controlled, the input conditions were found to have a significant impact on the performance of the system. Reducing the input flow rate by choking the flow between the reservoir and the model produced oscillations that were less frequent but much greater in amplitude.

The bulk of the power generated by the scale model was found to occur in short, sharp peaks corresponding to the driven body being forced upwards by a pressure surge. On average, these peaks were 18 times greater than the mean power available from the system, regardless of the driven body or the frequency of the system. Although the power available from the floating bodies was not found to be affected by oscillation amplitude, the piston was. It was found to have a maximum peak power of 1.36 W available in the largest oscillations and a corresponding mean of 0.07 W. The increase in power was such that the time-averaged power available from the piston was also greater in the larger oscillations, despite their diminished frequency.

A mathematical study of the behaviour of the WHES was presented in Chapter 4 and validated against the experimental data of Chapter 3. This focussed on characterising the behaviour of a system similar in design to the experimental test rig, yet where the behaviour of the valve was completely independent of the input conditions. This study demonstrated that the behaviour of the flow through the valve is the most significant factor affecting the performance of the WHES, with more power available when the peak discharge through the valve is greater and the valve closure frequency is low. This is because the momentum of the water within the drive pipe experiences a larger change in such conditions, producing a stronger pressure surge and a larger chamber oscillation. The input conditions were found to have little effect on system performance – provided the flow through the valve can be kept constant. This indicates that an appropriately designed WHES should be capable of operating reliably in pico scale conditions.

The effect of device size on performance was also investigated in Chapter 4. The results of these studies indicate that increasing the size of the device will increase efficiency at lower valve closure frequencies in comparison to smaller devices, with the opposite true at higher frequencies. This is due to the greater momentum changes that will occur within the drive pipe of a larger device at low frequencies. The peak hydrodynamic efficiency of the systems simulated in Chapter 4 was 17.8 %, for the largest 48 mm diameter device operating at a valve closure frequency of 0.4 Hz and a peak outflow rate of 1.81×10^{-3} m^3/s.

One drawback with the mathematical study was the use of a simplified model that neglected spatial effects, rather than solving the full partial differential equations that govern hydraulic transients within pipes. Despite this simplification, the variation in the chamber water level predicted by the model was found to show good agreement with the behaviour of the experimental test rig.

Although it was not defined as a research objective, the novel nature of the WHES meant that it was important to demonstrate that it is capable of generating useful power. This was achieved in Chapter 5, which presented two methods for extracting energy from the system. The first method used the WHES to drive a floating magnet up and down inside coils of copper wire, turning the device into a linear alternator. This method was used to successfully illuminate an LED, qualitatively demonstrating that the device is capable of functioning as intended. The peak power from the linear alternator was found to be 418 μW, with a mean power of 149 μW.

The second power take-off method presented was a piston-crank mechanism. This was developed to reduce the disparity between the peak stroke power and the mean overall power, and hence provide a more consistent power output. To ensure the pressure surges were generated when the crank was at the correct angle, the system was timed with a cam and push rod actuating the valve. The crank drove a 2 V brushless DC motor as a generator, so that electrical power could be measured.

The crank reduced the maximum frequency of the device to 1.76 Hz, from 3.6 Hz for the free closing valve. The ratio between the mean and peak power was found to fall from 18 for the uncoupled piston to 8.7, indicating that the crank provides a more consistent power output. The time-averaged mechanical efficiency of the crank (as determined using motion tracking) was found to be 1.09 %, with peak values of 10 - 25 % occurring during a pressure surge at the beginning of the upstroke. Despite this, the electrical power generated by the system was very low, with a mean value of 43.5 μW. This is ascribed to the extremely low efficiency of the generator at the low angular velocity of the crank. Using a purpose-built low speed generator, or a gearbox to increase the angular velocity at the generator, would be an effective method for improving the efficiency of this power take-off system.

Despite this, the experiment showed that the piston-crank is also a viable method for extracting energy from the WHES. The fact that this occurred in an input head of 570 mm and input mass flow rate of 0.130 kg/s also shows that the WHES can operate in the low input conditions targeted by this research. With further development and optimisation, the electrical and mechanical efficiency of the power take-off system could be improved, increasing the overall effectiveness of the device. This will be required if the system is to be used successfully, however it was not attempted in this work as it fell out of the research scope.

Finally, to meet Objective 4, a case study was conducted to investigate the amount of energy a theoretical device could supply if operating at a range of

sites around Poole Harbour. The flow data for this sites was taken from a numerical model of the harbour that was created by the company HR Wallingford as part of a study into the effects of deepening the main shipping channel.

The case study results answer the research question that was posed in Section 1.3: "*what is the maximum hydrodynamic efficiency of a purpose-designed pico scale hydropower system and how much energy can one supply from both tidal and conventional hydropower sites over the course of a year?*"

A 1 m^2 device operating in the mouth of Poole Harbour would reach a peak hydrodynamic efficiency of 9.97 %. Given the power available from the flow, this would be sufficient to extract up to 33.4 MWh of energy annually. Assuming an arbitrary generation efficiency of 30 %, such a device could meet the average annual electricity consumption of 2 typical UK homes. In doing so, it might also offset 5.6 tonnes of CO_2 if it were to replace natural gas generation. If the device with a 30 % efficient power take-off were operating in a continuous flow of 1.69 m/s (the peak flow available in the harbour mouth), it could supply enough electricity over the course of a year for 11 typical homes, offsetting 28.4 tonnes of CO_2 from gas generation in the process.

Although these figures are small individually, they could provide a small but significant supply of renewable energy if multiple devices were deployed at a range of sites as part of a distributed power grid. Given the potential hydrodynamic efficiency of the WHES and its capability to operate in slow waters, this suggests that, with further research and development, it may be a feasible method for harnessing pico scale hydropower resources.

7.2 Contribution to knowledge

This thesis makes the following contributions to knowledge:

- Assessment of the the suitability of current tidal technologies for pico scale hydropower generation.

The state of the art of tidal energy has been presented and the factors governing a variety of technologies, including tidal barrages, lagoons, axial flow turbines, cross flow turbines, oscillating hydrofoils and tidal kites, have been discussed. Cross flow turbines were deemed the most suitable technology for accessing pico scale sites, due to their potentially high efficiencies and the relative ease with which they can be scaled to fit a particular site. Due to their relatively large size requirements, barrages and lagoons were deemed to be the least effective method for generating pico scale power.

- Proposal of a system for generating pico scale power from low head, low flow sites.

The novel Water Hammer Energy System and its mode of operation have been presented and discussed. The WHES was deemed to have several advantages for pico scale generation: the power take-off can be located above the waterline, allowing shallow waters to be accessed, while the pressure surges it generates - and by extension the power - are ultimately dependent upon the change in momentum experienced by the water in the drive pipe, rather than the initial flow speed or head. Two methods for generating electricity using the WHES (a linear alternator and a piston-crank mechanism) have been demonstrated, showing that the idea is capable of functioning as intended.

- Investigation of system hydrodynamics and the factors affecting power output and efficiency.

The effect of input flow rate and head, valve behaviour and system size on performance have been investigated through a mixture of experimental and mathematical studies. The effect of these factors on performance have been quantified, although several of these relations are design dependent. The behaviour of the valve, in particular the closure frequency and peak discharge rate, are the most important factors governing system performance. If peak outflow rate is kept constant, the performance of the system is unaffected by the input head, which indicates that it has the potential to exploit low input sites.

- Identification of the energy such a system could supply in various real world locations.

The theoretical efficiency curve of a 1 m^2 device was derived from the mathematical model of Chapter 4 and applied to a selection of sites in Poole Harbour. This system was found to be at its most efficient in the weakest flow speeds, again suggesting the device is suitable for pico scale generation in low input conditions. Combined with an arbitrary 30 % generator efficiency, the results suggest that a device operating in the mouth of Poole Harbour could provide an average of 1.14 kW of electrical power. Over the course of a year, this would provide enough energy to supply 2 typical UK houses and offset 5.55 tonnes of CO_2.

7.3 Suggestions for future work

This thesis had demonstrated that the Water Hammer Energy System can be used to generate power and suggests than an optimised device may be capable of providing sufficient energy to make such generation worthwhile. A considerable amount of further work must be done if this is to be achieved, however, and the following suggestions are therefore provided.

Firstly, the design of the valve and its control system will be of critical importance to the efficiency of the WHES. A standard swing check valve was used in the experimental device presented in this study, however this is felt to be an inefficient choice due to its inertia. A lightweight, linear valve that is capable of snapping shut as rapidly as possible, will not only provide more power pressure surges but also be more straightforward to control. Devices should also be constructed out of a more rigid material to maximise the speed of the pressure surges within the chamber, and studies undertaken to determine the number of cycles a given valve and drive pipe could operate for.

Additionally, during the mathematical study, the behaviour of the flow through the valve was approximated using a variety of periodic boundary conditions. It will be important to directly model the behaviour of the valve if an efficient system is to be realised in practice, since the input conditions will influence the valve behaviour and vice versa. There have been a number of studies conducted into modelling check valve behaviour; combining these with the equations governing hydraulic transients would be a suitable method for designing an effective valve. An alternative option would be to use computational fluid dynamics to model system performance. The mathematical study also neglected the spatial effects and the positioning of the chamber on the drive pipe. This should also be examined, preferably while directly modelling the valve.

The power-take off subsystem of the WHES will also need considerable optimisation work if an efficient system is to be achieved. For the linear alternator, the following is suggested:

- Increasing the strength of the magnetic field within the chamber while minimising the distance and material between coils and magnets.
- Increasing the number of turns of wire in the coils
- Driving the magnets with a piston rather than a float.

For the piston-crank mechanism, the following work should provide a more efficient system:

- Reducing the distance between the crankshaft and the water level within the chamber
- Minimising the friction between the control system and the crankshaft.
- Designing an effective power transmission between the crankshaft and the generator
- Developing a generator that is capable of operating efficiently in the RPM and torque range provided by the power transmission.
- Coupling multiple devices onto a single crank to create an engine arrangement.

The final areas that this thesis has neglected are mooring methods, device superstructure and the conditioning and transmission of electrical power. One suggestion, particularly if the WHES is to be deployed floating on a river or stream, is to position it inside a small artificial channel. This could be used to set up a hydraulic jump between the inlet and outlet of the device to ensure there is sufficient head for the valve to close and the system to function.

References

ABP Marine Environmental Research Ltd. Atlas of UK Marine Renewable Energy Resources. Technical Report R.1106, DTI, 2008.

Ackermann, T., Andersson, G., and Söder, L. 2001, Distributed generation: a definition. *Electric power systems research.* 57 (3), 195–204.

Aghaei, J. and Alizadeh, M. 2013, Demand response in smart electricity grids equipped with renewable energy sources: A review. *Renewable and Sustainable Energy Reviews.* 18, 64–72.

Ahmadian, R., Falconer, R., and Lin, B. 2010a, Hydro-environmental modelling of proposed Severn barrage, UK. *Proceedings of the ICE - Energy.* 163, 107–117.

Ahmadian, R., Morris, C., and Falconer, R. 2010b, Hydro-environmental modelling of off-shore and coastally attached impoundments of the North Wales Coast. In *The First IAHR European Congress*, Edinburgh, UK.

Ahmadian, R., Falconer, R., and Bockelmann-Evans, B. 2012, Far-field modelling of the hydro-environmental impact of tidal stream turbines. *Renewable Energy.* 38 (1), 106–116.

Ahmadian, R., Olbert, A., Hartnett, M., and Falconer, R. 2014, Sea level rise in the Severn Estuary and Bristol Channel and impacts of a Severn Barrage. *Computers and Geosciences.* 66, 94–105.

Alanne, K. and Saari, A. 2006, Distributed energy generation and sustainable development. *Renewable and Sustainable Energy Reviews.* 10 (6), 539–558.

Alaska Energy. Eetg: Nenana hydrokinetic turbine. `http://energy-alaska.wdfiles.com/local--files/nenana-hydrokinetic-turbine/RIVGen_rendering.jpg`, 2013.

Allan, G., Eromenko, I., Gilmartin, M., Kockar, I., and McGregor, P. 2015, The economics of distributed energy generation: A literature review. *Renewable and Sustainable Energy Reviews.* 42, 543–556.

Allen, S., Hammond, G., and McManus, M. 2008, Prospects for and barriers to domestic micro-generation: A United Kingdom perspective. *Applied Energy*. 85 (6), 528–544.

AMSC. SeaTitan 10 MW Wind Turbine. `http://www.amsc.com/documents/seatitan-10-mw-wind-turbine-data-sheet/`, 2012.

Apsley, D. Unsteady flow in pipes. `http://personalpages.manchester.ac.uk/staff/david.d.apsley/lectures/hydraulics2/t5.pdf`, 2013.

Archer, A. and Hubbard, M. 2003, Highest tides of the world. *Geological Society of America Special Papers*. 151–174.

Arduino LLC. Arduino genuino. `https://www.arduino.cc`, 2017.

Asif, M. and Muneer, T. 2007, Energy supply, its demand and security issues for developed and emerging economies. *Renewable and Sustainable Energy Reviews*. 11 (7), 1388–1413.

Aslani, N., Noroozi, S., Yee, K., Chao, A., and Maggs, C. 2016, Simulation of gait asymmetry and energy transfer efficiency between unilateral and bilateral amputees. *Sports Engineering*. 1–8.

Bae, Y., Kim, K., and Choi, B. 2010, Lake Sihwa tidal power plant project. *Ocean Engineering*. 37 (5-6), 454–463.

Bahaj, A. and Myers, L. 2003, Fundamentals applicable to the utilisation of marine current turbines for energy production. *Renewable Energy*. 28, 2205–2211.

Bahaj, A., Molland, A., Chaplin, J., and Batten, W. 2007, Power and thrust measurements of marine current turbines under various hydrodynamic flow conditions in a cavitation tunnel and towing tank. *Renewable Energy*. 32 (3), 407–426.

Baker, C., Walbancke, J., and Leache, P. Tidal Lagoon Power Generation Scheme in Swansea Bay. `http://www.bright-sparks.biz/wp-content/uploads/2015/12/DTI-paper-on-Swansea-Bay-lagoon-scheme.pdf`, 2006.

Baker, J. 1983, Features to aid or enable self-starting of fixed pitch low solidity vertical axis wind turbines. *Journal of Wind Engineering and Industrial Aerodynamics*. 15 (1–3), 369–390.

Batten, W., Bahaj, A., Molland, A., and Chaplin, J. 2006, Hydrodynamics of marine current turbines. *Renewable Energy.* 31 (2), 249–256.

Belloni, C. *Hydrodynamics of Ducted and Open-Centre Tidal Turbines.* PhD thesis, University of Oxford, Balliol College, 2013.

Betz, A. 1920, Das Maximum der theoretisch möglichen Ausnützung des Windes durch Windmotoren. *Zeitschrift für das gesamte Turbinenwesen.* 26 (8), 307–309.

Black and Veatch Consulting Ltd. UK, Europe and global tidal steam energy resource assessment. Peer review issue 107799/D/2100/05/1, Carbon Trust, London, 2004.

Black and Veatch Consulting Ltd. Phase II UK Tidal Stream Energy Resource Assessment. Technical Report 107799/D/2200/03, The Carbon Trust, London, 2005.

Black and Veatch Consulting Ltd. UK Tidal Stream Resource and Economics. Technical report, London, 2011.

Blunden, L. and Bahaj, A. 2006, Initial evaluation of tidal stream energy resources at Portland Bill, UK. *Renewable Energy.* 31 (2), 121–132.

Blunden, L. and Bahaj, A. 2007, Tidal stream resource assessment for tidal stream generators. *Proceedings of the Institute of Mechanical Engineers, Part A: Journal of Power and Energy.* 221 (2), 137–146.

Bonin, C. 1960, Water-hammer damage to Oigawa power station. *Journal of Engineering for Power.* 82 (2), 111–116.

Borg, M. and Collu, M. 2014, A comparison on the dynamics of a floating vertical axis wind turbine on three different floating support structures. *Energy Procedia.* 53, 268–279.

Bourne Energy. Energy for the future. `http://www.bourneenergy.com/future.html`, 2014.

Bryden, I., Naik, S., Fraenkel, P., and Bullen, C. 1998, Matching tidal current plants to local flow conditions. *Energy.* 23 (9), 699–709.

Bryden, I., Grinsted, T., and Melville, G. 2004, Assessing the potential of a simple tidal channel to deliver useful energy. *Applied Ocean Research.* 26 (5), 198–204.

Bryden, I., Couch, S., A., O., and Melville, G. 2007, Tidal current resource assessment. *Proceedings of the Institution of Mechanical Engineers, Part A: Journal of Power and Energy*. 212 (2), 125–135.

Burton, T., Sharpe, D., and Jenkins, N. 2001, Handbook of wind energy.

Carballo, R., Iglesias, G., and Castro, A. 2009, Numerical model evaluation of tidal stream energy resources in the Ria de Muros (NW Spain). *Renewable Energy*. 34 (6), 1517–1524.

Charlier, R. 2007, Forty candles for the Rance River TPP tides provide renewable and sustainable power generation. *Renewable and Sustainable Energy Reviews*. 11 (9), 2032–2057.

Charlier, R. H. and Menanteau, L. 1997, The saga of tide mills. *Renewable and Sustainable Energy Reviews*. 1 (3), 171–207.

Chartrand, R. 2011, Numerical differentiation of noisy, nonsmooth data. *ISRN Applied Mathematics*.

Chaudhry, M. 2014, *Applied Hydraulic Transients*. Springer.

Coiro, D., De Marco, A., Nicolosi, F., Melone, S., and Montella, F. 2005, Dynamic Behaviour of the Patented Kobold Tidal Current Turbine: Numerical and Experimental Aspects. *Acta Polytechnica*. 45 (3).

Coiro, D., Maisto, U., Scherillo, F., Melone, S., and Grasso, F. 2006, Horizontal axis tidal current turbine: numerical and experimental investigations. In *Proceeding of Offshore wind and other marine renewable energies in Mediterranean and European seas, European seminar*, Rome, Italy.

Consul, C. *Hydrodynamic Analysis of a Tidal Cross-Flow Turbine*. PhD thesis, University of Oxford, Worcester College, 2011.

Consul, C., Willden, R., Ferrer, E., and McColloch, M. 2009, Influence of solidity on the performance of a cross-flow turbine. In *8th European Wave and Tidal Energy Conference*, Uppsala, Sweden.

Denny, E. 2009, The economics of tidal energy. *Energy Policy*. 37 (5), 1914–1924.

Department of Energy and Climate Change. Electricity generation costs 2013. `https://www.gov.uk/government/uploads/system/uploads/attachment_data/file/223940/DECC_Electricity_Generation_Costs_for_publication_-_24_07_13.pdf`, 2013.

Department of Energy and Climate Change. Electricity: Chapter 5, Digest of United Kingdom Energy Statistics (DUKES). https://www.gov.uk/government/statistics/electricity-chapter-5-digest-of-united-kingdom-energy-statistics-dukes, 2015.

Department of Energy and Climate Change. Final UK greenhouse gas emissions national statistics: 1990-2014. https://www.gov.uk/government/statistics/final-uk-greenhouse-gas-emissions-national-statistics-1990-2014, 2016.

Dlugokencky, E. and Tans, P. Trends in atmospheric carbon dioxide. www.esrl.noaa.gov/gmd/ccgg/trends/, 2016.

Doodson, A. T. 1921, The harmonic development of the tide-generating potential. *Proceedings of the Royal Society of London. Series A.* 100 (704), 305–329.

Dormand, J. and Prince, P. 1980, A family of embedded Runge-Kutta formulae. *Journal of computational and applied mathematics.* 6 (1), 19–26.

Draper, S., Adcock, T. A., Borthwick, A. G., and Houlsby, G. T. 2014, Estimate of the tidal stream power resource of the Pentland Firth. *Renewable Energy.* 63, 650–657.

Elbatran, A., Yaakob, O., Ahmed, Y. M., and Shabara, H. 2015, Operation, performance and economic analysis of low head micro-hydropower turbines for rural and remote areas: a review. *Renewable and Sustainable Energy Reviews.* 43, 40–50.

EMEC. Atlantis Resources Corporation, Available from: http://www.emec.org.uk/about-us/our-tidal-clients/atlantis-resources-corporation-2/.\newblock [Accessed 8 April 2014].

Entec UK Ltd. Tidal Technologies Overview. http://www.sd-commission.org.uk/data/files/publications/TidalPowerUK2-Tidal_technologies_overview.pdf, 2007.

Eriksson, S., Bernhoff, H., and Leijon, M. 2008, Evaluation of different turbine concepts for wind power. *Renewable and Sustainable Energy Reviews.* 12 (5), 1419–1434.

ETSU. Tidal stream energy review. Technical Report ETSU-T-05/00155/REP, Energy Technology Support Unit, DTI, 1993.

European Commission. The exploitation of tidal and marine currents. Wave energy. Project results. . `http://cordis.europa.eu/publication/rcn/199610441_en.html`, 1996.

European Marine Energy Centre. Tidal Developers, Available from: `{http://www.emec.org.uk/marine-energy/tidal-developers/}.\newblock` [Accessed 3 April 2014].

European Parliament and Council of the European Union. 2009, Directive 2009/28/EC of the European Parliament and and of the Council of 23 April 2009. On the promotion of the use of energy from renewable sources and amending and subsequently repealing Directives 2001/77/EC and 2003/30/EC. *Official Journal of the European Union*. L (140), 16.

Evans, D. and Porter, R. 1995, Hydrodynamic characteristics of an oscillating water column device. *Applied Ocean Research*. 17 (3), 155–164.

Evans Engineering and Power Company. Severn Tidal Power Reef. `http://severntidal.com/pdfs/Evans%20Tidal%20Power%20Reef%20Jan%202011.pdf`, 2011.

Fairley, I., Ahmadian, R., Falconer, R., Willis, M., and Masters, I. 2014, The effects of a Severn Barrage on wave conditions in the Bristol Channel. *Renewable Energy*. 68, 428–442.

Falcão, A. 2002, Control of an oscillating-water-column wave power plant for maximum energy production. *Applied Ocean Research*. 24 (2), 73–82.

Falconer, R. A., Xia, J., Lin, B., and Ahmadian, R. 2009, The Severn barrage and other tidal energy options: Hydrodynamic and power output modeling. *Science in China Series E: Technological Sciences*. 51 (11), 3413–3424.

Field, C. B., Campbell, J. E., and Lobell, D. B. 2008, Biomass energy: the scale of the potential resource. *Trends in ecology and evolution*. 23 (2), 65–72.

Fraenkel, P. and Musgrove, P. 1979, Tidal and river current energy systems. In *International conference on future energy concepts*, 114–117, London. Institution of Electrical Engineers.

Fraenkel, P. 2006, Tidal current energy technologies. *Ibis*. 148 (s1), 145–151.

Frau, J. 1993, Tidal energy: promising projects: La Rance, a successful industrical-scale experiment. *IEEE Transactions on Energy Conversion*. 8 (3), 552–558.

Gaden, D. and Bibeau, E. 2010, A numerical investigation into the effect of diffusers on the performance of hydro kinetic turbines using a validated momentum source turbine model. *Renewable Energy*. 35 (6), 1152–1158.

Garrett, C. and Cummins, P. 2004, Generating power from tidal currents. *Journal of waterway, port, coastal and ocean engineering*. 130 (3), 114–118.

Garrett, C. and Cummins, P. 2005, The power potential of tidal currents in channels. *Proceedings of the Royal Society of London. Series A*. 461, 2563–2572.

Garrett, C. and Cummins, P. 2007, The efficiency of a turbine in a tidal channel. *Journal of Fluid Mechanics*. 588, 243–251.

Garrett, C. and Cummins, P. 2008, Limits to tidal current power. *Renewable Energy*. 33, 2485–2490.

Ghidaoui, M. S., Zhao, M., McInnis, D. A., and Axworthy, D. H. 2005, A review of water hammer theory and practice. *Applied Mechanics Reviews*. 58 (1), 49–76.

Gibescu, M., Brand, A. J., and Kling, W. L. 2009, Estimation of variability and predictability of large-scale wind energy in The Netherlands. *Wind Energy*. 12 (3), 241–260.

Gill, A. 2005, Offshore renewable energy: ecological implications of generating electricity in the coastal zone. *Journal of Applied Ecology*. 42, 605–615.

Gorban, A., Gorlov, A., and Silantyev, V. 2001, Limits of the Turbine Efficiency for Free Fluid Flow. *Journal of Energy Resources Technology*. 123 (4), 311–317.

Gorlov, A. 1995, The helical turbine: a new idea for low-head hydropower. *Hydro Review*. 14 (5), 44–50.

Hardisty, J. 2009, *The analysis of tidal stream power*. John Wiley and Sons.

Heath, T. 2012, A review of oscillating water columns. *Philosophical Transactions of the Royal Society of London A: Mathematical, Physical and Engineering Sciences*. 370 (1959), 235–245.

Heming, L., Waley, P., and Rees, P. 2001, Reservoir resettlement in china: past experience and the three gorges dam. *The Geographical Journal*. 167 (3), 195–212.

HM Government. Climate change act. `http://www.legislation.gov.uk/ukpga/2008/27/pdfs/ukpga_20080027_en.pdf`, 2008.

HM Government. The carbon plan: Delivering our low carbon future. `https://www.gov.uk/government/uploads/system/uploads/attachment_data/file/47613/3702-the-carbon-plan-delivering-our-low-carbon-future.pdf`, 2011.

Howell, R., Qin, N., Edwards, J., and Durrani, N. 2010, Wind tunnel and numerical study of a small vertical axis wind turbine. *Renewable Energy*. 35 (2), 412–422.

Humphreys, J. 2005, Salinity and Tides in Poole Harbour: Estuary or Lagoon? *The Ecology of Poole Harbour*. 35–47.

Humphreys, J. and May, V. 2005, Introduction: Poole Harbour in Context. *The Ecology of Poole Harbour*. 1–23.

IPCC. 2013, *Climate Change 2013: The Physical Science Basis. Contribution of Working Group I to the Fifth Assessment Report of the Intergovernmental Panel on Climate Change*. Cambridge University Press, Cambridge, United Kingdom and New York, NY, USA.

IPCC. 2014, *Climate Change 2014–Impacts, Adaptation and Vulnerability: Regional Aspects.* Cambridge University Press.

Jeon, M., Lee, S., and Lee, S. 2014, Unsteady aerodynamics of offshore floating wind turbines in platform pitching motion using vortex lattice method. *Renewable Energy*. 65, 207–212.

Jones, K. D., Lindsey, K., and Platzer, M. 2003, An investigation of the fluid-structure interaction in an oscillating-wing micro-hydropower generator. *WIT Transactions on The Built Environment*. 71.

Jorant, C. 2011, The implications of Fukushima: the European perspective. *Bulletin of the Atomic Scientists*. 67 (4), 14–17.

Joukowsky, N. 1900, Uber den hydraulischen stoss in wasserleitungsro hren. (on the hydraulic hammer in water supply pipes). *Memoires de l'Academie Imperiale des Sciences de St.-Petersbourg*. 8 (9).

Kadiri, M., Ahmadian, R., Bockelmann-Evans, B., Rau, W., and Falconer, R. 2012, A review of the potential water quality impacts of tidal renewable energy systems. *Renewable and Sustainable Energy Reviews.* 16 (1), 329–341.

Kadlec, E. G. Characteristics of Future Vertical-Axis Wind Turbines. Technical Report SAND79-1068, Sandia National Laboratories, Albuquerque, 1978.

Kampa, M. and Castanas, E. 2008, Human health effects of air pollution. *Environmental Pollution.* 151 (2), 362–367.

Kelly, K., McManus, M. and Hammond, G. 2012, An energy and carbon life cycle assessment of tidal power case study: The proposed Cardiff–Weston severn barrage scheme. *Energy.* 44 (1), 692–701.

Kim, G., Lee, M., Lee, K., Park, J., Jeong, W., Kang, S., Soh, J., and Kim, H. 2012, An overview of ocean renewable energy resources in Korea. *Renewable and Sustainable Energy Reviews.* 16 (4), 2278–2288.

Kim, Y., Kim, M., and Kim, W. 2013, Effect of the Fukushima nuclear disaster on global public acceptance of nuclear energy. *Energy Policy.* 61, 822–828.

Kinsey, T., Dumas, G., Lalande, G., Méhut, A., Viarouge, P., Lemay, J., and Jean, Y. 2011, Protype testing of a hydrokinetic turbine based on oscillating hydrofoils. *Renewable Energy.* 36 (6), 1710–1718.

Kirby, R. and Shaw, T. 2005, Severn Barrage, UK - environmental reappraisal. *Proceedings of the ICE - Engineering Sustainability.* 158 (1), 31–39.

Kirke, B. and Lazauskas, L. 2008, Variable Pitch Darrieus Water Turbines. *Journal of Fluid Science and Technology.* 3 (3), 430–438.

Kirke, B. and Lazauskas, L. 2011, Limitations of fixed pitch darrieus hydrokinetic turbines and the challenge of variable pitch. *Renewable Energy.* 36 (3), 893–897.

Kyozuka, Y. 2008, An Experimental Study on the Darrieus-Savonious Turbine for the Tidal Current Power Generation. *Journal of Fluid Science and Technology.* 3 (3), 439–449.

Ladenburg, J., Termansen, M., and Hasler, B. 2013, Assessing acceptability of two onshore wind power development schemes: A test of viewshed effects and the cumulative effects of wind turbines. *Energy.* 54, 45–54

Lamb, H. 1994, *Hydrodynamics.* Cambridge University Press, 6th edition.

Lanchester, F. W. 1915, A contribution to the theory of propulsion and the screw propeller. *Journal of the American Society for Naval Engineers*. 27 (2), 509–510.

Lebarbier, C. 1975, Power from tides - the Rance Tidal Power Station. *Naval Engineers Journal*. 87, 57–71.

Ligon, F., Dietrich, W., and Trush, W. 1995, Downstream Ecological Effects of Dams. *BioScience*. 45 (3), 183–192.

Ltd, T. E. P. Tidal Energy PTY Ltd Website. `http://tidalenergy.com.au/faq.html`, 2015.

Marine Current Turbines. World-leading tidal energy system achieves 5GWh milestone. `http://www.marineturbines.com/News/2012/09/05/world-leading-tidal-energy-system-achieves-5gwh-milestone`, 2016a.

Marine Current Turbines. Seagen technology. `http://www.marineturbines.com/Seagen-Technology`, 2016b.

Marine Technology Ltd. OpenHydro and Marine Technology Ltd. `http://www.marinetechnology.ie/single-post/2015/12/17/OpenHydro-and-Marine-Technology-Ltd`, 2015.

Maritime Journal. Deep green flies kite for tidal energy. `http://www.maritimejournal.com/news101/marine-renewable-energy/deep_green_flies_kite_for_tidal_energy`, 2009.

Massachusetts Institute of Technology. Unsteady Bernoulli Equation. `https://ocw.mit.edu/courses/mechanical-engineering/2-25-advanced-fluid-mechanics-fall-2013/inviscid-flow-and-bernoulli/MIT2_25F13_Unstea_Bernou.pdf`, 2013.

MathWorks. ode45. `https://uk.mathworks.com/help/matlab/ref/ode45.html`.

MathWorks. MATLAB and Image Proessing Toolbox Release 2015b. Natick, Massachussetts, USA, 2015.

McAdam, R., Holsby, G., Oldfield, M., and McColloch, M. 2010, Experimental testing of the Transverse Horizontal Axis Water Turbine. *IET Renewable Power Generation*. 4 (6), 510–518.

MHI Vestas. V164-8.0 MW® breaks world record for wind energy production. `http://www.mhivestasoffshore.com/v164-8-0-mw-breaks-world-record-for-wind-energy-production/`, 2015.

Minesto. Deep Green Technology, Available from: `http://www.minesto.com/deepgreentechnology/.\newblock` [Accessed 3 March 2014].

Minesto. 2014, Deep Green Technical Data. In *RenewableUK Wave and Tidal 2014*.

Mohammed, S. 2007, Design and construction of a hydraulic ram pump. *Leonardo Electronic Journal of Practices and Technologies*. 6 (11), 59–70.

Myers, L. and Bahaj, A. 2006, Power output performance characteristics of a horizontal axis marine current turbine. *Renewable Energy*. 31 (2), 197–208.

NASA. Space shuttle launch motion analysis. `https://www.nasa.gov/pdf/522589main_AP_ST_Phys_ShuttleLaunch.pdf`, 2011.

Newman, B. 1983, Actuator-disk theory for vertical-axis wind turbines. *Journal of Wind Engineering and Industrial Aerodynamics*. 15 (1–3), 347–355.

Newman, B. 1986, Multiple actuator-disc theory for wind turbines. *Journal of Wind Engineering and Industrial Aerodynamics*. 24 (3), 215–225.

Nigus, H. 2015, Kinematics and load formulation of engine crank mechanism. *Mechanics, Materials Science & Engineering Journal*.

O Rourke, F., Boyle, F., and Reynolds, A. 2010, Tidal energy update 2009. *Applied Energy*. 87 (2), 398–409.

O'Doherty, T., Mason-Jones, A., O'Doherty, D., and Byrne, C. 2009, Experimental and Computational Analysis of a Model Horizontal Axis Tidal Turbine. In *8th European Wave and Tidal Energy Conference (EWTEC)*, Uppsala, Sweden.

ofgem. ofgem. `www.ofgem.gov.uk/ofgem-publications/76112/domestic-energy-consump-fig-fs.pdf`, 2011.

Parsons Brinckerhoff Ltd. Strategic environmental assessment of proposals for tidal power development in the Severn Estuary: options definition report. `https://www.gov.uk/government/uploads/system/uploads/attachment_data/file/50260/3._Options_Definition_Report_Vol_1.pdf`, 2010.

Pearce-Higgins, J. W., Stephen, L., Douse, A., and Langston, R. H. 2012, Greater impacts of wind farms on bird populations during construction than subsequent operation: results of a multi-site and multi-species analysis. *Journal of Applied Ecology.* 49 (2), 386–394.

Pelc, R. and Fujita, R. M. 2002, Renewable energy from the ocean. *Marine Policy.* 26 (6), 471–479.

Petley, S. and Aggidis, G. 2016, Swansea bay tidal lagoon annual energy estimation. *Ocean Engineering.* 111, 348–357.

Polagye, B., Copping, A., Kirkendall, K., Boehlert, G., Walker, S., Wainstein, M., and Cleve, B. V. 2010, Environmental Effects of Tidal Energy Development: A Scientific Workshop. In *Workshop Briefing Paper. University of Washington, Seattle, Washington.*

Posford Haskoning and HR Wallingford. Poole Harbour Approach Channel Deepening and Beneficial use of Dredged Material Environmental Statement. Technical Report 9P0171/R/mas/Exet, Borough of Poole and Poole Harbour Commissioners, 2004.

Premalatha, M., Abbasi, T., and Abbasi, S. 2014, Wind energy: Increasing deployment, rising environmental concerns. *Renewable and Sustainable Energy Reviews.* 31, 270–288.

Pulse Tidal. Our Technology: Overview. `http://pulsetidal.com/our-technology.html`, 2014.

Ramsbottom, J. Poole Harbour Monitoring Report 2012. Technical Report 432-1301, Poole Harbour Commissioners, 2012.

Roh, S. and Kang, S. 2013, Effects of a blade profile, the Reynolds number, and the solidity on the perferomance of a straight bladed vertical axis wind turbine. *Journal of Mechanical Science and Technology.* 27 (11), 3299–3307.

Sardianou, E. and Genoudi, P. 2013, Which factors affect the willingness of consumers to adopt renewable energies? *Renewable Energy.* 57, 1–4.

Schluntz, J. and Willden, R. 2015, The effect of blockage on tidal turbine rotor design and performance. *Renewable Energy.* 81, 432–441.

Schubel, P. and Crossley, R. 2012, Wind turbine blade design. *Energies.* 5 (9), 3425–3449.

Sempreviva, A., Barthelmie, R., and Pryor, S. 2008, Review of Methodologies for Offshore Wind Resource Assessment in European Seas. *Surveys in Geophysics*. 29 (6), 471–497.

Shields, M., Woolf, D., Grist, E., Kerr, S., Jackson, A., Harris, R., Bell, M., Beharie, R., Want, A., Osalusi, E., Gibb, S., and Side, J. 2011, Marine renewable energy: the ecological implications of altering the hydrodynamics of the marine environment. *Ocean and Coastal Management*. 54 (1), 2–9.

Shiono, M., Suzuki, K., and Kiho, S. 2000, An Experimental Study of the Characteristics of a Darrieus Turbine for Tidal Power Generation. *Electrical Engineering in Japan*. 132 (3), 781–787.

Shives, M. and Crawford, C. 2010, Overall Efficiency of Ducted tidal current turbines. In *OCEANS 2010*, 1–6, Seattle, Washington, USA.

Stephenson, D. J. 1984, *Pipeflow Analysis*. Elsevier Science.

Sustainable Development Commission. Turning the Tide: Tidal Power in the UK. `http://www.sd-commission.org.uk/data/files/publications/Tidal_Power_in_the_UK_Oct07.pdf`, 2007.

The Crown Estate. UK Wave and Tidal Key Resource Areas Project: Summary Report. Technical report, The Crown Estate, 2012.

The Crown Estate. UK Wave and Tidal Key Resource Areas Project: Technical Methodology Report. Technical report, The Crown Estate, 2013.

The Engineering Business Ltd. Stingray Tidal Stream Energy Device – Phase 2. Technical Report T/06/00218/00/REP, Department of Trade and Industry, 2003.

The Engineering Business Ltd. Stingray Tidal Stream Energy Device – Phase 3. Technical Report T/06/00218/00/REP, Department of Trade and Industry, 2005.

The United Kingdom Hydrographic Office. Your EasyTide Prediction. `http://www.ukho.gov.uk/EasyTide/EasyTide/ShowPrediction.aspx?PortID=0036A&PredictionLength=7`, 2016.

Tijsseling, A. and Anderson, A. 2004, The joukowsky equation for fluids and solids. In *Proceedings of the 9th International Conference on Pressure Surges*, 739–751.

underthecblog.org. Tidal power devices. `https://underthecblog.org/2014/07/07/tidal-power-devices/`, 2014.

US Energy Information Administration. How much carbon dioxide is produced per kilowatthour when generating electricity with fossil fuels? `http://www.eia.gov/tools/faqs/faq.cfm?id=74&t=11`.

Vennell, R. 2010, Tuning turbines in a tidal channel. *Journal of Fluid Mechanics.* 663, 253–267.

Vennell, R. 2011a, Estimating the power potential of tidal currents and the impact of power extraction on flow speeds. *Renewable Energy.* 36 (12), 3558–3565.

Vennell, R. 2011b, Tuning tidal turbines in-concert to maximise farm efficiency. *Journal of Fluid Mechanics.* 671, 587–604.

Vennell, R. 2012a, The energetics of large tidal turbine arrays. *Renewable Energy.* 48, 210–219.

Vennell, R. 2012b, Realizing the potential of tidal currents and the efficiency of turbine farms in a channel. *Renewable Energy.* 47, 95–102.

Victor, D., Zhou, D., Ahmed, E., Dadhich, P., Olivier, J., Rogner, H., Sheikho, K., and Yamaguchi, M. 2014, *Climate Change 2014: Mitigation of Climate Change. Contribution of Working Group III to the Fifth Assessment Report of the Intergovernmental Panel on Climate Change*, chapter Introductory chapter. Cambridge University Press, Cambridge, United Kingdom and New York, NY, USA.

Voith Hydro. Tidal current power stations. `http://www.voith.com/en/products-services/hydro-power/ocean-energies/tidal-current-power-stations--591.html`, 2014.

Walker, J., Flack, K., Lust, E., Schultz, M., and Luznik, L. 2014, Experimental and numerical studies of blade roughness and fouling on marine current turbine performance. *Renewable Energy.* 66, 257–267.

Walkington, I. and Burrows, R. 2009, Modelling tidal stream power potential. *Applied Ocean Research.* 31 (4), 239–245.

Waters, R., Stålberg, M., Danielsson, O., Svensson, O., Gustafsson, S., Strömstedt, E., Eriksson, M., Sundberg, J., and Leijon, M. 2007, Experimental results from sea trials of an offshore wave energy system. *Applied Physics Letters.* 90 (3), 034105.

Werkstatt Workshop. Arduino. `https://goo.gl/images/opELd9`, 2016.

Whelan, J., Graham, M., and Peiró, J. 2009, A free-surface and blockage correction for tidal turbines. *Journal of Fluid Mechanics*. 624, 281–291.

wikimedia.org. Aerial view of the tidal barrage on the Rance and of Saint Malo. `https://en.wikipedia.org/wiki/Rance_Tidal_Power_Station#/media/File:Barrage_de_la_Rance.jpg`, 2007.

Williamson, S., Stark, B., and Booker, J. 2011, Low Head Pico Hydro Turbine Selection using a Multi-Criteria Analysis. In *World Renewable Energy Congress 2011*, 1377–1385, Linköping, Sweden.

Wolsink, M. 2012, The research agenda on social acceptance of distributed generation in smart grids: Renewable as common pool resources. *Renewable and Sustainable Energy Reviews*. 16 (1), 822–835.

Wyman, P. and Peachey, C. 1979, Tidal current energy conversion. In *International Conference on future energy concepts*, 164–166, London. Institution of Electrical Engineers.

Wyre Tidal Energy. How a barrage works. `http://http://www.wyretidalenergy.com/tidal-barrage/how-a-barrage-works`, 2014.

Xia, J., Falconer, R., and Lin, B. 2010a, Impact of different operating modes for a Severn Barrage on tidal power and flood inundation in the Severn Estuary, UK. *Applied Energy*. 87 (7), 2374–2391.

Xia, J., Falconer, R., and Lin, B. 2010b, Numerical Model Assessment of Tidal Stream Energy Resources in the Severn Estuary, UK. *Proceedings of the Institution of Mechanical Engineers, Part A: Journal of Power and Energy*. 224 (7), 969–983.

Xia, J., Falconer, R., Lin, B., and Tan, G. 2012, Estimation of annual energy output from a tidal barrage using two different methods. *Applied Energy*. 93, 327–336.

Xia, J., Falconer, R., and Lin, B. 2010c, Impact of different tidal renewable energy projects on the hydrodynamic processes in the Severn Estuary, UK. *Ocean Modelling*. 32, 86–104.

Xu, J.-a. and Sun, H.-y. 2015, Fluid dynamics analysis of passive oscillating hydrofoils for tidal current energy extracting. In *Mechatronics and Automation (ICMA), 2015 IEEE International Conference on*, 2017–2022. IEEE.

Yang, B. and Shu, X. 2012, Hydrofoil optimization and experimental validation in helical vertical axis turbine for power generation from marine current. *Ocean Engineering*. 42, 35–46.

Yaqoot, M., Diwan, P., and Kandpal, T. C. 2016, Review of barriers to the dissemination of decentralized renewable energy systems. *Renewable and Sustainable Energy Reviews*. 58, 477–490.

Young, B. 1995, Design of hydraulic ram pump systems. *Proceedings of the Institution of Mechanical Engineers, Part A: Journal of Power and Energy*. 209 (4), 313–322.

Zhang, Y., Zou, Q., and Greaves, D. 2012, Air–water two-phase flow modelling of hydrodynamic performance of an oscillating water column device. *Renewable Energy*. 41 (159–170).

Zhou, J., Falconer, R., and Lin, B. 2014, Refinements to the EFDC model for predicting the hydro-environmental impacts of a barrage across the Severn Estuary. *Renewable Energy*. 62, 490–505.

Appendices

Appendix A

Load cell codes

Arduino code

```
#include "HX711.h"

// DEFINE INPUT

HX711 scale(A1, A0);
HX711 scale1(A3, A2);

// BEGIN READING INPUT

void setup() {

  Serial.begin(38400);

  scale.set_gain(128);
  scale1.set_gain(128);

}

// WRITE DATA TO SERIAL PORT

void loop() {

    Serial.print(scale.read());
    Serial.print("\t");
    Serial.println(scale1.read());

}
```

MATLAB code

```
%%% CALIBRATION DATA

Force = [0 3000 6000 9000 12000 15000 18000 21000 24000 27000 30000 33000 36000↙
39000];
ml = [0    -176    -309    -446    -578    -704    -845    -995    -1133    -1268↙
-1405     -1542    -1678    -1825];
ml=-ml;
pl=polyfit(ml,Force,2);

cCoeff = 1.119*1.569*1.041*1.0317*0.985; %% secondary correction factors

%%% CREATE SERIAL COMMUNICATION OBJECT ON ARDUINO PORT

arduin=serial('/dev/cu.usbmodemFA131','BaudRate',38400);
fopen(arduin); % initiate arduino communication

%%% CREATE ARRAYS IN MEMORY

lenn2=1000; %% define array length

aa0=zeros(lenn2,1);
aa1=zeros(lenn2,1);
rez0=zeros(lenn2,1);

rez11=zeros(lenn2,1);
cc1=zeros(lenn2,1);
elapsedTime=zeros(lenn2,1);

%%% TAKE 20 S AVERAGE TO ZERO DATA

tic %% Initiate timer

while (toc<=20)

    readz3=fscanf(arduin,'%f'); %% Read data from Arduino

    %STRAIN
    CH1=readz3(1)/512; %% stores data from 1st load cell pair
    CH2=readz3(2)/512; %% stores data from 2nd load cell pair
    rez=CH1+CH2; %% combines load cell data

    %%% Write load cell data to array

    aa0 = [aa0(2:end) ; CH1];
    aa1 = [aa1(2:end) ; CH2];
    rez0 = [rez0(2:end) ; rez];

    %%% Plot load cell data in real time

    figure(1)
    plot(aa0,'linewidth',1,'color','r');
    hold on
    plot(aa1,'linewidth',1,'color','g');
    hold on
    plot(rez0,'linewidth',2,'color','b');

    hold off

    INITIAL=mean(rez); %% Define zero value

end

%%% RECORD LOAD FOR 200 s PERIOD

tic %% restart timer
```

```
while (toc<=200)

  readz3=fscanf(arduin,'%f'); %% read data from Arduino

    %STRAIN
    CH33=readz3(1)/512; %% Assigns data from 1st load cell pair
    CH44=readz3(2)/512; %% Assigns data from 2nd load cell pair

    rez22=CH33+CH44; %% Combine data from the two load cell pairs
    rez22 = rez22 - INITIAL; %% Subtract zero value
    rez11 = [rez11(2:end) ; rez22]; %% Write signal data to array

    cc = polyval(pl,rez22) * cCoeff; %% Convert signal to mass data
    cc1 = [cc1(2:end) ; cc]; %% Write data to array
    elapsedTime = [elapsedTime(2:end); toc]; %% Write time to array

    %%% Plot data in real time

    figure(3)
    subplot (2,1,1)
    plot(cc1,'linewidth',1.6,'color','b');
    subplot (2,1,2)
    plot(cc1,'linewidth',1.6,'color','b');

end
```

Appendix B

Numerical differentiation code (Chartrand, 2011)

```
function u = TVRegDiff( data, iter, alph, u0, scale, ep, dx, plotflag, diagflag )
% u = TVRegDiff( data, iter, alph, u0, scale, ep, dx, plotflag, diagflag );
% u = tvdiff( e, dx, iter, ep, alph );
% Rick Chartrand (rickc@lanl.gov), Apr. 10, 2011
% Please cite Rick Chartrand, "Numerical differentiation of noisy,
% nonsmooth data," ISRN Applied Mathematics, Vol. 2011, Article ID 164564,
% 2011.
%
% Inputs:  (First three required; omitting the final N parameters for N < 7
%           or passing in [] results in default values being used.)
%       data        Vector of data to be differentiated.
%
%       iter        Number of iterations to run the main loop.  A stopping
%                   condition based on the norm of the gradient vector g
%                   below would be an easy modification.  No default value.
%
%       alph        Regularization parameter.  This is the main parameter
%                   to fiddle with.  Start by varying by orders of
%                   magnitude until reasonable results are obtained.  A
%                   value to the nearest power of 10 is usally adequate.
%                   No default value.  Higher values increase
%                   regularization strenght and improve conditioning.
%
%       u0          Initialization of the iteration.  Default value is the
%                   naive derivative (without scaling), of appropriate
%                   length (this being different for the two methods).
%                   Although the solution is theoretically independent of
%                   the intialization, a poor choice can exacerbate
%                   conditioning issues when the linear system is solved.
%
%       scale       'large' or 'small' (case insensitive).  Default is
%                   'small'.  'small' has somewhat better boundary
%                   behavior, but becomes unwieldly for data larger than
%                   1000 entries or so.  'large' has simpler numerics but
%                   is more efficient for large-scale problems.  'large' is
%                   more readily modified for higher-order derivatives,
%                   since the implicit differentiation matrix is square.
%
%       ep          Parameter for avoiding division by zero.  Default value
%                   is 1e-6.  Results should not be very sensitive to the
%                   value.  Larger values improve conditioning and
%                   therefore speed, while smaller values give more
%                   accurate results with sharper jumps.
%
%       dx          Grid spacing, used in the definition of the derivative
%                   operators.  Default is the reciprocal of the data size.
%
%       plotflag    Flag whether to display plot at each iteration.
%                   Default is 1 (yes).  Useful, but adds significant
%                   running time.
%
%       diagflag    Flag whether to display diagnostics at each
%                   iteration.  Default is 1 (yes).  Useful for diagnosing
%                   preconditioning problems.  When tolerance is not met,
%                   an early iterate being best is more worrying than a
%                   large relative residual.
%
% Output:
%
%       u           Estimate of the regularized derivative of data.  Due to
%                   different grid assumptions, length( u ) =
%                   length( data ) + 1 if scale = 'small', otherwise
%                   length( u ) = length( data ).

%% Copyright notice:
% Copyright 2010. Los Alamos National Security, LLC. This material
% was produced under U.S. Government contract DE-AC52-06NA25396 for
```

```
% Los Alamos National Laboratory, which is operated by Los Alamos
% National Security, LLC, for the U.S. Department of Energy. The
% Government is granted for, itself and others acting on its
% behalf, a paid-up, nonexclusive, irrevocable worldwide license in
% this material to reproduce, prepare derivative works, and perform
% publicly and display publicly. Beginning five (5) years after
% (March 31, 2011) permission to assert copyright was obtained,
% subject to additional five-year worldwide renewals, the
% Government is granted for itself and others acting on its behalf
% a paid-up, nonexclusive, irrevocable worldwide license in this
% material to reproduce, prepare derivative works, distribute
% copies to the public, perform publicly and display publicly, and
% to permit others to do so. NEITHER THE UNITED STATES NOR THE
% UNITED STATES DEPARTMENT OF ENERGY, NOR LOS ALAMOS NATIONAL
% SECURITY, LLC, NOR ANY OF THEIR EMPLOYEES, MAKES ANY WARRANTY,
% EXPRESS OR IMPLIED, OR ASSUMES ANY LEGAL LIABILITY OR
% RESPONSIBILITY FOR THE ACCURACY, COMPLETENESS, OR USEFULNESS OF
% ANY INFORMATION, APPARATUS, PRODUCT, OR PROCESS DISCLOSED, OR
% REPRESENTS THAT ITS USE WOULD NOT INFRINGE PRIVATELY OWNED
% RIGHTS.

%% BSD License notice:
% Redistribution and use in source and binary forms, with or without
% modification, are permitted provided that the following conditions
% are met:
%
%      Redistributions of source code must retain the above
%      copyright notice, this list of conditions and the following
%      disclaimer.
%      Redistributions in binary form must reproduce the above
%      copyright notice, this list of conditions and the following
%      disclaimer in the documentation and/or other materials
%      provided with the distribution.
%      Neither the name of Los Alamos National Security nor the names of its
%      contributors may be used to endorse or promote products
%      derived from this software without specific prior written
%      permission.
%
% THIS SOFTWARE IS PROVIDED BY THE COPYRIGHT HOLDERS AND
% CONTRIBUTORS "AS IS" AND ANY EXPRESS OR IMPLIED WARRANTIES,
% INCLUDING, BUT NOT LIMITED TO, THE IMPLIED WARRANTIES OF
% MERCHANTABILITY AND FITNESS FOR A PARTICULAR PURPOSE ARE
% DISCLAIMED. IN NO EVENT SHALL THE COPYRIGHT HOLDER OR
% CONTRIBUTORS BE LIABLE FOR ANY DIRECT, INDIRECT, INCIDENTAL,
% SPECIAL, EXEMPLARY, OR CONSEQUENTIAL DAMAGES (INCLUDING, BUT NOT
% LIMITED TO, PROCUREMENT OF SUBSTITUTE GOODS OR SERVICES; LOSS OF
% USE, DATA, OR PROFITS; OR BUSINESS INTERRUPTION) HOWEVER CAUSED
% AND ON ANY THEORY OF LIABILITY, WHETHER IN CONTRACT, STRICT
% LIABILITY, OR TORT (INCLUDING NEGLIGENCE OR OTHERWISE) ARISING IN
% ANY WAY OUT OF THE USE OF THIS SOFTWARE, EVEN IF ADVISED OF THE
% POSSIBILITY OF SUCH DAMAGE.

%% code starts here
% Make sure we have a column vector.
data = data( : );
% Get the data size.
n = length( data );

% Default checking. (u0 is done separately within each method.)
if nargin < 9 || isempty( diagflag )
    diagflag = 1;
end
if nargin < 8 || isempty( plotflag )
    plotflag = 1;
end
if nargin < 7 || isempty( dx )
    dx = 1 / n;
```

```
end
if nargin < 6 || isempty( ep )
    ep = 1e-6;
end
if nargin < 5 || isempty( scale )
    scale = 'small';
end

% Different methods for small- and large-scale problems.
switch lower( scale )

    case 'small'
        % Construct differentiation matrix.
        c = ones( n + 1, 1 ) / dx;
        D = spdiags( [ -c, c ], [ 0, 1 ], n, n + 1 );
        clear c
        DT = D';
        % Construct antidifferentiation operator and its adjoint.
        A = @(x) chop( cumsum( x ) - 0.5 * ( x + x( 1 ) ) ) * dx;
        AT = @(w) ( sum( w ) * ones( n + 1, 1 ) - [ sum( w ) / 2; cumsum( w ) - w / 2↙
] ) * dx;
        % Default initialization is naive derivative.
        if nargin < 4 || isempty( u0 )
            u0 = [ 0; diff( data ); 0 ];
        end
        u = u0;
        % Since Au( 0 ) = 0, we need to adjust.
        ofst = data( 1 );
        % Precompute.
        ATb = AT( ofst - data );

        % Main loop.
        for ii = 1 : iter
            % Diagonal matrix of weights, for linearizing E-L equation.
            Q = spdiags( 1 ./ ( sqrt( ( D * u ).^2 + ep ) ), 0, n, n );
            % Linearized diffusion matrix, also approximation of Hessian.
            L = dx * DT * Q * D;
            % Gradient of functional.
            g = AT( A( u ) ) + ATb + alph * L * u;
            % Prepare to solve linear equation.
            tol = 1e-4;
            maxit = 100;
            % Simple preconditioner.
            P = alph * spdiags( spdiags( L, 0 ) + 1, 0, n + 1, n + 1 );
            if diagflag
                s = pcg( @(v) ( alph * L * v + AT( A( v ) ) ), g, tol, maxit, P );
                fprintf( 'iteration %4d: relative change = %.3e, gradient norm = %.↙
3e\n', ii, norm( s ) / norm( u ), norm( g ) );
            else
                [ s, ~ ] = pcg( @(v) ( alph * L * v + AT( A( v ) ) ), g, tol, maxit, P↙
);
            end
            % Update solution.
            u = u - s;
            % Display plot.
            if plotflag
                plot( u, 'ok' ), drawnow;
            end
        end

    case 'large'
        % Construct antidifferentiation operator and its adjoint.
        A = @(v) cumsum(v);
        AT = @(w) ( sum(w) * ones( length( w ), 1 ) - [ 0; cumsum( w( 1 : end - 1 ) )↙
] );
        % Construct differentiation matrix.
        c = ones( n, 1 );
```

```
        D = spdiags( [ -c c ], [ 0 1 ], n, n ) / dx;
        D( n, n ) = 0;
        clear c
        DT = D';
        % Since Au( 0 ) = 0, we need to adjust.
        data = data - data( 1 );
        % Default initialization is naive derivative.
        if nargin < 4 || isempty( u0 )
            u0 = [ 0; diff( data ) ];
        end
        u = u0;
        % Precompute.
        ATd = AT( data );

        % Main loop.
        for ii = 1 : iter
            % Diagonal matrix of weights, for linearizing E-L equation.
            Q = spdiags( 1./ sqrt( ( D * u ).^2 +  ep ), 0, n, n );
            % Linearized diffusion matrix, also approximation of Hessian.
            L = DT * Q * D;
            % Gradient of functional.
            g = AT( A( u ) ) - ATd;
            g= g + alph * L * u;
            % Build preconditioner.
            c = cumsum( n : -1 : 1 ).';
            B = alph * L + spdiags( c( end : -1 : 1 ), 0, n, n );
            droptol = 1.0e-2;
            R = ichol( B,struct('type','ict','droptol',droptol)); %% REPLACED cholinc(↙
B, droptol )
            % Prepare to solve linear equation.
            tol = 1.0e-4;
            maxit = 100;
            if diagflag
                s = pcg( @(x) ( alph * L * x + AT( A( x ) ) ), -g, tol, maxit, R', R↙
);
                fprintf( 'iteration %2d: relative change = %.3e, gradient norm = %.↙
3e\n', ii, norm( s ) / norm( u ), norm( g ) );
            else
                [ s, ~ ] = pcg( @(x) ( alph * L * x + AT( A( x ) ) ), -g, tol, maxit,↙
R', R );
            end
            % Update current solution
            u = u + s;
            % Display plot.
            if plotflag
                plot( u, 'ok' ), drawnow;
            end
        end
end

% Utility function.
function w = chop( v )
w = v( 2 : end );
```

Appendix C

Peak analysis code

```
%%% DATA FILE INFORMATION

Ndata = 10; %% Number of data columns

fileName = 'dataAnalysis21March.xlsx';  %% Data file name

cols = ['A:A';'B:B';'C:C';'D:D';'E:E';'F:F';'G:G';'H:H';'I:I';'J:J';'K:K';...
        'L:L';'M:M';'N:N';'O:O';'P:P';'Q:Q';'R:R';'S:S';'T:T';'U:U';'V:V';...
        'W:W';'X:X';'Y:Y';'Z:Z'];  %% data column identifiers

colStr = cellstr(cols);

t = 1/240; %% data sample rate

%%% FILTER VALUES

a = 1;
b = [1/3 1/3 1/3]; %% 3 point moving average filter

% PEAK ANALYSIS

for m = 1:NData

    %%% READ DATA FROM FILE

    xlCol = xlsread(fileName,'9g',colStr{m});
    xlCol2 = (1.01*max(xlCol)) - xlCol; %%% Used for minimum values

    %%% CREATE TIME DATA

    time = 0:t:(t*length(xlCol)-t);
    time = time';
    Time{m} = time(3:end);

    %%%FILTER DATA AND IDENTIFY POSITION OF MAXIMA AND MINIMA

    xlCol = filter(b,a,xlCol);
    xlData{m} = xlCol(3:end);
    [pks,maxLoc] = findpeaks(xlCol,'MinPeakProminence',0.0005);
    maxLoc = time(maxLoc);
    maxima{m} = pks;
    maxLocs{m} = maxLoc;

    [min,minLoc] = findpeaks(xlCol2,'MinPeakProminence',0.0005);
    min = xlCol(minLoc);
    minima{m} = min;
    minLoc = time(minLoc);
    minLocs{m} = minLoc;

    %%% CALCULATE PERIOD BETWEEN MAXIMA AND MINIMA

    maximaPeriod{m} = diff(maxLoc);
    minimaPeriod{m} = diff(minLoc);

    %%% COMPUTE UPSTROKE AND DOWNSTROKE AMPLITUDES

    mina = min(1:length(min)-1);
    minb = min(2:length(min));
    maxa = pks(1:length(pks)-1);
    maxb = pks(2:length(pks));

    minLoca = minLoc(1:length(minLoc)-1);
    minLocb = minLoc(2:length(minLoc));
    maxLoca = maxLoc(1:length(maxLoc)-1);
    maxLocb = maxLoc(2:length(maxLoc));

    if maxLoc(1) > minLoc(1) %% if 1st maximum occurs after 1st minimum
```

```
        if maxLoc(end) > minLoc(end) %% if last point is maximum
            downPeriod = minLocb - maxLoca;
            upPeriod = maxLoc - minLoc;
            totalPeriod = downPeriod + upPeriod(1:length(upPeriod)-1);
            amplitude = pks - min;

        else
            downPeriod = minLocb - maxLoc;
            upPeriod = maxLoc - minLoca;
            totalPeriod = downPeriod + upPeriod;
            amplitude = pks - mina;

        end

    else %% if 1st maximum occurs before 1st minimum

        if maxLoc(end) > minLoc(end) %% if last point is maximum
            downPeriod = minLoc - maxLoca;
            upPeriod = maxLocb - minLoc;
            totalPeriod = downPeriod(2:length(downPeriod)) + upPeriod(1:length↙
(upPeriod)-1);
            amplitude = maxb-min;

        else
            downPeriod = minLoc - maxLoc;
            upPeriod = maxLocb - minLoca;
            totalPeriod = downPeriod(2:length(downPeriod)) + upPeriod;
            amplitude = maxb - mina;
        end

    end;

    %%% WRITE DATA TO CELL ARRAYS

    stroke{m} = amplitude;
    upT{m} = upPeriod;
    downT{m} = downPeriod;
    totalFrequencyC = 1./totalPeriod;
    totalFrequency{m} = totalFrequencyC;

    mW{m} = mean(xlCol);

    xlCol = [];
    xlCol2 = [];

end;
```

Appendix D

Mathematical model code

```
function solveCoupled = SolveCoupledThesisMaths(H0,Q0,rp,rc,L,F,V0,Fric)

%%% Define system size

Ap = pi*((rp)^2);
Ac = pi*((rc)^2);
Ap2 = Ap^2;

%%% Initial conditions

y10=0;
y20=0;

%%% Time step and run span

t = 0.16;
tspan = 0:t:60;

%%% Solve differential equations

[x,Y] = ode45(@(x,Y) coupled(x,Y,H0,Q0,rp,rc,L,F,Fric),tspan,[y10;y20]);

Qp = Y(:,1);
Yc = Y(:,2);

%%% Compute additional information

Vc = [zeros(1,1);(diff(Yc)/t)];
dQp = [zeros(1,1);(diff(Qp)/t)];

P = (H0*998.2*9.81)-((998.2/(2*Ap2)).*(Qp.*(Qp)))-(998.2*9.81.*Yc)-(998.2*L*(dQp/Ap));

Pow = Ac.*Vc.*P;
Pow(Ap.*Vc.*P<0)= 0;
inp = ((998.2*9.81*(H0)))*V0*Ap;

Eff=Pow./inp;

Eff(isinf(Eff)) = 0;
solveCoupled = [x,Qp,Yc,P,Pow,Eff];


function dYdt = coupled(x,Y,H0,Q0,rp,rc,L,F,Fric)

%%% System parameters

g = 9.81;

Dp = rp*2;
Ap = pi*((rp)^2);
Ap2 = Ap^2;
Ac = pi*((rc)^2);
a = g/L;

f = Fric/Dp;

K = 0.5;

C = (1./(2*g*Ap2))*(1+K+(f*L));

%%% Periodic boundary condition

Q = Q0*(0.5*(1+sawtooth(2*pi*F*x)));

%%% Equation definition

dYdt = [(a*Ap)*(H0-Y(2)-(C*(Y(1)*abs(Y(1)))));(1/Ac)*(Y(1)-Q)];
```